



Universidad de Valladolid



PROGRAMA DE DOCTORADO EN  
INVESTIGACIÓN BIOMÉDICA

TESIS DOCTORAL:

**SELF-ASSEMBLING NANOSYSTEMS  
BASED ON ELASTIN-LIKE  
RECOMBINAMERS AND  
ANTIMICROBIAL PEPTIDES FOR  
BIOMEDICAL APPLICATIONS**

Presentada por Sergio Acosta Rodríguez  
para optar al grado de  
Doctor por la Universidad de Valladolid

Dirigida por:

Dr. José Carlos Rodríguez-Cabello



*A mi familia*



**Our greatest weakness lies  
in giving up. The most certain  
way to succeed is always to try  
just one more time.**

Thomas Alva Edison



# Agradecimientos

Esta Tesis es el resultado de varios años de trabajo, durante los cuales he vivido multitud de experiencias tanto profesionales como personales que me han permitido evolucionar y crecer como investigador y madurar como persona. Con estas líneas me gustaría agradecer a todo el mundo que ha compartido conmigo su tiempo durante estos años y que directa o indirectamente han contribuido al desarrollo de esta Tesis.

En primer lugar, quería expresar mis agradecimientos a mis directores de tesis, Carlos, por la oportunidad de iniciar mi carrera investigadora en su grupo de investigación, por toda la formación recibida y enseñarme a trabajar en ciencia.

Quiero continuar agradeciendo a todos los profesores e investigadores senior del grupo. Gracias Matilde, Luis, Javi, Merche y Alessandra por los buenos momentos, por vuestra amabilidad, vuestros consejos y vuestra ayuda.

Durante todo este tiempo he tenido la oportunidad de compartir poyata con muchos y muy dispares compañeros, de los que he aprendido mucho de todos y con cada uno de ellos. Muchas gracias por regalarme tantos y tan buenos recuerdos, habéis sido una parte muy importante de este viaje. Gracias a Isra, Rocío, Menchu, Mohammed, Alicia, Arturo, Guille, Laura, Chus, Lucia, Soraya, Reinal, Eduardo, Dorian, Ito, Filippo, Leander, Miguel, Sofía, Juan, Marcos, Fernando, Irene y Sara. Y en especial a Tatjana que tanto me ha aguantado. Muchas gracias también a Irene y a Teresa por su amabilidad y comprensión, y a Beatriz por su simpatía y buena disposición.

Quiero dar las gracias a Conrado por haberme acogido en su grupo de investigación en dos ocasiones, por haberme ayudado tanto desde el primer

momento en mis andaduras minnesotas, y por ser además de un referente profesional, un buen amigo. I would like to thank all my colleagues from the MDRCBB, to Prof. Rudney and Prof. Gorr for offering me the opportunity to learn in their labs. I am also grateful to Ms. Ruoqiong Chen for her good humor and invaluable help.

A mis amigos, por estar ahí, por escucharme y servir de vía de escape para desconectar siempre que lo he necesitado. Por último, mil gracias a mis padres y hermana, por creer en mí y por su incondicional apoyo en todo lo que hago. ¡Gracias por vuestra paciencia! A todos, ¡¡Gracias!!







## Resumen

**A**umentar el conocimiento de la naturaleza y sus componentes alimenta nuestra capacidad para el desarrollo de biomateriales funcionales y viceversa. Comprender las funciones de las proteínas, la macromolécula más abundante de las células, y sus características estructurales es esencial para producir biomateriales avanzados para aplicaciones biomédicas. En este sentido, la aparición de la tecnología del ADN recombinante proporciona un método sostenible para la producción de proteínas naturales, pero, además para diseñar nuevos materiales proteicos, entre ellos los que destacan los polímeros proteicos recombinantes.

Los polímeros proteicos recombinantes o recombinámeros, son polipéptidos diseñados genéticamente basados en motivos presentes en proteínas estructurales, como el colágeno, la fibroína de la seda de gusano o la resilina, entre ellos, destacan aquellos derivados de la elastina de mamífero o recombinámeros tipo elastina (“elastin-like recombinamers”, ELRs, en inglés). Los ELRs son polipéptidos basados en la repetición del pentapéptido Val-Pro-Gly-X-Gly, presente en los dominios hidrofóbicos de la tropoelastina y de este modo, mimetizan sus propiedades estructurales y biológicas, como su desorden intrínseco a nivel estructural, su transición de fase dependiente de temperatura o sus excelentes propiedades mecánicas entre otros.<sup>[1]</sup> Todo ello junto a su composición polimérica y extrema versatilidad, los convierten en perfectos candidatos para el estudio de procesos biológicos y la fabricación de materiales ‘a medida’ para su uso en aplicaciones biomédicas como la ingeniería de tejidos o la liberación de fármacos o péptidos bioactivos. Por todo ello, esta Tesis tiene como objetivo el diseño, la producción y el procesado de ELRs, focalizados en su aplicación biomédica como nanosistemas autoensamblados y

---

recubrimientos antimicrobianos. Para ello, estudiaremos distintos diseños modulares empleando ELRs y péptidos antimicrobianos (antimicrobial peptides o AMPs, en inglés). Los AMPs son pequeños péptidos catiónicos con la capacidad de matar agentes patógenos, directamente o indirectamente mediante la modulación del sistema inmune y, por lo tanto, constituyen una de las alternativas más prometedoras frente a las infecciones resistentes a antibióticos. En el **Capítulo 1** se presenta una revisión general de las posibles aplicaciones biomédicas tanto de los AMPs como de los ELRs. Actualmente existen una gran variedad de opciones para el tratamiento de estos materiales para la fabricación de hidrogeles, recubrimientos y nanoestructuras que permiten el desarrollo de dispositivos funcionales para múltiples aplicaciones en el campo de la bio(nano)medicina.

## 1. Objetivos

Como objetivo general, en esta tesis se plantea ampliar la comprensión y la complejidad de los biomateriales basados en polímeros proteicos intrínsecamente desordenados (IDPPs) y péptidos antimicrobianos (AMPs) para el desarrollo de materiales avanzados con aplicación en biomedicina, utilizando ELRs como IDPPs modelo.

Más concretamente, el primer objetivo específico es el estudio del ensamblado supramolecular de IDPPs, como modelos para proteínas intrínsecamente desordenadas más complejas. Así, en el **Capítulo 2**, se investigará el efecto de la distribución de cargas en la nanoestructuración de ELRs anfífilicos con diseño dibloque (ELdcRs). Para ello, se diseñará y biosintetizará una biblioteca de polímeros proteicos mediante técnicas recombinantes donde la longitud de la cadena y la densidad de carga varíen. Tras esto, la capacidad de formar estructuras supramoleculares de los distintos ELRs será estudiada mediante diferentes técnicas que incluyen la

microscopía electrónica, la espectroscopía de dicroísmo circular y la dispersión dinámica de luz, entre otras.

Como segundo objetivo se planteará el diseño y la síntesis de polipéptidos híbridos con diseño modular, empleando ELRs y AMPs como bloques funcionales. Específicamente, se propondrán dos estrategias para su evaluación como nanoestructuras autoensamblables en solución (**Capítulo 3**) o como recubrimientos covalentes en superficie (**Capítulo 4 y 5**).

De este modo, en el **Capítulo 3**, se abordará la utilización de AMPs como dominios funcionales capaces de dirigir el autoensamblado de polipéptidos termosensibles. Para ello, se diseñarán y bioproducirán ELRs anfifílicos con diseño dibloque que incorporen un AMP en el extremo de su bloque hidrofílico. Tras ello, se evaluará su comportamiento térmico y nanoestructuración en solución mediante técnicas de microscopía y de difracción de luz.

En los **Capítulos 4 y 5**, se desarrollará una plataforma recombinante multifuncional para la inmovilización de AMPs en dispositivos médicos. El polipéptido híbrido, basado en un ELR policatiónico, presentará un dominio para la funcionalización de superficies y un AMP. En el **Capítulo 4** se probará la capacidad del nuevo polipéptido (AMP-ELR) para formar monocapas autoensambladas en superficie. La inmovilización del biomaterial se evaluará mediante técnicas de caracterización física y química (XPS, WCA, QCM-D) y se analizarán las bioactividades de los recubrimientos frente células bacterianas y humanas.

Finalmente, en el **Capítulo 5**, los ELR híbridos se utilizarán para la funcionalización de superficies de titanio de grado clínico. El anclaje covalente se realizará utilizando organosilanos. Después de probar la resistencia de los recubrimientos, se evaluará su potencial antimicrobiano

---

frente a dos modelos complejos de biofilms orales en condiciones dinámicas y su citocompatibilidad frente células humanas primarias gingivales.

## 2. Metodología

### 2.1. Materiales

Todo el material de vidrio utilizado fue lavado previamente con ácido clorhídrico (1%), detergente Alconox, y fue aclarado de forma secuencial con agua destilada, acetona, agua destilada y agua ultrapura tipo II. Tras esto, se procedió a su secado en una estufa a 80 °C. El material de plástico desechable (puntas de pipetas, placas Petri, placas de pocillos, tubos de centrífuga etc.) fue adquirido estéril o se esterilizó mediante autoclavado a 121 °C, 1 atm durante 20 min en un autoclave Autotester E-75 (Selecta, España). Los reactivos empleados se detallan en la **Tabla 1**.

**Tabla 1.** Reactivos empleados durante el desarrollo de esta tesis.

Reactivo	Proveedor
Ácido acético	Sigma-Aldrich, EE.UU.
Ácido clorhídrico	ThermoFisher Scientific, EE.UU.
Ácido etilendiaminatetraacético (EDTA)	Sigma-Aldrich, EE.UU.
Ácido fórmico	Sigma-Aldrich, EE.UU.
Acrilamida/Bis-acrilamida 37,5:1 40% (p/v)	Amresco LLC, EE.UU.
AEBSF	Apollo Scientific, Reino Unido
Agar	BD Biosciences, EE.UU.

---

Agarosa Seakem	Cambrex, EE.UU.
Agua ultrapura tipo I	MilliporeSigma, EE.UU.
Agua ultrapura tipo II	MilliporeSigma, EE.UU.
Alconox	Sigma-Aldrich, EE.UU.
Azul alcian	Sigma-Aldrich, EE.UU.
Antiespumante 204	Sigma-Aldrich, EE.UU.
Ampicilina	Apollo Scientific, Reino Unido
Arginina	Sigma-Aldrich, EE.UU.
Azul de Alcian	Sigma-Aldrich, EE.UU.
Azul de bromofenol	Sigma-Aldrich, EE.UU.
BacTiter-Glo™ Microbial Cell Viability Assay	Promega, EE.UU.
Bromuro de cianógeno (CNBr)	Sigma-Aldrich, EE.UU.
Cloruro de cobre (CuCl <sub>2</sub> )	Sigma-Aldrich, EE.UU.
Cloruro de potasio (KCl)	Sigma-Aldrich, EE.UU.
Cloruro de sodio (NaCl)	ThermoFisher Scientific, EE.UU.
Cristal violeta	Sigma-Aldrich, EE.UU.
Dimetilsulfóxido deuterado (DMSO-d <sub>6</sub> )	Sigma-Aldrich, EE.UU.
Dodecilsulfato sódico (SDS)	Sigma-Aldrich, EE.UU.
E-64	Apollo Scientific, EE.UU.

---

Enzimas endonucleasas ( <i>SapI</i> , <i>EaeI</i> , <i>EcoRI</i> , <i>DpnI</i> , <i>XhoI</i> , <i>XbaI</i> ) y enzimas (T4 DNA ligasa, FastAP, SAP)	ThermoFisher Scientific, EE.UU.
Etanol	Panreac Química S.L.U., España
Extracto de levadura	BD Biosciences, EE.UU.
Fluoruro de fenilmetilsulfato (PMSF)	Apollo Scientific, EE.UU.
Gentamicina/Anfotericina	ThermoFisher Scientific, EE.UU.
Glicerol	Sigma-Aldrich, EE.UU.
Glicina	Sigma-Aldrich, EE.UU.
Glucosa	Panreac Química S.L.U., España
Glutaraldehído	Sigma-Aldrich, EE.UU.
Hemina	Sigma-Aldrich, EE.UU.
Hidróxido de sodio (NaOH)	ThermoFisher Scientific, EE.UU.
Kit de extracción de ADN en geles de agarosa “PureLink Quick Gel Extraction”	Invitrogen, EE.UU.
Kit de purificación de ADN MasterPure™	Epicenter, Illumina, Inc., EE.UU.
Kit de purificación de plásmidos (NucleoSpin Plasmid)	Macherey-Nagel, Germany
Leupeptina	Apollo Scientific, EE.UU.
Marcador de ADN (1kb Plus Ladder)	Invitrogen, EE.UU.
Marcador de proteínas (Pierce Unstained)	ThermoFisher Scientific, EE.UU.

---



---

Medio de cultivo de auto-inducción (Terrific Broth, TB)	Formedium, Reino Unido
Medio de cultivo de lisogenia (Luria Bertani, LB)	Conda, España
Medio de cultivo Mueller Hinton tipo II (MHB)	Sigma-Aldrich, EE.UU.
Medio de cultivo Todd Hewitt Broth (THB)	BD Biosciences, EE.UU.
Medio de cultivo Tryptone Soy Broth (TSB)	Sigma-Aldrich, EE.UU.
Medios de cultivo (DMEM 1g/L glucosa, Medium 200)	Gibco, EE.UU.
Menadiona (vitamina K3)	Sigma-Aldrich, EE.UU.
Mucina gástrica porcina parcialmente purificada	Sigma-Aldrich, EE.UU.
Penicilina/Estreptomicina	Gibco, EE.UU.
Pepstatina A	Apollo Scientific, EE.UU.
Peptona (Triplicate peptone)	Sigma-Aldrich, EE.UU.
Proteosa-peptona	Sigma-Aldrich, EE.UU.
Suero fetal bovino (FBS)	Gibco, EE.UU.
Tampón fosfato salino (PBS)	Gibco, EE.UU.
Tetrametiletilendiamina (TEMED)	Sigma-Aldrich, EE.UU.
Tetróxido de osmio (OsO <sub>4</sub> )	Sigma-Aldrich, EE.UU.
Tinción de ADN (SimplySafe)	Eurx, Polonia
Tinción de viabilidad Filmtracer LIVE/DEAD	ThermoFisher Scientific, EE.UU.
Tripsina/EDTA 0.05%	Gibco, EE.UU.

---

---

Tris(hidroximetil)aminometano (Tris)	Sigma-Aldrich, EE.UU.
Azul Tripan	Invitrogen, EE.UU.
Urea	Sigma-Aldrich, EE.UU.
$\beta$ -Mercaptoetanol	Sigma-Aldrich

---

Adicionalmente, distintas cepas bacterianas o líneas celulares humanas fueron empleadas para llevar a cabo la construcción génica, test antimicrobianos y pruebas de citocompatibilidad (**Tabla 2**).

**Tabla 2.** Cepas bacterianas y líneas celulares empleadas en el desarrollo de esta tesis.

<b>Ensayo</b>	<b>Cepa bacteriana/Línea celular</b>	<b>Proveedor</b>
Clonaje	<i>Escherichia coli</i> XL-1 Blue competent cells	Agilent, EE.UU.
Subclonaje	<i>Escherichia coli</i> XL-1 Blue subcloning	Agilent, EE.UU.
Producción recombinante	<i>Escherichia coli</i> BLR (DE3)	ThermoFisher Scientific, EE.UU.
Actividad antimicrobiano	<i>Staphylococcus aureus</i> 25923	ATCC, EE.UU.
Actividad antimicrobiano	<i>Staphylococcus epidermidis</i> 35984	ATCC, EE.UU.
Actividad antimicrobiano	<i>Streptococcus gordonii</i> DL-1	Prof. Joel Rudney (Universidad de Minnesota, EE.UU.)
Actividad antimicrobiano	<i>Pseudomonas aeruginosa</i> PAO1 Xen41	PerkinElmer Inc., Waltham, EE.UU.

---

Actividad antimicrobiana	<i>Microcosmo oral</i> 769-NS	Prof. Joel Rudney (Universidad de Minnesota, EE.UU.)
Análisis de la citocompatibilidad	Fibroblastos de prepucio humano (HFF-1)	Life Technologies, España
Análisis de la citocompatibilidad	Fibroblastos primarios gingivales de origen humano	ATCC, EE.UU.

---

## 2.2. Métodos

### 2.2.1. Síntesis recombinante de ELRs

Todos los ELRs empleados durante el desarrollo de esta Tesis fueron producidos recombinantemente y de forma exclusiva para el desarrollo de la misma. En primer lugar, se llevó a cabo la construcción de los genes codificantes de los ELRs y AMP-ELRs mediante ingeniería genética siguiendo el método iterativo-recursivo previamente descrito.<sup>[2]</sup> Los genes codificantes de las secuencias monoméricas de los ELRs o de las secuencias específicas, como AMPs, fueron producidos por una empresa externa (NZYTech, Portugal). Estos genes se clonaron en el plásmido de clonación pDriveAll utilizando *E. coli* XL1 como cepa de clonación. Dicho plásmido proviene del vector de clonación comercial pDrive (Novagen), en el que se mutaron las dianas de reconocimiento de las endonucleasas tipo II *SapI* y *EarI*, para llevar a cabo la construcción de los genes de manera controlada y direccional.<sup>[2]</sup>

Una vez alcanzada la construcción final, ésta se introdujo en el plásmido de expresión p7, desarrollado también en el grupo Bioforge a partir del vector comercial pET25(+) (Novagen, EE.UU.).<sup>[3]</sup> Este vector de expresión incorpora las secuencias de reconocimiento para su sobreexpresión en cepas *E. coli* con sistema de expresión basado en la ARN

---

polimerasa del fago T7. En nuestro caso, los plásmidos de expresión con los constructos deseados fueron transformados en la cepa BLR (DE3), cepa derivada de BL21 que carece de la recombinasa *recA*,<sup>[4]</sup> favoreciendo, de este modo, la expresión de secuencias poliméricas.

Tras esto, se realizó un screening de las cepas hiperproductoras mediante electroforesis en condiciones desnaturalizantes (SDS-PAGE) y la cepa que mayor expresión mostró se empleó para inocular un fermentador de 15 L (Applikon Biotechnology). La fermentación se llevó a cabo en condiciones de pH, temperatura, agitación y concentración de O<sub>2</sub> controladas durante 16-18 horas. Seguidamente, tras el lavado de las bacterias con tampón salino, se extrajo el biomaterial mediante disrupción de las mismas en un disruptor mecánico (homogeneizador GEA Lab PandaPLUS 2000, GEA Farm Technologies, Nueva Zelanda) y se purificó mediante ciclos de calentamiento-centrifugación (40 °C) y enfriamiento-centrifugación (4 °C) consecutivos aprovechando la separación de fase reversible dependiente de la temperatura de los ELRs. El solvente para disolver los ELRs fue agua y se añadió una concentración de 1.5 M de NaCl para contribuir a la precipitación en caliente de los biomateriales. Tras 3-4 ciclos de purificación se verificó que los ELRs estén completamente puros mediante SDS-PAGE, se dializaron frente agua destilada (3 cambios) y agua ultrapura (1 cambio) para eliminar todo tipo de sales, se filtraron a través de filtros de 0.22 µm (Nalgene, EE.UU.) para conseguir un producto estéril que se liofilizaron (FreeZone 1, LABCONCO) y congelaron a -20 °C hasta su uso.

### *2.2.2. Modificación de ELRs*

Durante esta tesis se han realizado dos modificaciones químicas de ELRs expuestas a continuación.

### *Liberación bloque protector*

Los AMP-ELRs híbridos fueron diseñados como pro-polipéptidos de tal modo que se incorporó un bloque protector con varias funciones: (i) aumentar expresión del constructo híbrido, (ii) proteger al microorganismo huésped de posibles efectos secundarios dañinos, (iii) incorpora una Met en el extremo C-terminal, de tal modo que es fácilmente escindible en un único paso mediante CNBr y (iv) su naturaleza catiónica facilita su separación del constructo de interés mediante precipitación ácida.

La liberación del bloque protector se llevó a cabo disolviendo el ELR a una concentración de 20 mg mL<sup>-1</sup> en ácido fórmico (70%) y añadiendo CNBr (200:1 relación molar CNBr:Met). Tras 20 h de incubación en oscuridad a *T* ambiente, el exceso de CNBr se eliminó en un rotavapor y se dializó frente a agua destilada (4 pasos).

### *Modificación de ELRs con D-péptidos*

Se probó a incorporar en los ELRs péptidos antimicrobianos compuestos por D-amino ácidos, los cuales no son producidos de manera natural por el microorganismo productor *E. coli*. El péptido empleado (D-GL13K) fue sintetizado químicamente por la empresa Pepscan (Holanda) con una pureza superior al 90% e incluyendo un grupo azida (N<sub>3</sub>) en su extremo C-terminal (N<sub>3</sub>-Gkiiklkaslkll-NH<sub>2</sub>).

Los grupos azida reaccionan selectivamente con grupos ciclooctinos en condiciones fisiológicas sin precisar de solventes químicos que comprometan la citocompatibilidad. De este modo, se modificaron con grupos ciclooctino los grupos amino de las cadenas laterales de las Lys presentes en el ELR, siguiendo el protocolo previamente desarrollado en el grupo Bioforge.<sup>[5]</sup>

---

### 2.2.3. Caracterización físico-química de los ELRs

#### *Electroforesis en gel de poliacrilamida*

La electroforesis en geles de poliacrilamida se realizó en condiciones desnaturalizantes, añadiendo el detergente SDS, que desnaturaliza las proteínas, para una migración a través del gel dependiente de su peso molecular (MW). Para ello, empleamos el sistema de electroforesis vertical “MiniVE” de Hoefer (Amersham Pharmacia Biotec, Reino Unido) donde se corrieron las muestras a una intensidad fija de 25 mA por gel. Los geles se prepararon siguiendo el protocolo descrito por Laemmli.<sup>[6]</sup>

Cuando el frente de proteínas salió del gel, éstos se tiñeron utilizando una disolución acuosa de  $\text{CuCl}_2$  (0.3 M). Las imágenes de los geles se tomaron con el sistema Gel Doc<sup>TM</sup> EZ Imager (Bio-Rad, EE.UU.).

#### *Espectrometría de masas y análisis de aminoácidos*

De manera complementaria, el peso molecular de los ELRs se evaluó mediante espectrometría de masas del tipo “Matrix-assisted laser desorption/ionization–Time-of-flight” (MALDI-TOF) utilizando el equipo Voyager STR (Applied Biosystems, EE.UU.). Además, la composición aminoacídica fue analizada mediante cromatografía tras la hidrolización de la muestra empleando un equipo de “High-Performance Liquid Chromatography” (HPLC) en gradiente Waters 600 acoplado a un detector de UV Waters 2487 (Waters, EE.UU.). Ambas técnicas se llevaron a cabo en el Laboratorio de Técnicas Instrumentales (LTI) de la Universidad de Valladolid.

#### *Caracterización del comportamiento térmico*

Para caracterizar el comportamiento térmico de los ELRs a altas concentraciones se empleó el equipo de calorimetría diferencial de barrido, Mettler Toledo 822e, con refrigeración mediante nitrógeno líquido. La

concentración utilizada fue de 50 mg mL<sup>-1</sup> y se empleó un volumen de 20 µL. Los experimentos consistieron en una primera etapa isotérmica a 5 °C durante 5 minutos, seguida de una etapa de calentamiento, desde 5 a 60 °C, a una velocidad de 5 °C min<sup>-1</sup>.

La caracterización a bajas concentraciones (1 mg mL<sup>-1</sup>) se llevó a cabo mediante medidas de turbidimetría o de dispersión dinámica de luz (DLS). Se prepararon las muestras a 25 µM en agua ultrapura. Para medir la turbidimetría de las muestras respecto la temperatura se programaron rampas de calentamiento de 5 a 40 °C (con una velocidad de 0.25 °C min<sup>-1</sup> y se registró el valor de la absorbancia de la muestra a 350 nm cada grado en el espectrofotómetro Cary 100UV-Vis (Agilent, EE.UU.).

Para calcular la temperatura de transición mediante DLS, se registró la intensidad de luz dispersada cada 4 °C desde 5 hasta 53 °C en un equipo ZetaSizer Nano (Malvern Instruments, Reino Unido). Las muestras se estabilizaron durante 2 minutos a cada temperatura y se midieron por triplicado con 11 corridas por medición. La temperatura a la cual la intensidad dispersada alcanzó el 50% de la intensidad se consideró como la temperatura de solución crítica baja.

#### *Dicroísmo circular*

Los espectros de dicroísmo circular (CD) se obtuvieron utilizando un espectropolarímetro Jasco J-810 (Jasco, EE.UU.) equipado con un controlador de temperatura en los servicios técnicos a la investigación (SSTI) de la Universidad de Alicante (España). Las muestras de ELR se disolvieron a 5 mM y se midieron en células de cuarzo de 0.1 cm en el rango de 190-250 nm. La temperatura se estabilizó a 37 °C durante 10 minutos antes de la medición. Los porcentajes de estructura secundaria se determinaron usando el servidor web BeStSel (Beta Selection Structure, o

---

selección de estructuras beta) [7,8] en el rango de 200-250 nm, siempre y cuando el voltaje del dinodo se encontrara por debajo de 500 nm.

*Caracterización de nanoestructuras mediante técnicas de dispersión de luz dinámica*

La distribución del tamaño de las nanopartículas y el potencial zeta se midieron en agua ultrapura utilizando el equipo Zetasizer Nano (Malvern Instruments, Reino Unido), con un ángulo de dispersión de 173° y equipado con un láser HeNe (633 nm) con una potencia de salida de 10 mW. Las distribuciones de tamaño se analizaron en un rango de concentraciones por encima de la concentración micelar crítica. Cada muestra se midió por triplicado.

*Caracterización de nanoestructuras mediante microscopía electrónica de transmisión*

Las muestras para microscopía electrónica de transmisión (TEM) se prepararon sobre rejillas de cobre recubiertas con una película de carbono y con soporte de malla 300 (C300Cu). En primer lugar, las rejillas fueron hidrofilizadas mediante un tratamiento con plasma de 20 segundos de duración, usando para ello el equipo PDC-002 (Harrick Plasma, EE. UU.) a baja potencia (7,2 W aplicado a la bobina de RF). Tras esto, situamos 15 µL de las distintas soluciones de ELR pre-incubadas a la temperatura y concentración deseada, de agua ultrapura y de una solución de acetato de uranilo (1% p/v) sobre una tira de Parafilm® colocada sobre una superficie de vidrio atemperada a la temperatura deseada. Las rejillas hidrofilizadas se depositaron sobre la gota de ELR durante 90 s, seguidamente sobre la de agua ultrapura durante 60 s, y finalmente, sobre solución de tinción negativa durante otros 60 s, empleando papel de filtro (Whatman® Gel Blot GB003) para eliminar el exceso de solución después de cada paso. Las imágenes se



tomaron usando un microscopio Tecnai Thermionic T20 operado a 200kV (SAI, Universidad de Zaragoza, España).

*Caracterización de nanoestructuras mediante criomicroscopía electrónica de transmisión*

Las muestras para el análisis mediante criomicroscopía electrónica de transmisión (Cryo-TEM) se disolvieron a una concentración de 25  $\mu$ M en agua ultrapura a 5 °C durante 24 h y se calentaron a 37 °C durante 30 min. Se prepararon muestras Cryo-TEM antes y después del calentamiento para evaluar los cambios en el ensamblado de las muestras respecto a la temperatura.

La preparación y visualización de muestras Cryo-TEM se realizó en la "Plataforma de Microscopía Electrónica" (CICbioGUNE, Universidad del País Vasco, España). Se colocaron cuatro microlitros de la muestra en una rejilla de malla 300 con recubrimiento de carbono lacey (LC300-Cu; Microscopy Sciences) y se incubaron dentro de la cámara de un Vitrobot Mark III (FEI Inc., Holanda) a la temperatura deseada (4 o 37 °C) y a una humedad relativa cercana a la saturación (95% HR) durante 30 s. La mayor parte del líquido en la rejilla se eliminó mediante transferencia (3 s en un desplazamiento de -3 mm) y se vitrificó sumergiéndolo en etano líquido, previamente enfriado con nitrógeno líquido a aproximadamente -180 °C.

Las imágenes se tomaron a temperatura de nitrógeno líquido en el microscopio electrónico de transmisión JEM-2200FS / CR (JEOL Europe, Croissy-sur-Seine, Francia) operado a 200 kV. Un filtro de energía en columna (filtro Omega) permitió obtener imágenes con contraste y relación señal/ruido mejorado. Las imágenes digitales se grabaron en una cámara Ultrascan4000 <sup>TM</sup> de 4K  $\times$  4K (Gatan, Inc.) utilizando el software DigitalMicrograph <sup>TM</sup> (Gatan, Inc.).

---

### *Análisis de hidrogeles mediante microscopía electrónica de barrido*

Para visualizar la morfología de las muestras que formaron hidrogeles físicos, éstas se incubaron durante 1 hora a una concentración de 2.5 mM a 37 °C. Tras esto se criofracturaron en N<sub>2</sub> líquido y se liofilizaron. Las imágenes fueron tomadas con un microscopio FEI Quanta 200 FEG (FEI Company, EE. UU.) en modo de bajo vacío (SAI, Universidad de Zaragoza, España). Se aplicó una capa de Pd de 20 nm con un aplicador de vacío Leica EM ACE200 para evitar efectos de carga. Las imágenes SEM se analizaron utilizando el software ImageJ.

### *Caracterización de hidrogeles mediante reología*

Las propiedades mecánicas de los hidrogeles se analizaron realizando medidas de cizallamiento oscilante y de flujo en un reómetro AR2000 (TA Instruments) utilizando una geometría paralela con un diámetro de 40 mm. Las medidas se realizaron con un volumen de muestra de 1300 µL (espacio entre geometría y superficie de 1100 µm) a 37 °C, controlando la temperatura con una placa Peltier. Después de la deposición de la muestra a 4 °C, la formación de gel se realizó *in situ*. Los datos se registraron utilizando el software TRIOS (v4.1.1.33073). Para las mediciones de cizallamiento oscilatorio, se realizó un barrido de deformación desde 0.01% hasta 15% a una frecuencia angular de 1 Hz para determinar la región de viscoelasticidad lineal (LVR, de sus siglas en inglés). Los barridos de frecuencia se llevaron a cabo secuencialmente en el rango de 0.1 a 50 Hz, con una tensión constante de 0.3% (correspondiente al LVR). El módulo de almacenamiento ( $G'$ ) y el de pérdidas ( $G''$ ) se obtuvieron a partir de las mediciones reológicas. El factor de pérdidas ( $\tan \delta \equiv G'' / G'$ , donde  $\delta$  es el ángulo de fase entre la respuesta de salida al estímulo de entrada) y la magnitud del módulo complejo ( $|G^*|^2 = (G')^2 + (G'')^2$ ) se calcularon utilizando los valores anteriores. Además, se llevaron a cabo medidas de

flujo para calcular la viscosidad. Las muestras se acondicionaron con un cizallamiento previo de  $500 \text{ s}^{-1}$  durante 1 minuto, tras esto, se midió la viscosidad en una rampa de flujo de 500 a  $0.1 \text{ s}^{-1}$ . Todas las mediciones se realizaron al menos por triplicado.

#### 2.2.4. Caracterización de recubrimientos

##### *Ángulo de contacto*

Las mediciones del ángulo de contacto con el agua se realizaron utilizando un instrumento OCA 15plus (DataPhysics, Alemania) equipado con una cámara CCD. Se analizaron al menos 10 gotas de agua ultrapura ( $0.5 \mu\text{L}$ ) por grupo. Todas las imágenes se recogieron después de la estabilización durante 15 s, y se promediaron los ángulos izquierdo y derecho.

##### *Espectroscopía fotoelectrónica de rayos X*

Se usó un espectrómetro de fotoelectrones de rayos X K-Alpha (ThermoFisher Scientific, EE. UU.) (SSTII, Universidad de Alicante, España) para analizar las superficies de las muestras de oro modificadas. El cual utiliza radiación monocromática de Al – K ( $1486.6 \text{ eV}$ ) para recolectar todos los espectros, con un punto de rayos X elíptico (longitud del eje mayor de  $400 \mu\text{m}$ ) a  $3 \text{ mA} \times 12 \text{ kV}$ . El analizador alfa hemisférico funcionó en modo de energía constante con energías de survey de  $200 \text{ eV}$  para medir toda la banda de energía y  $50 \text{ eV}$  en un análisis fino para medir selectivamente los elementos particulares (C 1s, N 1s, O 1s y Au 4f). Los espectros XPS se analizaron con el software Advantage.

##### *Microbalanza de cuarzo con disipación*

La microbalanza de cuarzo con disipación (QCM-D) se utilizó para calcular el espesor de los recubrimientos covalentes.<sup>[9,10]</sup> Esta técnica

---

permite mediciones simultáneas de los cambios de frecuencia y de disipación de energía. El equipo utilizado fue el Q-Sense Explorer System (Biolin Scientific, Suecia). Cada solución se perfundió con una bomba peristáltica a través del circuito de flujo circular a  $20 \mu\text{L min}^{-1}$ . Todas las pruebas se realizaron a  $23 \text{ }^\circ\text{C}$ . Se usó como sensor un cristal de cuarzo recubierto de oro de 5 MHz con corte AT con una rugosidad superficial estimada de 1 nm, según las especificaciones técnicas del fabricante (QSX301 Gold, Biolin Scientific, Suecia). Los sensores se limpiaron con plasma de argón en un limpiador de plasma durante 5 minutos inmediatamente antes de su uso.

La siguiente secuencia de flujos (o eventos) se aplicó en cada medición QCM-D. Primero, dado que las soluciones estudiadas se prepararon en agua ultrapura, se pasó agua ultrapura a través de la cámara durante 2 minutos para definir una línea base estable, seguido de la solución de péptido o polipéptido ( $200 \mu\text{M}$ ) durante 25 minutos, y un lavado final con agua ultrapura durante 20 min. Se realizaron tres réplicas para cada medición.

Los datos experimentales QCM-D se ajustaron numéricamente al modelo viscoelástico Voigt (continuo) utilizando el algoritmo Simplex de Dantzig,<sup>[11]</sup> tal como viene implementado en el software de Biolin Scientific (Q-Sense Dfind). Se utilizó un ajuste incremental descendente, con la calidad del ajuste determinada por el parámetro  $\chi^2$  (los valores más bajos de  $\chi^2$  indican un mejor ajuste). Siempre se obtuvo un valor de  $\chi^2$  menor que 2 en los ajustes numéricos.

### 2.2.5. Ensayos antimicrobianos

#### *Concentración mínima inhibitoria*

La actividad antimicrobiana de los polipéptidos híbridos (AMP-ELRs) se evaluó mediante ensayos de valoración de la actividad mínima inhibitoria (minimal inhibitory concentration o MIC) frente la cepa Gram (+) *Streptococcus gordonii* DL-1 y frente a la cepa Gram (-) *Pseudomonas aeruginosa* PAO1 *Xen*41 (PerkinElmer Inc., Waltham, MA, EE.UU.) siguiendo protocolos estandarizados descritos previamente.<sup>[12]</sup> Brevemente, se picaron 3-5 colonias de *S. gordonii* o *P. aeruginosa* y se inocularon en un tubo estéril de 15 mL con 2 mL de medio de cultivo de infusión de corazón y cerebro (BHI) y de medio Mueller-Hinton (MHB), respectivamente para cada una de las cepas. Después de la incubación durante 16 h a 37 °C en condiciones aeróbicas (*P. aeruginosa*) o con 5% de CO<sub>2</sub> (*S. gordonii*), los inóculos se diluyeron hasta  $5 \times 10^5$  unidades formadoras de colonia (UFC) por mL en BHI o MHB. Paralelamente, se prepararon diluciones seriadas de los AMP-ELRs a partir de una solución de 1280 µM, de las cuales se emplearon 10 µL para incubar junto a 90 µL de esta la solución bacteriana en placas de polipropileno de 96 pocillos a 37 °C y 100 rpm, durante 20 h. El crecimiento bacteriano se evaluó visualmente y por densidad óptica a 570 nm en un lector de placas Synergy HT (BioTek, Winooski, EE.UU.). Además, los péptidos de diseño GL13K-NH<sub>2</sub> y 1018-NH<sub>2</sub> (adquiridos por Pepscan (Holanda) con una pureza de más del 97%) se probaron como controles positivos. Cada experimento fue repetido al menos tres veces.

#### *Evaluación de biofilm mediante microscopía de fluorescencia, confocal y electrónica*

Tras crecer los biofilm bacterianos sobre las superficies, éstas se lavaron cuidadosamente con NaCl (0.9%) para eliminar las bacterias no adheridas. Después, las muestras se observaron mediante microscopía de

---

fluorescencia, confocal y microscopía electrónica de barrido (SEM). Para la visualización mediante fluorescencia, las muestras se tiñeron usando el kit LIVE/DEAD BacLight Bacterial Viability (ThermoFisher Scientific, EE.UU.) siguiendo las instrucciones del fabricante, luego se montaron en un portamuestras de vidrio y se visualizaron usando un microscopio Nikon Eclipse Ti E (Japón). Para su análisis mediante microscopía confocal se tiñeron de la misma manera, pero en este caso, gracias a que se empleó un objetivo de inmersión en agua (Apo 25X LWD, 1.1 NA, Nikon) se pudieron observar los biofilm directamente sobre el disco, empleando para ello un microscopio confocal multifotón (A1R-HD, Nikon Instruments Inc., Japón). Las emisiones de fluorescencia se recogieron a 488 nm para Syto9 (células vivas) y a 561 nm para yoduro de propidio (células muertas). El área escaneada fue de 1024 x 1024 píxeles ( $0.12 \mu\text{m px}^{-1}$ ) con un Z-stack cada 0.375  $\mu\text{m}$ . Las imágenes se analizaron utilizando el software NIS-Elements Advanced Research analysis software (versión 4.5, Nikon Corporation, Japón).

Para la visualización de los biofilms mediante SEM, se fijaron siguiendo protocolos previamente descritos.<sup>[13]</sup> Para ello, tras la incubación las superficies fueron incubaron en una solución de fijación primaria (glutaraldehído al 2.5% y azul Alcian al 0.15% en tampón fosfato 0.1 M, pH 7.4, durante 60 minutos). Después de lavar las superficies en 0.1 M PB, se empleó una solución de fijación secundaria ( $\text{OsO}_4$  al 1% en 0.1 M PB, 60 min). Las muestras se lavaron y se procedió a su deshidratación mediante su sumersión en soluciones de etanol con concentraciones graduales (50%, 70%, 80%, 95% y 100%) y se secaron sustituyendo el etanol por  $\text{CO}_2$  líquido y llevándolo a su punto crítico en un equipo Emitech K850. Se recubrieron con una capa de oro de 50 Å (Emitech K575X) y se visualizaron en un

microscopio electrónico de barrido ambiental (ESEM) FEI-Quanta 200 Field Emission Gun.

*Cuantificación de biofilm: cristal violeta, ATP, UFC y ADN*

La capacidad antibiofilm de los recubrimientos se cuantificó mediante tres técnicas diferentes: tiñéndolos con cristal violeta, midiendo la actividad metabólica remanente en la superficie, la cantidad de unidad formadoras de colonia o la cantidad total de ADN de la muestra. El colorante cristal violeta (CV) tiñe la biomasa total restante, lo que proporciona una idea de la reducción de biofilm sin discriminar entre células vivas y muertas. Para aplicarlo se siguió el protocolo descrito por O'Toole.<sup>[14]</sup> Las superficies con los biofilm fueron sumergidas en una solución de CV al 0.1% durante 15 minutos, se lavaron 4 veces con agua destilada y se secaron a temperatura ambiente durante 16 h. Con una solución de ácido acético (30%) se solubilizó el CV de las superficies y se cuantificó el colorante en una placa de 96 pocillos midiendo la absorbancia a 590 nm en un lector de microplacas SpectraMax M2e (Molecular Devices, EE.UU.). Si la absorbancia era demasiado alta ( $Abs_{590} > 1$ ), la solución de CV se diluyó con agua ultrapura aplicando el factor de dilución correspondiente.

La actividad metabólica de biofilms estafilococales formados en condiciones estáticas se midió cuantificando el ATP usando el kit de ensayo de viabilidad de células microbianas BacTiter-Glo (Promega, EE.UU.) que da una señal luminiscente en presencia de ATP. Para ello, se añadieron 330  $\mu$ L de la solución del kit a cada superficie en una placa de 24 pocillos y las muestras se incubaron durante 5 minutos en la oscuridad, luego se transfirió una alícuota de 100  $\mu$ L a una placa blanca de 96 pocillos y se cuantificó la luminiscencia con un lector de microplacas SpectraMax L (Molecular Devices).

---

Para la evaluación de los biofilm formados en el reactor por goteo (drip flow biofilm reactor, DFBR), se recogió la biomasa adherida a los discos testados mediante sonicación en 330 o 660  $\mu\text{L}$  de solución salina (NaCl al 0.9%) atemperada a 4  $^{\circ}\text{C}$ , dependiendo de si se trataban de biofilms de monoespecies *S. gordonii* o microcosmos orales, respectivamente. Posteriormente, se incubaron 100  $\mu\text{L}$  del extracto bacteriano durante 2 horas a 37  $^{\circ}\text{C}$  para reactivar la actividad metabólica de las bacterias, luego se midió el ATP utilizando el kit BacTiter-Glo™. La solución de bacterias se mezcló con 100  $\mu\text{L}$  de la solución del kit en una placa blanca de 96 pocillos y se incubó durante 5 minutos en la oscuridad. La luminiscencia se midió posteriormente en un luminómetro de microplacas (BioTek, EE.UU.).

Adicionalmente, los biofilms de *S. gordonii* fueron evaluados por conteo de UFC. Para ello, se realizaron diluciones seriadas en NaCl al 0.9% a 4  $^{\circ}\text{C}$ , y 10  $\mu\text{L}$  de cada dilución se sembraron en placas de agar THB. Las placas de agar se incubaron a 37  $^{\circ}\text{C}$  durante 16 h, luego se contaron las UFC.

En el caso del modelo de biofilm 769-NS basado en un microcosmos oral, al contener al menos 103 taxones bacterianos diferentes, el control de las condiciones de incubación en placas de agar para un recuento de UFC completo y de confianza no es posible debido a los diferentes requisitos nutricionales y de tiempo de incubación de las diferentes cepas. De forma alternativa, después de la recolección de muestras de biofilm mediante sonicación, se usaron 500  $\mu\text{L}$  de extracto bacteriano para la extracción y purificación de ADN mediante el kit de Purificación de ADN MasterPure™ (Epicenter, Illumina, Inc., EE. UU.). La concentración de ADN se cuantificó utilizando un espectrofotómetro Nanodrop 2000c (ThermoFisher Scientific, EE. UU.).



*Ensayo de citocompatibilidad*

La citocompatibilidad de los recubrimientos se probó utilizando células de fibroblastos de prepucio humano (HFF-1), que se adquirieron de Life Technologies S.A. (Madrid, España) y fibroblastos gingivales primarios humanos (HGF; PCS-201-018, ATCC, EE.UU.). Se sembraron 5000 células HFF-1 por  $\text{cm}^2$  en medio DMEM (suplementado con 15% de FBS y  $100 \text{ U mL}^{-1}$  a  $100 \mu\text{g mL}^{-1}$  de penicilina-estreptomicina) a  $37 \text{ }^\circ\text{C}$  y 10% de  $\text{CO}_2$ . Mientras que para la expansión de los fibroblastos primarios se sembraron  $20,000 \text{ células cm}^{-2}$  en medio basal de fibroblastos (PCS-201-030, ATCC, EE.UU.) suplementado acorde a las indicaciones del distribuidor (PCS-201-041, ATCC, EE. UU.) sin añadir rojo de fenol ni antibióticos, a  $37 \text{ }^\circ\text{C}$ , 5% de  $\text{CO}_2$ .

En el primer caso, se emplearon células HFF-1 en pasajes entre 5 y 8 en todos los experimentos. Y los niveles de citocompatibilidad se determinaron utilizando el reactivo de viabilidad celular AlamarBlue (AB) (ThermoFisher Scientific, EE.UU.). Siguiendo las instrucciones del fabricante, después de los tiempos de incubación deseados (5 h, 48 h y 7 días) las superficies se incubaron durante 4 h a  $37 \text{ }^\circ\text{C}$  con una solución de AB al 10% en medio de cultivo y se registró la fluorescencia usando un Lector de microplacas SpectraMax M2e (Molecular Devices, EE. UU.).

En el segundo caso, las muestras fueron incubadas a  $37 \text{ }^\circ\text{C}$  durante 3 h para permitir la unión celular, y se añadió un exceso de medio para el cultivo adicional. Después de 1 y 3 días, las muestras se tiñeron con el kit LIVE/DEAD<sup>®</sup> (ThermoFisher Scientific, EE.UU.) y se visualizaron en un microscopio de fluorescencia invertido (Nikon Eclipse Ti-E acoplado a una cámara digital Nikon DS-2MBWc, Nikon Corporation, Japón) para confirmar la viabilidad celular en los diferentes discos. Las imágenes fueron

---

adquiridas y procesadas utilizando el software NIS-Elements Advanced Research (versión 4.5, Nikon Corporation, Japón).

### *Análisis estadístico*

El análisis estadístico ha sido realizado mediante un análisis de la varianza (ANOVA) de una vía con la prueba post-hoc de comparación múltiple Holm-Sidak usando el software Statgraphics XVII. Las diferencias significativas se exponen del siguiente modo: (\*)  $p < 0.05$ ; (\*\*)  $p < 0.001$ ; (\*\*\*)  $p < 0.0001$ . Los datos presentados en esta tesis se presentan como la media  $\pm$  desviación estándar ( $n \geq 3$ , según lo especificado en cada apartado concreto).

## **3. Resultados**

El **Capítulo 2** se centra en el estudio del papel que desempeña la distribución de cargas en el autoensamblado y separación de fases de polímeros proteicos intrínsecamente desordenados (intrinsically disordered protein polymers, IDPPs). Para ello, una librería de ELRs basada en dibloques anfifílicos fue diseñada y producida alternando la longitud de cadena y la distribución de cargas mediante técnicas de ADN recombinante. Tras esto, se procedió a la caracterización físico-química de la capacidad de formación de estructuras supramoleculares a distintas escalas de tamaño (nano-, meso- y microescala) en el rango de concentraciones entre 25  $\mu\text{M}$  y 2.5 mM. El estudio de la nanoestructuración de los ELRs mediante DLS, CD, TEM y medición ZP, determinaron que la influencia de la distribución de la carga compromete la capacidad de autoensamblado. Al aumentar la densidad de carga en la corona pudimos acceder a nuevos diseños estructurales con la capacidad de ensamblarse en estructuras micelares a bajas concentraciones y de evolucionar a estructuras jerárquicas de mayor orden que el ensamblado micelar.

A altas concentraciones (2.5 mM) se evaluó la capacidad de formar hidrogeles. Sólo aquellas construcciones que mostraron una mayor inestabilidad micelar, agregándose en entramados de micelas a bajas concentraciones presentaron una transición sol-gel cuando se incubaron a 37 °C. Los hidrogeles físicos fueron caracterizados mediante un análisis reológico y mediante microscopía electrónica, observando que la distribución de cargas aparte de la capacidad de gelación también influye en las propiedades de los hidrogeles resultantes. La incorporación de repulsión electrostática como una variable en la organización supramolecular permite alcanzar ensamblados alternativos e impulsar la transición de fase sol-gel.

En el **Capítulo 3** se describe el desarrollo de un polipéptido híbrido basado en AMPs y ELRs. En este capítulo se investigó el uso de AMPs como dominios autoensamblables y la relación entre AMPs y ELRs en el proceso de autoensamblado con el objetivo de crear nanoreservorios para AMPs. Los ELRs híbridos producidos se basaron en un diseño de dibloque anfifílico, donde los péptidos de diseño GL13K y 1018 se incorporaron en el bloque hidrofílico. Tras la síntesis recombinante, se caracterizó su comportamiento térmico y su capacidad de autoensamblado mediante turbidimetría, DLS, TEM y cryo-TEM. La combinación de ambos dominios funcionales resultó en un polipéptido polivalente con capacidad de auto-ensamblado dual, dominado por la naturaleza del AMP. Los AMPs dirigieron la formación de nanofibras por debajo de la temperatura de transición del ELR que, además, retuvieron el comportamiento termosensible de estos. De este modo, aumentando la temperatura se pudo dirigir selectivamente un segundo ensamblado en agregados de fibras.

Finalmente, en los **Capítulos 4 y 5** se presenta la creación de recubrimientos covalentes basados en ELRs y AMPs para la prevención de la formación de biofilms sobre dispositivos biomédicos. Más

---

concretamente, en el **Capítulo 4** se describe la asociación sinérgica entre las propiedades anti-adhesivas de un ELR y la actividad antibiofilm de un AMP, en un polímero proteico híbrido. Se produjo un polipéptido basado en tres bloques funcionales (el AMP GL13K, un ELR policatiónico y un motivo basado en cisteínas para el anclaje selectivo sobre superficies). Este diseño modular permitió la inmovilización covalente sobre superficies modelo de oro, formando monocapas autoensambladas (self-assembled monolayers, SAMs) como demostraron los análisis mediante XPS, ángulo de contacto y QCM-D. La actividad antibiofilm de las SAMs se testó frente a dos cepas de estafilococo, *S. aureus* y *S. epidermidis*, las cuales son responsables de la mayoría de infecciones nosocomiales relacionadas con dispositivos implantables. Se incubaron las superficies modificadas en condiciones estáticas y medio TSB suplementado con glucosa para favorecer la formación de biofilm y se observaron mediante microscopía de fluorescencia y electrónica de barrido. De forma complementaria, se cuantificó la reducción de biofilm valorando la cantidad de biomasa remanente mediante tinción con cristal violeta y mediante un test de actividad metabólica cuantificando el ATP. De este modo, se observó que la combinación del AMP y del ELR en un diseño híbrido permite fabricar recubrimientos covalentes con una actividad sinérgica incrementando el efecto antibiofilm del AMP. Además, los recubrimientos demostraron una excelente citocompatibilidad frente a células humanas.

Siguiendo con esta línea de investigación, en el **Capítulo 5** se explora la aplicación de recubrimientos basados en AMP-ELRs para implantes de titanio. Además del polipéptido híbrido recombinante empleado en el Capítulo 4, un segundo AMP-ELR fue desarrollado mediante derivación química, uniendo enantiómeros D del péptido GL13K al ELR. Discos de titanio comercial (grado II) fueron recubiertos covalentemente empleando

organosilanos. La efectividad de la funcionalización y su resistencia se testó mediante XPS y midiendo el ángulo de contacto dinámico. Tras esto, se procedió a evaluar su actividad antibiofilm frente a dos modelos de biofilms orales (*Streptococcus gordonii* y un modelo de microcosmo oral) en condiciones dinámicas en un reactor de biofilm por goteo. Los ensayos antibiofilm y de citocompatibilidad mostraron la efectividad del estereoisómero D del AMP como agente antibiofilm y bactericida cuando se encuentra unido al ELR sin efectos secundarios tóxicos frente a células humanas.

En resumen, esta Tesis aporta nuevas perspectivas al diseño y fabricación de nanosistemas autoensamblados basados en polímeros proteicos diseñados genéticamente. De manera específica, se describe la caracterización físico-química y biológica de múltiples ELRs e híbridos AMP-ELRs y confirma su potencial como plataformas multivalentes para el estudio de procesos de ensamblado de proteínas y para el desarrollo de biomateriales avanzados con propiedades antimicrobianas.

## **4. Conclusiones**

### **4.1. Ingeniería genética, biosíntesis y caracterización de ELRs**

En esta Tesis, se ha demostrado con éxito el desarrollo de múltiples biomateriales basados en ELRs con diseño modular. Gracias a su naturaleza recombinante, se ha llevado a cabo la producción de ELRs introduciendo diferentes bloques funcionales. En el Capítulo 2, se diseñó y biosintetizó una biblioteca de ELRs con diseño dibloque (ELdcRs) anfifílicos con el fin de estudiar la influencia de la distribución de carga en la organización supramolecular de IDPPs. En los capítulos 3 y 4, se diseñó un sistema de producción recombinante para polipéptidos híbridos basados en AMPs y ELRs. La incorporación de un bloque protector en el extremo N-terminal

---

permitió la sobreexpresión de AMP-ELR híbridos evitando efectos tóxicos no deseados para el microorganismo huésped. Además, su diseño funcional permitió su posterior liberación sin introducir residuos aminoacídicos adicionales en el dominio AMP, que pudieran interferir en sus propiedades biológicas.

La construcción de los distintos genes codificantes de los polipéptidos se evaluó mediante electroforesis en gel de agarosa y secuenciación de ADN. Los ELRs o AMP-ELRs se hiperexpresaron adicionalmente en *Escherichia coli* como proteínas heterólogas obteniendo rendimientos entre 220 y 600 mg por L de medio de cultivo. Además, su purificación mediante ciclos de transición inversa (ITC) permitió obtener productos altamente puros y monodispersos como se comprobó mediante técnicas de caracterización fisicoquímica como SDS-PAGE, MALDI-TOF y HPLC.

Finalmente, en el Capítulo 5, demostramos que la versatilidad de los ELRs también puede explotarse para su conjugación química con péptidos bioactivos y así, explorar nuevos diseños que no pueden lograrse mediante síntesis recombinante. De esta manera, el enantiómero D de un AMP se bioconjugó a un ELR mediante química ‘clic’ (SPCC).

## **4.2. Distribución de carga como modulador molecular de la nanoestructuración en ELR**

Se ha demostrado que la repulsión electrostática juega un papel clave en el ensamblado supramolecular de polímeros proteicos intrínsecamente desordenados, utilizando ELdCRs como modelos moleculares

La caracterización mediante TEM y DLS determinó que al aumentar la densidad de carga en dibloques IDPPs anfifílicos se contribuye a estabilizar el ensamblado micelar a bajas concentraciones, incluso en

diseños altamente desproporcionados (ratio de longitud entre bloques hidrófilo:hidrofóbico  $<0.3$ ). De este modo, la presencia de residuos cargados en el bloque hidrofílico permite romper los límites preestablecidos para el diseño de nanoestructuras basadas en ELdCRs.

En contraposición, a altas concentraciones, la presencia de residuos cargados impulsó la desestabilización de la micela favoreciendo la formación de estructuras de orden superior a concentraciones superiores (a partir de  $125 \mu\text{M}$ ), como agregados de micelas. Además de contribuir a la transición de fase sol-gel y la consiguiente formación de geles físicos a  $2.5 \text{ mM}$ .

En resumen, la distribución de carga parece ser un importante modulador del autoensamblado a diferentes escalas de longitud, afectando a la formación de estructuras jerárquicas y a la separación de fases permitiendo alcanzar arquitecturas moleculares alternativas con gran interés para la fabricación de biomateriales aplicables a la ingeniería de tejidos o administración de fármacos. Además, este trabajo no sólo contribuye a sentar las bases para el diseño racional de dispositivos jerárquicamente autoensamblados basados en ELdCRs, sino que también contribuye a arrojar luz sobre la compleja relación estructura-función de las IDPs y los parámetros que contribuyen a su transición de fase y, por lo tanto, a la formación de condensados biomoleculares u orgánulos sin membrana.

### **4.3. Estudio del autoensamblado en polipéptidos híbridos diseñados genéticamente: interacción entre AMPs y ELRs**

Se demostró que los AMPs pueden ser empleados como dominios de autoensamblado para cadenas polipeptídicas de mayor tamaño mediante construcciones híbridas basadas en ELRs con diseño modular.

---

La evaluación del comportamiento térmico sugirió que la tendencia al ensamblado de los AMPs contribuye a la transición de fase de los ELRs, disminuyendo la  $T_i$  y aumentando la histéresis térmica.

Los AMPs indujeron la formación de en nanofibras por debajo de la  $T_i$ , mientras que condujeron a la formación de agregados fibrilares por encima de la  $T_i$ . En función de la naturaleza del AMP, el mecanismo de nanoestructuración fue diferente, formando nanofibras de tamaños variables. Además, los nanosistemas híbridos conservaban termosensibilidad de los ELRs, demostrando de este modo, la fabricación de nanosistemas capaces de ensamblarse de manera dual.

La interacción dinámica entre los AMPs y los ELRs en la formación de nanoestructuras con capacidad de estímulos abre un abanico de oportunidades que van desde la producción escalable de AMPs hasta el diseño de nanomateriales avanzados que recapitulen las propiedades de los AMPs y de los ELRs.

#### **4.4. Desarrollo de monocapas autoensambladas con actividad antibiofilm basadas en AMPs y ELRs**

Hemos demostrado el anclaje covalente y de forma selectiva de ELRs y AMP-ELRs en superficies modelo de oro. La incorporación de un motivo basado en Cys en el extremo carboxilo terminal permitió la formación de monocapas autoensambladas.

La inmovilización de los ELRs proporcionó un efecto de antiadherente que permitió reducir la formación de biofilms frente a dos cepas estafilocócicas de relevancia médica: *S. aureus* y *S. epidermidis*. Además, cuando el híbrido AMP-ELR fue inmovilizado, la actividad antiadherente del ELR y el efecto antimicrobiano del AMP convergieron sinérgicamente, mejorando el potencial de antibiofilm del recubrimiento.



Los ensayos de viabilidad celular mostraron una excelente citocompatibilidad de los recubrimientos, destacando su potencial como recubrimientos seguros para evitar la formación de biofilms en dispositivos biomédicos.

#### **4.5. Biofabricación de recubrimientos antibiofilm para prevenir infecciones asociadas a implante**

Se ha demostrado con éxito la biofabricación de recubrimientos basados en AMP-ELRs sobre superficies de titanio de grado médico. El motivo basado en Cys sirvió para inmovilizar los polipéptidos híbridos covalentemente de manera selectiva mediante organosilanos, permitiendo la flexibilidad de las moléculas en el recubrimiento.

Los recubrimientos híbridos que contenían el enantiómero D del péptido GL13K fueron capaces de retener el potencial de antibiofilm del AMP frente dos modelos de biofilm oral en condiciones dinámicas. Los ensayos de citocompatibilidad demostraron que la toxicidad de los recubrimientos frente a bacterias no compromete la proliferación de células humanas primarias, confirmando, la fiabilidad de este método. La inmovilización de AMPs usando ELRs como plataformas multivalentes que pudieran incorporar biofuncionalidades adicionales y mejorar la respuesta biológica de los recubrimientos de antibiofilm.



---

# Table of contents

<b>Abstract</b> .....	7
<b>Chapter I: General introduction</b> .....	<b>13</b>
1.1. Recombinant protein polymers in biomaterials science: Elastin-like recombinamers.....	15
1.1.1. Disorder, phase transition and elasticity.....	16
1.1.2. Recombinant synthesis: gene engineering, expression and purification.....	19
1.1.3. Biomedical applications of elastin-like recombinamers .....	21
Nanoparticles .....	21
Hydrogels.....	24
Coatings .....	25
1.2. Antimicrobial biomaterials: Antimicrobial peptides.....	27
1.2.1. Therapeutic applications of antimicrobial peptides .....	30
Chemical conjugation.....	31
Supramolecular assemblies.....	33
Coatings .....	33
Objectives .....	36
<b>Chapter II: Charge distribution as molecular modulator of nanostructuration in ELRs</b> .....	<b>39</b>
2.1. Introduction .....	41
2.2. Results and Discussion.....	43
2.4. Experimental section .....	58
2.4.2. Recombinant synthesis of the ELdcRs.....	58
Agarose gel electrophoresis.....	60
SDS-PAGE .....	60
2.4.3. Thermal behavior characterization.....	60
2.4.4. Circular dichroism.....	61
2.4.5. Nanoparticle size and zeta potential analysis .....	61
2.4.6. Transmission electron microscopy.....	61

---

2.4.7.	Physical hydrogel formation and characterization .....	62
	Rheological analysis.....	62
	Scanning electron microscopy .....	63
2.5.	Appendix .....	64
<b>Chapter III: Self-assembly of genetically engineered polymers: the interplay between AMPs and ELRs .....</b>		<b>71</b>
3.1.	Introduction .....	73
3.2.	Results and Discussion .....	75
3.2.1.	Molecular design strategy and production .....	75
3.2.2.	Phase behavior characterization .....	76
3.2.3.	Self-assembly dynamics of the hybrid AMP-ELRs.....	78
3.2.4.	Thermo-responsive nanostructures.....	85
3.3.	Conclusions .....	86
3.4.	Experimental section .....	87
3.4.1.	Gene construction .....	87
3.4.2.	Bioproduction and purification.....	87
3.4.3.	Protective block cleavage and purification.....	88
3.4.4.	Phase transition characterization .....	89
3.4.5.	Physical characterization of the nanostructuration .....	89
	Dynamic light scattering.....	89
	Transmission electron microscopy .....	90
	Circular dichroism spectroscopy .....	90
3.4.6.	Cryogenic TEM.....	90
3.4.7.	Minimal inhibitory concentration.....	91
3.5.	Appendix .....	93
<b>Chapter IV: Development of self-assembled monolayers (SAMs) with antibiofilm activity based on AMPs and ELRs .....</b>		<b>101</b>
4.1.	Introduction .....	103
4.2.	Results and Discussion .....	105
4.2.1.	Rationale of the hybrid polypeptide design and biosynthesis .....	105

---

---

4.2.2.	SAMs biofabrication and characterization .....	107
4.2.3.	Evaluation of the antibiofilm activity of recombinant SAMs .....	112
4.2.4.	Combining low-fouling ELR with AMP: Synergistic convergence of antimicrobial properties.....	116
4.2.5.	Selective toxicity against bacteria.....	118
4.3.	Conclusions.....	119
4.4.	Experimental section .....	119
4.4.1.	Bacterial strains.....	119
4.4.2.	Synthesis and characterization of the ELR and AMP-ELR ... ..	119
4.4.3.	EGVC cleavage.....	120
4.4.4.	Peptide synthesis .....	120
4.4.5.	Preparation of SAMs .....	120
4.4.6.	Water contact angle .....	121
4.4.7.	X-ray photoelectron spectroscopy .....	121
4.4.8.	Quartz crystal microbalance with dissipation .....	122
4.4.9.	Antistaphylococcal assays .....	123
4.4.10.	Fluorescence microscopy.....	123
4.4.11.	Scanning electron microscopy .....	123
4.4.12.	Antibiofilm activity quantification.....	124
4.4.13.	Cytocompatibility assay.....	125
4.4.14.	Statistical analysis .....	125

**Chapter V: Biofabrication of antibiofilm coatings to prevent implant-associated infections ..... 133**

5.1.	Introduction.....	135
5.2.	Results and Discussion.....	138
5.2.1.	Hybrid ELRs design and synthesis.....	138
5.2.2.	Coating fabrication and stability .....	139
5.2.3.	Antibiofilm activity against monospecies biofilm .....	145
5.2.4.	Antibiofilm activity against oral microcosm biofilms.....	148

---

5.2.5.	Cytocompatibility of the antimicrobial coatings.....	152
5.3.	Conclusions .....	153
5.4.	Experimental section .....	153
5.4.1.	AMP/ELR/AMP-ELRs synthesis .....	153
5.4.2.	Covalent functionalization of titanium surfaces.....	154
5.4.3.	Physicochemical characterization of the coatings.....	155
	Water Contact Angle.....	155
	X-ray photoelectron spectroscopy.....	155
5.4.4.	Mechanical and thermal stability of the coatings .....	156
5.4.5.	Oral biofilms culture.....	156
5.4.6.	Antibiofilm potency: CFU, ATP and DNA quantification ....	
	.....	157
5.4.7.	Bacterial viability assay .....	158
5.4.8.	Scanning electron microscopy .....	159
5.4.9.	Cytocompatibility assay.....	159
5.4.10.	Statistical analysis .....	160
	<b>Chapter VI: Conclusions .....</b>	<b>167</b>
	<b>Chapter VII: References .....</b>	<b>175</b>
	<b>Chapter VIII: Appendix .....</b>	<b>197</b>
	List of abbreviations .....	199
	List of biomaterials developed.....	201
	Author's contributions .....	205

---

---



## Abstract

A more thorough understanding of Nature and its building blocks feeds our ability to develop functional biomaterials and *vice versa*. Understanding the functions of proteins, the most abundant and diverse macromolecules of a cell, has been crucial for the development of advanced biomaterials for biomedical applications. In this sense, the advent of recombinant DNA technology provided a sustainable production method for of natural proteins, but also the engineering of new protein-based materials, including recombinant protein polymers.

Recombinant protein polymers, or recombinamers, are genetically engineered polypeptides based on conserved motifs found in structural proteins. Within this type of biomaterials, we can find elastin-like recombinamers (ELRs). ELRs are polypeptides based on the repetition of the pentapeptide Val-Pro-Gly-X-Gly, found in the hydrophobic domains of tropoelastin that allowed them to mimic its structural and biomechanical properties. Therefore, ELRs are characterized by intrinsic structural disorder, reversible phase transition behavior and excellent biological and mechanical properties. These properties in addition to low-complexity polymeric composition and outstanding tunability, make them an excellent candidate for the study of biological processes and the generation of tailored materials for biomedical applications. Thus, this Thesis is focused on the design, production and processing ELRs, targeting its biomedical application as self-assembled nanosystems and antimicrobial coatings. To this end, different modular designs will be studied using ELRs and antimicrobial peptides (AMPs) as building blocks. AMPs are short cationic peptides with the ability to kill microbes directly or indirectly modulating the host immune system and hence, they constitute one of the most

---

promising alternative to conventional antibiotics in the treatment of drug-resistant infections. A comprehensive review on biomedical applications of AMPs and ELRs is presented in **Chapter 1**. A great variety of options enables the processing of these biomaterials into gels, coatings or nanostructures for any of a number of biomedical applications, such as extracellular-matrix-mimicking 3D networks for tissue engineering or self-assembled nanocarriers for drug delivery.

In particular, **Chapter 2** is focused on the study of the role of charge distribution in self-assembly and phase separation of intrinsically disordered protein polymers (IDPPs). For this purpose, a library of ELRs based on amphiphilic diblocks was designed altering chain length and charge density. Physico-chemical characterization of the nanostructuration in a range of concentrations determined that charge distribution strongly affects self-assembly of IDPPs at different scale lengths. The incorporation of electrostatic repulsion as a variable in the supramolecular organization of ELRs enabled to reach alternative assemblies and to drive liquid-gel phase transition.

**Chapter 3** describes the development of a hybrid polypeptide based on AMPs and ELRs. This chapter seeks to explore the usage of AMPs as self-assembling domains (SADs) and to elucidate the interplay between AMPs and ELRs in the self-assembly with the further objective of creating nanoreservoirs for AMPs. The hybrid design consists in an amphiphilic diblock, where the designer peptides GL13K and 1018 were fused to the hydrophilic block. After recombinant biosynthesis, thermal behavior and self-assembly abilities were characterized. The combination of the two functional domains resulted in a multifaceted polypeptide with a dual self-assembly governed by the composition of the AMP-domain. The AMPs triggered the formation of nanofibers that retained the characteristic

thermo-responsiveness of the ELRs. Therefore, increasing the temperature, the hierarchical assembly into fibrillar aggregates could be driven. The interplay of the different SADs (ELR or AMP) offers opportunities for the development of new nanocarriers to deliver AMPs and to study the molecular mechanism that control the bactericidal properties of the AMP linked to biopolymers.

Finally, **Chapters 4 and 5** present the creation of covalent coatings based on AMPs and ELRs for the prevention of biofilm formation onto biomedical devices. Specifically, **Chapter 4** describes the synergistic association of a low-fouling ELR and the antibiofilm designer peptide GL13K. For this purpose, a hybrid polypeptide based on three functional blocks (GL13K, polycationic ELR and a Cys-motif for the selective tethering onto surfaces) was bioproduced. The modular design enabled the covalent immobilization onto model gold surfaces, forming self-assembled monolayers (SAMs). Antibiofilm activity of the SAMs was tested against two staphylococcal strains of medical relevance in the development of nosocomial infections. The combination of the AMP and ELR in the hybrid design (AMP-ELR-coating) provided a synergistic activity increasing the antibiofilm effect of AMP-coatings under static conditions. Additionally, the nanocoatings demonstrated an excellent cytocompatibility against human cells.

In the same vein, **Chapter 5** explores the implementation of AMP-ELR for titanium implants. In addition to the recombinant hybrid polypeptide employed in Chapter 4, a second AMP-ELR was developed by chemical derivation attaching the D-enantiomer of the GL13K to the ELR backbone. Commercially pure (grade II) titanium discs were coated using organosilanes as covalent linkers. Then, antibiofilm activity was tested against two different oral biofilm models (monospecies *Streptococcus gordonii*

---

and an oral microcosm model) under dynamic conditions in a drip flow biofilm reactor (DFBR). Antibiofilm and cytocompatibility assays showed the strong antibiofilm and bactericidal effect of the D-enantiomer when is linked to an ELR with non-toxic side effects against human cells.

In summary, this Thesis provides new insights on the design and fabrication of self-assembled nanosystems based on genetically engineered polymers. Specifically, it describes the physico-chemical and biological characterization of several novel ELRs and hybrid AMP-ELRs and confirms their potential as multivalent platforms for the study of protein self-assembly processes and for the development of advanced biomaterials with antimicrobial properties.





# Chapter I

---

General introduction

---





## 1.1. Recombinant protein polymers in biomaterials science: Elastin-like recombinamers

In the past few decades, the combination of materials science, cellular biology, molecular biology and biochemistry has given rise to a new generation of biomaterials: genetically engineered biomaterials. Genetically engineered or recombinant biomaterials are protein-based biomaterials that aim to mimic the outstanding biological and mechanical properties of native proteins *in vivo*, and at the same time overcome some limitations of natural and synthetic biomaterials. In this sense, the application of recombinant DNA technology to biomaterials science provides a scalable, cost-effective and environmentally friendly source for protein materials with a precise control over the composition, molecular weight and monodispersity.

Genetically engineered biomaterials, specifically recombinant protein polymers, are attractive for biotechnological and medical approaches because of their intrinsic biocompatibility and the extreme versatility.<sup>[15]</sup> Their recombinant nature enables to create modular building blocks with simplified repetitive sequences that recreate the properties of more complex proteins while simultaneously incorporating diverse structural and biological motifs. Thus, producing multivalent platforms, we can design tailored biomaterials with specific features for the desired application. Herein, we will focus on the polymeric derivatives of the elastin, the elastin-like recombinamers (ELRs) or polypeptides (ELPs).

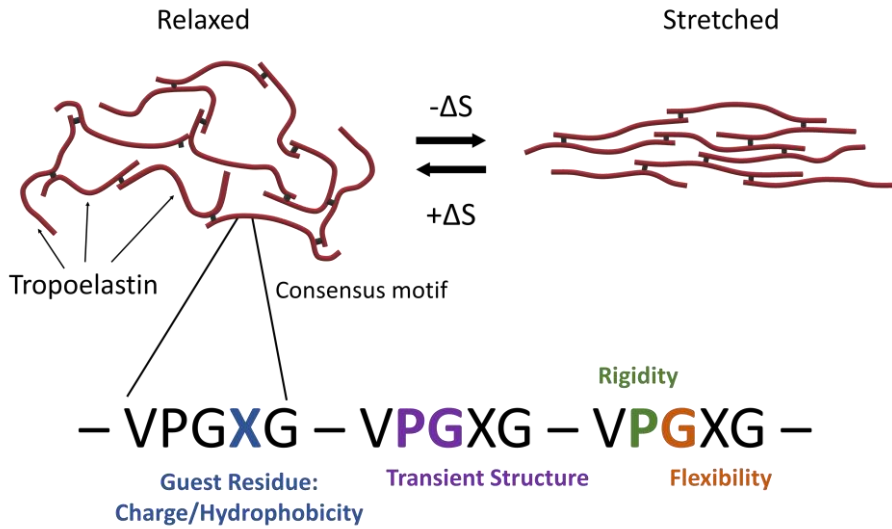
Elastin is a polymeric extracellular matrix (ECM) protein, found predominantly in tissues as varied as the skin, lungs, blood vessels, and

ligaments, providing elasticity and resilience.<sup>[16]</sup> Its precursor, tropoelastin, is a soluble 60 kDa protein that is composed by alternating hydrophobic and hydrophilic crosslinking domains. Tropoelastin is secreted into the extracellular space by the elastogenic cells (such as fibroblasts, endothelial cells, smooth muscle cells, chondrocytes and keratinocytes), where is crosslinked, thus resulting in the formation of insoluble elastin.<sup>[17]</sup>

ELRs are recombinant polymers inspired on conserved motifs present in the hydrophobic domains of tropoelastin. They are generally composed by the repetition of the pentapeptides Val-Pro-Gly-X-Gly, where the guest amino acid (X) can be any amino acid except L-Pro (**Figure 1.1**). However, there are other variants including penta- (XPGVG) hepta- (LGAGGAG) or nonapeptides (LGAGGAGVL) that show the same behavior.<sup>[18]</sup> In this way, ELRs mimic physicochemical properties of tropoelastin which include intrinsic disorder, stimulus-responsive phase transition and mechanical properties, accompanied by an excellent biocompatibility,<sup>[19]</sup> making them excellent candidates for the development of self-assembled devices for (nano)biomedical applications.

#### *Disorder, phase transition and elasticity*

Disorder is inherent to proteins structure and it plays an important role in Nature.<sup>[20,21]</sup> Though the classical ‘sequence-structure-function’ paradigm establishes the relationship between protein functionality and defined 3D structure (lock and key model),<sup>[22,23]</sup> protein functionality is not always associated with the presence of unique conformation and many protein functions rely on disordered protein sequences.<sup>[24–26]</sup> In fact, intrinsically disordered proteins (IDPs) or regions (IDPRs) are highly abundant in nature (40% of eukaryotic genome)<sup>[20]</sup> and they are involved in multiple biological activities, such as structural functions, cell signaling, regulation, recognition and in the pathogenesis of different human diseases.<sup>[21]</sup>

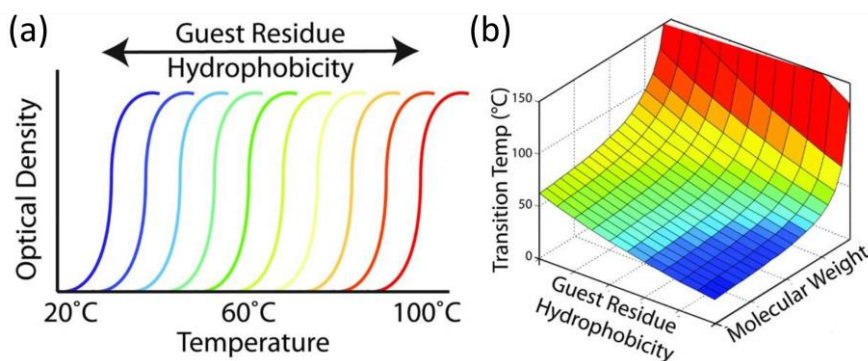


**Figure 1.1.** ELRs are generally based on the repetition of the consensus pentapeptide VPGXG found in tropoelastin that confers high conformational flexibility. The high content in Pro and Gly promotes structural disorder. Above the transition temperature ( $T_i$ ), these polypeptides tend to form transient  $\beta$ -turns and  $\beta$ -sheets in solution that quickly revert to random coil. Adapted with permission from reference [27].

In addition, other attractive feature of many IDPRs for biomaterial science is their stimuli-responsive phase transition behavior. Liquid-liquid phase transition is the driving force for subcellular compartmentalization and formation of membraneless organelles, so-called biomolecular conjugates.<sup>[28]</sup> Phase transition is also an essential first step that precedes the formation of fibrillar protein structures in the ECM. For instance, during elastogenesis, elastin monomer (tropoelastin) is secreted as soluble form. Subsequently, tropoelastin undergoes coacervation in the extracellular space forming spherical nanoparticles that evolve into microspherules and microaggregates which are crosslinked to form elastic fibers following the molecular template provided by microfibrills.<sup>[17]</sup> Thus, phase transition or coacervation is crucial for the elastic fiber formation.<sup>[17]</sup> In the same way, phase transition plays a crucial role in the supramolecular assembly of other important proteins including resilin, an insect elastomeric protein; titin, one of the responsible of muscular elasticity; abductin, the protein that forms

the flexible hinges of bivalves, spider and cocoon silks; or the squid sucker ring teeth proteins among others.<sup>[29–31]</sup>

Phase transition of ELRs is a thermodynamically driven process. Below a particular temperature, named lower critical solution temperature (LCST) or transition temperature ( $T_t$ ), the ELR chains are completely soluble because a hydrophobic hydration.<sup>[32]</sup> It has been proposed that in the hydrated state, water molecules are forming clathrate-like structures surrounding hydrophobic residues. Thermodynamically, this decreases enthalpy and entropy comparing with bulk water. Raising the temperature above the  $T_t$ , the energy provided to the system destabilizes the hydrogen bonds that maintained the clathrate-like structures, increasing the entropy, and the chain folds.<sup>[32]</sup>



**Figure 1.2.** LCST or  $T_t$  can be finely tuned by the control of the amino acid sequence. Guest residue and molecular weight of the polypeptide are the main intrinsic parameters that affect the  $T_t$ . (a) Phase transition measured by optical density, plotted against temperature. (b) A 3-dimensional plot of the predicted  $T_t$  as a function of the guest residue composition and the molecular weight of the chain. Adapted with permission from reference <sup>[33]</sup>.

Nevertheless, the folded structure remains disordered.<sup>[27]</sup> Recent studies using molecular dynamics in combination with solid-state NMR and spectroscopic studies (circular dichroism and Raman spectroscopy) established the presence of ensemble of fluctuating secondary structures ( $\beta$ -turns) with intrinsic disorder in the coacervated state.<sup>[34–37]</sup> This intrinsic

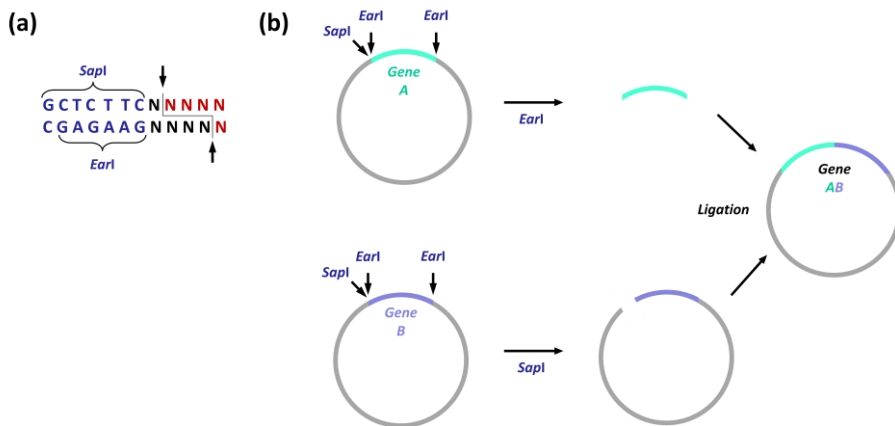
disorder is essential for the elasticity and resilience of these biomaterials. Intrinsic disorder has been proposed as the driving force sustaining phase transition and the elastic properties of elastin (**Figure 1.1**).<sup>[38]</sup> When hydrated, the disorder of the system is decreased if the material is stretched; if the deformation force disappears, elastic relaxation takes place driven by the recovery of a maximum entropy (entropic spring).

LCST behavior can be precisely tuned in ELRs (**Figure 1.2**). Depending on the guest residue, the polarity of the ELR chain can be modified and hence, the  $T_t$ . Hydrophobicity coefficients can be calculated and the  $T_t$  predicted upon guest amino acid.  $T_t$  is also affected by concentration and chain length.<sup>[39]</sup> Given the cooperative nature of the phase transition,<sup>[40]</sup> the higher concentration, the lower  $T_t$  to reach and drive phase transition. In the same vein, with increasing chain length, the  $T_t$  decreases. Additionally, other external parameters, such as pressure,<sup>[41,42]</sup> pH,<sup>[43]</sup> or the presence of salts and other solutes<sup>[44–46]</sup> also affect the phase transition. In light of this, ELRs can be considered as smart polymers, since they are able to respond to several external stimuli, thereby sensing their microenvironment and undergoing changes in response to it.

### 1.1.1. Recombinant synthesis: gene engineering, expression and purification

Although the first elastin-like polypeptides made by Urry *et al.* were produced by chemical methods, their complexity and large molecular weight precise recombinant production to guarantee highly pure and monodisperse products in high yield.<sup>[1]</sup> Gene construction of polymeric proteins is performed by the iterative recursive method in order to avoid PCR difficulties associated to the use of repetitive sequences.<sup>[47]</sup> This methodology enables the directional concatenation of the desired monomeric genes. For this, it is necessary that the DNA construct is

flanked by type IIS endonucleases restriction sites. Type IIS restriction enzymes are characterized by recognizing asymmetric DNA sequences and cleaving outside of the recognition DNA sequence, thus avoiding the introduction of undesired base pairs. As shown in **Figure 1.3**, ELR genes must be flanked by sites of a IIS endonuclease (*EarI*) that enables to excise the insert, but also one of these sites must be recognized by a secondary IIS endonuclease (*SapI*) in order to linearize the plasmid.



**Figure 1.3.** (a) Recognition and cleavage sites of the type IIS endonucleases *SapI* and *EarI*. (b) Iterative-recursive method using both restriction enzymes. *EarI* recognizes all *SapI* sites but the opposite does not occur. The asymmetrical ends after cleavage enable the subsequent ligation of the constructs.

The newly constructed gene is transformed into the host organism, *Escherichia coli*. *E. coli* is a Gram-negative bacterial species used preferentially due to cost-effectiveness and feasibility of scaling-up. However, other organisms have been used for the production of ELRs as heterologous proteins including yeasts,<sup>[48]</sup> fungi<sup>[49]</sup> and plants.<sup>[50]</sup>

Once the ELRs are expressed, purification is carried out exploiting that ELRs undergo thermo-responsive phase separation. Thus, heating and/or adding salts precipitates the ELR which is collected by centrifugation. The ELR precipitate is then resuspended in cold water and centrifuged again to eliminate undesired contaminants. Repeating these steps yields highly pure

products.<sup>[2]</sup> This process, named inverse transition cycling (ITC), enables the purification of multiple fusion partners, making it a promising approach for the industrial production of protein products without chromatographic methods.<sup>[51]</sup> In addition, endotoxin removal protocols can be applied during ITC.<sup>[52]</sup>

### 1.1.2. Biomedical applications of elastin-like recombinamers

Genetically engineered elastin-like polypeptides are promising candidates for biomedical applications. Their inherent self-assembling behavior, biocompatibility and biodegradability combined with an exceptional tunability due to their recombinant nature, make them a powerful platform for the design of devices with advanced features for drug delivery and regenerative medicine.<sup>[53]</sup>

One of the advantages of ELRs is their polymeric sequence. This enables the synthesis of recombinamers with modular design controlling the number and density of functional motifs for multiple purposes, including self-assembling, crosslinking or bioactive domains such as cell-binding or proteolytic sites.

#### *Nanoparticles*

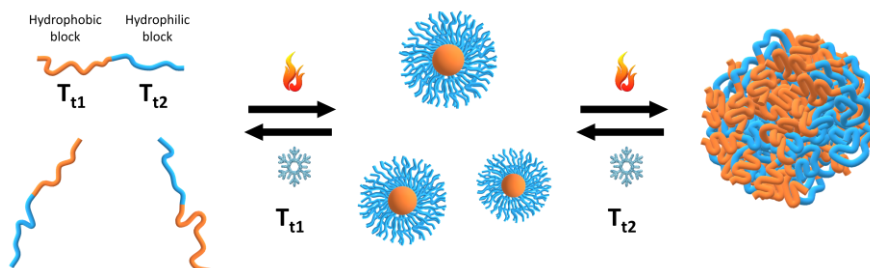
One of the most important property of the ELRs is stimulus-responsive phase transition. The biofabrication of multiblock designs combining multiple ELR-blocks with different hydrophilicities and therefore, different  $T_t$ , opens up opportunities for the *de novo* design of self-assembled nanoparticles.

Multiple modular designs have been investigated using ELRs as building blocks in block co-recombinamer constructions or combined with other functional protein domains in biohybrid designs. Conticello and

colleagues were the first to report the production of self-assembled nanoparticles based on elastin-like block co-recombinamers (ELbcRs).<sup>[54]</sup> They designed amphiphilic diblock co-recombinamers based on hydrophobic and hydrophilic individual blocks, with  $T_t$  below and above physiological temperature, respectively. Thus, at 37 °C, the hydrophobic block collapses triggering the formation of hydrophobic cores surrounded by a hydrophilic corona, made of hydrophilic blocks. If the temperature was increased above the  $T_t$  of the hydrophilic block, the corona would collapse forming macromolecular aggregates and undergoing phase separation (**Figure 1.4**). This means that the ELbcR can exist in at least three different phases: hydrated molecules in solution, nanoparticle assembly or micrometric aggregates.

Due to the potential use of self-assembled structures as nanocarriers, self-assembly of diblock co-recombinamers has been exhaustively studied experimentally and theoretically.<sup>[55]</sup> First, evaluating self-assembling behavior of non-charged amphiphilic diblocks, Dreher et al. defined two physico-chemical requirements for the micellar assembly: significant difference must be between  $T_t$  of the hydrophilic and hydrophobic block, and a molecular weight ratio of 1:2 to 2:1 between both blocks is needed.<sup>[56]</sup> Then, after analyzing phase transition by spin probing continuous wave electron paramagnetic resonance (CW EPR) spectroscopy, Widder et al. specified that hydrophilic : hydrophobic weight ratio must be greater than or equal to 0.3 to guarantee micellar assembly.<sup>[57]</sup> Lastly, a minimum length of the hydrophobic block is also needed to produce stable nanoparticles (greater than 48 pentapeptides).<sup>[58]</sup>





**Figure 1.4.** Schematic representation of the micelle formation and phase separation driven by an amphiphilic ELR with diblock design.  $T_{t1}$  correspond with the  $T_i$  of the hydrophobic block, whereas  $T_{t2}$  is the  $T_i$  of the hydrophilic one.

On the other hand, we are able to control relevant parameters for the disposition of the nanostructures in solution.<sup>[59,60]</sup> Size and shape of the micelles can be modulated by tuning the size of the individual blocks in the diblock design.<sup>[58]</sup> It has been observed that size and shape can be modulated in diblock co-recombinamers introducing gradients of alternated hydrophilic and hydrophobic blocks.<sup>[61]</sup> As a function of the length of the individual blocks in the interfacial gradient, we can control the molecular weight, aggregation number, or the hydrodynamic diameter of the ELbcR-micelles, crucial parameters for the production of delivery nanocarriers.

Furthermore, other supramolecular assemblies can be reached, including vesicles,<sup>[62,63]</sup> cylindrical micelles or nanofibers.<sup>[64–68]</sup> The exquisite versatility of ELRs enables the ability to introduce other protein self-assembly domains or bioactive molecules, recombinantly or chemically, by modification of their amino acid side-groups. Thus, exploiting biocompatibility<sup>[69]</sup> and biodegradability of ELRs,<sup>[70]</sup> tailored stimuli-responsive nanoparticles have been developed for different therapies. Biofabrication of ELR nanoparticles for cancer therapy has enabled to improve the pharmacokinetics and tumor accumulation of hydrophobic drugs,<sup>[56,71–73]</sup> tumor targeting,<sup>[74,75]</sup> decrease cancer drug resistance,<sup>[76,77]</sup> or

increase cellular uptake,<sup>[78–80]</sup> in addition to develop emerging therapies such as local delivery of radioisotopes for brachytherapy<sup>[53]</sup> or immunotherapy.<sup>[68,81]</sup>

Furthermore, fusion of bioactive peptides to the hydrophilic corona enables the production of self-assembled nanocarriers for other applications. It has been demonstrated that ELR nanocarriers can improve stability and half-life of small peptides and their effective delivery, including peptide drugs,<sup>[82]</sup> growth factors<sup>[83,84]</sup> or bacterial antigens.<sup>[85]</sup>

### *Hydrogels*

Supramolecular assemblies based on ELRs can be extended to the micro and macroscale for the development of three dimensional networks that simulate the native ECM for their use in tissue engineering. ELRs with modular designs enabled to obtain tailored multifaceted scaffolds with tunable architecture, biofunctionalities, mechanical properties and biodegradability, key parameters that strongly affect cell behavior.<sup>[86–88]</sup> Thus, matrix-cell communication can be modulated through mechanotransduction,<sup>[89,90]</sup> exposition of cell-binding domains<sup>[91–93]</sup> or growth factors,<sup>[94–96]</sup> or by the matrix remodeling,<sup>[97–100]</sup> which results in the control of cell behavior, including adhesion, migration, proliferation and stem cell fate.

Furthermore, other biomaterials can be integrated with ELRs to produce hybrid or composite scaffolds with improved features. Thus, ELRs have been combined with protein materials (e.g. collagen,<sup>[101–104]</sup> fibrin,<sup>[105]</sup> peptide amphiphiles<sup>[106]</sup>) polysaccharides (e.g. hyaluronic acid,<sup>[107–109]</sup> chitosan<sup>[110]</sup>) or synthetic polymers (e.g. polyethylene glycol<sup>[111,112]</sup>).

On the other hand, ELRs are also compatible with multiple manufacturing technologies in addition to the great variety of crosslinking

strategies, based on physical<sup>[113–116]</sup> or chemical crosslinks.<sup>[5,99,117–120]</sup> Scaffold fabrication techniques such as electrospinning or salt leaching can be used for the production of ELR scaffolds with precise architectures.<sup>[121–125]</sup>

### *Coatings*

Biofunctionalization of surfaces is an effective approach to improve biological response of indwelling devices. In this sense, properties of the ELRs have been exploited for the improvement of clinical materials. Intrinsic properties of the ELRs, such as thermo-responsiveness<sup>[126]</sup> or biocompatibility,<sup>[127]</sup> can be transferred to the coated biomaterial by the functionalization of these recombinant polypeptides. ELR coatings were also applied to vascular grafts, demonstrating their intrinsic ability to enhance the hemocompatibility and inhibit thrombosis related complications *in vivo*.<sup>[128,129]</sup>

In contrast to tropoelastin, cells do not recognize the polyVPGXG and consequently, ELRs show an intrinsic low-fouling behavior that prevents the unspecific protein attachment and cell binding.<sup>[130,131]</sup> However, if cell-binding motifs, such as the integrin-mediated adhesion tripeptide RGD, is incorporated into the ELR backbone, cell adhesion and proliferation are greatly increased.<sup>[132,133]</sup> The control of cell-binding motifs exposure by the thermoresponsive behavior of the ELR coating enables to harvest cell sheets with potential application in tissue regeneration.<sup>[134]</sup>

Furthermore, as different cell types recognize preferentially different cell-binding motifs, the regulation of these bioactive cues density and spatial location can be used to produce cell patterns.<sup>[135,136]</sup> Besides binding motifs, other functional domains can be incorporated onto the ELR coatings such as different bioactive peptides<sup>[137]</sup> and crosslinking sites,<sup>[138]</sup> providing

innovative surface engineering approaches to develop tailored bioactive substrates for multiple biomedical applications.

In conclusion, ELRs are attractive biomaterials to create nanostructured devices for tissue engineering and drug delivery. Their inherent reversible phase transition behavior, biocompatibility and feasibility to introduce functionalities, chemically or by co-expression, make them excellent candidates for multiple biomedical applications.

## 1.2. Antimicrobial biomaterials: Antimicrobial peptides

In recent years, antimicrobial resistance (AMR) to conventional antibiotics has become an uncontrollable health problem. Last report from the World Health Organization to the Secretary-General of the United Nations calls for the global cooperation in the development of alternatives to treat drug-resistant infections, a threat that is estimated to provoke 10 million annual deaths and USD 2.9 trillion expected cumulative losses in the Organization for Economic Cooperation and Development (OECD) countries, in 2050.<sup>[139]</sup>

Overuse and overdependence of antimicrobials (antibiotics, antifungals and antivirals), heavy metals and biocides has driven to AMR in the environment.<sup>[140]</sup> Against this, health organizations must establish strict policies to control the usage of these compounds in health services, industry, agriculture and animal husbandry, but also it is a crucial need to develop new drugs to treat drug-resistant infections. In this sense, antimicrobial peptides (AMP) are a promising alternative to conventional antibiotics.

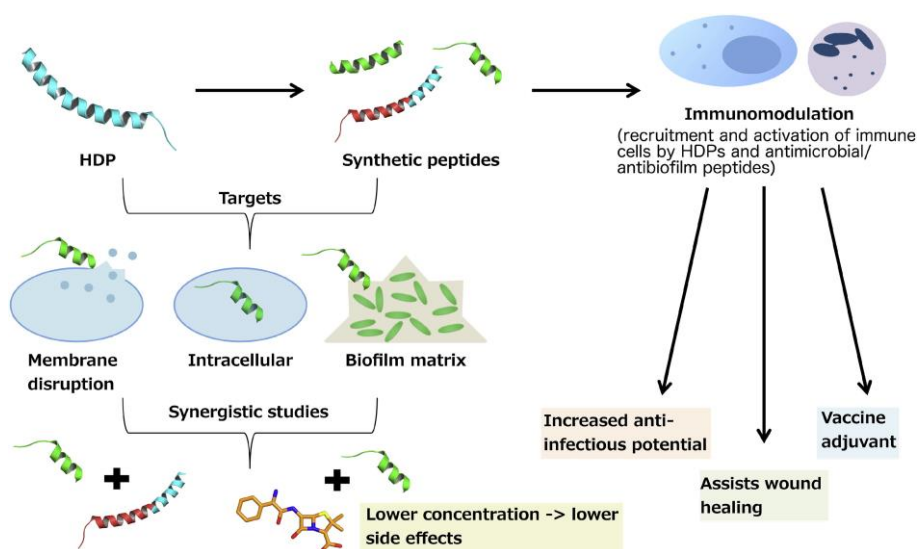
Antimicrobial peptides (AMPs) are short (10-50 amino acids), amphiphilic, generally cationic peptides produced by a wide variety of life forms, including invertebrate, plant and animal species.<sup>[141]</sup> Reflecting their wide diversity of sources, AMPs have a wide variety of conformational structures<sup>[142]</sup> and they are commonly classified according to the structure adopted in solution. Thus, we can distinguish 3 extensive groups:  $\alpha$ -helical peptides,  $\beta$ -sheet peptides and extended or random-coil peptides.<sup>[143]</sup> (i)  **$\alpha$ -helical family** consists of AMPs with helical structures (e.g. magainins and LL-37). (ii)  **$\beta$ -sheet family** is composed by AMPs with  $\beta$ -sheets usually stabilized by disulfide bonds, forming rigid structures (e.g. human  $\alpha$  and  $\beta$ -defensins). (iii) **Extended/random-coil family** contains AMPs with

undefined secondary structures or random coils which are often rich in specific amino acids such as tryptophan and arginine (e.g. indolicidin) or histidines (e.g. histatin).

Their amphipathicity allows them to acquire different conformations and interact with multiple molecular targets.<sup>[144]</sup> The modes of action are wide and varied, specific to each AMP. Traditionally, they were considered as membrane pore formers because of the high affinity with bacterial membranes and consequently their disruption,<sup>[144]</sup> but also AMPs are able to target intracellular components, inhibiting metabolic processes, such as nucleic acid synthesis, cell wall biosynthesis or protein folding, among others<sup>[145][146]</sup> and impeding biofilm formation.<sup>[147,148]</sup> In this sense, AMPs play an important role as part of the innate immune response, showing broad-spectrum activity against most bacterial pathogens, antiparasitic,<sup>[149]</sup> antiviral,<sup>[150]</sup> antifungal activities<sup>[151]</sup> and even against some kinds of cancer.<sup>[152]</sup> Additionally, recent studies have demonstrated their ability to interact and modulate the host response, defining them as host-defense peptides (HDPs) due to their multifaceted roles<sup>[153]</sup> (**Figure 1.5**).

There exist thousands of different AMPs, data repository of antimicrobial peptides (DRAMP) database contains 19,899 entries of natural and designer AMPs (October 2019), 5,084 of which are general AMPs (containing natural and synthetic AMPs) and 14,739 patented.<sup>[154]</sup> However, currently there are only 76 AMPs in preclinical or clinical stages.<sup>[154]</sup> Despite the promising properties of natural AMPs, they also show potential limitations that hinder their clinical use and commercialization.<sup>[142]</sup> First, AMPs are highly sensitive to environmental conditions. The presence of salts in the medium or pH changes can compromise their antimicrobial potential.<sup>[155–157]</sup> Second, AMPs can be rapidly inactivated by proteolysis or by adsorption on plasma proteins, showing short plasma half-life. Third,

some of them present cytotoxic or hemolytic associated activities. Fourth, despite the development of resistance occurs in a much lesser degree than conventional antibiotics, pathogens are also able to develop mechanisms of resistance against AMPs. Last, the cost of chemical synthesis hampers the scale-up of their production.



**Figure 1.5.** Schematic representation of the multiple bioactivities developed by AMPs and potential applications. Adapted with permission from reference [147].

Fortunately, several strategies have been developed to overcome these limitations. The increasing number of structure-activity relationship studies along with the application of computational modelling enable to shed light into the biological function of the distinct residues in order to produce simplified AMPs with improved features, including selectivity, high potency or the ability to penetrate mammal cells to combat intracellular infections.<sup>[147,158]</sup> Moreover, the use of D-enantiomeric forms,<sup>[159]</sup>  $\beta$ -amino acids<sup>[160]</sup> and other non-canonical amino acids allow not only to improve bactericidal properties but also to decrease proteolytic degradation and evade resistance mechanisms.<sup>[161,162]</sup>

Finally, one of the main drawbacks that limit the widespread clinical use is their chemical synthesis. In this sense, multiple recombinant approaches have been developed as scalable and cost-effective production using distinct host organisms. *E. coli* is the most commonly used due to their fast and low-cost growth and also because is a well-established expression system.<sup>[163,164]</sup> However, other alternatives have been used such as eukaryotic cells (e.g. fungi, plants or mammal cells).<sup>[165–167]</sup>

### 1.2.1. *Therapeutic applications of antimicrobial peptides*

AMPs constitute a promising alternative to conventional antibiotics for the treatment of drug-resistant infections due to their antimicrobial and immunomodulatory properties. Despite the aforementioned limitations, their potent bactericidal activity in addition to their low-frequency of resistance emergency<sup>[168]</sup> can be efficiently used for the treatment of certain infections.

One avenue that is being explored is to use them as topical agents. In humans, AMPs are produced by different epithelial cells (e.g. keratinocytes, conjunctival epithelial cells) and they act as multifunctional modulators of wound healing.<sup>[169]</sup> Several studies revealed that they are upregulated in multiple stages.<sup>[170]</sup> Apart from the inherent antimicrobial activity, they play important roles in chemotaxis and angiogenesis, particularly important in the regeneration of skin.<sup>[171]</sup> In fact, their ability to accelerate healing of chronic wounds has been demonstrated, acting as a damper of inflammation<sup>[172]</sup> and enhancing regeneration and wound closure.<sup>[173]</sup> In this sense, AMPs have been used for the treatment of infected wounds,<sup>[174][170]</sup> specifically for the treatment of drug-resistant pathogens,<sup>[175]</sup> such as resistant forms of *Staphylococcus aureus*, the most frequently isolated pathogen from human skin infections.<sup>[176]</sup>



Furthermore, AMPs have demonstrated that they can show synergistic effects with other antibiotic molecules, including other AMPs,<sup>[177,178]</sup> conventional antibiotics<sup>[179–181]</sup> or metallic nanoparticles.<sup>[182,183]</sup> The wide variety of AMPs and their multiple potential molecular targets opens up possibilities for the design of combined therapies for the treatment of drug-resistant infections, increasing efficacy and preventing side-effects and resistance. Thus, synergetic activity can be reached by co-delivery or through chemical conjugation.

### *Chemical conjugation*

Chemical conjugation of AMPs consists in the covalent bonding of AMPs with other molecules in order to improve their antimicrobial properties or delivery (see for instance <sup>[184–186]</sup>). AMPs can be functionalized to generate more stable peptides (e.g. amidation of the terminal carboxyl group), but also to incorporate additional properties.

For example, several studies have demonstrated that coupling AMPs with conventional antibiotics increases the bactericidal activity against resistant strains, such as vancomycin resistant *Enterococci*.<sup>[187,188]</sup> To enhance membrane permeability, AMPs have been also combined with lipid chains and cell-penetrating peptides, which resulted in an increase of the selectivity and toxicity.<sup>[189–191]</sup>

AMPs can be conjugated with other biomaterials in order to improve their delivery. Morris *et al.* demonstrated that PEGylation minimizes cytotoxicity of a synthetic AMP.<sup>[192]</sup> They created hybrid AMPs by N-terminal PEGylation that were tested successfully for the treatment of pulmonary infections. Furthermore, conjugation of AMPs with nanoparticles has been explored. Coating AMPs onto the surface of nanoparticles aims to increase the local concentration and bioavailability in

addition to prevent the adsorption by other plasma proteins. Thus, metallic nanoparticles have been decorated with AMPs,<sup>[193–196]</sup> enhancing the antimicrobial properties and pharmacokinetics.<sup>[197,198]</sup>

Self-assembled structures can also be designed in order to increase the bioavailability. For instance, creating *in situ* gelling biodegradable hydrogels. By conjugating AMPs within the backbone of copolymers that drive gelation, it is possible to develop antimicrobial and biodegradable dressings to protect chronic wounds and prevent infections.<sup>[199]</sup>

Other avenue to overcome chemical synthesis and lack of availability is the recombinant coproduction with other protein materials that undergo phase transition, such as silk<sup>[200,201]</sup> or ELRs.<sup>[202,203]</sup> In this sense, thermo-responsive behavior of ELRs provides a cost-effective and scalable purification methodology, avoiding chromatographic methods.<sup>[188]</sup> However, they also provide a versatile stimulus-responsive platform to control the supramolecular assembly and develop nanostructured devices such as films or nanoparticles.<sup>[202,203]</sup> da Costa *et al.* coproduced AMPs with an ELR based on 200 repetitions of the Val-Pro-Ala-Val-Gly pentapeptides, that shows plastic behavior.<sup>[207]</sup> Exploiting the self-assembling ability of the ELR, films were prepared by solvent-casting. The presence of the AMPs provided bactericidal and antifungal activity making them an interesting alternative in the prevention of wound infections.<sup>[202]</sup> In another study, they developed antimicrobial nanoparticles based in the same ELR design.<sup>[203]</sup> Above the  $T_t$  of the ELR, the polypeptide chain collapsed forming self-assembled nanoparticles that showed antimicrobial properties against Gram-positive (*B. subtilis*, *S. aureus*) and Gram-negative (*E. coli*, *P. auroginosa*) bacteria.

*Supramolecular assemblies*

Amphipathic behavior of AMPs confers them the ability to acquire different conformations in solution and recently, great attention has been devoted to those AMPs that are able to self-assemble into higher-order supramolecular assemblies, such as well-defined fibers,<sup>[208]</sup> nanoparticles,<sup>[209]</sup> twisted nanoribbons<sup>[210]</sup> or hydrogels.<sup>[211–214]</sup>

Self-assembly of AMPs is governed by non-covalent interactions and AMPs are generally associated with hydrophobic interactions between non-polar side chains that drive the stabilization into amyloid-like fibrils.<sup>[215]</sup> To that end, since AMPs are positively charged, it is needed to reduce the electrostatic repulsion of ionic groups and consequently, self-assembly is usually associated to changes in pH.<sup>[208,210,216]</sup> Self-assembly can enhance the antimicrobial activity,<sup>[217]</sup> but also the aggregation of AMP may induce cytotoxicity.<sup>[218]</sup> Therefore, further studies must be performed in order to shed light in the structure–self-assembly–activity relationship and set the basis for the design of self-assembled materials based on AMPs. The use of AMPs as building blocks offers the opportunity to engineer delivery systems for AMPs and even scaffolds for tissue regeneration with antimicrobial properties.

*Coatings*

Stable immobilization of AMPs onto surfaces is another effective approach to overcome protease degradation and increase bioavailability.<sup>[219]</sup> It increases the local concentration of the peptide and provides an alternative to prevent biomaterial-associated infections (BAIs).

Ageing of population and development of modern medicine have exponentially increased the used of permanent or temporary devices. The introduction of a foreign body implicitly increases the risk of infection.<sup>[220]</sup>

Microorganisms can adhere to the surface and develop biofilm that serve as pathogen reservoirs, facilitating resistance to antibiotic agents.<sup>[221]</sup> AMP-based coatings have demonstrated to be an effective approach to prevent biofilm formation without compromising the cytocompatibility of the device. Different strategies have been evaluated with promising results. AMPs can be physisorbed or chemically linked onto a wide variety of biomaterials, including titanium,<sup>[222,223]</sup> chitosan<sup>[224]</sup> or synthetic polymers such as silicone<sup>[225,226]</sup> among others.<sup>[227–229]</sup> AMPs can be directly immobilized, randomly or in an oriented way, however, the incorporation of a flexible spacer usually results in an increased antimicrobial activity.<sup>[219,230]</sup>

In summary, AMPs are one of the most promising alternatives to antibiotics to treat drug-resistant infections. Their versatility in sequence and bioactivities can lead to new therapeutics against AMR. However, it must be noted there are no silver bullets against this threat and AMPs need further improvements to tackle the global challenge of AMR.



## Objectives

- In this thesis, we aim to expand the understanding and complexity of biomaterials based on intrinsically disordered protein polymers (IDPPs) and antimicrobial peptides (AMPs) for the development of advanced materials for biomedical applications. For this purpose, we have chosen elastin-like recombinamers (ELRs) as IDPPs due to their biological and mechanical properties inherent to natural tropoelastin and their recombinant nature that provides an outstanding versatility.
- The first concrete aim of this Thesis is the study of the hierarchical assembly of IDPPs, as models for complex IDPs. Specifically, in **Chapter 2** we aim to investigate the influence of the charge distribution in the self-assembly of ELRs based on amphiphilic diblock design. For this, a library of protein polymers will be designed and biosynthesized by recombinant techniques varying the composition and length of the hydrophilic block. Then, supramolecular assembly of the ELRs will be characterized by different techniques including Electronic Microscopy, Circular Dichroism spectroscopy and Dynamic Light Scattering among others.
- Conversely, we aim to design and biosynthesize a library of hybrid polypeptides with modular design using ELRs and AMPs as building blocks. We will propose two modular designs for their evaluation in solution (**Chapter 3**) and covalent coated onto surfaces (**Chapter 4 and 5**).

In **Chapter 3**, we address the use of AMPs as self-assembly domains in genetically engineered polypeptides with thermo-responsiveness. For this, we will design and bioproduce an amphiphilic diblock ELR which incorporate the AMP into their hydrophilic block and we will evaluate their thermal behavior and supramolecular structuration.

- In **Chapter 4** and **5**, we will develop a multifaceted platform based on ELRs intended for the immobilization of AMPs onto medical devices. The hybrid polypeptide will contain a grafting domain for the selective covalent attachment onto surfaces. In this way, in **Chapter 4** we will test the ability of the new polypeptide to form self-assembled monolayers on model gold surfaces. Covalent immobilization will be assessed by physical and chemical characterization techniques and the bioactivities of the coatings against bacterial and human cells will be assayed. To test the antibiofilm activity two staphylococcal biofilm models will be grown under static conditions.
- Finally, in **Chapter 5**, hybrid ELRs will be used for the functionalization of titanium surfaces (commercially pure grade II). Covalent tethering will be performed using organosilanes as covalent linkers. After testing the resistance of the coatings, their antimicrobial potential will be assessed against two complex oral biofilm models using a drip-flow biofilm reactor. Additionally, cytocompatibility will be verified against human gingival cells.





# Chapter II

---

Charge distribution as a  
molecular modulator of the  
nanostructuration in ELRs

---



## 2.1. Introduction

**P**rotein-based polymers, and their recombinant versions (recombinamers), are a group of materials typically inspired by the repetition and combination of conserved peptide motifs present in structural proteins such as resilin, collagen or elastin, amongst others.<sup>[231]</sup> Consequently, their unique physical, chemical and biological properties have enabled various applications in molecular biology, drug delivery or regenerative medicine.<sup>[15,16]</sup> In this context, elastin-like recombinamers (ELRs) or polypeptides (ELPs) have to be highlighted. Recombinant polymers that are typically based on the repetition of a tropoelastin-derived pentapeptide Val-Pro-Gly-Xaa-Gly,<sup>[232]</sup> which provides extraordinary elastic properties and a thermo-responsive phase-transition behavior mainly characterized by a lower critical solution temperature (LCST) phase behavior driven by the reversible formation of molecular aggregates above a certain temperature.<sup>[233]</sup> Additionally, due to their low complexity, their intrinsic disordered nature and their recombinant production, ELRs can be described to be intrinsically disordered protein polymers (IDPPs).<sup>[234]</sup> Thus, ELRs constitute a powerful model for understanding the structural properties that drive the phase separation of complex intrinsically disordered protein regions (IDPRs).<sup>[27,235]</sup>

IDPRs are protein sequences that, despite the lack of a defined 3D structure carry out vital biological functions, such as cell communication, gene regulation or cell cycle control.<sup>[25,236,237]</sup> Moreover, IDPRs can fold into different dynamic conformations and undergo phase separation depending on the presence of binding partners or the environmental conditions, which may lead to the formation of so-called biomolecular condensates.<sup>[28,238]</sup> Biomolecular condensates, are defined as dynamic, protein-rich, supramolecular assemblies that provide microenvironments which are

chemically different from the surrounding medium.<sup>[238]</sup> Phase transition, and thus biomolecular condensate formation, is driven by low complexity proteins that can assemble into liquid, gel or solid-like condensates stabilized by weak and multivalent interactions.<sup>[239–241]</sup> Appropriate assembly between these IDPRs predetermines their correct functionality. Thus, an understanding of the complex physicochemical forces that govern the formation and organization of these biomolecular condensates is critical for understanding their function and to derive implications for cellular processes and IDPR-associated diseases.<sup>[238,242]</sup> In this sense, IDPPs, especially ELRs are a powerful tool for studying the parameters that modulate formation of these protein-rich condensates. Thus, biomolecular condensates based on engineered protein and ribonucleoprotein systems have been produced in order to provide interesting insights into the dynamic intermolecular interactions of ELRs during coacervate formation.<sup>[243,244]</sup>

Charge interactions are one of the parameters that mediate folding of IDPRs.<sup>[245–247]</sup> However, this parameter is still poorly understood. As such, herein, we aim to evaluate the influence of charge distribution and density on the phase separation of model IDPPs (ELRs) with an amphiphilic diblock design, from the solute state to hydrophobically crosslinked hydrogels, via nanostructured assemblies. The self-assembly and structural parameters of elastin-like diblock co-recombinamers (ELdcRs) that contribute to the nanostructuration have been extensively studied due to their potential application of these systems as nanocarriers for drug delivery or nanovaccine production.<sup>[54–57,248,249]</sup> Although charge density has not yet been considered, charged ELdcR designs have been employed for the development of self-assembled nanocarriers and as fusion proteins.<sup>[54,85,250,251]</sup> Most recently, Schiller and coworkers have demonstrated the

ability of these systems to form subcellular compartmentalization *in vivo* and to produce dynamic protein membranes, thus directly linking them with biomolecular condensates formation.<sup>[252–254]</sup>

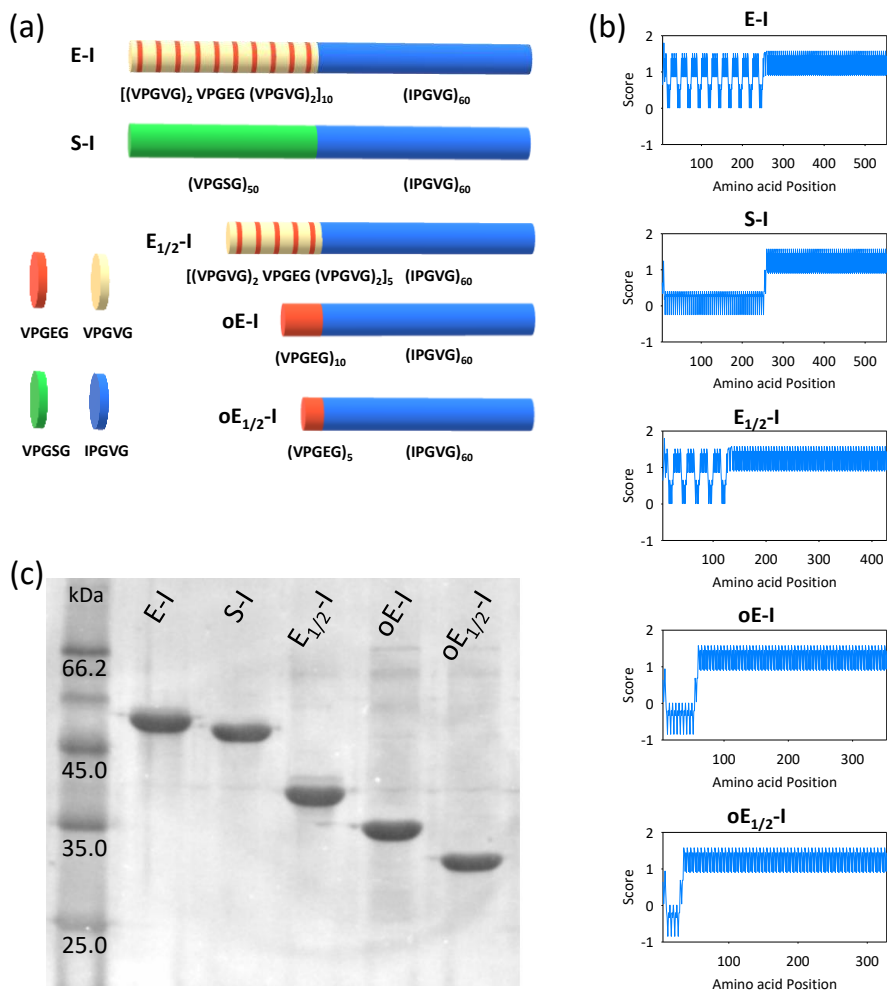
In this study, the length and charge density of amphiphilic diblocks designs were varied to produce charged amphiphiles with unbalanced length ratios between the hydrophobic and hydrophilic blocks (charged unbalanced ELdcRs, cuELdcRs). Circular dichroism (CD) spectroscopy, dynamic light scattering (DLS), transmission and scanning electron microscopy (TEM and SEM) and rheological characterization were performed in order to obtain a comprehensive overview of hierarchical self-assembly of the cuELdcRs on the nano- and microscale. On the basis of the results, charge repulsion is seen to be a critical parameter for nanostructure complexity and consequently, contributes to hierarchical assembly into higher-order structures, such as physically crosslinked gels.

## 2.2. Results and Discussion

In order to study the influence of charge on self-assembly, an ELdcR library was designed based on the sequence of a diblock ELR developed previously in our group.<sup>[85]</sup> The original diblock design, referred to as E-I, was based on an anionic hydrophilic block E [(VPGXG)<sub>50</sub>; X=V/E in a 4:1 ratio] and a hydrophobic block I [(XPGVG)<sub>60</sub>, X=I], with an LCST above and below physiological temperature, respectively. This design enables the formation of self-assembled micelles or physical hydrogels depending on the concentration under physiological conditions.<sup>[250]</sup> In order to study the influence of charge density and size on the corona during the self-assembly, the length and composition of the hydrophilic block was varied; the hydrophobic block was the same for all the constructs. Thus, four new ELdcRs were recombinantly produced as heterologous proteins in *E. coli*:

(i) an uncharged diblock with the same amino acid length for the E-I but based on uncharged L-serine as polar amino acid (S-I), (ii) a diblock in which the length of the charged hydrophilic block E was decreased by half ( $E_{1/2}$ -I), (iii) a diblock in which only the glutamic acid pentapeptides of the original hydrophilic E-block were maintained (oE-I) and (iv) a related system in which these pentapeptides were decreased by half (o $E_{1/2}$ -I). A schematic representation of the ELdcR library designs, hydropathy plots and complete amino acid sequences and size ratios of the ELdcRs can be found in **Figure 2.1a** and **Table 2.1**, respectively. Condensation of the charged pentapeptides in the oE-blocks may have an impact on the hydropathy of the block, as shown the Kyte-Doolittle plots (**Figure 2.1b**). The Kyte Doolittle algorithm predicts the hydrophilic and hydrophobic tendencies of a polypeptide chain by the progressive evaluation (from the N-terminus to the C-terminus) of the average hydropathy following the Kyte-Doolittle scale, where the larger the number is, the more hydrophobic the amino acid. The most hydrophilic amino acids are arginine (-4.5) and lysine (-3.9), whereas the most hydrophobic ones are isoleucine (4.5) and valine (4.2).

Purification by inverse transition cycling (ITC) enabled us to obtain highly pure and monodisperse products with extreme control of the sequence,<sup>[58]</sup> as confirmed by sodium dodecyl sulfate–polyacrylamide gel electrophoresis (SDS-PAGE) (**Figure 2.1c**), by matrix-assisted laser desorption/ionization time-of-flight (MALDI-TOF) (**Figure 2.1-2.5** and **Table 2.2**) and by high performance liquid chromatography (HPLC) (**Table A2.1**).



**Figure 2.1.** (a) Schematic representation of the ELdR sequences (b) and their hydropathy plot calculated using the Kyte-Doolittle scale. (c) CuCl<sub>2</sub>-stained SDS-PAGE gel of the purified ELdRs. The first lane from left to right is the Pierce™ Unstained Protein MW Marker (ThermoFisher). Lanes 2 to 6 are the different ELdRs.

Self-assembly was studied at different scales in aqueous solution. First, ELdR behavior was evaluated on the nanoscale to assess the influence of charge density and the unbalanced hydrophilic/hydrophobic block length ratio on nanostructure formation. CD analyses confirmed the disordered secondary structure of the diblocks (**Figure 2.2a** and **2.2b**). Consistent with previous studies, differences in the composition of the hydrophilic blocks barely affected the secondary structure of the ELdRs. <sup>[58]</sup> Indeed the

characteristic negative peak for IDPs at around 197 nm appeared in all the CD spectra as did the characteristic maximum at 210 nm indicating the presence of  $\beta$ -turns in ELRs.<sup>[255,256]</sup> However, it must be noted that slight differences in secondary structure were found among the ELdcRs after deconvolution of the CD data using the BeStSel algorithm (**Figure 2.2b**).<sup>[7,8]</sup> A decrease in ordered structures (higher amount of undefined structures) was found for cuELdcRs. Although this did not affect their self-assembly, it appears that a high charge density in the reduced and condensed hydrophilic region may increase the disordered nature of the polypeptides, mainly by reducing the anti-parallel proportion.

**Table 2.1.** Hydrophilic-hydrophobic block length ratio, comparison of the theoretical and experimental molecular weights (MW) calculated by MALDI-TOF and complete sequence of the ELdcRs.

	Ratio	Theo. MW (Da)	Exp. MW (Da)	Sequence
<b>E-I</b>	1:1.2	46972.8	46916.3 $\pm$ 7.1	MESLLP-[(VPGVG) <sub>2</sub> -VPGE $\bar{G}$ -(VPGVG) <sub>2</sub> ] <sub>10</sub> -VG-(IPGV $\bar{G}$ ) <sub>59</sub> -IPGV
<b>S-I</b>	1:1.2	46070.2	45996.3 $\pm$ 16.9	MESLLP-(VPG $\bar{S}$ G) <sub>50</sub> -VG-(IPGV $\bar{G}$ ) <sub>59</sub> -IPGV
<b>E<sub>1/2</sub>-I</b>	1:2.4	36585.8	36609.8 $\pm$ 8.9	MESLLP-[(VPGVG) <sub>2</sub> -VPGE $\bar{G}$ -(VPGVG) <sub>2</sub> ] <sub>5</sub> -VG-(IPGV $\bar{G}$ ) <sub>59</sub> -IPGV
<b>oE-I</b>	1:6	30593.4	30580.5 $\pm$ 3.6	MESLLP-(VPGE $\bar{G}$ ) <sub>10</sub> -VG-(IPGV $\bar{G}$ ) <sub>59</sub> -IPGV
<b>oE<sub>1/2</sub>-I</b>	1:12	28396.0	28380.3 $\pm$ 4.4	MESLLP-(VPGE $\bar{G}$ ) <sub>5</sub> -VG-(IPGV $\bar{G}$ ) <sub>59</sub> -IPGV

Nanostructure formation was followed by DLS, measuring the scattered light as a function of temperature. All ELdcRs exhibited a similar transition temperature ( $T_t$ ) phase behavior in their DSC thermograms (below 25 °C, **Figure 2.2c** and **A2.3**), in accordance with the hydrophobic



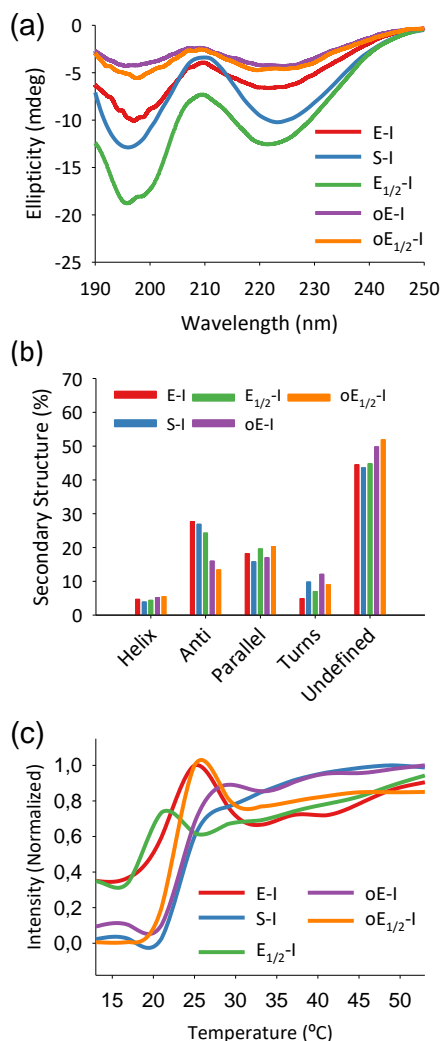
block (I) present in all ELdRs. Differences in the  $T_t$  measured by DLS and DSC corresponded mainly to differences in the ELdR concentrations used in each technique.

**Table 2.2.** LCST (degrees celsius) of the ELdRs measured by DLS and DSC in ultrapure water at physiological pH.

	DLS (°C)	DSC (°C)
<b>E-I</b>	20.1	19.6
<b>S-I</b>	24.4	18.2
<b>E<sub>1/2</sub>-I</b>	18.7	17.8
<b>oE-I</b>	23.8	17.2
<b>oE<sub>1/2</sub>-I</b>	22.5	19.1

DLS temperature trends and the low scattering intensity, below the  $T_t$ , suggested complete hydration and solubility of the ELdR molecules (**Table 2.2**). When the temperature was increased above the  $T_t$  of the hydrophobic block (I), the collapsed I-block formed hydrophobic cores surrounded by the hydrophilic blocks. The increase in scattering intensity suggested the formation of spherical micelles triggered by the hydrophobic block collapse, as described previously.<sup>[54,56,58]</sup>

Micellar assembly was studied in a concentration range (25-250  $\mu$ M) in order to compare the nanostructuration of the diverse ELdRs. In comparison with E-I polypeptide, DLS measurements and TEM images revealed that all the ELdR designs were able to form similar nanostructures in solution at low concentrations (25  $\mu$ M) (**Figure 2.3**). The unbalanced diblock designs also allowed self-assembly into spherical micelles despite of the fact that the length ratio between both blocks was outside the limits (**Table 2.1**) previously predetermined in the literature for micellar formation of uncharged amphiphilic ELdRs ( $1:2 \leq$  length ratio  $\leq 2:1$ <sup>[56]</sup> and the most recent, hydrophilic : hydrophobic ratio  $\geq 0.3$ ).<sup>[57]</sup>

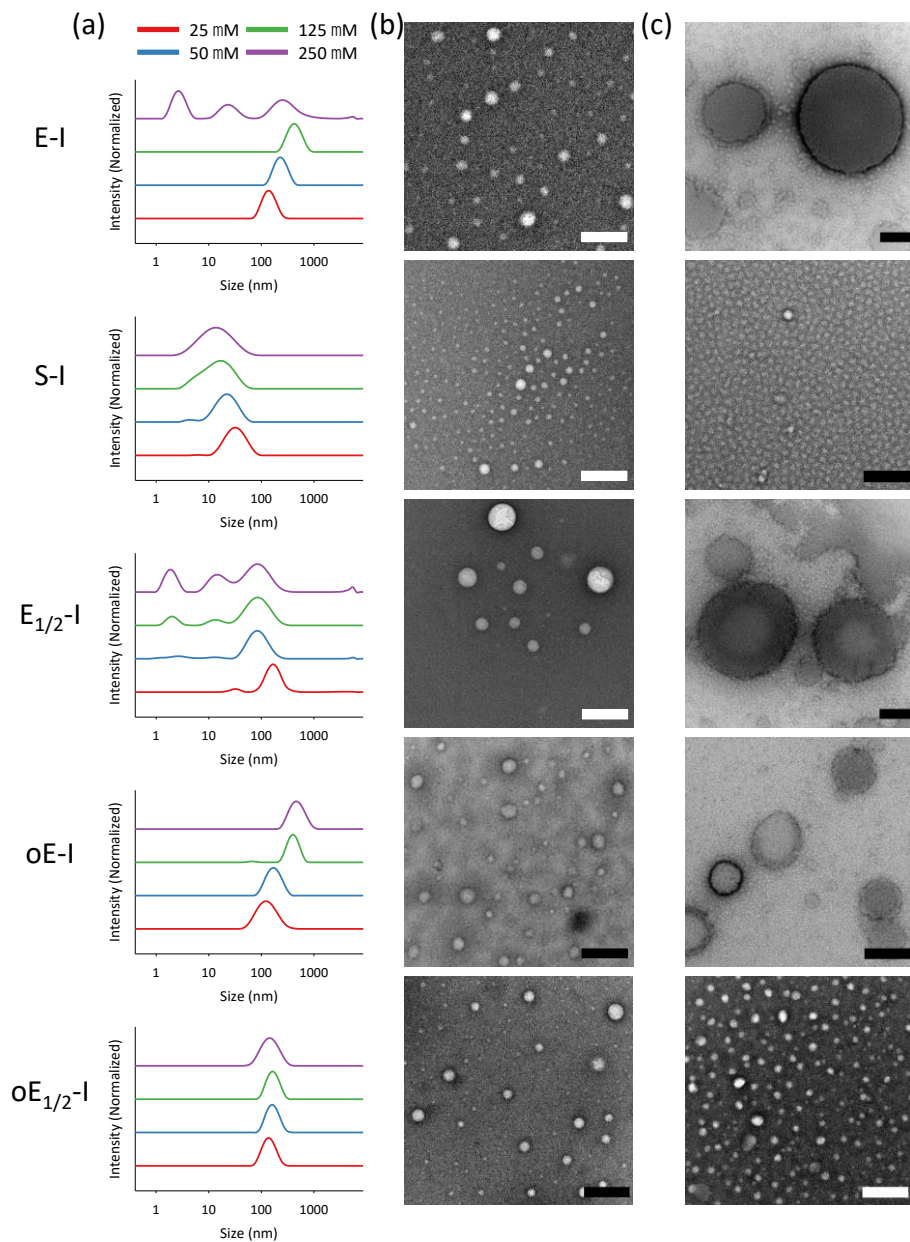


**Figure 2.2.** Secondary structure characterization of the ELdcRs above the  $T_i$ : (a) CD spectra at 37 °C and (b) secondary structure quantification using the BeStSel algorithm. (c) Characterization of nanoparticle formation by DLS. All the ELdcRs showed a  $T_i$  below 25 °C. (d)  $T_i$  (degrees celsius) of the ELdcRs measured by DLS and DSC in ultrapure water at physiological pH.

E-I, which has a block length ratio of 1:1.2, self-assembled into monodisperse and completely stable spherical nanoparticles in solution at low concentrations ( $D_h = 142$  nm, PDI = 0.154 at 25  $\mu$ M). Nevertheless, its hydrodynamic diameter ( $D_h$ ) increased as a function of concentration. At 250  $\mu$ M, the micellar structuration was compromised and the monomodal

distribution evolved towards more complex distributions, as revealed by intensity plots and correlograms (**Figure 2.3a** and **A2.4**, respectively). Moreover, a TEM-based morphology analysis of the nanostructures revealed that ELdcR assemblies could progress from spherical nanoparticles to large spherical aggregates as a function of the concentration (**Figure 2.3b** and **2.3c**). In agreement with previous findings, these larger assemblies seemed to be formed by the aggregation of smaller micellar structures (**Figure 2.3c**).<sup>[54,250]</sup> In contrast, non-charged S-I diblock self-assembled into smaller ( $D_b = 35$  nm, PdI = 0.173 at 25  $\mu$ M) and more stable micelles comparing to E-I. A lack of charges in the corona seemed to decrease  $D_b$  and stabilize the micellar assembly. A monomodal distribution was found over the entire concentration range (**Figure 2.3** and **A2.4b**), and the TEM evaluation confirmed the homogeneous size and shape of the nanoparticle S-I population.

In contrast, in the  $E_{1/2}$ -I diblock co-recombinamer, the hydrophilic block was halved, thus resulting in a length ratio of 1:2.4. It showed similar behavior to the E-I diblock design. As shown by TEM micrographs (**Figure 2.3b** and **2.3c**), nanostructures derived from the self-assembly were similar to those found in the E-I samples. However, the  $E_{1/2}$ -I micelles showed a multimodal distribution and higher polydispersities (PdI = 0.357 at 25  $\mu$ M) over the whole concentration range (**Figure 2.3a**), possibly due to the reduced length of the hydrophilic block.



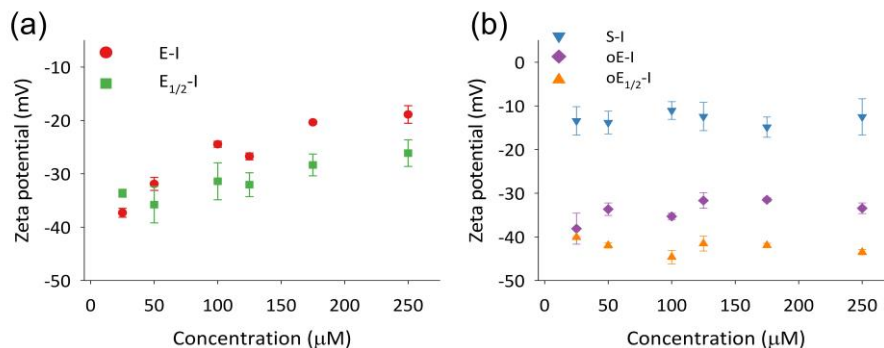
**Figure 2.3.** Physical characterization of the nanostructures formed by self-assembly of the ELdcRs. (a) Intensity size distributions in the concentration range 25–250  $\mu$ M at 37  $^{\circ}$ C. TEM images: (b) all the ELdcR designs self-assembled into spherical micelles at 25  $\mu$ M at 37  $^{\circ}$ C in aqueous solution, (c) increasing the concentration (250  $\mu$ M) drives the formation of hierarchical aggregates in some of the ELdcR designs (E-I,  $E_{1/2}$ -I and oE-I) whereas micellar assembly was stabilized in the others (S-I and  $oE_{1/2}$ -I). The size of all scale bars is 200 nm.

Spherical nanoparticles were also formed from upon the self-assembly of the cuELdRs. Despite their unbalanced ratio between their hydrophilic:hydrophobic block lengths (1:6 and 1:12 for oE-I and oE<sub>1/2</sub>-I, respectively), an increase in charge density in the corona allowed the formation of micellar structures. Both cuELdRs self-assembled into spherical nanoparticles with similar  $D_b$  and PdI values to E-I ( $D_b = 137$  and PdI = 0.223 for oE-I, and  $D_b = 135$  and PdI = 0.115 for oE<sub>1/2</sub>-I) at 25  $\mu$ M. Moreover, the micellar populations maintained monomodal distributions over the whole concentration range in the cuELdRs (**Figure 2.3a** and **A2.4**) as well as in the non-charged diblock (S-I). However, there were significant differences between both cuELdRs. In the oE-I,  $D_b$  increased as a function of concentration. Larger spherical assemblies were found at 250  $\mu$ M (**Figure 2.3a** and **A2.4d**), similar to those found in E-I and E<sub>1/2</sub>-I. In contrast, as shown by the intensity size distributions and correlation functions, the  $D_b$  value for the oE<sub>1/2</sub>-I micelles remained constant and stable over the whole concentration range (**Figure 2.3a** and **A2.4e**). Morphological evaluation by TEM confirmed an improved stability of the micellar assembly of the oE<sub>1/2</sub>-I polypeptide even at 250  $\mu$ M, similar to that for S-I.

The zeta potential (ZP) of the nanostructures was then measured in the same concentration range in order to evaluate their electrostatic stability and to verify the interactions between the coronas (**Figure 2.4**). All the ELdRs showed a negative ZP, even S-I, due to the composition of the N-terminal leader sequence (MESLLP, **Table 2.1**). The presence of glutamic acids in the anionic ELdRs provided a ZP above the general stability dividing line ( $\pm 30$  mV) at low concentrations (below 100  $\mu$ M).

In accordance with the DLS results (**Figure 2.3a**), the evolution of ZP in the polypeptides E-I and E<sub>1/2</sub>-I confirmed the hypothesis of an

interaction between the coronas of the micelles hiding part of the charges within the higher-order aggregates (**Figure 2.4a**). ZP increase with concentration suggests an interaction between the coronas and, hence, the agglomeration of nanoparticles. These interactions may be favored by the amphiphilic nature of the E-block (**Figure 2.1b**).



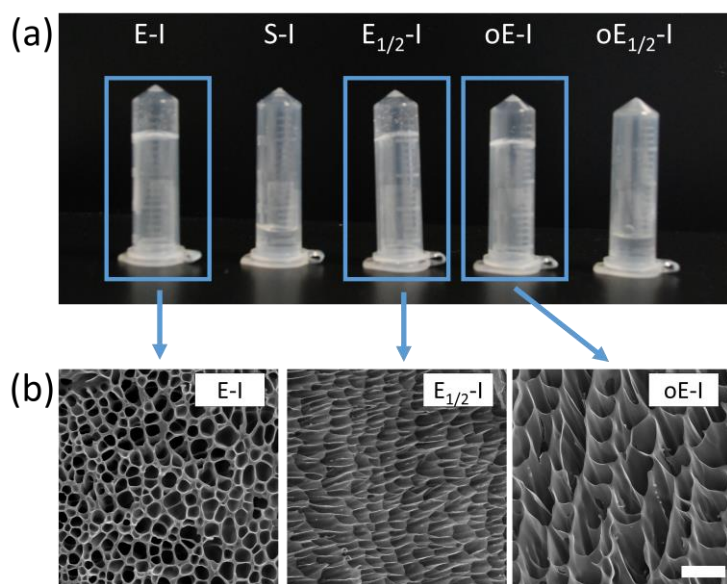
**Figure 2.4.** Effect of concentration on the zeta potential. Whereas the zeta potential increased with the concentration in the ELdcRs with amphiphilic corona (a), it remained stable in the uncharged and cuELdcRs (b).

In the other three ELdcRs, in contrast, ZP remained stable (**Figure 2.4b**). The lack of charged pentapeptides in the S-I, and the increased charge density in the hydrophilic block of the cuELdcRs provided an apparent electrostatic stability in this concentration range. When comparing the cuELdcRs, it is important to note that the most unbalanced diblock design (o $E_{1/2-I}$ ) showed the most negative ZP (always below -40 mV). Even though o $E_{1/2-I}$  contains half the charge of oE-I, a stronger ZP indicates a greater electrostatic stability of the o $E_{1/2-I}$  micellar assembly.

Additionally, as the polypeptide E-I undergoes a phase transition towards physical hydrogels driven by concentration,<sup>[250]</sup> we also investigated the influence of the corona composition on gelation. After the incubation of 2.5 mM solutions of the ELdcRs at 37 °C, we found that only three ELdcRs, namely E-I,  $E_{1/2-I}$  and oE-I, had undergone phase transition (**Figure 2.5a**). These findings agree with nanostructure characterization on

nano- and mesoscale, and micellar instability seems to be directly related to the ability to undergo gelation.

Only those diblock nanoparticles that showed an increasing  $D_b$  with concentration and self-assembly into higher-order assemblies were able to drive a liquid-gel transition because of a possible coronal interaction, charge repulsion or both. Although phase transition was driven by hydrophobic collapse of I-block after the incubation above its  $T_i$ , the hydrophilic block composition also seemed to be affect the liquid-gel phase transition and, therefore, for the supramolecular organization of the polypeptides in the physically crosslinked hydrogel.

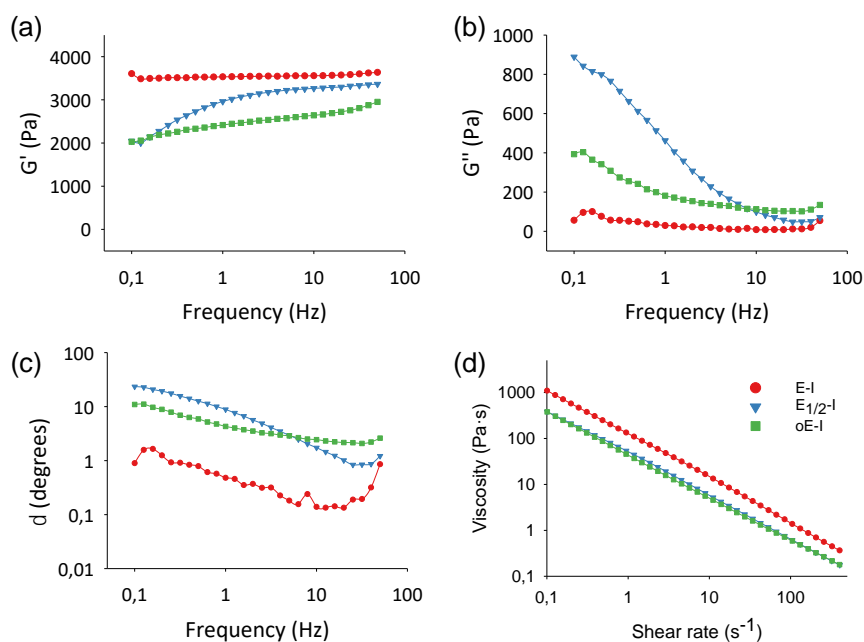


**Figure 2.5.** (a) Physical hydrogel formation in 2.5 mM solutions at 37 °C. (b) SEM micrographs of the cryo-fractured hydrogels. The size of all SEM images is 25 x 25  $\mu\text{m}$  and the size of scale bar is 4  $\mu\text{m}$ .

To explore the contribution of the hydrophilic block to supramolecular assembly in the gel form, we evaluated the hydrogel properties qualitatively by SEM. After gel formation, hydrophilic block length seemed to play a part in the pore morphologies. Thus, as can be seen in **Figure 2.5b**, the

SEM micrographs show that the physical gel formed by E-I had a different appearance to those formed by E<sub>1/2</sub>-I and oE-I. However, the pore size was similar in E-I and E<sub>1/2</sub>-I gels (around 2 μm), but larger (up to ≈ 3 μm) for oE-I. Moreover, in the later, the pore wall thickness was so small that some pores were joined together to form “macropores”.

In light of these results, we characterized the rheological properties of the hydrogels in order to quantify their viscoelastic properties. First, the linear viscoelastic region was determined by carrying out a swept of the strain amplitude. As can be seen from **Figure A2.5**, no significant changes were observed in the complex modulus magnitude up to a strain amplitude of around 1%. A 0.3% strain was selected for all the oscillatory measurements.



**Figure 2.6.** Rheological characterization of the ELdcRs that undergo a liquid-gel phase transition at 37 °C: (a) Evolution of storage ( $G'$ ) and (b) loss ( $G''$ ) moduli as a function of frequency. (c) Evolution of phase angle ( $\delta$ ) as a function of frequency and (d) ELdcR hydrogel viscosity as a function of shear rate at 37 °C under continuous flow.



**Figure 2.6** shows the frequency response of both the storage ( $G'$ , **Figure 2.6a**) and loss ( $G''$ , **Figure 2.6b**) moduli. While no noticeable dependence of  $G'$  on frequency was observed for E-I, both  $E_{1/2}$ -I and oE-I exhibit a clear evolution with frequency. At 1 Hz, the higher storage modulus corresponds to E-I (see **Table 2.3**), whereas  $E_{1/2}$ -I and oE-I have a value of around 2.5 kPa.

As for  $G''$ , a clear difference was observed at frequencies lower than 1 Hz. Thus, whereas no significant frequency dependence was found for E-I, a strong evolution was observed for oE-I and, especially, for  $E_{1/2}$ -I. As can be seen in **Table 2.3**, the loss modulus for  $E_{1/2}$ -I at 1 Hz is considerably higher than for oE-I and E-I (in a ratio of 2.7 and 15, respectively). At the highest frequencies, similar values of about 150 Pa were found for all hydrogels.

The phase angle can be calculated from the ratio of the loss and storage modulus the phase angle can be calculated (**Figure 2.6c**). A very high elastic behavior was suggested for E-I since phase angles lower than  $1^\circ$  were obtained. This elastic behavior was partially lost in the other two hydrogels at low frequencies, especially for  $E_{1/2}$ -I, where values higher than  $10^\circ$  were reached. The phase angle evaluated at 1 Hz confirmed this trend (**Table 2.3**).

**Table 2.3.** Mean  $G'$ ,  $G''$  and  $\delta$  for the different ELdcRs at 37 °C. Values were chosen from the linear viscoelastic region (LVR) (0.3% strain) at a frequency of 1 Hz.

	E-I	$E_{1/2}$ -I	oE-I
<b><math>G'</math> (Pa)</b>	3404.7±428.2	2824.3±261.3	2420.7±45.6
<b><math>G''</math> (Pa)</b>	32.03±2.2	480.2±58.6	180.9±5.2
<b><math>\delta</math> (degrees)</b>	0.55±0.05	9.7±1.57	4.27±0.05

Finally, the viscosity of the three hydrogels was measured as a function of shear rate using flow measurements. All three hydrogels exhibited a shear

thinning behavior, with the hydrogel viscosity decreasing linearly by up to four orders of magnitude for the three orders of magnitude swept for shear rate (**Figure 2.6d**).

Amphiphilic block co-polypeptides can form self-assembled micelles in solution with block length and distribution being key parameters for supramolecular assembly and stabilization.<sup>[56,61]</sup> The hydrophilic corona is responsible for avoiding aggregation and maintaining the hydrophobic core in solution. Thus, small coronas cannot sustain the micellar conformation and a minimum length ratio between the two blocks in the amphiphilic diblock design is required.<sup>[56,57]</sup>

However, if the corona is charged, we face a different scenario in which electrostatic repulsion between charges enables the established limits to be overcome and new molecular designs to be obtained. Thus, an increase in charge density in the corona seems to contribute to micelle stabilization of highly unbalanced diblocks at low concentrations. Therefore, micellar assembly is favored in the  $oE_{1/2}$ -I design (length ratio 1:12), just as it is also favored in the non-charged ELdcR (S-I). Electrostatic repulsion then contributes to micellar destabilization, promoting hierarchical assembly into higher-order structures. In the other three charged ELdcRs (E-I,  $E_{1/2}$ -I and  $oE$ -I), micellar assemblies evolve into larger assemblies on the mesoscale upon increasing the concentration. As such, electrostatic repulsion between charges seems to be the driving force for micellar destabilization, and the hydrophilic block length appears to be important for stabilization of the higher-order assemblies.

Finally, charge distribution also contributes to liquid-gel transition and viscoelastic behavior of the hydrogel. Hydrophilic block length and composition modulate the rheological properties. Thus, whereas E-I (1:1.2 length ratio) forms elastic hydrogels with a viscoelastic behavior

independent of the frequency,  $E_{1/2-I}$ , which has a higher length ratio (to 1:2.4) but the same composition shows a strong frequency dependence for the loss modulus ( $G''$ ). In addition, an increase in charge density (oE-I, length ratio 1:6) compensates the frequency dependence observed in the  $E_{1/2-I}$  hydrogel despite the condensed oE-block.

In summary, the incorporation of charged residues into the backbone of IDPPs leads to the emergence of molecular interactions that trigger new molecular dynamics and behaviors, such as shear thinning of the gel form, which may find applications in tissue engineering or drug delivery. Our results also shed light on the folding of IDPPs that may be useful for understanding complex protein aggregates based on IDPRs such as biomolecular condensates.

## **2.3. Conclusion**

We have studied charge distribution as a molecular trigger in the supramolecular assembly of IDPPs. An IDPP library based on ELdCRs with an amphiphilic diblock design have been bioproduced, varying the hydrophilic block while maintaining the hydrophobic block composition in order to evaluate their influence on nanostructuration and phase transition.

In addition, we have demonstrated that incorporating charges into the molecular design strongly contribute to assembly on the nano-, meso- and microscale. Electrostatic repulsion enables the micellar structuration of unbalanced diblock co-recombinamers at low concentrations and can, in turn, further contribute liquid-gel transition at higher concentrations.

Finally, charge distribution seems to modulate the protein polymer entanglements within hydrogels and, hence, viscoelastic behavior. As such, this study represents a successful step toward the design of self-assembled

protein devices for biomedical applications but also toward gaining further insight into the molecular mechanisms that govern the formation and maturation of biomolecular condensates.

## 2.4. Experimental section

### 2.4.1. Materials

Glassware was dried at 120 °C overnight prior to use. Chemicals were purchased from Sigma-Aldrich and used as received unless otherwise mentioned. Ultrapure water (15 M $\Omega$ ·cm) was used from Milli-Q A-10 Synthesis and Elix 10 Millipore.

Restriction enzymes, shrimp alkaline phosphatase (SAP) and T4 ligase were purchased from ThermoFisher Scientific Inc. (USA). For the construction and expression of the encoding genes of the ELdcRs, we employed the cloning vector pDriveAll and the expression vector p7. These plasmids were constructed in our group from the commercial pDrive (Qiagen, Germany) and pET-25b (+) vectors (Novagen), respectively. <sup>[3]</sup> The DNA miniprep purification kit (Nucleospin<sup>®</sup> plasmid) and the Quick Gel Extraction Kit (PureLink<sup>™</sup>) were purchased from Macherey-Nagel (Germany) and Invitrogen (USA), respectively.

### 2.4.2. Recombinant synthesis of the ELdcRs

To generate the battery of genes that encodes the ELdcR library the iterative-recursive method was employed. <sup>[2]</sup> Gene construction was performed in the pDriveAll vector using *Escherichia coli* strain XL-1 blue (Agilent, USA). Encoding genes were then cloned into a the p7 vector (**Figure A2.1** and **A2.2**) and transformed for expression in *E. coli*

BLR(DE3) strain (Novagen). Transformation in *E. coli* BLR(DE3) was carried out following the simple method developed by Chung et al. [257]

Hyperexpression of the heterologous polypeptides was screened and the best clones were selected for the fermentation. Bacterial fermentation was performed in Terrific Broth (Formedium, UK) supplemented with glycerol (8 mL L<sup>-1</sup>) in a 15-L bioreactor (Applikon biotechnology, USA), at 37 °C with agitation (500 rpm). Then, bacteria were collected by centrifugation and resuspended in pre-chilled ‘wash’ buffer (20 mM Tris Base, 140 mM NaCl, pH=7). This step was repeated until supernatant was clear. Then, bacteria were resuspended in ‘disruption’ buffer (20 mM Tris Base, 1 mM EDTA, 1mM PMSF, pH=8) and the polypeptides were liberated from the inclusion bodies by disruption in a GEA Lab PandaPLUS 2000 homogenizer (GEA Farm Technologies, New Zealand).

ELdcRs were purified by inverse transition cycling (ITC)<sup>[2]</sup> adding 1.5 M NaCl for precipitation above the  $T_i$ . Pure products were dialyzed against deionized and ultrapure water for three days (12,000 MwCO, Medicell Membranes Ltd, UK), neutralized with NaOH (pH≈7.0), filtered (0.22 μm Nalgene™, ThermoFisher Scientific, USA), lyophilized and stored at -20 °C until further use. A final yield of 425-640 mg L<sup>-1</sup> of cells was obtained, depending the diblock construct.

The monodispersity and purity of the ELdcRs were evaluated by sodium dodecyl sulfate– polyacrylamide gel electrophoresis (SDS-PAGE), matrix assisted laser desorption/ionization time-of-flight (MALDI-TOF) mass spectrometry and by high performance liquid chromatography (HPLC). MALDI-TOF and HPLC were carried out in the Laboratorio de Técnicas Instrumentales of the University of Valladolid.

The theoretical hydrophobicity of the ELdcRs was calculated using the ProtScale algorithm and the Kyte-Doolittle scale.<sup>[258,259]</sup>

#### *Agarose gel electrophoresis*

Agarose gels were prepared with and run in Tris-acetate EDTA (TAE) buffer (40 mM Tris-acetate, 1mM EDTA, pH 8). Analytical and preparative gels were run at 90 and 60 V, respectively. SimplySafe™ (EURx®, Poland) was used as stain for detecting nucleic acids in the agarose gel.

#### *SDS-PAGE*

Proteins were run under denaturing conditions on polyacrylamide gels following the protocol described by Laemmli.<sup>[6]</sup> Gels were stained using CuCl<sub>2</sub> solution (0.3 M in distilled water).

#### *2.4.3. Thermal behavior characterization*

The thermal behavior of the diblock co-recombinamers were characterized by dynamic light scattering and differential scanning calorimetry. The transition temperature at low concentrations was calculated measuring by DLS at 25 μM in ultrapure water. Thus, the scattered light intensity was recorded every 4 °C from 13 to 53 °C. Samples were stabilized for 2 min at each temperature and measured in triplicate with 11 runs per measurement. The temperature at which the scattered intensity reached 50% of the intensity was considered as the low critical solution temperature.

DSC experiments were performed using a Mettler Toledo 822e equipment with liquid nitrogen cooler. Thus, 20 μL of at 50 mg mL<sup>-1</sup> solution of the ELdcR in ultrapure water was placed in a standard 40-μL

aluminium pan and sealed. The samples were stabilized at 5 °C for 5 min, then the temperature was increased by 5 °C min<sup>-1</sup> from 5 to 60 °C.

#### *2.4.4. Circular dichroism*

CD spectra were recorded using a Jasco J-810 spectropolarimeter (Jasco, USA) equipped with a temperature controller (Research Technical Services, University of Alicante, Spain). Samples were dissolved at 0.2 mg mL<sup>-1</sup> and measured in 0.1 cm quartz cells in the range 190-250 nm. The temperature was stabilized at 37 °C for 10 min prior to measurement. Secondary structure percentages were determined using the BeStSel (Beta Structure Selection)<sup>[7,8]</sup> web server in the 200-250 nm range (when the dynode voltage was below 500 nm). Data were smoothed using a 15pt Savitzky-Golay filter.

#### *2.4.5. Nanoparticle size and zeta potential analysis*

The nanoparticle size distribution and zeta potential were measured in ultrapure water using a Zetasizer Nano (Malvern Instruments, UK), with a 173° scattering angle and equipped with a HeNe laser (633 nm) with an output power of 10 mW. Size distribution was analyzed in a range of concentrations (25–250 μM) above the critical micelle concentration of the E-I polypeptide,<sup>[85]</sup> to evaluate nanoparticle stability and aggregation. Zeta potential measurements were carried out in the same concentration range, at 37 °C. Each sample was measured in triplicate.

#### *2.4.6. Transmission electron microscopy*

TEM samples were prepared on 300-mesh carbon coated copper grids (C300Cu) with negative staining. To that end, grids were rendered hydrophilic by plasma treatment using a PDC-002 plasma cleaner (Harrick

Plasma, USA). Low power setting (7.2 W applied to the RF coil) for 20 s. Then, 15  $\mu\text{L}$  of the pre-incubated ELdcR (1 h at 37 °C at a concentration of 25  $\mu\text{M}$ ), ultrapure water and uranyl acetate (1% w/v) solutions were dropped on Parafilm<sup>®</sup> strip over a pre-heated (37 °C) glass surface. Plasma treated grids were placed onto the ELR drop for 90 s, on ultrapure water for 60 s, and finally, on the negative staining solution for another 60 s. Blotting filter paper (Whatman<sup>®</sup> Gel Blot GB003) was used to remove excess solution after every step by touching the edge of the grid.

Images were taken using a Tecnai Thermionic T20 microscope operated at 200kV (SAI, University of Zaragoza, Spain).

#### 2.4.7. *Physical hydrogel formation and characterization*

Samples were dissolved in ultrapure water at a concentration of 2.5 mM in ultrapure water at 4 °C, then incubated at 37 °C for 30 min to qualitatively test the ability to form physical hydrogels.

##### *Rheological analysis*

The mechanical properties of the hydrogels were tested by performing oscillatory shear and flow measurements in an AR2000 rheometer (TA Instruments) using a parallel plate with a diameter of 40 mm. Measurements were performed with a sample volume of 1300  $\mu\text{L}$  (gap = 1100  $\mu\text{m}$ ) 37 °C, controlling the temperature with a Peltier plate. After sample deposition at 4 °C, gel formation was accomplished *in situ*. Data were recorded using TRIOS software (v4.1.1.33073). For the oscillatory shear measurements, a strain sweep was performed from 0.01% to 15% at an angular frequency of 1 Hz to test the LVR. Frequency sweeps were carried out sequentially from 0.1 to 50 Hz, with a constant strain of 0.3% (corresponding to the LVR). The storage ( $G'$ ) and loss modulus ( $G''$ ) were obtained from the

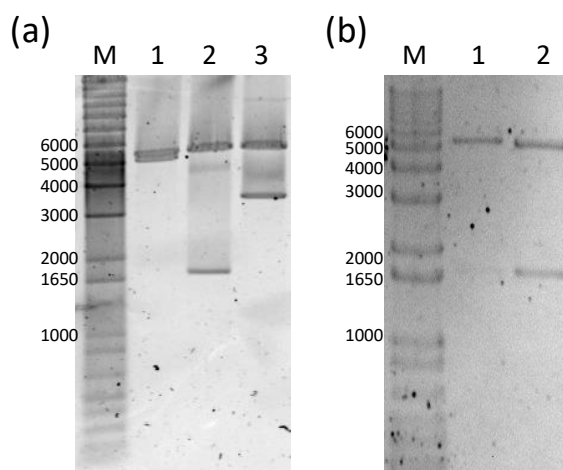


rheological measurements. The loss factor ( $\tan \delta \equiv G''/G'$ , where  $\delta$  is the phase angle between the output response to the input stimulus) and the complex modulus magnitude ( $|G^*|^2 = (G')^2 + (G'')^2$ ) were then calculated using the values obtained. Flow measurements were employed to measure the viscosity. Samples were conditioned with a pre-shear of  $500 \text{ s}^{-1}$  for 1 min, then the viscosity was measured in a flow ramp from  $500$  to  $0.1 \text{ s}^{-1}$  using a continuous ramp in a logarithmic descending series of discrete steps. Overall measurement took 10 min, acquiring 10 points for each order of magnitude. All measurements were performed at least in triplicate.

#### *Scanning electron microscopy*

In order to visualize the morphology of those samples that formed hydrogels, samples were incubated for 1 day at a concentration of 2.5 mM at  $37 \text{ }^\circ\text{C}$ . They were then cryo-fractured in liquid  $\text{N}_2$  and lyophilized. SEM micrographs were obtained using a FEI Quanta 200 FEG (FEI Company, USA) microscope in low vacuum mode (SAI, University of Zaragoza, Spain). A 20 nm layer of Pd was applied with a Leica EM ACE200 vacuum coater to avoid charging effects. SEM images were analyzed using the ImageJ software.

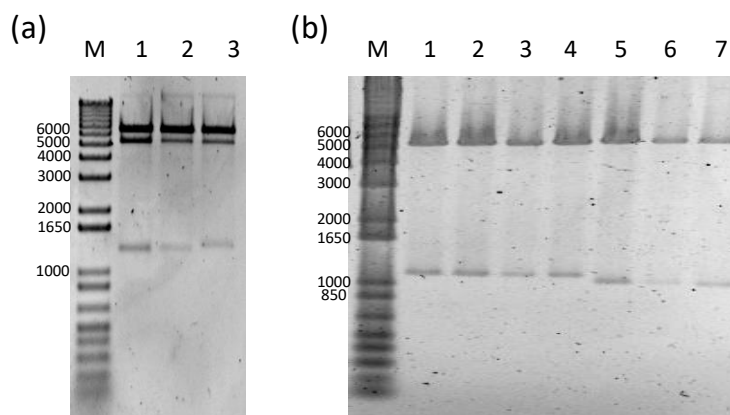
## 2.5. Appendix



**Figure A2.1.** Enzymatic analysis of the expression vector p7 with the constructs (a) E-I and (b) S-I cut with *XhoI* and *XbaI* endonucleases. M = 1kb Plus DNA Ladder (Invitrogen, USA)

**Gel a.** Results of the ligation of a p7 vector (5547 bp) linearized with *SapI* with the E-I insert (1650 bp). Lane 1: p7 containing the insert (E-I) x3. Lane 2: p7 containing the insert (E-I) x1. Lane 3: p7 containing the insert (E-I) x2.

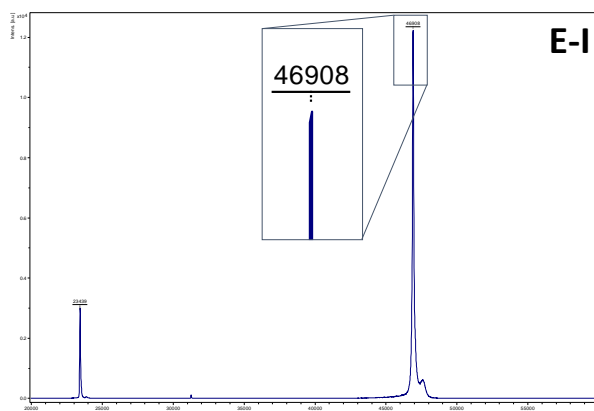
**Gel b.** Results of the ligation of a p7 vector (5547 bp) linearized with *SapI* with the S-I insert (1650 bp). Lane 1: p7 linearized. Lane 2: (p7 containing the insert S-I).



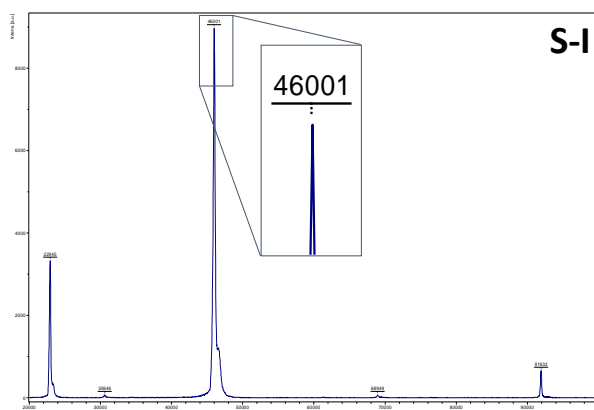
**Figure A2.2.** Enzymatic analysis of the expression vector p7 with the constructs (a)  $E_{1/2}$ -I and (b) oE-I, o $E_{1/2}$ -I cut with *XhoI* and *XbaI* endonucleases. M = 1kb Plus DNA Ladder (Invitrogen, USA)

**Gel a.** Lane 1-3: p7 plasmids containing the insert  $E_{1/2}$ -I (1275 bp).

**Gel b.** Lane 1-4: p7 plasmids containing the insert oE-I (1050 bp). Lane 5-7: p7 plasmids containing the insert o $E_{1/2}$ -I (975 bp).



**Figure A2.3.** MALDI-TOF spectra of E-I polypeptide.



**Figure A2.4.** MALDI-TOF spectra of S-I polypeptide.



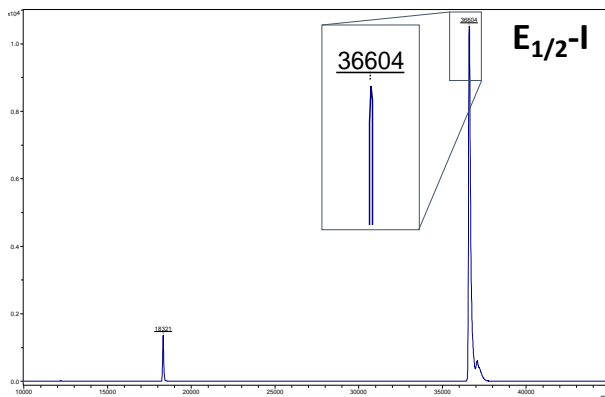


Figure A2.5. MALDI-TOF spectra of E<sub>1/2</sub>-I polypeptide.

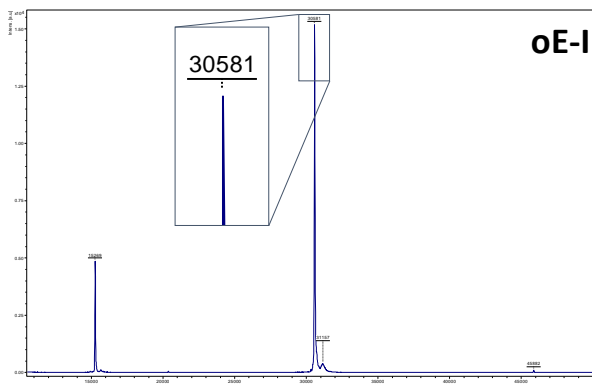


Figure A2.6. MALDI-TOF spectra of oE-I polypeptide.

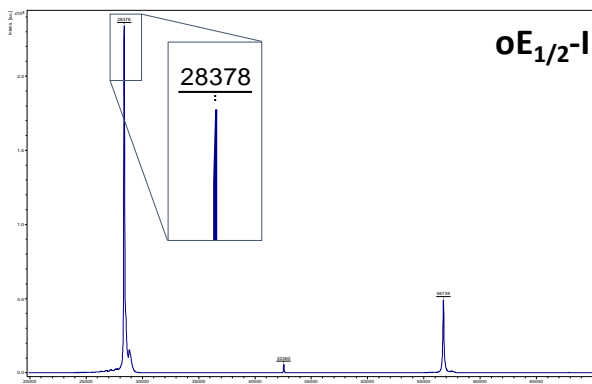
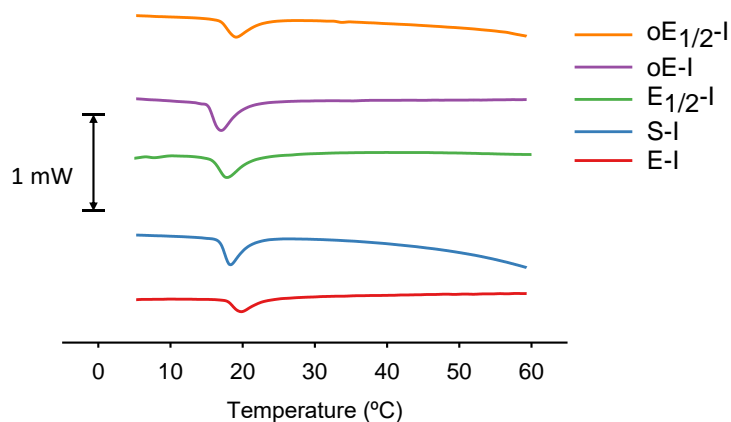


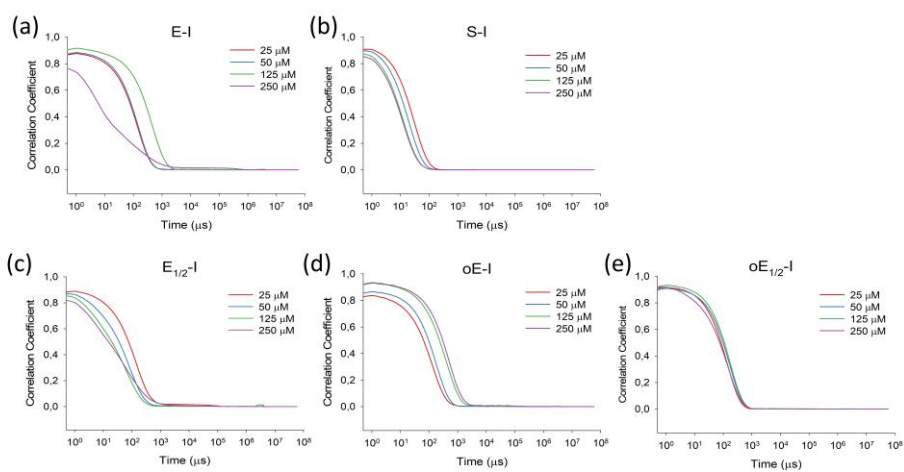
Figure A2.7. MALDI-TOF spectra of oE<sub>1/2</sub>-I polypeptide.

**Table A2.1.** Amino acidic composition of the ELdcRs calculated by HPLC. It is represented the theoretical composition comparing to the experimental values obtained.

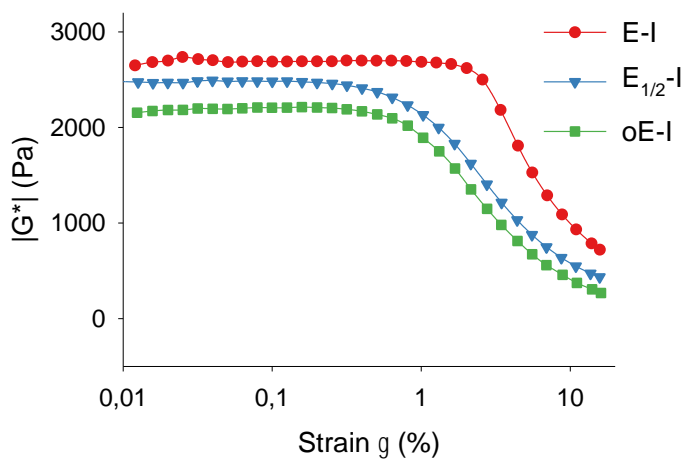
Amino acid	E-I		S-I		E <sub>1/2</sub> -I		oE-I		oE <sub>1/2</sub> -I	
	Theo	Exp	Theo	Exp	Theo	Exp	Theo	Exp	Theo	Exp
Asp	-	-	-	-	-	-	-	-	-	-
Glu	11	12.02	1	1.17	6	6.66	11	14.51	6	7.18
Asn	-	-	-	-	-	-	-	-	-	-
Ser	1	1.52	51	50.35	1	1.32	1	1.05	1	1.17
Gln	-	-	-	-	-	-	-	-	-	-
His	-	-	-	-	-	-	-	-	-	-
Gly	220	224.45	220	222.91	170	170.56	140	142.99	130	129.48
Thr	-	-	-	-	-	-	-	-	-	-
Arg	-	-	-	-	-	-	-	-	-	-
Ala	-	-	-	-	-	-	-	-	-	-
Tyr	-	-	-	-	-	-	-	-	-	-
Cys	-	-	-	-	-	-	-	-	-	-
Val	151	139.68	111	105.83	106	97.22	71	59.87	66	61.91
Met	1	1.26	1	1.15	1	1.22	1	1.09	1	1.19
Trp	-	-	-	-	-	-	-	-	-	-
Phe	-	-	-	-	-	-	-	-	-	-
Ile	60	61.05	60	61.87	60	62.56	60		60	61.49
Leu	2	2.73	2	2.46	2	2.61	2	2.79	2	2.74
Lys	-	-	-	-	-	-	-	-	-	-
Pro	111	115.48	111	111.89	86	89.52	71	72.18	66	66.04
<b>Total aas</b>	557	558.2	557	557.63	432	431.7	357	356.8	332	331.21



**Figure A2.8.** DSC thermographs for 50 mg mL<sup>-1</sup> solutions in ultrapure water at pH $\approx$ 7 of E-I, S-I, oE-I, E<sub>1/2</sub>-I and oE<sub>1/2</sub>-I polypeptides.



**Figure A2.9.** Raw correlation functions obtained by DLS for the diverse ELdcRs at different concentrations (25, 50, 125 and 250  $\mu$ M) in ultrapure water.



**Figure A2.10.** Strain sweep rheology of the physically cross-linked hydrogels at 37 °C, 1 Hz.





# Chapter III

---

Self-assembly of genetically  
engineered polymers:  
the interplay between  
AMPs and ELRs

---



### 3.1. Introduction

**A**ntimicrobial peptides (AMPs) or host defense peptides (HDPs) are one of the most promising alternatives to conventional antibiotics in the treatment of the increasingly frequent drug-resistant infections.<sup>[260,261]</sup> Their broad-spectrum antimicrobial activity and their immunomodulatory properties rely on their amphipathicity that confers the ability to interact with several molecular targets,<sup>[148,262]</sup> or even undergo self-assembly. Recent investigations have demonstrated their ability to form supramolecular assemblies including fibers,<sup>[208]</sup> nanoparticles,<sup>[209]</sup> twisted nanoribbons<sup>[210]</sup> or hydrogels.<sup>[211–214]</sup> Moreover, peptide assembling can predetermine their biological effects, enhancing antimicrobial activity,<sup>[217]</sup> but it may induce cytotoxic effects<sup>[218]</sup> or other unforeseen side effects.<sup>[263]</sup> As mentioned in **Chapter 1**, AMPs present some drawbacks that limit their clinical use. They are highly sensitive to environmental conditions, they show short plasma-half-life because their sensitiveness to proteolytic degradation and the high cost of their chemical synthesis hinder the scale-up of their production.<sup>[141]</sup> Therefore, in many cases, their therapeutic use has been restricted to topic applications.

To overcome these limitations, AMPs often require molecular carriers to control their delivery. In this context, AMPs have been integrated into synthetic or natural polymers in order to decrease their cytotoxicity, protect them from the protease degradation and control their delivery.<sup>[264]</sup> Additionally, the use of self-assembled polymers enables to obtain interesting architectures for their biomedical application, including vesicles, fibers or hydrogels.<sup>[265]</sup> In this sense, recombinant smart polymers constitute highly interesting candidates. On the one hand, their extreme versatility and sequence control given by their inherent recombinant nature provides a sustainable alternative for the co-production of AMPs as fusion partners.

On the other hand, their stimulus-responsiveness can be used in a synergistic combination with the self-assembly behavior of the AMPs to design advanced functional nanomaterials for biomedical applications.

Therefore, we aim to investigate in this chapter the interplay of self-assembling AMPs and smart protein polymers. As smart polymers, we employed an ELR with modular design based on an amphiphilic diblock, where the AMP was fused into the hydrophilic block through a spacer. In this way, both potential self-assembling domains (SADs) (AMP and hydrophobic block of the ELR) were located in the two ends of the molecule. We designed two different hybrid polypeptides containing the well-characterized designer peptides: GL13K and 1018. These AMPs have similar physicochemical properties and both have proven to self-assemble in solution.<sup>[210,218]</sup> Moreover, GL13K and 1018 show potent antibiofilm properties combined with broad spectrum bactericidal activity and immunomodulatory properties, respectively.<sup>[172,261]</sup>

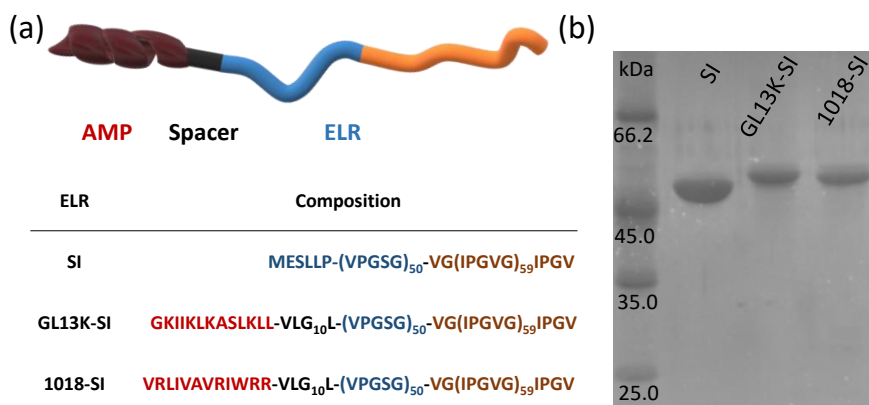
Herein, we propose an alternative approach for the design of hierarchical self-assembled nanomaterials exploiting the self-assembly behavior of AMPs and the thermo-responsiveness of the ELRs. We hypothesized that the combination of both SADs in both ends of a hybrid polypeptide could lead the hierarchical assembly through a dual process. First, AMP-domain would drive the self-assembly hiding the antimicrobial sequences and consequently protecting them from the environment. Then, the thermo-responsive ELR-domain would trigger a secondary assembly creating molecular aggregates increasing the local concentration of the peptide. Following this rationale, nanoreservoirs for AMPs could be developed. This approach seeks to shed light into the mechanisms that govern into the supramolecular assembly of hybrid protein-polymers based

on AMPs in order to set the basis for the *de novo* design of functional nanocarriers to safely treat drug-resistant infections.

## 3.2. Results and Discussion

### 3.2.1. Molecular design strategy and production

Hybrid AMP-ELRs were engineered and biosynthesized by recombinant DNA technology using a modular design (**Figure 3.1**). Two different domains can be differentiated. On the one hand, the ELR domain was based on the amphiphilic, non-charged, diblock design, SI, developed in **Chapter 2**. SI polypeptide contains hydrophilic [(VPGSG)<sub>50</sub>] and hydrophobic block [(IPGVG)<sub>60</sub>] whose LCST are below and above physiological temperature, respectively. At 37 °C, the hydrophobic block (I) collapses into hydrophobic cores surrounded by hydrophilic corona (S) and therefore, driving the formation of micellar nanostructures. On the other hand, designer AMP sequences (GL13K or 1018) were located on the N-terminus, connected to the hydrophilic block (S) through a flexible polyGly spacer. In this way, both potential SADs were located in two ends of the molecule (**Figure 3.1a**).



**Figure 3.6.** (a) Schematic representation of the modular design of the hybrid polypeptide and sequence of the polypeptides. (b) Copper stained SDS-PAGE of the pure ELRs.

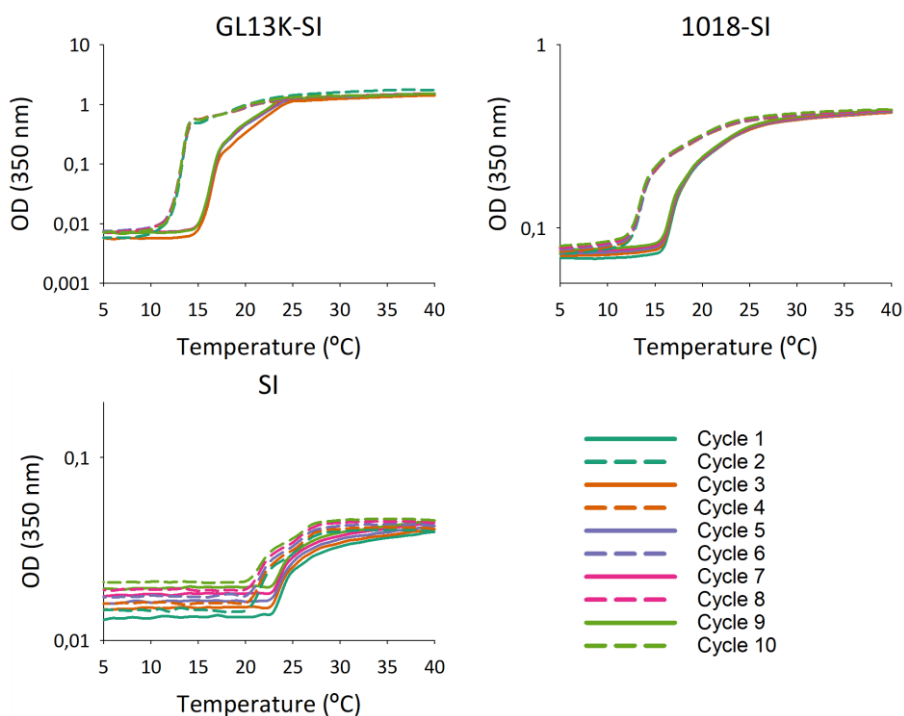
AMP-ELR were produced as pro-polypeptides. We introduced a sacrificial ELR-block in the N-terminus of the AMP, named HE, in order to: (i) protect to the producing strain to toxic side effects of the AMP during the fermentation; (ii) increase the expression levels; (iii) enable site-specific cleavage, a Met was incorporated in its C-terminus that allowed us to release the AMP-ELRs with no extra amino acid that may affect the AMP bioactivities; and (iv) facilitate the AMP-ELR purification with an His-tag intended for the selective removal of the HE-block and the uncleaved constructs from the AMP-ELRs.

After recombinant production, ITC purification and chemical cleavage of the sacrificial block, AMP-ELRs were purified with a nickel-charged agarose resin (**Figure A3.1** and **A3.2**). Monodisperse and highly pure products were obtained as revealed SDS-PAGE, MALDI-TOF and HPLC analysis (**Figure 3.1b**, **A3.3**, **A3.4** and **Table A3.3**).

### 3.2.2. Phase behavior characterization

Given the thermo-sensitiveness of the ELRs, we studied the thermal behavior of the three recombinamers in aqueous solution. We monitored the evolution of the optical density at 350 nm ( $OD^{350}$ ) during consecutive heating and cooling cycles in the range 5-40 °C (**Figure 3.2**). All the three polypeptides (ELRs or AMP-ELRs) showed a reversible LCST behavior with a transition temperature ( $T_t$ ) below physiological temperature. However, a slight increase of the  $OD^{350}$  after cooling down the samples was observed. This may indicate that the process was not completely reversible. Below the  $T_t$  (**Table 3.2**), SI polypeptides were soluble. Raising temperature above the  $T_t$ , triggered the collapse of the I-block and the formation of hydrophobic cores which stabilized in solution by a surrounding hydrophilic coronas (S-blocks) and thus, SI self-assembled into micellar

nanostructures.<sup>[58,85]</sup> When the samples were cooling down, micelles disassembled and the  $OD^{350}$  decreased. However, a minimal fraction of the hydrophobic interactions between Ile-side chains seemed to remain and hence,  $OD^{350}$  was greater than the pre-heated state, as it occurs in the poly(VPGLG).<sup>[266]</sup> Furthermore, as well as poly(VPGLG), thermal hysteresis appeared during cooling cycles, possibly due to these hydrophobic interactions.



**Figure 3.2.** Thermal behavior of the ELRs monitored by turbidimetry. Optical density at 350 nm ( $OD^{350}$ ) evolution as a function of the temperature demonstrated that all the ELRs behave a reversible liquid-liquid phase separation. The presence of the AMPs contributed to the phase transition and thermal hysteresis.

Similarly, hybrid AMP-ELRs also behave a reversible phase transition but with substantial differences. First,  $OD^{350}$  values reached above the  $T_t$  were significantly greater than SI. SI self-assembled into stable nanostructures in solution. Consequently,  $OD^{350}$  was below 0.1. In contrast,

OD<sup>350</sup> was much higher for the hybrid AMP-ELRs when the temperature was above the  $T_t$ . As previously observed for AMP in solution, AMP-domains may self-interact and therefore, they contributed to assembly into larger aggregates that increased the OD<sup>350</sup>.<sup>[210]</sup> Comparing to SI, OD<sup>350</sup> values were one or two orders of magnitude greater for 1018-SI and GL13K-SI, respectively.

**Table 3.1.** Transition temperatures ( $T_t$ ) and hysteresis ( $\Delta T_t$ ) of the ELRs.

	SI	GL13K-SI	1018-SI
<b><math>T_t</math> heating (°C)</b>	24.1	22.7	19.3
<b><math>T_t</math> cooling (°C)</b>	21.8	17.7	15.3
<b>Hysteresis (<math>\Delta T_t</math>) (°C)</b>	2.3	5.0	4.0

Then, the presence of AMP affected the phase transition (Table 2) in comparison with the SI polypeptide.  $T_t$  decreased and thermal hysteresis increased in spite of AMP-domains introduced charged residues. This suggests that the interactions between AMPs contributed to the cooperative phase transition of the ELR-domains, reducing  $T_t$ . Coherently, the AMP-domains also enhanced thermal hysteresis. AMP aggregation may drive the formation of ordered structures<sup>[210,267]</sup> which could increase the intermolecular order in the coacervate state and hence, the hysteresis. This behavior is consistent with previous studies where order-promoting domains (polyAla) were introduced in the ELR backbone.<sup>[116]</sup>

### 3.2.3. Self-assembly dynamics of the hybrid AMP-ELRs

Phase transition characterization suggested that AMP-domains may play an important role in the supramolecular assembly of the AMP-ELRs. They may contribute to the formation of higher-order aggregates and to the stabilization of the assembled structure, thus increasing thermal hysteresis.

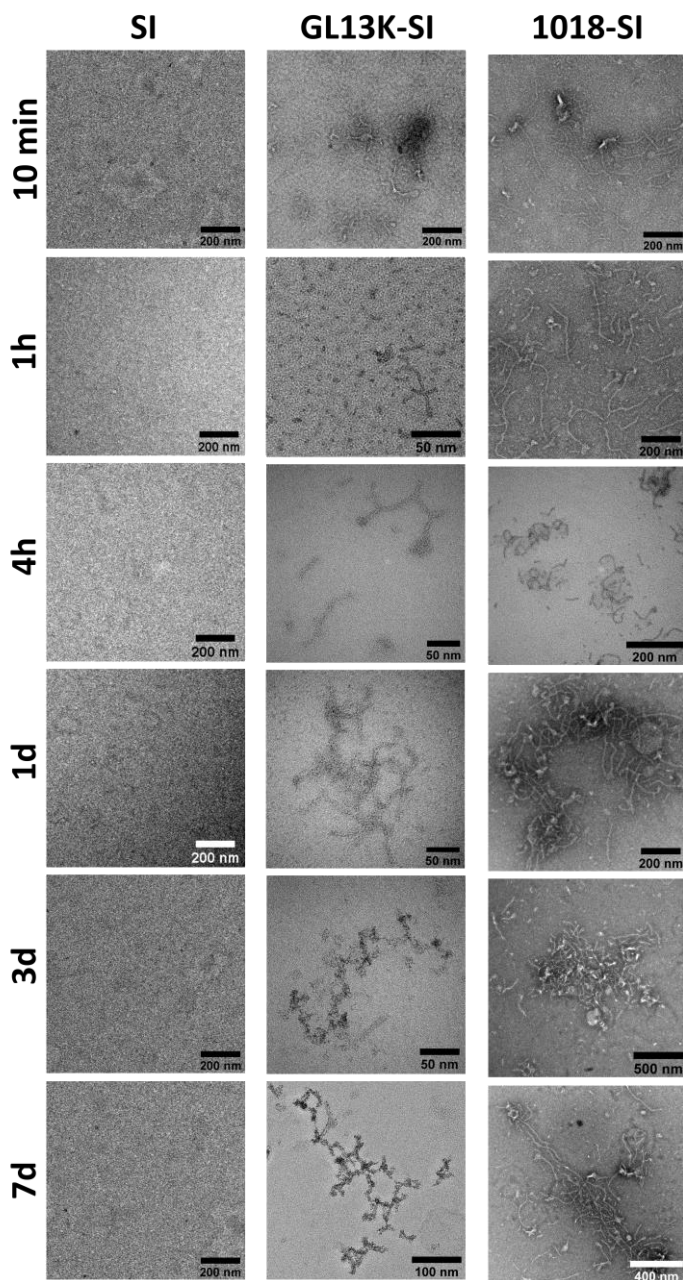


Therefore, we proceeded to characterize the self-assembly dynamics in particular detail below and above the  $T_t$  of the I-block.

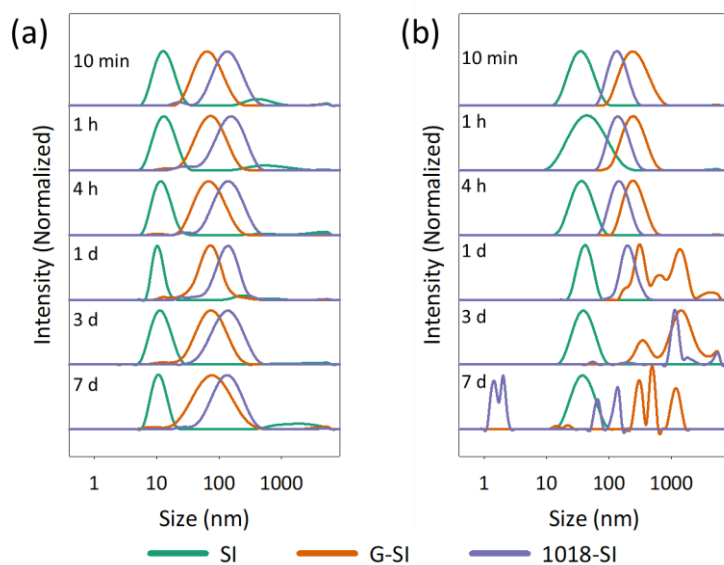
At 5 °C, below the LCST, ELR molecules were completely soluble. SI polypeptide did not form any nanostructures (Figure 3 and 4a). DLS distribution around 10 nm corresponded with the soluble macromolecules.<sup>[268]</sup> In contrast, the presence of the AMPs within the recombinant polypeptides triggered the self-assembly into fibrillar nanostructures. The aggregation of the peptides 1018 and GL13K had been previously observed in solution and it was found to be dependent on the pH or the presence of salts.<sup>[210,218]</sup> Electrostatic repulsion between the positively charged side-groups have to be neutralized to favor the interaction between the peptides and to form higher-order assemblies. Interestingly, self-assembly of the hybrid polypeptides occurred in salt-free solution and at slightly acid pH ( $\approx 6$ ). This suggests that the combination of a larger polypeptide chain with the AMP may have induced a cooperative effect that facilitated the aggregation of the AMP-domains.

Additionally, fibrillar nanostructures formed by the AMP-ELRs underwent a dynamic behavior. In both cases, nanofibers evolved over time but different aggregation patterns were observed for each hybrid polypeptide. 1018-SI formed longer nanofibers than GL13K-SI as TEM characterization revealed (**Figure 3.3**, second and third column). The growth of GL13K-SI nanofibers seemed to be spatially constrained, thus limiting the fiber elongation in favor of nanofibers with repeated patterns. DLS analysis verified the size differences between both fibrillar populations after short periods of time (**Figure 3.4a**). However, it must be noted that the large nanofibers found in 1018-SI samples after 1 day of incubation could not be monitored by DLS, possibly because large fibrillar aggregates

were not stable in solution and they precipitated, making impossible their detection.



**Figure 3.3.** Negatively stained TEM micrographs of the ELR/AMP-ELRs after the incubation at 5 °C. The presence of the AMP drove the formation of nanofibers after short incubation periods (10 min, 1 h), that showed a dynamic behavior.



**Figure 3.4.** DLS intensity distributions of the three polypeptides below (a, 5 °C) and above (b, 37 °C) the  $T_c$ .

It is interesting to speculate on the reasons why the AMPs can trigger different supramolecular assemblies. Both AMPs have similar molecular properties, which may suggest similar self-assembly mechanisms, however, their self-assembly dynamics are substantially different. The diverse spatial distribution of the charged and hydrophobic residues in the AMPs seems to modulate the driving forces for peptide aggregation and hence, L-1018 promotes the formation of longer fibers than L-GL13K. Consistently, recent studies have demonstrated the divergence of the aggregation tendencies of both peptides. Although both mechanisms of aggregation are pH dependent, L-GL13K peptides self-assembly require pH values of 9.6 or greater at 25 °C,<sup>[210,269]</sup> whereas aggregation tendency of L-1018 is noticeable from pH values greater than 2, and it is highly influenced by the presence of anions.<sup>[218]</sup> Additionally, it must be noted that the C-terminal conjugation of the peptides with the ELR chain implicitly introduce steric effects which may affect the assembly process.

In parallel, we also studied the nanostructuration at physiological temperature (**Figure 3.3b** and **3.4**). Above the  $T_t$ , I-block underwent phase transition and, as consequence, led the formation of spherical nanostructures. These micellar assemblies were observed in the three polypeptides after short incubation periods (10 min, 1 h and 4 h). However, in the hybrid AMP-ELRs, micellar populations coexisted with small nanofibers, akin to those observed below  $T_t$  (**Figure 3.2**).

DLS and TEM demonstrated the stability and monodispersity of the micelles formed by SI ( $D_h = 35.5$  nm, PDI = 0.125, after 1 week at 37 °C). In contrast, the presence of the AMP in the hydrophilic corona induced instability driving a secondary self-assembly in the hybrid AMP-ELRs (**Figure 3.3b**). They formed larger aggregates based on interconnected fibers. These aggregates showed a continuous growth until precipitation. Consistently with the characterization below the  $T_t$ , different shapes were observed in the aggregates depending on the AMP. GL13K-SI formed spherical aggregates while 1018-SI aggregates were more elongated with undefined shapes. (**Figure 3.5**).

In both cases, the AMPs seemed to be hidden inside the fibrillar aggregate. To assess this hypothesis, we performed minimal inhibitory concentration (MIC) assays against Gram-positive *Streptococcus gordonii* and Gram-negative *Pseudomonas aeruginosa* to verify if the AMPs were exposed on the surface of the nanostructures.

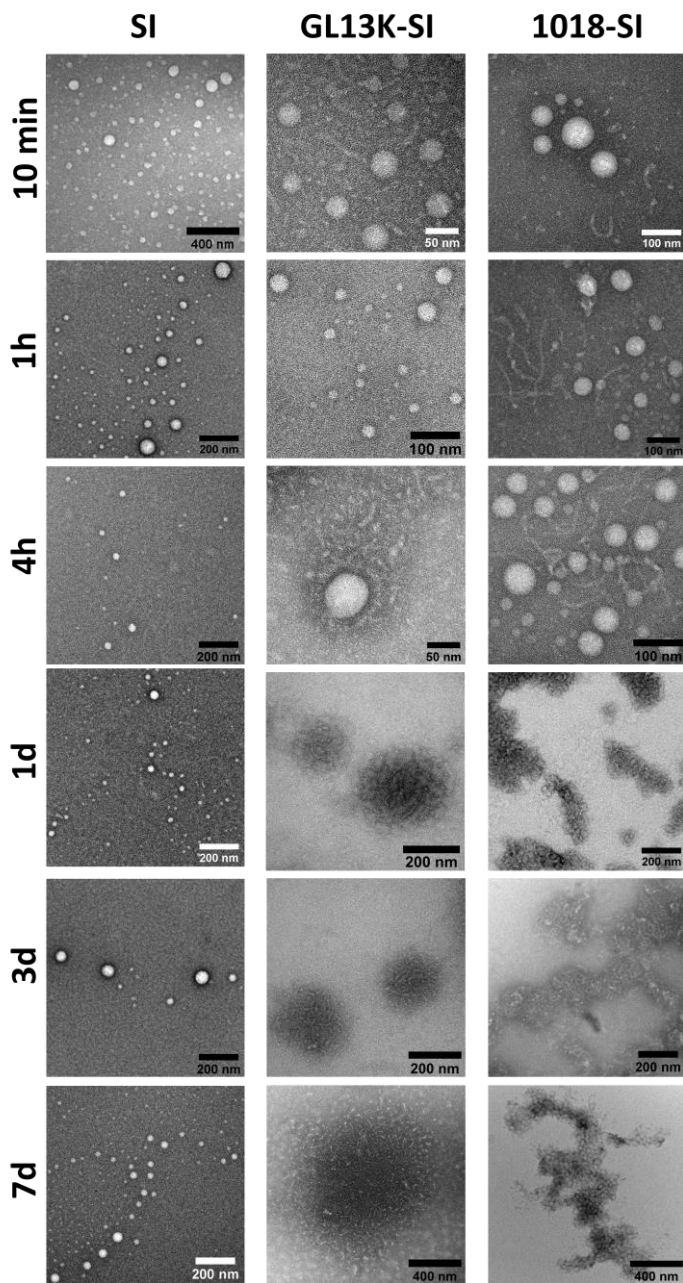
Both AMPs have demonstrated that they retain their bactericidal potential when they are immobilized on surfaces.<sup>[216]</sup> In this way the lack of antimicrobial activity of the hybrid polypeptides may indicate that the AMPs were protected inside the nanostructures (**Table 3.5**).

**Table 3.1.** MIC of SI, G13K-SI, 1018-SI polypeptides and GL13K and 1018 peptides against *S. gordonii* DL-1 and *P. aeruginosa* Xen41

	MIC ( $\mu\text{M}$ )	
	<i>S. gordonii</i>	<i>P. aeruginosa</i>
SI	>128	>128
GL13K-SI	>128	>128
1018-SI	>128	>128
GL13K-NH <sub>2</sub>	32	32
1018-NH <sub>2</sub>	32	32

Additionally, structural studies were performed. Secondary conformation of the ELRs was studied using circular dichroism spectroscopy (**Figure A3.5**). CD spectra of all the ELRs were very similar at the different time points below and above the  $T_i$ . Below the  $T_i$ , the characteristic negative peak at  $\approx 197$  nm indicated undefined structure. The low molecular weight of the AMP-domains comparing to the ELRs ( $\approx 1.5$  kDa versus 46 kDa) only enabled us to detect modest differences in the ellipticity of the 197 nm peak.

When the temperature was raised over the  $T_i$ , ELR self-assembly correlated with shift in secondary structure. In the three spectra appeared the characteristic peak of intrinsically disordered proteins at  $\approx 197$  nm and a maximum at  $\approx 210$  nm indicating the presence of  $\beta$ -turns, which are characteristic in ELRs.<sup>[255,256]</sup> In this case, the presence of the AMP in the hybrid ELRs resulted in a substantial decrease of the peak at 197 nm. It must be noted that after 1 day of incubation at 37 °C, CD signals of 1018-SI decreased significantly, probably due to the phase separation and the consequent precipitation of the aggregates.



**Figure 3.5.** Negatively stained TEM micrographs of the ELR/AMP-ELRs after the incubation at 37 °C. The presence of the AMP drove a second self-assembly, triggering the formation of hierarchical structures. Fibrillar aggregates with globular or amorphous shapes were found when the GL13K or the 1018 peptide were within the hybrid polypeptide, respectively.

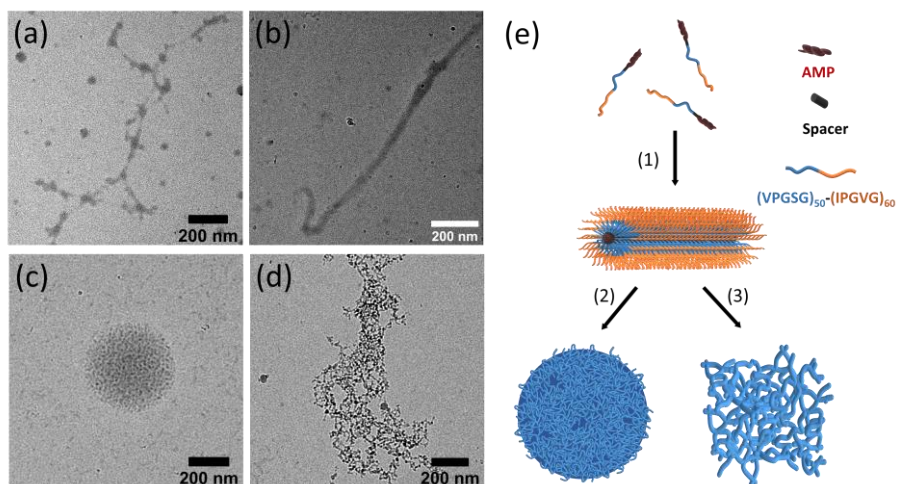
### 3.2.4. *Thermo-responsive nanostructures*

Lastly, we evaluated if the fibrillary nanostructures formed by the self-assembly of the AMPs behave the LCST behavior characteristic of the ELRs. For this, first, polypeptides solutions were incubated at 5 °C for 24 h, in order to pre-form the nanofibers and then we carried out a second incubation at physiological temperature for 30 min to assess the influence of the temperature on the nanostructuration. Samples were prepared for cryo-TEM visualization before and after second incubation at 37 °C (**Figure 3.6** and **A3.6**).

As expected, incubation below the both  $T_i$  allowed AMP-domains to drive the supramolecular assembly of the hybrid polypeptides into nanofibers and thus, the AMPs were hidden inside the fibrillar nanostructure (schematically represented in **Figure 3.6e.1**). Then, the second incubation at physiological temperature induced the coacervation of the hydrophobic block of the ELR (I-Block, in orange in **Figure 3.6e**), and as consequence exposed the hydrophilic ELR-block (S-block). Nanofibers aggregated into fibrillar networks with spherical or undefined shapes, depending on the AMP (**Figure 3.6c** and **3.6d**). Moreover, hydrophobic collapse of the I-block could be used for the encapsulation of conventional hydrophobic antibiotics.<sup>[270]</sup>

In this way, we demonstrated not only the self-assembly ability of AMPs to trigger the supramolecular structuration of larger protein-polymers, but also that thermo-sensitiveness of the ELRs remained in the fibrillar assembly. Therefore, it could be used to trigger the condensation of the nanofibers, increasing the local concentration of the AMPs, in addition to driving further assemblies with potential application as nanostructured reservoirs for AMP delivery. Lastly, it is noteworthy to

mention that the presence of the spacer between the AMP-domain and the ELR diblock, did not compromise the hierarchical assembly. Thus, the introduction of functional spacers, including sensitive sequences to biological or physical stimuli (e.g. protease degradation or pH) opens up a range of possibilities in the development of release-controlled nanocarriers for AMPs.



**Figure 3.6.** Cryo-TEM micrographs of the AMP-ELRs: (a) and (c) correspond to GL13K-SI samples and (b) and (d) to 1018-SI samples. (a, b) After the incubation at 5 °C for 24 h, the AMP triggered the fibrillar assembly, whereas (c, d) when the fibers were incubated at 37 °C, the coacervation of the ELR drove the formation of aggregates. (e) Schematic representation of the hierarchical self-assembly of the hybrid polypeptides.

### 3.3. Conclusions

In conclusion, the use of AMPs combined with stimuli-responsive protein polymers is a promising strategy for the design of self-assembled nanomaterials for biomedical applications. We have shown that AMPs can be used as SADs to trigger the assembly of larger protein polymers, and depending on the AMP, different nanostructures can be achieved. Moreover, their combination with thermo-responsive polypeptides in modular designs enables to fabricate hierarchical nanostructures formed by a dual assembling process.



Therefore, our nanosystem represents a sound strategy in the fabrication of smart biomaterials incorporating AMPs. Their recombinant nature facilitates the edition of the modular design and the incorporation of other bioactive motifs with extreme control, in addition to a scalable method for their sustainable production and potential widespread use. This investigation provides a new insight in the development of delivery strategies for combating drug-resistant infections, but also engenders enormous opportunities for the production of self-assembled devices for tissue engineering and regenerative medicine applications taking advantage of the immunomodulatory properties of AMPs.

## **3.4. Experimental section**

### *3.4.1. Gene construction*

ELR encoded genes construction was performed using previously described procedures (**Chapter 1** and **2**). Encoding genes for the AMPs were purchased from NZYTech, Lda. (Portugal) and cloned into a modified pDrive plasmid flanked by *EcoRI* restriction sites,<sup>[47]</sup> using *E. coli* XL-1 blue (Agilent, USA) as cloning strain. Then, by iterative recursive method, the final genetic constructions (HE-AMP-SI) were completed.

### *3.4.2. Bioproduction and purification*

All the polypeptides used in this work were recombinantly bioproduced. Briefly, encoding genes were cloned into pET-25b (+) expression vectors and transformed into *E. coli* BLR (DE3) for heterologous expression. After overnight fermentation in a 15 L bioreactor (Applikon Biotechnology, The Netherlands), the polypeptides were purified by inverse transition cycling (ITC) adding 1.5 M NaCl for their warm precipitation.<sup>[47]</sup> After 3 cycles, we assessed the purity and

moniodispersity by SDS-PAGE and we dialyzed them against ultrapure water, lyophilized and stored them at -20 °C. The yields observed ranged from 380 to 600 mg L<sup>-1</sup> of purified ELR per liter of bacterial culture.

### 3.4.3. *Protective block cleavage and purification*

AMP-ELRs were designed and bioproduced in *E. coli* BLR(DE3) as pro-polypeptides (HE-AMP-SI, **Table A3.1**). After the recombinant expression, we verified by SDS-PAGE that the pro-AMP-ELRs were completely pure (**Figure A3.1**). We removed the sacrificial block, HE. For this, pro-polypeptides were incubated with CNBr solution (70% formic acid, FA) in a molar ratio 1:200, Met:CNBr. The reaction was released for 20 h at room temperature in the darkness and under anaerobic conditions. Then, CNBr was eliminated in a rotary evaporator. The ELRs were resuspended in ultrapure water and dialyzed. After four dialyzing steps against cold ultrapure water and lyophilization, we purified the cleaved AMP-ELR using HisPur™ Ni-NTA resin (ThermoFisher Scientific, USA) by batch methodology. In short, lyophilized products were dissolved in denaturing buffer (4M urea, 20 mM sodium phosphate, 500 mM NaCl) in order to prevent physical interactions between the AMP. 30 mL of the dialyzed solution was mixed with 15 mL of the resin in 50 mL-tubes and incubated at 200 rpm for 3 h at 4 °C. Then, resin was centrifuged. Due to the presence of the His-tag within the sacrificial block, HE and HE-AMP-SI polypeptides bonded the resin, whereas the AMP-ELR was in the supernatant. After two purification steps, AMP-ELR polypeptides were completely purified (**Figure A3.2**). Finally, the polypeptide solutions were dialyzed, filtered (0.22 µm Nalgene™, ThermoFisher Scientific, USA) lyophilized and stored at -20 °C until further use.

Monodispersity and purity of the hybrid AMP-ELRs were assessed by SDS-PAGE (**Figure 3.1, A3.2**), MALDI-TOF (**Figure A3.3** and **Table A3.2**) and HPLC (**Table A3.3**). MALDI-TOF and HPLC analysis were performed in the 'Laboratorio de técnicas instrumentales' (LTI) at the University of Valladolid (Spain).

#### *3.4.4. Phase transition characterization*

Thermal behavior was evaluated by turbidimetry. Absorbance at 350 nm was measured in the range of 5-40 °C with a scan rate of 1 °C with a Cary 100 UV-Vis spectrophotometer (Agilent). Heating and cooling ramps were performed at 0.25 °C min<sup>-1</sup>. All the samples were prepared in ultrapure water at a concentration of 25 μM.

#### *3.4.5. Physical characterization of the nanostructuration*

Self-assembly dynamics of the hybrid polypeptides were evaluated below and above the transition temperature of the hydrophobic block (I) and compared with the ELR control, SI. For this, 25 μM solutions in ultrapure water were prepared under sterile conditions and incubated at 5 or 37 °C for 10 min, 1 h, 4 h, 1 d, 3 d, and 7 d. After that, nanostructuration of the polypeptides were analyzed by dynamic light scattering and transmission electron microscopy.

##### *Dynamic light scattering*

Nanoparticle size distribution was evaluated using a Zetasizer Nano (Malvern Instruments, UK), with a 173° scattering angle and equipped with a HeNe laser (633 nm) with an output power of 10 mW. Each sample was measured in triplicate.

### *Transmission electron microscopy*

TEM samples were prepared on 300-mesh carbon coated copper grids with negative staining. For this, first, grids were rendered hydrophilic by plasma treatment in a PDC-002 plasma cleaner (Harrick Plasma, USA) at low power setting (7.2 W applied to the RF coil) for 20 s. Then, 15  $\mu\text{L}$  of the pre-incubated ELRs, ultrapure water and uranyl acetate (1% w/v) solutions were dropped on Parafilm<sup>®</sup> strip over a pre-chilled (5 °C) or pre-heated (37 °C) glass surfaces. Plasma treated grids were placed onto the ELR drop for 90 s, on ultrapure water for 60 s, and finally, on the negative staining solution for another 60 s. Blotting filter paper was used to remove excess solution after every step.

Images were taken using a Tecnai Thermionic T20 microscope operated at 200kV (SAI, University of Zaragoza, Spain).

### *Circular dichroism spectroscopy*

ELRs or AMP-ELRs solutions were prepared at 5  $\mu\text{M}$  in pre-chilled ultrapure water and incubated at 5 or 37 °C for 10 min, 1 h, 4 h, 1 d, 3 d, and 7 d. The CD signal was measured from a 200  $\mu\text{L}$  solution in a quartz cuvette (1 mm path-length) using a CD spectrometer (Jasco J-815, Easton, MD, USA). It was scanned over a range of 260-190 nm with a data pitch of 1 nm, a scanning rate of 50 nm min<sup>-1</sup> and a response time of 2 s. All measurements were subtracted from the background signal from ultrapure water in the quartz cuvette and repeated in triplicates.

### *3.4.6. Cryogenic TEM*

To test the thermo-responsiveness of the fibrillar structures formed by the AMP-ELRs, we preformed nanofibers and then we evaluated by cryo-

TEM the behavior of the nanostructures. For this, 25  $\mu\text{M}$  solutions in ultrapure water of the three ELRs (SI, GL13K-SI and 1018-SI) were incubated at 5  $^{\circ}\text{C}$  for 24 h, in order to drive the AMP fibrillar assembly. Then, samples were heated at 37  $^{\circ}\text{C}$  for 30 min. Cryo-TEM samples were prepared before and after heating to evaluate changes in the nanostructuration.

Cryo-TEM samples preparation and visualization were carried out at the ‘Electron Microscopy Platform’ (CICbioGUNE, University of the Basque Country, Spain). For this, four microliters of the sample were placed onto a glow-discharged 300-mesh lacey-carbon coated grids (Lacey Carbon film on 300 mesh copper; LC300-Cu; Electron Microscopy Sciences) and incubated inside the chamber of a Vitrobot Mark III (FEI Inc., The Netherlands) at 4  $^{\circ}\text{C}$  and at a relative humidity close to saturation (95% rH) for 30 s. Most of the liquid in the grid was removed by blotting (3 s at an offset of -3 mm) and vitrified by plunging into liquid ethane, previously cooled with liquid nitrogen at approximately -180  $^{\circ}\text{C}$ .

Images were collected at liquid nitrogen temperature on a JEM-2200FS/CR (JEOL Europe, Croissy-sur-Seine, France) field emission gun transmission electron microscope operated at 200 kV. An in-column energy filter (Omega filter) produced images with improved contrast and signal-to-noise ratio by zero-loss filtering. The energy slit width was set up at 15 eV. Digital images were recorded on a 4K  $\times$  4K Ultrascan4000<sup>TM</sup> charge-coupled device (CCD) camera (Gatan, Inc.) using DigitalMicrograph<sup>TM</sup> (Gatan, Inc.) software.

#### *3.4.7. Minimal inhibitory concentration*

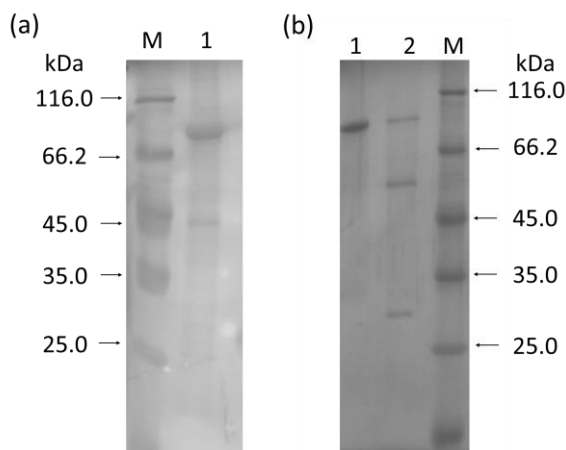
The antimicrobial activity of the hybrid polypeptides was evaluated by MIC assays against Gram-positive *Streptococcus gordonii* DL-1 and Gram-

negative *Pseudomonas aeruginosa* PAO, Xen 41 (PerkinElmer Inc., Waltham, MA, USA) following the protocol described elsewhere.<sup>[12]</sup> Briefly, 3-5 colonies of *S. gordonii* or *P. aeruginosa* were picked from fresh plates and inoculated in a sterile 15-mL falcon tube with 2 mL of brain heart infusion (BHI) broth or Mueller-Hinton Broth (MHB), respectively. After overnight incubation at 37 °C under aerobic conditions (*P. aeruginosa*) or with 5% CO<sub>2</sub>, inocula were diluted until  $5 \times 10^5$  CFU mL<sup>-1</sup> in BHI or MHB and 90 µL of this solution was incubated with a 10 µL serial peptide dilution from a 1280 µM stock solution in 96-well polypropylene plates at 37 °C for 20 h. The bacterial growth was evaluated visually and by optical density (OD) at 570 nm in a Synergy HT plate reader (BioTek, Winooski, VT). Additionally, designer peptides GL13K-NH<sub>2</sub> and 1018-NH<sub>2</sub> (purchased by Pepscan (The Netherlands) with a purity of more than 97%) were tested as positive controls. Each experiment was repeated at least three times.

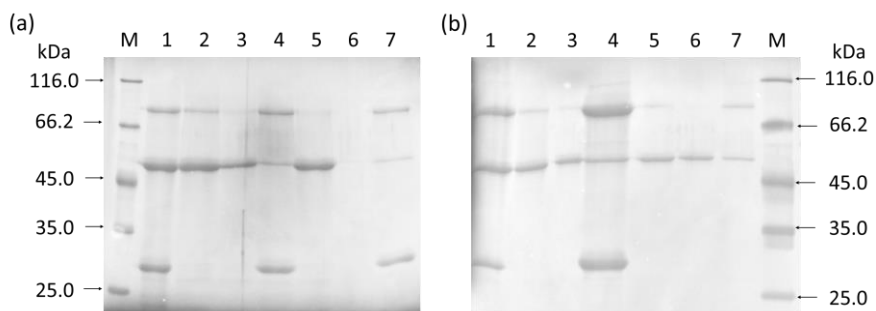
## 3.5. Appendix

**Table A3.2.** Complete sequence of the engineered block co-recombinamers.

	Sequence
<b>HE</b>	MESLLPVG <sub>5</sub> H <sub>6</sub> G <sub>5</sub> [(VPGVG) <sub>2</sub> (VPGEG)(VPGVG) <sub>2</sub> ] <sub>10</sub> VM
<b>HE-GL13K-SI</b>	MESLLPVG <sub>5</sub> H <sub>6</sub> G <sub>5</sub> [(VPGVG) <sub>2</sub> (VPGEG)(VPGVG) <sub>2</sub> ] <sub>10</sub> VM GKIIKCLKASLKLLV LG <sub>10</sub> L (VPGSG) <sub>50</sub> VG(IPGVG) <sub>59</sub> IPGV
<b>HE-1018-SI</b>	MESLLPVG <sub>5</sub> H <sub>6</sub> G <sub>5</sub> [(VPGVG) <sub>2</sub> (VPGEG)(VPGVG) <sub>2</sub> ] <sub>10</sub> VM VRLIVAVRIWRR VLG <sub>10</sub> L (VPGSG) <sub>50</sub> VG(IPGVG) <sub>59</sub> IPGV
<b>GL13K-SI</b>	GKIIKCLKASLKLLVLG <sub>10</sub> L(VPGSG) <sub>50</sub> VG(IPGVG) <sub>59</sub> IPGV
<b>1018-SI</b>	VRLIVAVRIWRRVLG <sub>10</sub> L(VPGSG) <sub>50</sub> VG(IPGVG) <sub>59</sub> IPGV

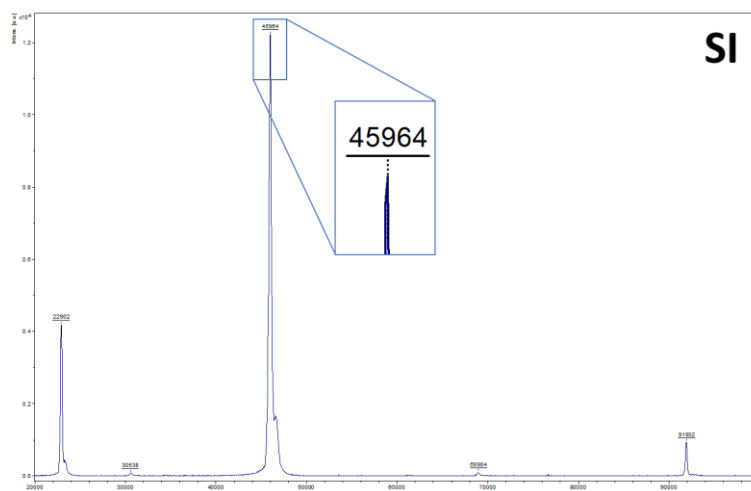


**Figure A3.7.** Copper stained SDS-PAGE (12.5%) electrophoresis of (a) HE-1018-SI and (b) HE-GL13K-SI (lane 1) recombinamers and band pattern after chemical treatment with CNBr (lane2). Lane M is Pierce™ Unstained Protein MW Marker.



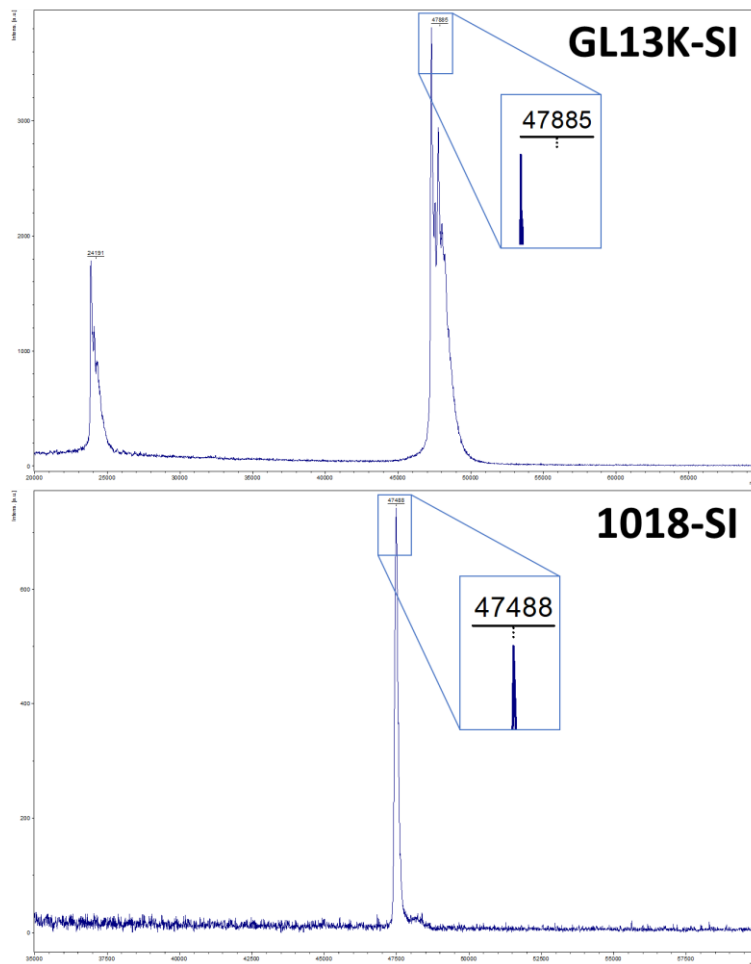
**Figure A3.8.** Analysis of the purification of 1018-SI (a) and GL13K-SI (b) after CNBr cleavage by 12.5% SDS-PAGE visualized with copper staining. Lane M is Pierce™ Unstained Protein MW Marker (ThermoFisher). We obtained highly pure and monodisperse products after two purification steps by batch method, using the HisPur™ Ni-NTA resin.

Lanes 1: After CNBr treatment. Lanes 2: After incubation 1 with the resin. Lanes 3: Wash 1. Lanes 4: Eluted from the resin. Lanes 5: After incubation 2 with the resin. Lanes 3: Wash 2. Lanes 4: Eluted (2) from the resin.



**Figure A3.4.** MALDI-TOF spectra of the purified ELR SI.





**Figure A3.4.** MALDI-TOF spectra of the purified AMP-ELRs GL13K-SI and 1018-SI.

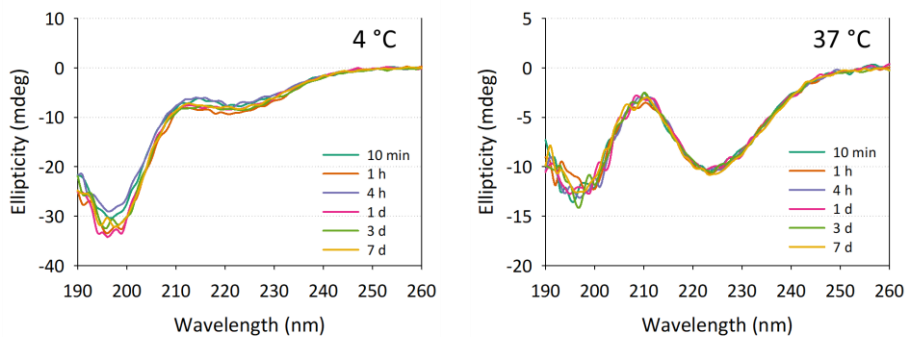
**Table A3.3.** Comparison of the theoretical and experimental MW calculated by MALDI-TOF.

	Theo. MW (Da)	Exp. MW (Da)
<b>SI</b>	46070	46006±52
<b>GL13K-SI</b>	47702	47845±34
<b>1018-SI</b>	47814	47528±43

**Table A3.4.** Amino acidic composition of the ELdcRs calculated by HPLC. It is represented the theoretical (Theo) composition comparing to the experimental (Exp.) values obtained.

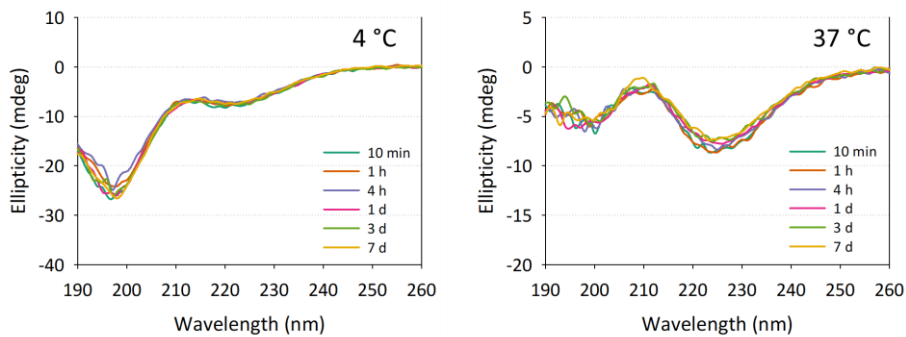
Amino acid	SI		GL13K-SI		1018-SI	
	Theo.	Exp.	Theo.	Exp.	Theo.	Exp.
Asp	-	-	-	-	-	-
Glu	1	1.17	-	-	-	-
Asn	-	-	-	-	-	-
Ser	51	50.35	51	49.91	51	47.54
Gln	-	-	-	-	-	-
His	-	-	-	-	-	-
Gly	220	222.91	231	229.86	230	225.42
Thr	-	-	-	-	-	-
Arg	-	-	-	-	4	6.08
Ala	-	-	-	-	1	3.85
Tyr	-	-	-	-	-	-
Cys	-	-	-	-	-	-
Val	111	105.83	112	102.96	112	105.1
Met	1	1.15	0	0.36	0	0.33
Trp	-	-	-	-	-	-
Phe	-	-	-	-	-	-
Ile	60	61.87	62	62.19	62	61.75
Leu	2	2.46	6	6.53	4	9.21
Lys	-	-	4	8.02	-	-
Pro	111	111.89	110	113.43	110	111.24
<b>Total aas</b>	<b>557</b>	<b>557.63</b>	<b>573</b>	<b>577</b>	<b>574</b>	<b>571</b>

## SI



III

## GL13K-SI



## 1018-SI

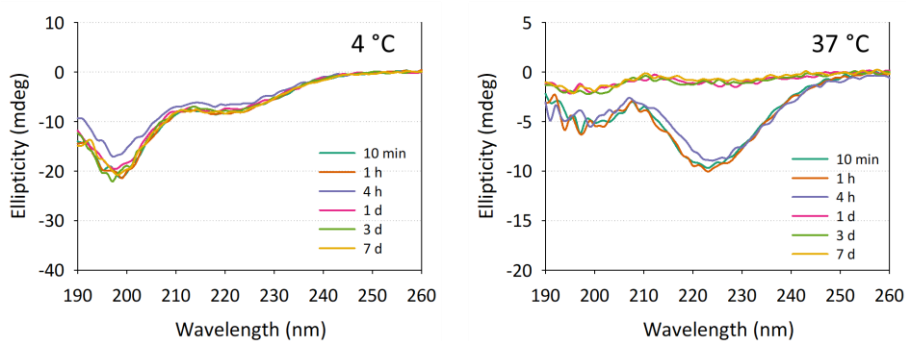
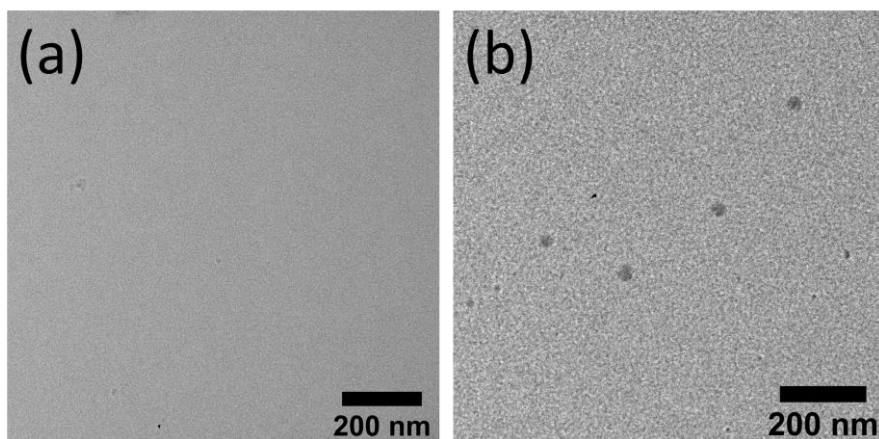


Figure A3.5. Secondary structure characterization by CD spectroscopy.



**Figure A3.6.** Cryo-TEM images of the SI polypeptide (25  $\mu\text{M}$  in ultrapure water). (a) After the incubation at 5  $^{\circ}\text{C}$  for 24 h and (b) with an extra incubation of 30 min at 37  $^{\circ}\text{C}$ .





# Chapter IV

---

Development of self-  
assembled monolayers with  
antibiofilm activity based on  
AMPs and ELRs

---

Parts of this Chapter have been published as:  
S. Acosta\*, L. Quintanilla Sierra, M. Alonso, C. Aparicio, J.C.  
Rodríguez Cabello, *ACS Biomater. Sci. Eng.* 2019, 5, 9, 4708-4716





## 4.1. Introduction

The aging of the population combined with technological developments in the field of biomaterials have resulted in the increasing use of biomedical devices. However, the implantation of temporary or permanent medical devices implicitly increases the risk of bacterial infections.<sup>[271]</sup> Indeed, biofilm-related infections and the increasing appearance of multidrug resistant bacteria make medical device-associated infections a significant economic and medical concern.<sup>[272,273]</sup> Although a wide range of bacteria are implicated in such infections, staphylococci, especially *Staphylococcus aureus* and *Staphylococcus epidermidis*, are of particular importance. Indeed, *S. aureus* and *S. epidermidis* are the leading cause of reported healthcare-associated infections and are particularly relevant in biomaterials-associated infections (BAIs) due to their ability to form biofilms, their prevalence and the occurrence of multi-drug resistant phenotypes.<sup>[274,275]</sup>

Significant efforts have been made to design bactericidal and antifouling coatings to prevent bacterial adhesion and inhibit biofilm formation on biomaterials,<sup>[276,277]</sup> including antimicrobial agent releasing-based, anti-adherent and contact-killing coatings. Traditional antibiotics,<sup>[278]</sup> metallic nanoparticles, such as Ag<sup>[279]</sup> or Zn,<sup>[280]</sup> and polymers<sup>[281]</sup> are the most widely used approaches and have proved effective against staphylococcal strains, although with significant limitations, such as antibiotic resistance,<sup>[282]</sup> toxicity at high concentrations,<sup>[283,284]</sup> and lack of biocompatibility.<sup>[285]</sup> As such, in recent years, the use of AMPs has increased markedly to develop antibiofilm coatings,<sup>[219]</sup> thereby demonstrating their potential applicability for the prevention of indwelling device-associated infections.

As mentioned in **Chapter 1**, AMPs have been directly immobilized onto biomedical materials<sup>[223,286–289]</sup> or bioconjugated with a polymeric scaffold that may improve their antimicrobial activity,<sup>[229,290,291]</sup> and they can also incorporate additional functionalities such as low-fouling behavior,<sup>[292,293]</sup> multiple and synergistic antimicrobial peptides,<sup>[294]</sup> or an ability to promote tissue integration.<sup>[295,296]</sup> Furthermore, the immobilization of AMPs may improve some of their limitations, minimize their toxic side effects and improve their susceptibility to proteases.<sup>[297]</sup>

The main limitation for the production and improvement of AMP-based coatings for clinical materials is the high cost of chemical manufacture, which impedes scale-up.<sup>[298]</sup> As such, the recombinant production of AMPs has been studied and several examples have been produced using this methodology.<sup>[299,300]</sup> Despite this, the recombinant production of AMPs usually involves the use of expensive techniques for purification of the final product that increase final costs, thereby hampering large-scale production.<sup>[301,302]</sup> In this regard, and because of their thermo-sensitive behavior, ELRs enable the efficient recombinant production and simple purification of fusion proteins in a cost-effective scalable process.<sup>[303,304]</sup> In addition, chimeric AMP coproduction with ELRs delivers highly monodisperse and pure products and, most importantly, enables the synthesis of sophisticated antimicrobial designs with improved properties and applications by taking advantage of the elastin-like smart behavior and their potential complex molecular architecture. Examples of the latter are films for wound healing<sup>[202]</sup> and self-assembling antimicrobial nanoparticles.<sup>[203]</sup> On the other hand, ELR-based matrices and coatings have been shown to exhibit protein antifouling activity, preventing the unspecific attachment of proteins.<sup>[130,131,305]</sup> Thus, the combination of AMPs

and ELRs is an attractive alternative for the development of advanced antimicrobial coatings for biomedical materials.

In this chapter, we develop self-assembled monolayers (SAMs) based on a multifunctional design, in which the antibiofilm properties of an AMP are enhanced upon combination with a low-fouling ELR. Antibiofilm properties of the coatings were tested against two staphylococcal single-strain biofilm models (*S. aureus* and *S. epidermidis*). Strong antibiofilm activity and cytocompatibility of these coatings was demonstrated, thus confirming the potential of recombinant approaches for the production of antimicrobial coatings with powerful features for biomedical devices.

## 4.2. Results and Discussion

### 4.2.1. Rationale of the hybrid polypeptide design and biosynthesis

The ELRs used in this study are based on a multimodular design. The first ELR, referred to as VC and used as control, comprises two modules, namely a polycationic backbone (VPGXG)<sub>40</sub> (where X is Val and Lys in a 5:1 ratio) and a cysteine-based C-terminal grafting motif (Cys-cys-motif) for covalent immobilization onto surfaces (**Table 4.1**). Cysteine side-chains have demonstrated that are excellent candidates for the selective covalent and functional immobilization of peptides and proteins onto multiple surfaces and biomedical materials for the biofabrication of surfaces with antimicrobial properties,<sup>[219,306]</sup> cell adhesion selectivity,<sup>[307,308]</sup> or enzymatically active.<sup>[309]</sup>

In contrast, the hybrid polypeptide (AMP-ELR), referred to as GVC, also incorporates the designer peptide GL13K at its N-terminus via a flexible spacer comprising ten glycines.<sup>[310]</sup> Polycationic ELRs provide a positive environment, and specific C-terminal attachment facilitates

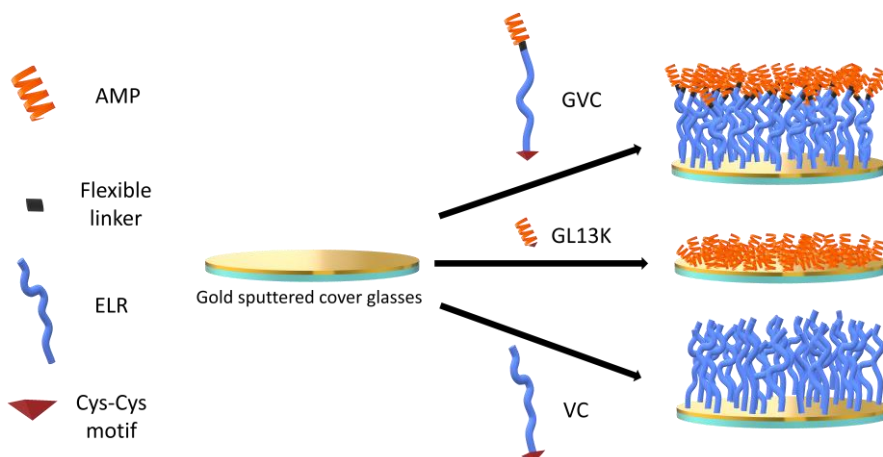
molecular flexibility that may increase the antimicrobial potential<sup>[311]</sup> while minimizing cytotoxic side reactions.<sup>[312]</sup>

**Table 4.1.** MWs and sequences of the AMP and ELRs used in this chapter.

	MW (Da)	Sequence
<b>GL13K</b>	1528.02	GKIIKLIKASLKLLC-NH <sub>2</sub>
<b>VC</b>	21038.0	MESLLPVG (VPGVG VPGKG (VPGVG) <sub>4</sub> ) <sub>8</sub> VCC
<b>GVC</b>	22670.0	GKIIKLIKASLKLLV LG <sub>10</sub> L VG (VPGVG VPGKG (VPGVG) <sub>4</sub> ) <sub>8</sub> VCC
<b>EGVC</b>	45241.3	MESLLP [(VGPVG) <sub>2</sub> VPGE(VGPVG) <sub>2</sub> ] <sub>10</sub> V LG <sub>10</sub> LVM GKIIKLIKASLKLLVLG <sub>10</sub> L VG (VPGVG VPGKG (VGPVG) <sub>4</sub> ) <sub>8</sub> VCC

The GVC recombinamer was designed produced as an EGVC, with a sacrificial block (E) being included immediately before the GL13K sequence as part of the modular design. This E block plays the same role as HE-block described in **Chapter 2**. Moreover, their polyanionic composition (**Table 4.1**) enables, after cleavage, the easy separation from the final product (GVC) by ITC in a single step in addition to the uncleaved original product (EGVC) using the same method.

After recombinant production and purification, purity was assessed by diverse characterization techniques, molecular weights and monodispersity were verified by SDS-PAGE (**Figure A4.2**) and MALDI-TOF (**Figure A4.3** and **Table A4.1**), and amino acid composition by HPLC analysis (**Table A4.2**).



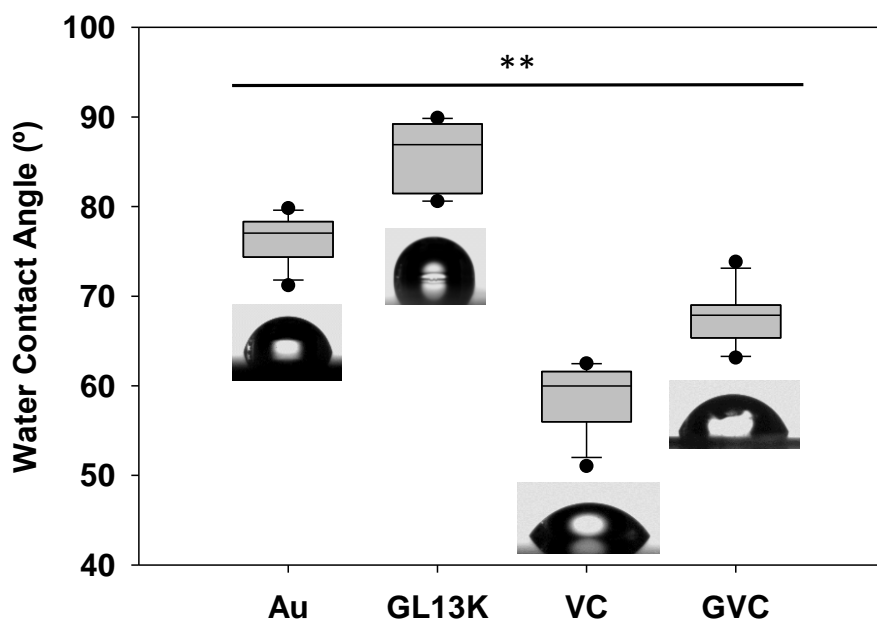
**Figure 4.1.** Schematic representation of the modular composition of the AMP-ELR and production of the AMP/ELR/AM-ELR self-assembled monolayers (SAMs) on gold surfaces.

#### 4.2.2. SAMs biofabrication and characterization

For the study of the bioactivities as covalent coatings, GVC polypeptides and controls (GL13K peptide and VC polypeptide) were covalently to model gold surfaces. Cys-Cys-motif allowed to generate SAMs from the functionalization of thiols on gold substrate (Schematically represented in **Figure 4.1**). Then, the surfaces were characterized by water contact angle (WCA), X-ray photoemission spectroscopy (XPS), and quartz crystal microbalance with dissipation (QCM-D). Physical and chemical characterization was performed, measuring the coating wettability by WCA and quantifying the elemental composition by XPS, respectively. Finally, to assess the effectiveness of AMP/ELR/AMP-ELR deposition, we used QCM-D to obtain the thickness of the coatings.

The wettability of the coatings was assessed by measuring the static contact angle of ultrapure water drops on the surfaces with a stabilization time of 15 s. The wettability of pristine gold surfaces ( $WCA = 76.4 \pm 2.5^\circ$ ) decreased after being coated with immobilized GL13K peptides ( $WCA =$

$85.6 \pm 3.8^\circ$ ) (**Figure 4.2**). The hydrophobicity of the surface increased as the hydrophobic residues of these amphipathic peptides became exposed at the solid/air interface.<sup>[287]</sup> The VC recombinamer, in contrast, is a hydrophilic cationic molecule, therefore the VC coatings showed higher wettability ( $WCA = 58.6^\circ \pm 3.4^\circ$ ) than pristine gold and GL13K-coated surface. However, due to the presence of the GL13K peptide, GVC coatings were slightly more hydrophobic than VC coatings ( $WCA = 67.5^\circ \pm 3.1^\circ$ ), thus indicating that GL13K folds and exposes its hydrophobic residues at the solid/air interface.<sup>[210]</sup>



**Figure 4.2.** Static water contact angle of the gold surfaces when the AMP/ELRs are covalently attached. Depending on the physicochemical properties of the molecules, the wettability of the surfaces changes significantly (\*\* $p < 0.001$ ). At least 10 different measurements for each surface are represented in the box diagram. Error bars represent standard deviation values.

The elemental composition was quantified by XPS. The atomic ratios of the coatings are shown in **Table 4.2**. After immobilization of the peptide/polypeptides C 1s, O 1s and N 1s peaks increased (**Figure A4.4**),

which resulted in an increase of the atomic ratios, demonstrated the deposition of the protein materials. Quantitatively, N/Au ratio (N 1s, characteristic peak for proteins) increased from an initial 0.04 in the pristine gold surfaces up to 0.74, 1.91 and 2.52 for GL13K, VC and GVC-coatings, respectively. Furthermore, when gold surfaces were modified with thiols, the energy for the Au 4f peak shifted, <sup>[313]</sup> thus indicating covalent attachment to the surface (**Figure A4.5**).

**Table 4.2.** Quantitative XPS analysis of the covalently anchored AMP/ELR SAMs on gold surfaces. Relative atomic ratios of the most representative elements (C, O and N) of the coated molecules are shown respect to substrate element, Au.

	C / Au	O / Au	N / Au
<b>Au</b>	0.56	0.08	0.04
<b>GL13K</b>	3.52	0.78	0.74
<b>VC</b>	9.24	2.23	1.91
<b>GVC</b>	10.71	2.87	2.52

Finally, the thickness and the area density of the SAMs were estimated quantitatively using the QCM-D technique.

First, the viscous penetration depth ( $\delta$ ) corresponding to ultrapure water, the solvent used, was estimated <sup>[314]</sup>. The decay rate of the oscillating wave with the distance from the sensor surface is indicated by (**Eq. 4.1**).

$$\delta = \sqrt{\frac{2\eta}{\rho\omega}} \quad (\text{Eq. 4.1})$$

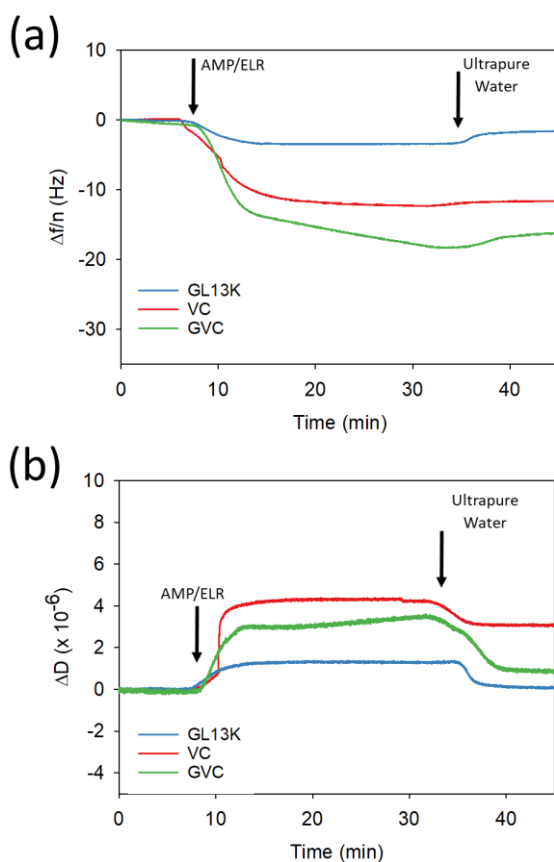
Where  $\eta$  and  $\rho$  are the viscosity and density of the solution employed for the measurement, respectively, and  $\omega$  is the oscillation frequency. For ultrapure water ( $\eta = 0.93 \text{ mPa}\cdot\text{s}$  and  $\rho = 0.998 \text{ g/cm}^3$ ),  $\delta$  is approximately 140 nm at 15 MHz (third overtone,  $n = 3$ ).

QCM-D measurements were performed at 23°C. The simultaneously measured shifts in frequency (normalized to the corresponding overtone,  $n$ ),  $\Delta f_n/n$  (**Figure 4.3a**), and energy dissipation,  $\Delta D_n$  (**Figure 4.3b**), obtained at  $n = 5$  (25 MHz) are plotted as a function of time. Although measurements were carried out up to the 13th overtone (65 MHz), only the fifth harmonic is shown in Figure 3 for clarity. Frequency and dissipation changes corresponding to the fifth, seventh and ninth overtones are reported in the Appendix (**Figure A4.6**).

Three events can be identified in the transient evolution: (i) flow of ultrapure water to establish the baseline, (ii) flow of the AMP/ELR solution, (iii) rinsing with ultrapure water. When frequency changes are considered (**Figure 4.3a**), at the beginning of the deposition stage, the slope of the frequency change was slightly higher for GVC than for VC deposition. In addition, the frequency stabilized for GL13K and VC during the deposition stage, whereas a roughly linear decrease of frequency with time was observed for GVC. Specifically, at the end of the deposition stage, the frequency changes observed were  $-3.6$ ,  $-12$ , and  $-18$  Hz, for GL13K, VC, and GVC, respectively. During the final rinsing stage, a slight increase in frequency of between  $+1$  and  $+2$  Hz was observed for all the biomaterials, thus indicating a minor desorption of molecules.

As far as dissipation is concerned (**Figure 4.3b**), a plateau was reached for GL13K and VC solutions during the deposition stage, whereas a slight slope in the dissipation was observed for GVC, similar to the frequency evolution. The rinsing stage resulted in a decrease in dissipation, and at the end of the rinsing stage a dissipation of close to zero was observed for the GL13K peptide, whereas values of around  $1 \times 10^{-6}$  and  $3 \times 10^{-6}$  were found for the ELRs GVC and VC, respectively.





**Figure 4.3.** (a) Normalized frequency and (b) energy dissipation shifts measured at 23 °C at the fifth ( $n = 5$ ) overtone for GL13K, VC, and GVC. Three events are distinguished: first, an ultrapure water stabilization flow for 2 min; second, the AMP/ELR solutions were exposed for 25 min; and finally, a stage of rinsing with ultrapure water for 20 min.

As a whole, the time evolution of the frequency change is similar for both ELRs (VC and GVC) and clearly differs from that for the peptide. The difference in molecular weights between these molecules may explain this behavior.

Because overtones are split in terms of both frequency and dissipation changes (**Figure A4.6**), the simple Sauerbrey model is not valid, therefore a viscoelastic model that enables thin film areas and masses to be calculated from multiple harmonics is required. In this case, a Voigt viscoelastic model based on a single layer was used.<sup>[315,316]</sup> In this model, the adsorbed film is

represented by a lateral homogeneous film with uniform thickness and density which, in our case, was estimated at  $1.1 \text{ g cm}^{-3}$  (corresponding to a hydrated protein).<sup>[317]</sup> The thickness of the adsorbed thin film was subsequently calculated using the QCM-D raw data.

At the end of the experiment, the Voigt model provides the thickness and the corresponding area density that characterize the stabilized thin film. The values for GL13K, VC, and GVC coatings are summarized in **Table 4.3**.

**Table 4.3.** Thickness and area density of the peptide/polypeptides immobilized on the gold surfaces at the end of the rinsing stage, as calculated using the Voigt model and the raw QCM-D experimental data.

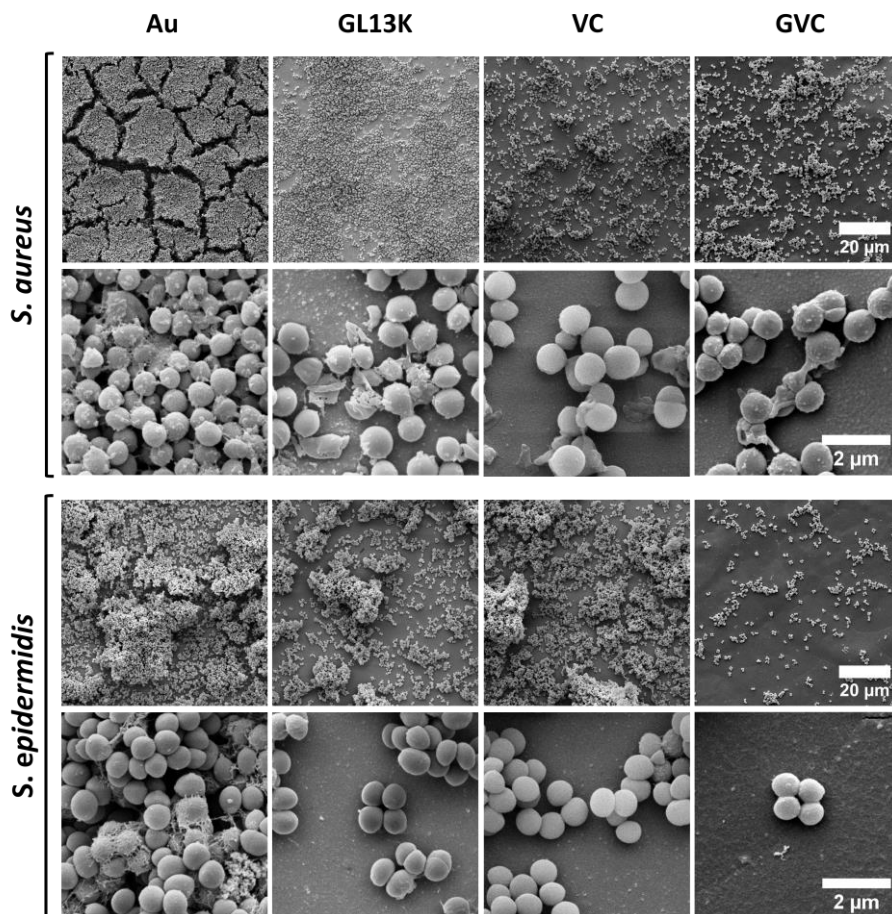
	GL13K	VC	GVC
<b>Thickness (nm)</b>	1.7±0.2	14.4±2.8	15.5±1.4
<b>Area density (ng cm<sup>-2</sup>)</b>	155±63.6	1575±318.2	1675±106.1

Similar thicknesses were obtained for VC and GVC coatings, with these values being clearly higher than the thickness for GL13K. This may be attributed to the molecular weight differences between the AMP and the ELRs. These results are consistent with the elemental quantification obtained by XPS.

#### 4.2.3. Evaluation of the antibiofilm activity of recombinant SAMs

SEM images (**Figure 4.4**) of the biofilms revealed that, after overnight incubation, the pristine gold surfaces (Au) were completely covered by multiple layers of bacteria and extracellular matrix for both staphylococcal strains. All SAMs had antibiofilm effects, even in the case of the recombinamer control (VC) coating. Indeed, all three coatings prevented the formation of a mature biofilm of both staphylococcal strains, but with

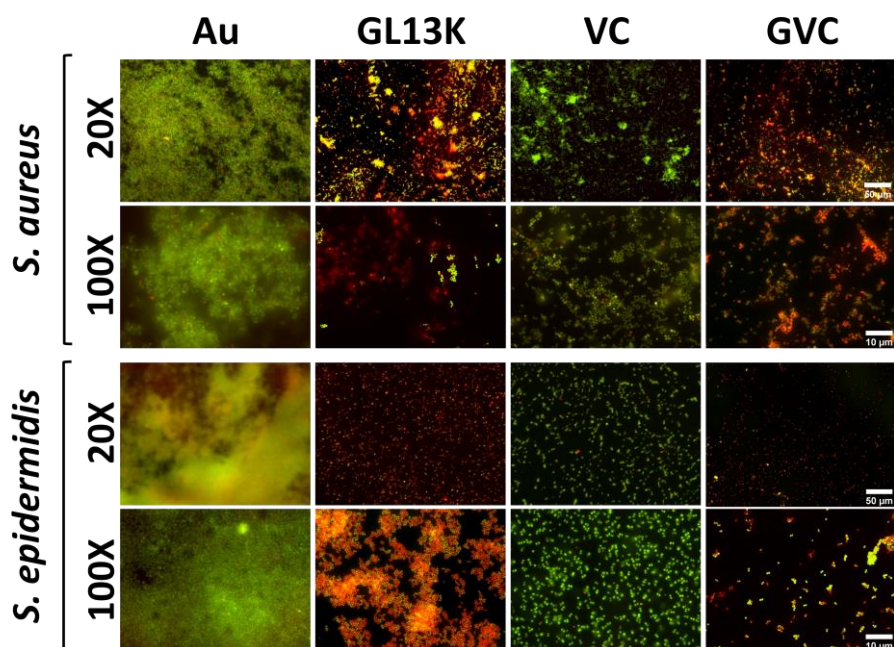
clear differences between the two strains. Thus, the antibiofilm activity of the nanocoatings seemed to be stronger against *S. aureus* than against *S. epidermidis*, except for GVC, as this coating showed a high potency of biofilm inhibition against both strains.



**Figure 4.4.** Representative SEM micrographs of the biofilms formed onto the different coatings and control Au surfaces after 24 h incubation. General view (1<sup>st</sup> and 3<sup>rd</sup> rows) and close-up (2<sup>nd</sup> and 4<sup>th</sup> rows) images of the *S. aureus* (1<sup>st</sup> and 2<sup>nd</sup> rows) and *S. epidermidis* (3<sup>rd</sup> and 4<sup>th</sup> rows) biofilms. Comparing to control gold surfaces (Au), all coatings had an antibiofilm effect that prevented the formation of a mature biofilm for both staphylococcal strains. *S. aureus* bacteria on GL13K and GVC coatings had disrupted walls and/or distorted shapes.

Fluorescence microscopy with LIVE/DEAD staining (**Figure 4.5**) confirmed that the VC coating had a low-fouling effect that hampered

biofilm formation in comparison to mature biofilms grown on control pristine gold surfaces. However, the VC coatings did not exhibit bactericidal activity (Figure 4.5, third column). Elastin-like coatings have previously been shown to exhibit antifouling properties,<sup>[130,131,305]</sup> which here could lead to low adhesion of staphylococci and, consequently, low biofilm formation.



**Figure 4.5.** LIVE/DEAD staining biofilms after 24 h of incubation on the surfaces. Green cells correspond to live cells, whereas red cells correspond with death or damaged cells. Gold surfaces were found completely covered by a multilayer biofilm, whereas all the coatings prevent the biofilm development. Bactericidal activity against *S. aureus* and *S. epidermidis* bacteria were also found on those coatings that show the GL13K peptide (GL13K and GVC).

In addition, we verified that the presence of the GL13K peptide on the surfaces (GL13K and GVC SAMs) prevented development of a mature biofilm and also exhibited bactericidal activity against the bacteria that reached the surface, thus minimizing bacterial colonization. It is worth noting that the bactericidal effects of the SAMs with GL13K peptides

resulted in shape distortion and bacterial disruption of *S. aureus* (**Figure 5.4**, second row), as described previously for oral Gram (+) bacteria, such as *Streptococcus gordonii*.<sup>[223]</sup>

Quantification of antibiofilm activity supported these conclusions (**Figure 4.6**). Thus, the CV assay showed a significant decrease in the total remaining biomass when the staphylococci were incubated on the SAMs when compared with control gold surfaces. Similarly, ATP quantification confirmed the antibiofilm and bactericidal effect of the coatings containing the GL13K peptide (GL13K and GVC). On these SAMs, the metabolic activity of the bacteria was significantly lower than that on control Au surfaces and VC coatings.

It is important to note that a divergence between the CV and ATP values for the control ELR (VC) was found. Thus, the bacterial biomass was significantly lower than for the control naked Au surfaces, whereas ATP values did not differ markedly. The minor differences observed in the metabolic activity between the biofilms formed on Au and VC surfaces may be due to biofilm heterogeneity. Despite the inhibition of mature biofilm development (see CV results and SEM images), VC coatings do not exhibit bactericidal activity (LIVE/DEAD images), thus meaning that the bacteria remaining are metabolically active. However, within a mature biofilm (gold surfaces), bacterial cells show physiological heterogeneity.<sup>[318]</sup> Bacterial immobilization on a surface triggers their adaptation to new environmental conditions, thus resulting in diverse bacterial subcommunities. In a mature biofilm, nutrients, oxygen and toxic metabolite concentration gradients differ depending on the spatial situation.<sup>[319]</sup> Thus, the bacteria that remain within the biofilm are in an averaged lower metabolic state when compared with recently attached or superficial bacteria. Thus, the combination of different techniques is of relevance in this case to allow a more

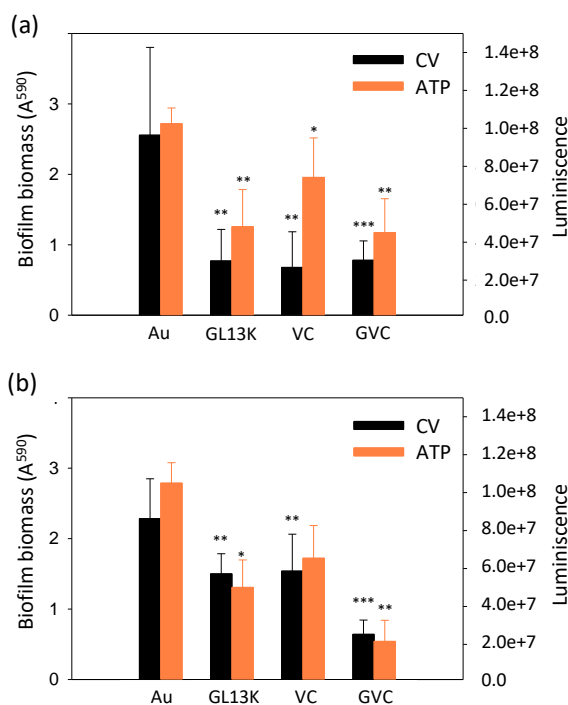
comprehensive set of antimicrobial properties to be assessed, thereby enabling a better description of the biofunctional activity of new coatings developed for preventing infection in biomedical applications.

#### 4.2.4. *Combining low-fouling ELR with AMP: Synergistic convergence of antimicrobial properties*

Striking differences were found between the antimicrobial effects of the coatings on each of the two staphylococcal strains. Thus, *S. aureus* biofilms were more sensitive to the antibiofilm activity of the SAMs than *S. epidermidis* biofilms. In addition, the CV values for *S. aureus* biofilms were 3-fold lower for all three SAMs than for control gold surfaces (**Figure 4.6**). However, the metabolic activity of *S. aureus* bacteria that remained onto the surfaces was significantly lower on those SAMs that showed the GL13K peptide (GL13K and GVC) compared with the VC coating ( $p < 0.05$ ), thus demonstrating that the presence of the GL13K peptide onto the surfaces also provided a bactericidal effect.

Interestingly, *S. epidermidis* biofilms seemed to be more resistant to the antibiofilm properties of only GL13K and the VC coated surfaces. Thus, although *S. epidermis* biofilm inhibition by these two coatings was also noticeable, it was less pronounced (**Figure 4.4**, third and fourth rows and **Figure 4.6b**) than against *S. aureus* biofilms (Figure 4, first and second rows and **Figure 4.6a**). However, the surfaces coated with GVC, which contains both the ELR and the AMP, was highly effective against both strains. Despite the fact that similar activity against *S. aureus* biofilms to that for GL13K was observed for the chimeric SAM (GVC), the low-fouling activity of the ELR and the antibiofilm and bactericidal activities of the AMP (GL13K peptide) converge in a synergistic manner, thereby

increasing the antibiofilm effect against the otherwise resistant *S. epidermidis* biofilms.



**Figure 4.6.** Antibiofilm activity of the coatings against (a) *S. aureus* ATCC25923 and (b) *S. epidermidis* ATCC35984 biofilms after 24 h of incubation in TSB medium with extra glucose (1%). Biofilm total biomass and ATP quantification demonstrated the strong and significant (\*\*\*)  $p < 0.0001$ , \*\*  $p < 0.001$ , \*  $p < 0.05$  comparing with control Au surfaces) antibiofilm activity of the coating GVC. Error bars are the standard deviation of at least four samples in each group.

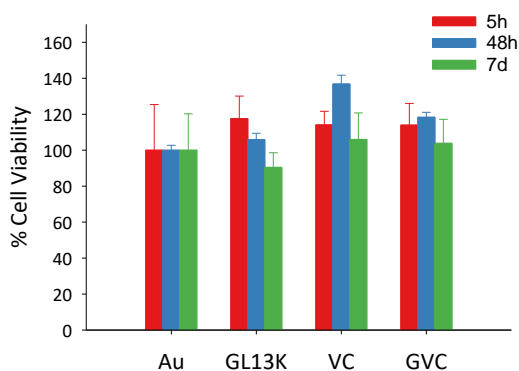
These differences in the antibiofilm activity against both staphylococcal biofilms could be a consequence of the diverse nature of both biofilms. Biofilm integrity is sustained by different biomolecules<sup>[320]</sup> (mainly extracellular DNA for *S. aureus* and poly-N-acetylglucosamine for *S. epidermidis*) and adherence proteins also differ widely.<sup>[321]</sup>

The molecular mechanisms describing the interactions of immobilized AMPs are still uncertain. Recent studies have proposed that the killing mechanism for cationic AMPs immobilized on surfaces may be mediated

simply by electrostatic interactions between the AMP and the bacterial surface,<sup>[322]</sup> with no cell membrane interactions, as reported for AMPs in solution.<sup>[144]</sup> Thus, in light of our results, we suggest that the conjugation of AMPs with ELRs enables the formation of highly potent antibiofilm coatings as the ELR provides a low-fouling scaffold for the bactericidal AMP, thus meaning that the recombinant SAMs synergistically combine antibiofilm activity and a decrease in bacterial attachment, consistent with recent studies on chemical anti-adherent coatings with AMPs.<sup>[229]</sup> These SAMs may also result in effective antimicrobial electrostatic interactions, thereby increasing the antibiofilm effect of the GL13K peptides.

#### 4.2.5. Selective toxicity against bacteria

Finally, the cytocompatibility of the surfaces was assessed to demonstrate that the toxic effect is selective for bacteria and does not affect the proliferation of human cells. thus, a metabolic assay with AlamarBlue<sup>®</sup> (**Figure 4.7**) proved that the recombinant coatings were not cytotoxic for human fibroblasts for in vitro culture periods of up to 7 days.



**Figure 4.7.** Cytocompatibility of GL13K, VC and GVC coatings after 5 h, 48 h and 1 week of incubation with human foreskin fibroblasts (HFF-1) using the AlamarBlue<sup>®</sup> assay. Results are expressed as % cell viability with respect to the control. Bars represent mean  $\pm$  standard deviation. No significant differences between coatings were found.



### 4.3. Conclusions

Using a multimodular design for ELRs, we have demonstrated that the conjugation of an AMP to a low-fouling ELR can be used to produce SAMs with strong and synergistic antibiofilm potency against staphylococcal strains. This biomolecular-based biomaterial was produced using recombinant technologies and sheds light on the potential of conjugating AMPs to recombinant polymers to form new antibiofilm agents for nanocoatings with excellent versatility, technical feasibility, and multifunctional properties. In addition, the easy and relatively cheap production and purification procedures for these recombinant compounds, which exploits the thermal sensitivity of their ELR part, facilitates scale-up of their production and potential widespread use.

### 4.4. Experimental section

#### 4.4.1. Bacterial strains

The biofilm-producing staphylococcus strains *S. aureus* ATCC 25923 and *S. epidermidis* ATCC 35984 were provided by the American Type Culture Collection (ATCC).

#### 4.4.2. Synthesis and characterization of the ELR and AMP-ELR

Recombinamers VC and EGVC were designed and cloned as described in **Chapter 1** and **2**. However, in order to introduce the Cys-cys-motif, we used an alternative p7 (p7CC) expression vector that incorporates the codons that encode for the two C-terminal cysteines before the stop codon.

After gene construction (**Figure A4.1**), ELRs expression in *E. coli* BLR (DE3) and ITC purification yields 190 and 270 mg L<sup>-1</sup> for VC and EGVC,

respectively. Then, ELRs were dialyzed (12,000 MwCO – Medicell Membranes Ltd., UK), filtered (0.22  $\mu\text{m}$  Nalgene, ThermoFisher Scientific), lyophilized and stored at  $-20\text{ }^{\circ}\text{C}$ .

#### 4.4.3. *EGVC cleavage*

The sacrificial block (E) was cleaved from the EGVC recombinamer by treatment with CNBr under acidic conditions (70% formic acid, FA) for 20 h at room temperature to release the GVC recombinamer. The solution was then dried in a rotary evaporator, resuspended in ultrapure water and dialyzed. As a result of the diverse physicochemical properties of the sacrificial block and the GVC, said block and the uncleaved EGVC were precipitated in a single centrifugation step ( $40\text{ }^{\circ}\text{C}$ ,  $\text{pH} < 4$  and  $\text{NaCl } 0.5\text{ M}$ ). The GVC was therefore completely purified in the supernatant (**Figure A4.2b** and **A4.2c**), which was dialyzed, filtrated, lyophilized and stored at  $-20\text{ }^{\circ}\text{C}$ .

#### 4.4.4. *Peptide synthesis*

The peptide GL13K was produced by Pepscan (The Netherlands) with a purity of more than 92%. An extra Cys was incorporated at the C-terminus for subsequent oriented attachment to gold surfaces.

#### 4.4.5. *Preparation of SAMs*

To study the AMP-ELR as a covalent coating, GL13K, VC, and GVC were covalently immobilized onto model gold surfaces (Figure 4.1) via the Cys residues present in the AMP/ELR/AMP-ELR.<sup>[523]</sup> To prepare the gold surfaces, cover glasses with a diameter of 12 mm (ThermoFisher Scientific, USA) were cleaned with Argon plasma for 15 min at a high power setting (29.6 W applied to the RF coil) using a PDC-002 plasma cleaner (Harrick Plasma, USA). These cover glasses were then covered with a 40 nm gold

layer using a sputter coater (Emitech K575X) with a gold layer with a purity of 99.99% (150 s, 30 mA). The resulting surfaces were immediately immersed in 200  $\mu$ M AMP/ELR/AMP-ELR solutions for 4 h, then washed three times with ultrapure water and ethanol to remove physisorbed molecules, dried under vacuum for 16 h and stored at  $-80$  °C for further use.

#### *4.4.6. Water contact angle*

Water contact angle measurements were performed using an OCA 15plus instrument (DataPhysics, Germany) equipped with a CCD camera. At least 10 drops of ultrapure water (0.5  $\mu$ l) were analyzed per group. All images were collected after stabilization 15 for seconds, and the left and right angles were averaged.

#### *4.4.7. X-ray photoelectron spectroscopy*

An X-ray Photoelectron K-Alpha (ThermoFisher Scientific, USA) spectrometer (SSTII, University of Alicante, Spain) was used to analyze the sample surfaces. Monochromatic Al-K radiation (1486.6 eV) was employed to collect all spectra, with an elliptical X-ray spot (major axis length of 400  $\mu$ m) at 3 mA x 12 kV. The alpha hemispherical analyzer was operated in constant energy mode with survey scan pass energies of 200 eV to measure the whole energy band and 50 eV in a narrow scan to selectively measure the particular elements (C 1s, N 1s, O 1s and Au 4f). XPS data were analyzed using Avantage software. A smart background function was used to approximate the experimental backgrounds, and surface elemental compositions were calculated from background-subtracted peak areas. Charge compensation was achieved using the system flood gun, which

provided low-energy electrons and low-energy argon ions from a single source.

#### 4.4.8. *Quartz crystal microbalance with dissipation*

The QCM-D technique was applied to estimate the thickness of the covalent coatings.<sup>[9,10]</sup> This technique allows simultaneous measurements of both frequency and energy-dissipation changes, which were recorded up to the 13th overtone number.

A Q-Sense Explorer System equipment (Biolin Scientific, Sweden) was used. Each solution was pumped with a peristaltic pump through the circular flow circuit at 20  $\mu\text{L min}^{-1}$ . All tests were performed at 23 °C.

An AT-cut 5 MHz gold-coated quartz crystal with an estimated surface roughness of 1 nm, according to the manufacturer's technical specifications, was used as sensor (QSX301 Gold, Biolin Scientific) The sensors were cleaned with Argon plasma in a plasma cleaner (using the same parameters indicated in section 2.5) for 5 min immediately prior to use.

The following sequence of flows (or events) was applied in each QCM-D measurement. First, since the peptide/polypeptides solutions were prepared in ultrapure water, ultrapure water was passed through the chamber for 2 min to define a stable baseline, followed by the peptide/polypeptides solution (200  $\mu\text{M}$ ) for 25 min, and a final rinse with ultrapure water for 20 min. Three replicates were performed for each measurement.

The QCM-D experimental data were numerically fitted to the Voigt (continuous) viscoelastic model using Dantzig's Simplex algorithm,<sup>[11]</sup> as implemented in the software from Biolin Scientific (Q-Sense Dfind). An explicit consideration of the frequency dependence of viscoelastic

properties was assumed according to a power law. A descending incremental fitting was used, with the quality of the fitting being determined by the parameter  $\chi^2$  (lower  $\chi^2$  values indicate a better fitting). A  $\chi^2$  value of less than 2 was always obtained in the numerical fittings.

#### *4.4.9. Antistaphylococcal assays*

To evaluate the antibiofilm properties of the coatings, two single-strain biofilm models were studied. Thus, the covalently coated surfaces were sanitized with UV light for 30 min/side and staphylococcal biofilms were grown on them. For this, 3–5 colonies from a fresh plate of *S. aureus* ATCC 25923 and *S. epidermidis* ATCC 35984 were inoculated in LB broth medium (Formedium) and incubated aerobically overnight at 37 °C and 200 rpm. The surfaces were then incubated for 24 h (37 °C, 60 rpm, aerobically) with a  $1 \times 10^6$  CFU mL<sup>-1</sup> inoculum prepared from the overnight preinoculum in fresh TSB medium (Oxoid, tryptic soy broth medium) with (extra) glucose (1%) to induce the adherent phenotype of the staphylococci.<sup>[324]</sup>

#### *4.4.10. Fluorescence microscopy*

After incubation, the surfaces were washed gently with NaCl (0.9%) to remove the unattached bacteria and the biofilms were evaluated by fluorescence microscopy. Samples were stained using the LIVE/DEAD BacLight Bacterial Viability kit (ThermoFisher Scientific, USA) following the manufacturer's instructions, then mounted on a glass sheet and visualized using a Nikon Eclipse Ti E microscope.

#### *4.4.11. Scanning electron microscopy*

After removal of unattached bacteria, the biofilms formed were immobilized on the surfaces as described elsewhere<sup>[13]</sup> and morphological

visualization by SEM was performed. Briefly, the surfaces were incubated in a primary fixation solution (2.5% glutaraldehyde and 0.15% Alcian blue in 0.1 M phosphate buffer (PB), pH 7.4, for 60 min). After washing the surfaces in 0.1 M PB, a secondary fixation solution was employed (1% OsO<sub>4</sub> in 0.1 M PB, 60 min). The samples were then washed and dehydrated in graded ethanol solutions (50%, 70%, 80%, 95% and 100%), critical point dried (Emitech K850) and coated with a 50 Å gold layer using a sputter coater (Emitech K575X). Finally, SEM visualization was carried out using an environmental scanning electron microscope (ESEM) FEI-Quanta 200 Field Emission Gun.

#### 4.4.12. *Antibiofilm activity quantification*

Antibiofilm activity was quantified by combining two different techniques. Thus, crystal violet (CV) dye was used to stain the remaining total biomass and the metabolic activity was evaluated by total ATP quantification. In brief, after bacterial incubation the surfaces were rinsed gently with 0.9% NaCl in a 24-well plate. Each surface was incubated in a 0.1% solution of CV for 15 min at RT, rinsed 4 times with deionized water and dried at RT overnight. Acetic acid solution (30%) was employed to solubilize the CV from the surfaces and the dye was quantified in a 96-well plate by measuring the absorbance at 590 nm using a SpectraMax M2e microplate reader (Molecular Devices, USA). If the absorbance was too high ( $Abs^{590} > 1$ ) the solubilized CV solution was diluted with ultrapure water and the corresponding dilution factor was applied. The metabolic activity was measured by quantifying ATP using the BacTiter-Glo kit (Promega, USA). To that end, after rinsing the coatings, 330 µL of the kit solution was added to a 24-well plate and the coatings were incubated for 5 min in the darkness, then a 100 µL aliquot was transferred into a white 96-

well plate and the luminescence measured using a SpectraMax L microplate reader (Molecular Devices).

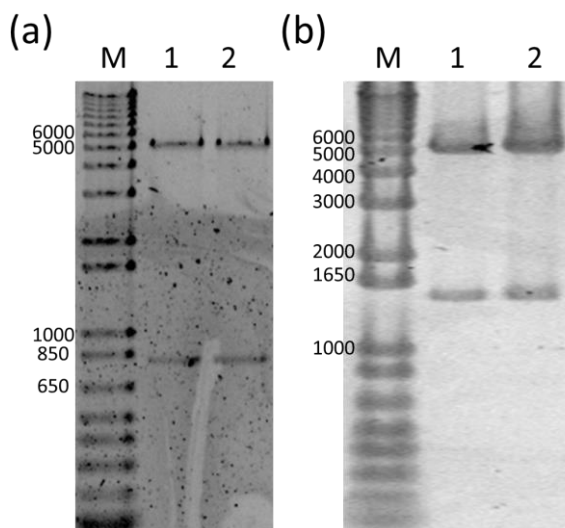
#### *4.4.13. Cytocompatibility assay*

The cytocompatibility of the coatings was tested using human foreskin fibroblast (HFF-1) cells, which were purchased from Life Technologies S.A. (Madrid, Spain). To that end, 5000 cells  $\text{cm}^{-2}$  were seeded onto the UV-sanitized surfaces in DMEM medium supplemented with 15% FBS and 100 U  $\text{mL}^{-1}$  to 100  $\mu\text{g mL}^{-1}$  penicillin-streptomycin at 37 °C and 10%  $\text{CO}_2$ . HFF-1 cells at passages between 5 and 8 were employed in all experiments. Cytocompatibility levels were determined using the AlamarBlue (AB) Cell Viability reagent (ThermoFisher Scientific, USA). Thus, according to the manufacturer's instructions, after the desired incubation times (5 h, 48 h, and 7 days) the surfaces were incubated for 4 h at 37 °C with a 10% AB solution in culture medium and the fluorescence recorded using a SpectraMax M2e microplate reader (Molecular Devices, USA).

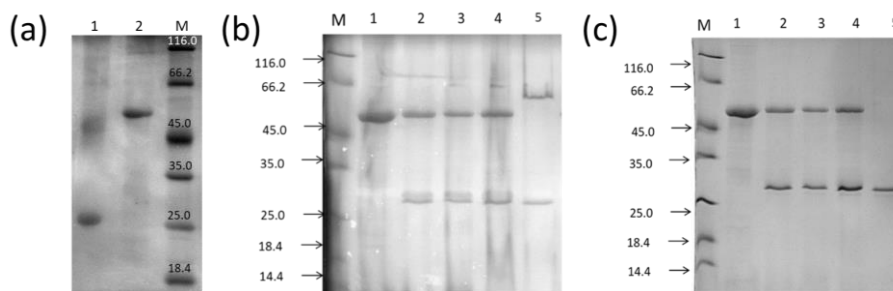
#### *4.4.14. Statistical analysis*

A one-way analysis of variance table (ANOVA) with posthoc multiple comparison Holm-Sidak test was used to evaluate the data and intergroup differences using Statgraphics XVII. A  $p$ -value of less than 0.05 was considered to be statistically significant ( $***p < 0.0001$ ,  $**p < 0.001$ ,  $*p < 0.05$ ). Results are shown as mean  $\pm$  standard deviation (SD) ( $n \geq 3$ ).

## 4.5. Appendix

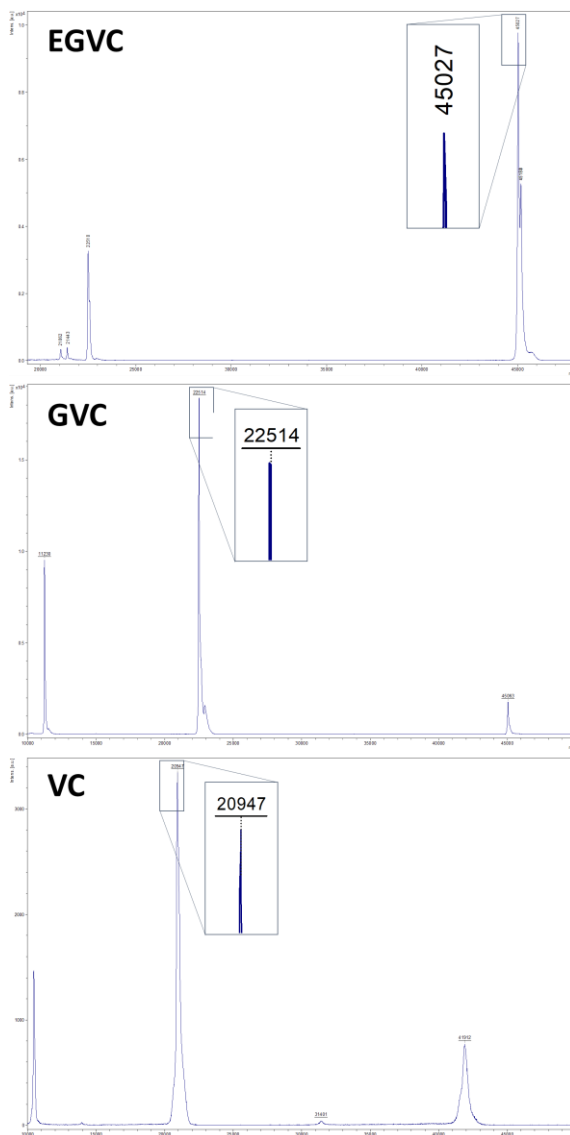


**Figure A4.1.** Enzymatic analysis of the expression vector p7Cys containing the encoding inserts for the ELRs cut with *XhoI* and *XbaI* endonucleases: (a) VC (720 bp) (b) EGVC (1593 bp). 1kb Plus DNA Ladder (Invitrogen, USA) used as marker (Lanes M).



**Figure A4.2.** SDS-PAGE gels of: **Gel a:** VC (Lane 1) and EGVC (Lane 2) recombinamers after the ITC purification. Stained with CuCl<sub>2</sub> **Gel b** and **c:** CNBr cleavage of EGVC and ITC purification of the GVC recombinamer. Stained with CuCl<sub>2</sub> (b) and Coomassie (c). EGVC pure (Lane 1). EGVC after 12 (Lane 2), 16 (Lane 3) and 20 (Lane 4) of incubation with CNBr (200X) in FA (70%). GVC pure after one-single centrifugation cycle at 40 °C, pH<4 (Lane 5). Unstained Protein MW Marker (ThermoFisher) used as marker (Lane M).





IV

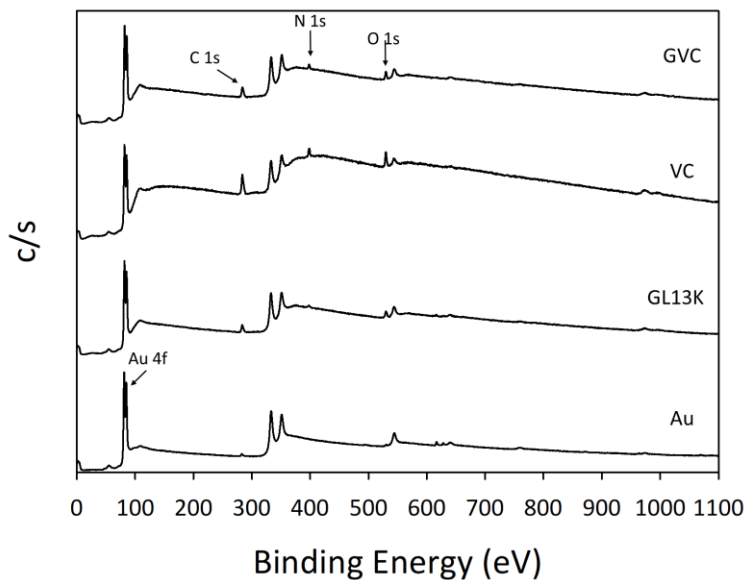
**Figure A4.3.** MALDI-TOF spectra of the EGVC, VC and GVC recombinanters.

**Table A4.1.** Comparison of the theoretical and experimental MW calculated by MALDI-TOF.

	Theo. MW (Da)	Exp. MW (Da)
EGVC	45241.3	45041.3±13.4
VC	21038	20928.6±9.6
GVC	22670	22513.7±2.6

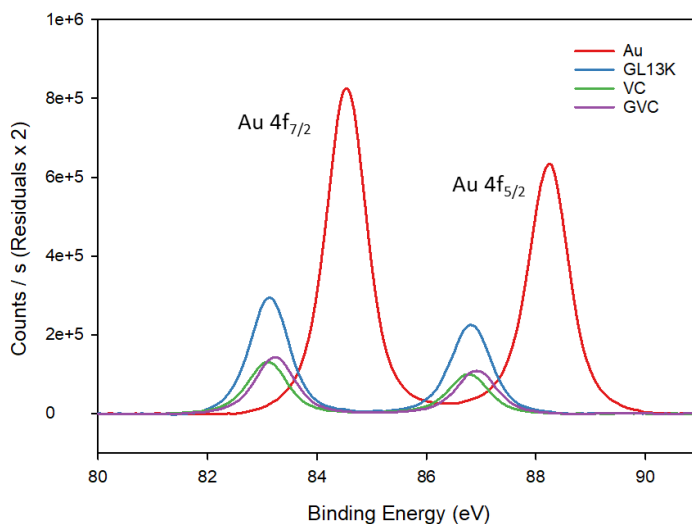
**Table A4.2.** Amino acidic composition of the VC and GVC recombinamers calculated by HPLC. It is represented the theoretical composition comparing to the experimental values obtained.

Amino acid	VC		GVC	
	Theo.	Exp.	Theo.	Exp.
Asp	-	-	-	-
Glu	1	1.05	-	-
Asn	-	-	-	-
Ser	1	1.39	1	0.98
Gln	-	-	-	-
His	-	-	-	-
Gly	97	99.71	108	116.83
Thr	-	-	-	-
Arg	-	-	-	-
Ala	-	-	1	1.41
Tyr	-	-	-	-
Cys	2	1.21	2	2.01
Val	91	84.7	91	87.76
Met	-	-	-	-
Trp	-	-	-	-
Phe	-	-	-	-
Ile	-	-	2	1.38
Leu	2	2.4	6	5.33
Lys	8	8.09	12	8.1
Pro	49	53.89	48	51.65
<b>Total aas</b>	<b>251</b>	<b>252.44</b>	<b>271</b>	<b>275.45</b>

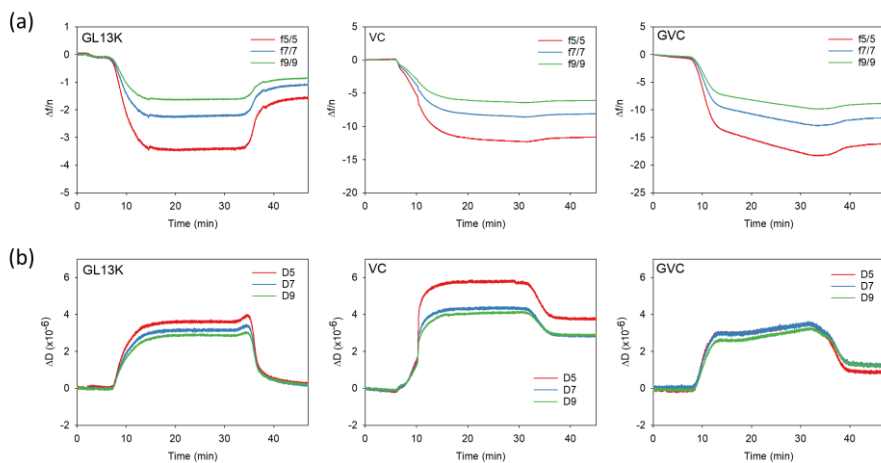


**Figure A4.4.** Representative survey scan spectra of the gold substrates after the immobilization of the peptide GL13K and the polypeptides VC and GVC.

IV



**Figure A4.5.** XPS detailed spectra of the Au4f region. The Au 4f shifted from approx. 85 eV from the pristine gold to approx. 83 eV indicating the Au-S bond and consequently the covalent immobilization of the AMP, ELR or the AMP-ELR onto the gold surfaces.



**Figure A4.6.** Quartz-crystal microbalance measurements: (a) normalized frequency and (b) energy dissipation shifts measured at 23 °C at the fifth ( $n=5$ ), seventh ( $n=7$ ) and ninth ( $n=9$ ) overtone for GL13K, VC and GVC.





# Chapter V

---

Biofabrication of antibiofilm coatings to prevent implant-associated infections

---





## 5.1. Introduction

Implantable biomedical devices have revolutionized patient rehabilitation, although their use increases the risk of infection. The implantation of a medical device provides an opportunity for nosocomial pathogens to colonize the site and form a biofilm on the device surface, thus leading to infections that may cause prolonged hospitalizations and higher mortality rates.<sup>[220]</sup> In fact, implant-associated infections (IAIs) are one of the most common and severe complications of healthcare interventions,<sup>[325,326]</sup> thereby creating an immense economic and social burden.<sup>[327]</sup> Furthermore, in many cases conventional antibiotics are ineffective at treating these types of infections due to the presence of biofilms and the increasing prevalence of antibiotic-resistant bacteria.<sup>[328]</sup> Thus, the development of new strategies to prevent device colonization and biofilm formation is essential.

As mentioned in **Chapter 4**, AMPs and designer AMPs are some of the most promising alternatives to conventional antibiotics. In solution, AMPs are able to interpenetrate the bacterial outer membrane or the cell wall, interacting with the cell membrane and intracellular targets and killing bacteria by inducing membrane permeability or inhibiting intracellular processes.<sup>[144]</sup> However, they may also show a toxicity and sensitivity to proteases that limits their application.<sup>[329]</sup> Notably, although immobilization of AMPs onto surfaces enhances their stability and increases their local concentration and biological availability, it compromises their ability to interact with multiple targets.<sup>[219]</sup> In addition, although AMPs may show bactericidal activity when directly immobilized onto surfaces,<sup>[223,287,330–332]</sup> recent studies suggest that attachment of the peptides to the substrate via a spacer enhances the flexibility, exposure and functional conformation of

the AMPs, thereby improving the anti-infective potential of the coatings.<sup>[230,333–335]</sup>

This approach can also be used to produce multivalent coatings with improved features for clinical use, such as anti-adhesive properties, high affinity for biomaterial, or biomimetic behavior to enhance tissue integration of permanent orthopedic and dental implants.<sup>[296,331,336]</sup> As such, the strategy used to immobilize AMPs plays a key role in the efficiency of the obtained antimicrobial coating. In this sense, ECM-mimicking polypeptides, such as elastin-like recombinamers (ELRs), are promising candidates for the production of bioactive coatings for implantable devices. In addition to their unique biological and mechanical properties, their recombinant nature enables their composition to be fine-tuned and thus bioactive domains to be incorporated with extreme control of the physicochemical properties. All these features make them attractive candidates for the development of covalent coatings for indwelling devices.<sup>[15]</sup> Indeed, ELRs have demonstrated their applicability as covalent coatings, offering a versatile coating to control the biological response of biomedical materials, improving tissue integration and biocompatibility of the device, or incorporating additional functionalities that include control of biomineralization or spatial control over cell adhesion to produce cellular micropatterns.<sup>[131,136–138,337]</sup>

Herein we have developed an ECM-mimicking platform for AMPs as an antibiofilm coating for permanent metallic implants by exploiting the intrinsically disordered nature of ELRs to produce a multivalent flexible platform that includes AMPs in the polypeptide backbone. These hybrid ELRs were produced by recombinant DNA technology or by chemical derivatization and displayed antimicrobial properties when used as covalent coatings. Specifically, the designer peptide GL13K (GKIIKLKASLKL-

NH<sub>2</sub>) was combined with a polycationic ELR (VC) with a C-terminal grafting motif for oriented molecular tethering. The D- and L- enantiomers of GL13K peptide have been shown to have different self-assembly properties that can predetermine their antimicrobial activity in solution.<sup>[210,338,339]</sup> Overall, the D-enantiomer of GL13K is a protease resistant peptide that can evade bacterial resistance.<sup>[159]</sup> In this study, the versatility of the biomimetic platform is demonstrated as both enantiomeric forms of GL13K were combined with the VC ELR. L-GL13K was co-expressed with the ELR and bioproduced in *E. coli* by recombinant DNA technology.<sup>[340]</sup> In contrast, D-GL13K was attached to modified Lys side chains of VC using click chemistry.<sup>[5]</sup>

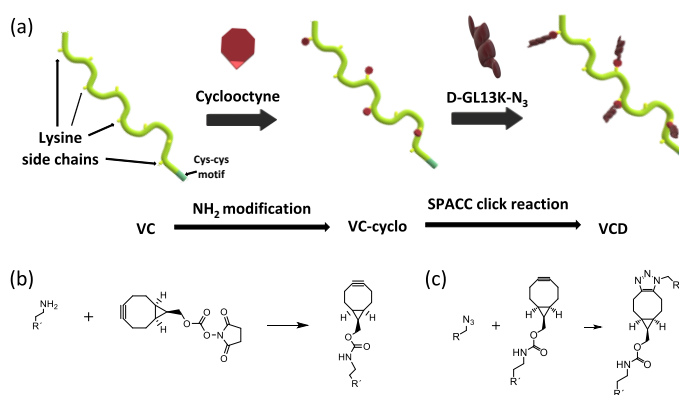
The resulting hybrid ELRs were subsequently tethered to commercially pure titanium discs and their biological response was tested. Their cytocompatibility was assessed against human primary cells and their antibiofilm efficacy against two biofilm models of clinical relevance. Thus, *Streptococcus gordonii* was tested since it is one of the most important early colonizers of the oral cavity. *S. gordonii* initiates dental plaque formation and facilitates the attachment of secondary pathogenic colonizers, such as *Porphyromonas gingivalis*.<sup>[341]</sup> An oral microcosm biofilm model derived from cariogenic dental plaque<sup>[342]</sup> was also assayed in order to mimic the high complexity and heterogeneity of the oral microbiota. Both oral biofilm models were evaluated under dynamic conditions using a drip flow biofilm reactor (DFBR). The DFBR enables *in vitro* simulation of some of the relevant conditions for bacteria biofilm development *in vivo*. A constant drip flow is provided during the whole incubation, thus mimicking the continuous nutritional supply and shear forces found in the oral cavity. Therefore, the antibiofilm properties of the coatings were tested under

more challenging and realistic conditions than when using conventional static culture methods.<sup>[223]</sup>

## 5.2. Results and Discussion

### 5.2.1. Hybrid ELRs design and synthesis

Hybrid polypeptides (AMP-ELR) were based on the polycationic ELR described in **Chapter 4** (VC) containing a C-terminal Cys-Cys motif intended for the site-specific tethering onto surfaces. L-GL13K was incorporated at the N-terminus of the VC using recombinant DNA techniques, thus resulting in the hybrid GVC. Both polypeptides (VC and GVC) were bioproduced in high yield as heterologous proteins in *E. coli*, followed by inverse transition cyclizing to obtain highly pure products with extreme control of their physicochemical properties, as previously described. In contrast, due to proteinogenic amino acids are all L-stereoisomers, chemical derivatization was needed for synthesize an ELR containing the D-enantiomer of the GL13K peptide (VCD) (**Figure 5.1**).



**Figure 5.1.** (a) Schematic representation of the covalent modification of the VC polypeptide with D-GL13K to produce the hybrid polypeptide, VCD. Detailed schemes of (b) the cyclooctyne-modification of ELR and (c) the subsequent strain-promoted azide-alkyne cycloaddition (SPAAC).

Amino side groups of the VC polypeptide enabled covalent attachment of functional peptide motifs via a strain-promoted alkyne-azide cycloaddition (SPAAC), or “click chemistry”, reaction.<sup>[96]</sup> In this study, azide-modified D-GL13K peptides were tethered to cyclooctyne-modified amino groups of the VC polypeptide, which resulted in two to four D-GL13K peptides per polypeptide, as revealed by MALDI-TOF (**Figure A5.1, A5.2 and A3**) (The full amino acid sequences of the ELRs are listed in **Table 5.1**).

**Table 5.1.** Theoretical molecular weights and sequences of the AMP/ELR/AMP-ELRs used to manufacture covalent coatings onto Ti substrates. The MW was experimentally calculated by MALDI-TOF.

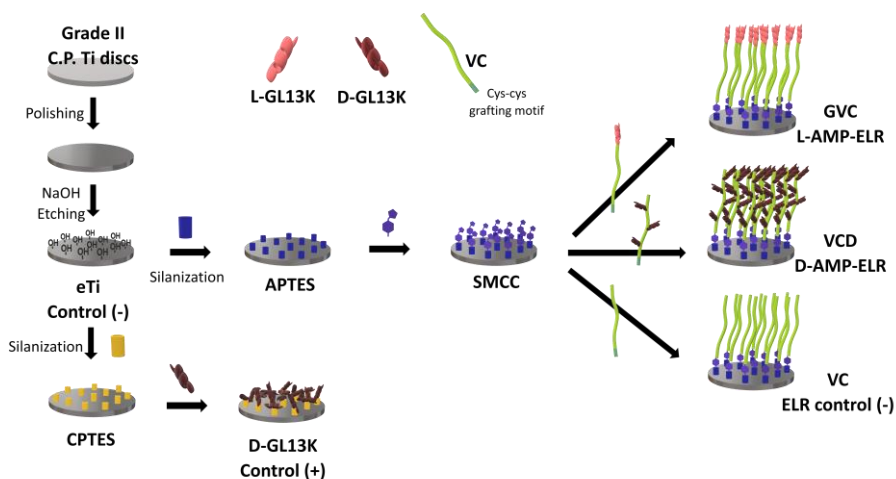
	MW (Da)	Sequence	AMP (no./molecule)
<b>D-GL13K</b>	1424.0	Gkiiklkaskll-NH <sub>2</sub>	D-GL13K (1)
<b>VC</b>	20819.8	MESLLPVG (VPGVGVPKG(VPGVG) <sub>4</sub> ) <sub>8</sub> VCC	- (0)
<b>GVC</b>	22513.7	GKIIKLKASLKLLVLG <sub>10</sub> LVG(V PGVGVPKG(VPGVG) <sub>4</sub> ) <sub>8</sub> VCC	L-GL13K (1)
<b>VCD</b>	26517.8	MESLLPVG (VPGVGVPK <sup>(a)</sup> G(VPGVG) <sub>4</sub> ) <sub>8</sub> V CC <sup>a</sup>	D-GL13K (2-4)

<sup>(a)</sup> Lysine side chains were modified by ‘click’ chemistry in order to incorporate the D-GL13K peptide.

### 5.2.2. Coating fabrication and stability

Covalent coatings of D-GL13K peptide or the polypeptides were produced by immobilization with organosilanes on Ti surfaces, as shown schematically in **Figure 5.1**. Physicochemical (water contact angle (WCA), **Figure 5.3 and A5.4**) and chemical (X-ray photoelectron spectroscopy

(XPS), **Table 5.2** and **Figure A5.5**) characterization demonstrated the effectiveness of the surface functionalization.

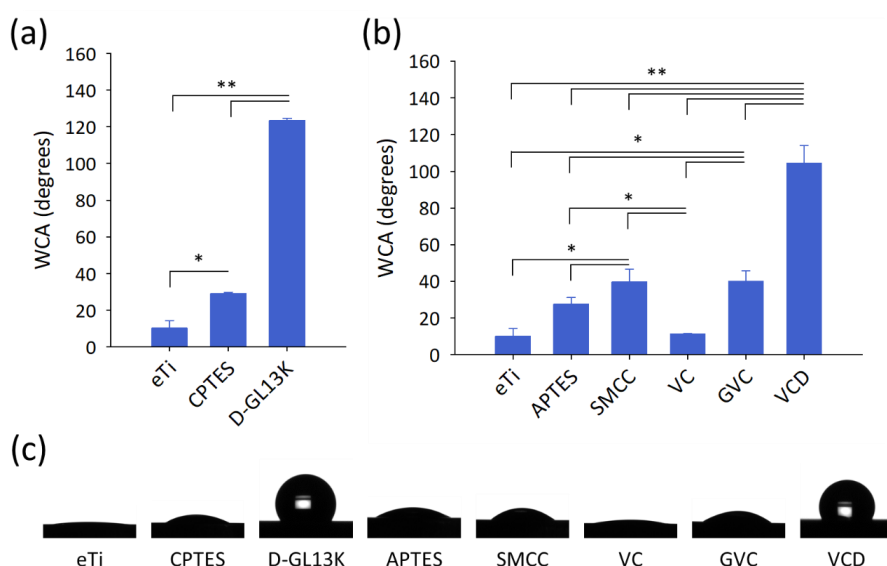


**Figure 5.2.** Schematic representation of the immobilization of D-GL13K peptides and the oriented tethering of the genetically engineered polypeptides onto titanium surfaces by titanium etching and silanization.

The NaOH etching of titanium (eTi) formed abundant polar hydroxyl radicals on the metal surface,<sup>[343]</sup> thus meaning that these surfaces were highly hydrophilic ( $WCA = 10.2^\circ \pm 4.2^\circ$ ). Silanization of the eTi surfaces with either CPTES or APTES significantly increased surface hydrophobicity ( $WCA = 29^\circ \pm 0.7^\circ$  and  $WCA = 27.6^\circ \pm 3.6^\circ$  for CPTES and APTES, respectively). Immobilization of the D-GL13K peptides on CPTES-treated surfaces produced highly hydrophobic surfaces ( $WCA = 123.4^\circ \pm 1.3^\circ$ ). As mentioned previously, GL13K peptides are amphipathic molecules that re-structure and self-assemble under the solution conditions used herein.<sup>[210]</sup> They then arrange at the surface of the metal so that the positively charged/hydrophilic groups of the free amines of the D-GL13K molecule (4 lysines and the N-terminus) are attracted to, and react with, the negatively charged and hydrophilic surface of the CPTES-treated titanium.

This molecular arrangement exposes the hydrophobic amino acids at the surface/air interface, which produces a highly hydrophobic surface.<sup>[216,223,344]</sup>

In contrast, ELRs were selectively immobilized on the surfaces via their C-terminal Cys-Cys motif. To that end bifunctional sulfo-SMCC was used as a linker between the APTES organosilane and the ELRs. Sulfo-SMCC deposition ( $WCA = 39.9^\circ \pm 6.8^\circ$ ) on APTES-silanized surfaces produced a moderate increase in surface hydrophobicity.



**Figure 5.3.** Water contact angle (WCA) of surfaces after different modification steps for covalent attachment of the AMP (a) or ELR/AMP-ELRs (b). Bars represent the WCA after stabilization for 60 s and error bars represent standard deviations ( $n=6$ ). (c) Representative images of the water drops on the different coatings. (\* $p < 0.05$ , \*\* $p < 0.001$ ).

Dynamic WCA analysis after immobilization of each of the three ELRs (VC, GVC or VCD) on sulfo-SMCC treated surfaces revealed that the ELR-coated surfaces were hydrophobic ( $WCA > 80^\circ$ ) immediately after the water drop was deposited. VC- and GVC-coated surfaces exhibited drastic drops in WCA (increase in hydrophilicity) over time, whereas VCD-coated surfaces maintained their high hydrophobicity throughout the WCA

analysis (100 s), with a final WCA of  $104.5^\circ \pm 9.7^\circ$ , which is almost as high as that for D-GL13K coated surfaces (Figure S4). The amphipathic nature of the ELRs means that they are able to rearrange in response to contact with water molecules,<sup>[305]</sup> thus explaining the notable evolution of WCA for VC- and GVC-coated surfaces as they progressively expose their hydrophilic blocks at the solid/water interface. The difference in the final hydrophilicity between these two ELRs reflects the effect of the presence and absence of L-GL13K in GVC (WCA =  $40.1^\circ \pm 5.7^\circ$ ) and VC (WCA =  $11.2^\circ \pm 0.3^\circ$ ), respectively. VCD contains between two and four D-GL13K peptides randomly located over the whole surface of the molecule. The interaction of the VCD-coating with water seems to be dominated by exposure of the ubiquitous peptide, as is also the case for the D-GL13K-coated surface. Thus, VCD-coated surfaces do not show major dynamic WCA changes.

**Table 5.2.** Quantitative XPS analysis of the titanium surfaces after different modification steps. Relative atomic ratios for the most representative elements (Si, N and C) in the coated molecules are shown with respect to the substrate element (Ti).

	Si / Ti	N / Ti	C / Ti
<b>eTi</b>	0.0003	0.003	0.523
<b>CPTES</b>	0.236	0.012	1.456
<b>D-GL13K</b>	0.186	1.972	9.511
<b>APTES</b>	0.156	0.132	1.232
<b>SMCC</b>	0.145	0.199	3.327
<b>VC</b>	0.105	5.416	20.663
<b>GVC</b>	0.111	5.762	21.365
<b>VCD</b>	0.020	5.948	22.503

XPS analysis confirmed the successful modification of the Ti substrates (**Table 5.2** and **Figure A5.5**). Thus, the Si 2p peak increased



after silanization of eTi with APTES or CPTES, which resulted in a marked increase in the Si/Ti atomic ratio from 0.0003 (eTi surfaces) to 0.236 and 0.156 (for CPTES- and APTES-silanized surfaces, respectively), thus confirming the presence of these silanes on the Ti surface. In contrast, after peptide/polypeptide modification, significant increases in C 1s and N 1s signals, and a substantial decrease in Ti 2p and Ti 2s, were observed. Quantitatively, the N/Ti atomic ratio increased from 0.012 (CPTES-silanized surfaces) to 1.972 after deposition of the D-GL13K peptide deposition and from 0.199 (SMCC-modified surfaces) to 5.416–5.948 for the ELR and AMP-ELRs (VC, GVC and VCD), thus demonstrating attachment of the peptide/polypeptide coatings. Higher N/Ti and C/Ti atomic ratios were observed after the deposition of the ELRs compared with the D-GL13K surfaces. This was expected because of the larger molecular weight of the ELRs compared with the AMP.

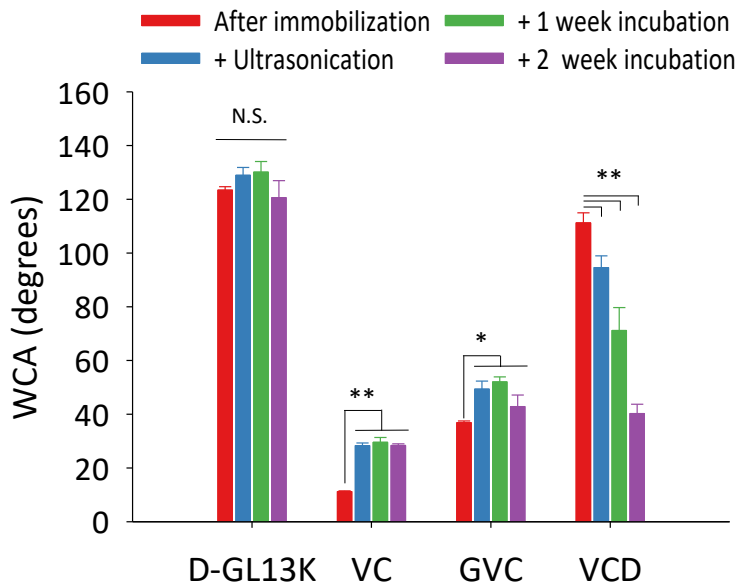
We then tested the mechanical and thermal stability of the coatings. To evaluate the resistance to degradation, the functionalized Ti discs were ultrasonicated for 2 h in ultrapure water before being incubated in PBS (1X) at 37 °C for 2 weeks. XPS and WCA analyses were performed after every challenge step. As shown in **Table 5.3**, the N/Ti atomic ratio decreased after ultrasonication in ultrapure water for all coatings. This was correlated with a slight increase in the Ti 2p signal (**Figure A5.6**), indicative of the removal of small number of peptides/polypeptides from the functionalized surfaces. During incubation in PBS, the N/Ti and C/Ti ratios remained stable in the D-GL13K coating, thus demonstrating its resistance to incubation under physiological conditions. In contrast, a progressive decrease in the N/Ti and C/Ti atomic ratios of the ELR/AMP-ELR coatings was observed during the first incubation week, with this stabilizing during the second incubation week (**Table 5.3** and **A5.1**, respectively).

**Table 5.3.** Evolution of the N/Ti atomic ratio of the modified Ti surfaces after ultrasonication for 2 hours in aqueous solution, followed by incubation in PBS (1X) at 37 °C for 1 and 2 weeks.

	N / Ti			
	After immobilization	After ultrasonication	After 1 week incubation	After 2 weeks incubation
D-GL13K	1.97	1.21	1.21	1.10
VC	5.42	1.91	0.97	1.14
GVC	5.76	3.35	1.03	1.25
VCD	5.95	4.69	1.89	2.42

Gradual removal of the polypeptides from the coatings may be due to their different degree of hydrophilicity and/or the chemical nature of the linker used for covalent immobilization. Thus, the D-GL13K peptide was nonspecifically attached to the CPTES-silanized surface via the free amines, thus exposing their apolar residues and producing highly hydrophobic coatings that provide impermeability to the surface.<sup>[330]</sup> The high hydrophobicity of these coatings could protect the organosilanes from hydrolysis, thereby preventing peptide removal. All D-GL13K coatings remained highly hydrophobic after the challenges ( $WCA = 120.6^\circ \pm 6.4^\circ$ ) (**Figure 5.4**). Conversely, ELRs were tethered in an oriented way via their C-terminal Cys-Cys motif, thus enabling them to rearrange in solution and, consequently, resulting in a greater degree of interaction with water molecules, which may drive a greater degree of hydrolysis of the organosilanes and detachment of molecules from the coating comparing with the D-GL13K coating. In addition, as can be seen from **Figure 5.4**, VC and GVC coatings were more hydrophilic than the D-GL13K coating. Despite a modest increase in hydrophobicity after ultrasonication ( $WCA = 28.3^\circ \pm 1.0^\circ$  and  $WCA = 49.33^\circ \pm 4.3^\circ$ , for VC and GVC respectively), this

lack of impermeability may also affect coating resistance. Finally, although VCD immobilization produced hydrophobic surfaces, a similar behavior to VC and GVC was observed. However, it is worth noting that the WCA for the VCD coating remained significantly higher than for the VC coating (ELR control) after the challenges ( $p < 0.001$ ), thus suggesting that D-GL13K peptides were still present in the coating.

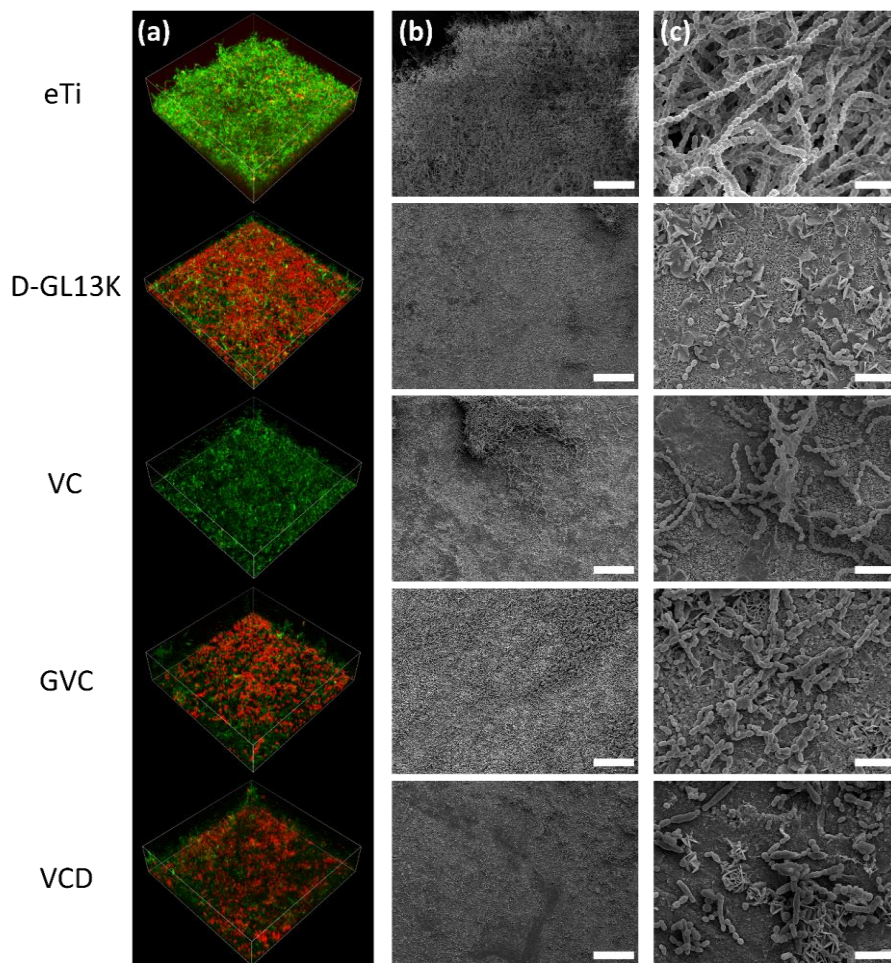


**Figure 5.4.** Physicochemical characterization of the coatings after the stability tests. Evolution of the N/Ti atomic ratio (a) and wettability (b) of the modified Ti surfaces after ultrasonication for 2 hours in aqueous solution, followed by incubation in PBS (1X) at 37 °C for 1 and 2 weeks (N.S. = non-significant, \* $p < 0.05$ , \*\* $p < 0.001$ ).

### 5.2.3. *Antibiofilm activity against monospecies biofilm*

Functionalized Ti surfaces were tested against *S. gordonii* biofilms under dynamic conditions in a DFBR to assess the antibiofilm capacity of the coatings. *S. gordonii* bacteria are relevant primary colonizers and plaque producers in the oral cavity that enable the attachment of other pathogenic bacteria in the biofilm, such as *P. gingivalis*.<sup>[341]</sup>

After incubation, LIVE/DEAD images of the biofilms (**Figure 5.5a**) revealed that eTi discs were completely covered by *S. gordonii* biofilm, while D-GL13K coatings provided antibiofilm and bactericidal activity to the surface, as reported previously.<sup>[223]</sup> ELR coatings also hindered biofilm maturation.



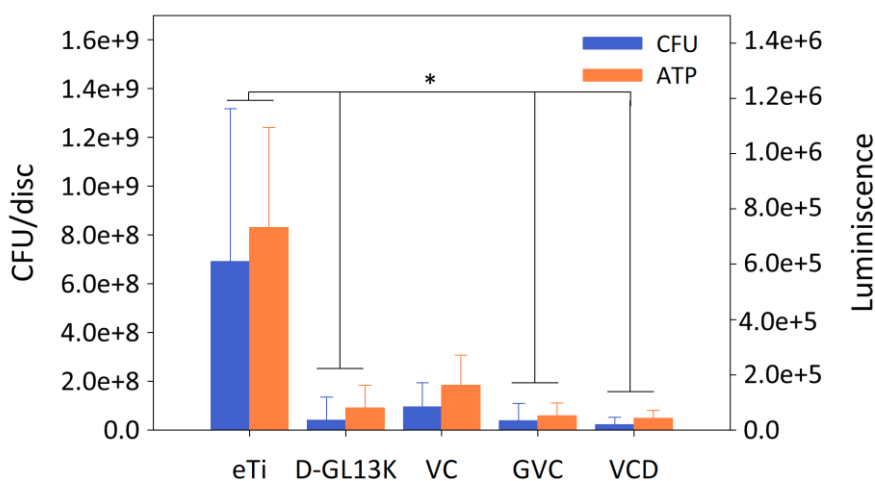
**Figure 5.5.** *S. gordonii* biofilms formed on the surfaces after incubation under dynamic conditions (DFBR): (a) LIVE/DEAD staining images of the streptococcal biofilms obtained by confocal laser scanning microscopy (CLSM). Green cells correspond to bacteria with intact membranes, whereas the bacterial membranes are compromised or damaged in red bacteria (area  $xy = 126 \times 126 \mu\text{m}$ ). (b) and (c) SEM micrographs of the immobilized biofilms on the surfaces. Scale bars =  $40 \mu\text{m}$  (b) and  $4 \mu\text{m}$  (c).

The VC coating (ELR control) prevented the formation of a mature biofilm but with no bactericidal effect due to a low-fouling effect.<sup>[340]</sup> However, the combination of GL13K peptides (L or D enantiomers) with the VC polypeptide in the hybrid coatings (GVC and VCD), provided additional bactericidal activity against the bacteria remaining on the surface.

SEM evaluation (**Figure 5.5b, 5.5c and A5.8**) confirmed the antibiofilm activity of the coatings against *S. gordonii*. Thus, eTi discs were covered by a thick biofilm, which fully prevented visualization of the Ti substrate underneath the bacteria, whereas all coatings hindered biofilm growth, as shown in the SEM images, by decreasing bacterial colonization of the surfaces in comparison to the eTi control substrate. Consistent with previous findings,<sup>[223]</sup> bacteria with morphological changes were found on the coatings containing AMPs (D-GL13K, GVC and VCD). This may be indicative of the effects of the AMP on *S. gordonii* cell walls and/or membranes. Thus, ruptured bacteria and/or elongated bacteria were found on the positive control (D-GL13K) and on the hybrid AMP-ELR (GVC and VCD) coated surfaces.

Furthermore, quantification of the antibiofilm activity of the coatings was successfully assessed by CFU counting and evaluation of the metabolic activity evaluation of the remaining biofilms after the incubation period (**Figure 5.6**). In comparison to eTi discs, all coatings reduced biofilm formation, with significantly lower CFU and ATP values. VC coatings showed a notable reduction in bacteria, as shown in **Figure 5.5**, but the CFU and ATP values revealed that the antimicrobial effect of these coatings was moderate and lower than for all other coatings. ELR-based coatings prevented nonspecific protein adsorption,<sup>[131]</sup> thus conferring antifouling properties on the surfaces,<sup>[134]</sup> that may hamper bacterial attachment and biofilm formation under static conditions, as described previously for other

Gram positive bacteria.<sup>[340]</sup> Nevertheless, this low-fouling activity of VC coatings was unable to significantly reduce *S. gordonii* biofilm development under dynamic conditions, compared with eTi substrates. In contrast, hybrid AMP-ELR coatings (GVC and VCD), with additional bactericidal activity conferred by the AMPs, significantly decreased biofilm formation on the surfaces compared to eTi, which is similar to the result obtained with D-GL13K coatings.

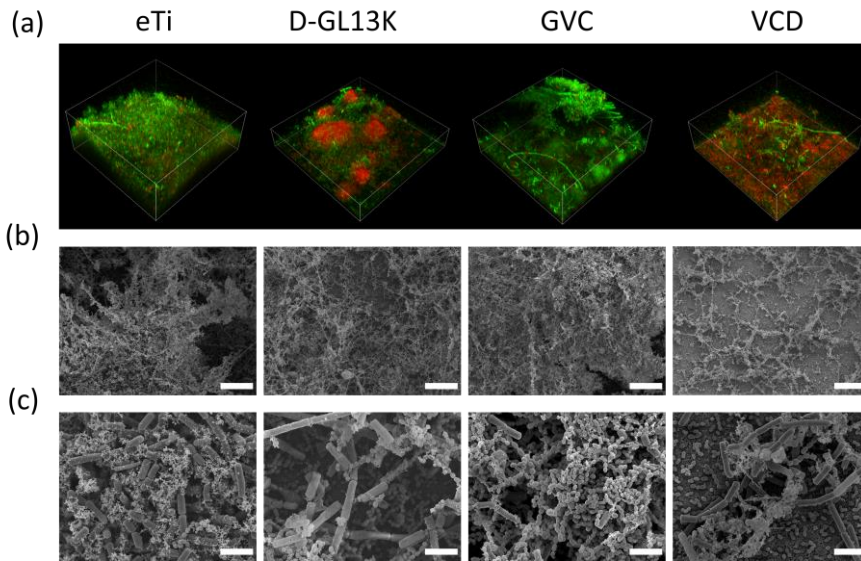


**Figure 5.69.** Quantification of antibiofilm activity by CFU counting and metabolic activity, as measured after incubation for 48 h under dynamic conditions. The presence of the GL13K (L or D enantiomer) in the hybrid ELR coatings significantly decreased biofilm formation with respect to uncoated eTi ( $*p < 0.05$ ).

#### 5.2.4. *Antibiofilm activity against oral microcosm biofilms*

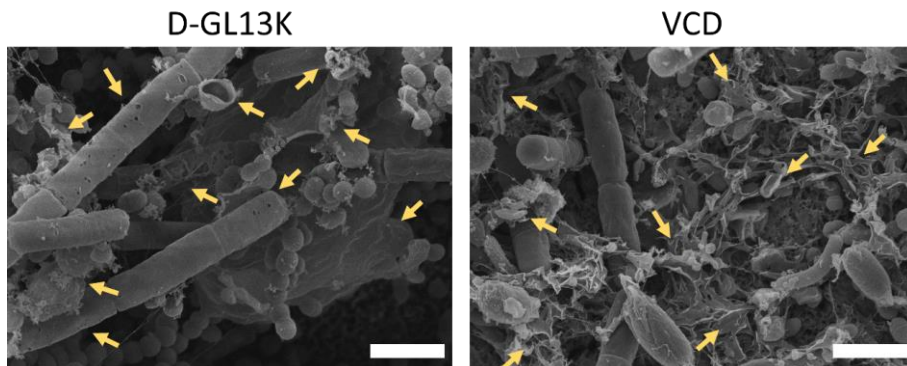
Following successful assessment of the antimicrobial effects of the hybrid ELR coatings against *S. gordonii* biofilms, we tested their antibiofilm potential by applying oral-simulating and more challenging *in vitro* conditions. Thus, a well characterized oral microcosm biofilm model collected from cariogenic patients<sup>[342]</sup> was grown onto the hybrid coatings (GVC and VCD) using a DFBR. eTi and D-

GL13K-coated surfaces were also tested in order to compare the efficacy of the hybrid coatings.



**Figure 5.7.** Representative CLSM and SEM images of oral microcosm biofilms after incubation in the DFBR for 6 days. (a) CLSM images of the biofilm with LIVE/DEAD staining (xy section = 126 x 126  $\mu\text{m}$ ). SEM micrographs: (b) general view (scale bar = 40  $\mu\text{m}$ ) and (c) magnified images of the biofilms (scale bar = 4  $\mu\text{m}$ ). eTi discs were found to be completely covered by a thick biofilm. Although all the coatings prevented the development of a mature biofilm, bactericidal activity was only found for those coatings containing D-GL13K peptides (D-GL13K and VCD).

After incubation of the surfaces with the oral microcosm biofilm model in the DFBR, under dynamic conditions, for 6 days, evaluation of the CLSM (**Figure 5.7a**) showed that a thick complex biofilm covered the whole surface of the eTi discs. In contrast, all coatings tested hampered

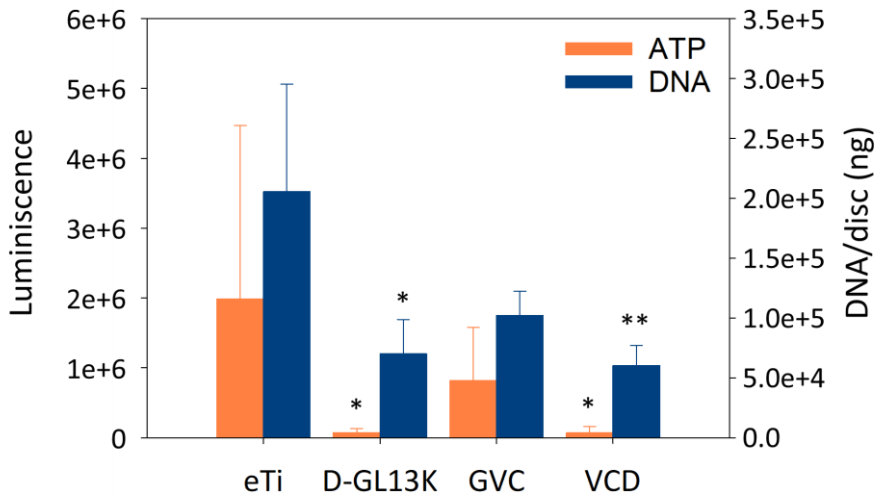


biofilm formation and/or growth, but with substantial differences in the way they did so. Thus, biofilm thickness was decreased on GVC coatings compared to eTi surfaces, but the coatings with this hybrid ELR exhibited no discernable bactericidal activity. On the other hand, coatings that included immobilized molecules containing D-GL13K peptides, that is D-GL13K and VCD coatings, exhibited both a decrease in the thickness of the biofilm in comparison to eTi surfaces and bactericidal activity against the bacteria that remained on the surface, as shown in the CLSM images.

**Figure 5.8.** SEM micrographs of the disrupted bacteria (yellow arrows) found in the surfaces containing D-GL13K peptides. Scale bar = 2  $\mu\text{m}$ .

SEM micrographs (**Figure 5.7b, c**) confirmed the strong antibiofilm activity of the immobilized D-GL13K peptide coatings against oral microcosm biofilms, either alone (D-GL13K coating) or via the VC polypeptide (VCD coating). The presence of the D-enantiomeric form of the GL13K peptide in the coatings prevented the formation of a mature biofilm and provoked cell wall damage in bacteria that remained on the surfaces (**Figure 5.8**). A continuous microcosm biofilm was formed on both eTi and GVC surfaces, but the biofilm was thinner on GVC coatings than on eTi surfaces (**Figure 5.7**). However, there were no significant differences in either metabolic activity (luminescence intensity) or DNA content between the bacteria remaining on the eTi surfaces and the GVC coatings (**Figure 5.9**). GVC is a full L-amino acid polypeptide due to its





**Figure 5.9.** Antibiofilm activity of the coatings against oral microcosm biofilms after incubation in the DFBR for 6 days. Metabolic activity and DNA quantification demonstrated the strong and significant antibiofilm activity of the coatings compared with eTi control.

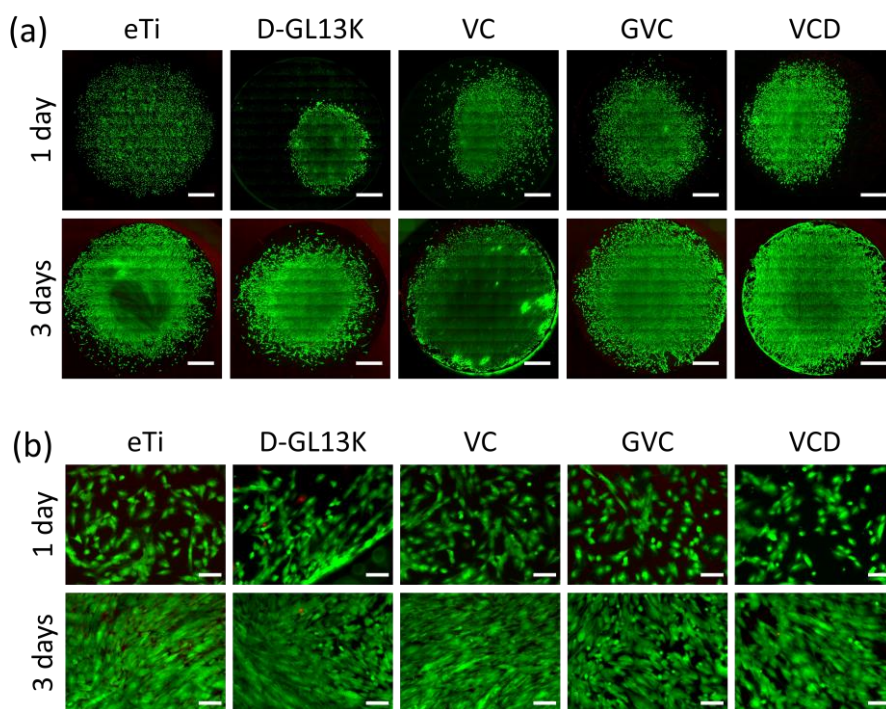
recombinant synthesis. Recently, it has been demonstrated that the L-enantiomer of the GL13K peptide is less potent against Gram (+), Gram (-) bacteria and bacterial microcosms,<sup>[210,216]</sup> and more sensitive to bacterial proteases, than the D-enantiomer.<sup>[159]</sup> In this regard, despite the antibiofilm potency of GVC against *S. gordonii* biofilms, its antimicrobial activity was limited to impeding surface colonization and formation of a biofilm with a more complex microbiota. In contrast, the presence of the D-enantiomer of the GL13K peptide in the coatings inhibited biofilm formation by more than 96% in terms of metabolic activity compared to eTi surfaces, irrespective of the manner of presentation of these D-GL13K peptides. Total DNA quantification provided an estimation of the total number of bacteria remaining on the surface. In comparison with the eTi control, D-GL13K and VCD coatings caused a significant reduction in the total remaining bacteria (a decrease of 65% and 70%, respectively). This demonstrates the efficacy of VCD coatings in the prevention of complex



oral biofilm growth under dynamic conditions. Consequently, these results suggest the potential application of ELRs as multivalent platforms for AMPs in the development of ECM-mimicking coatings for indwelling devices.

### 5.2.5. Cytocompatibility of the antimicrobial coatings

The antibiofilm coatings described here will potentially be used in dental applications. As such, it was of interest to assess their cytocompatibility with mammalian cells, more specifically with those present in the oral cavity. We therefore evaluated the viability of primary human gingival fibroblasts (HGFs) cultured on coated Ti discs, in comparison with the uncoated eTi.



**Figure 5.10.** HGFs on the Ti surfaces with LIVE/DEAD staining after incubation for 1 and 3 days. (a) Composite images of whole Ti discs (scale bar = 1 mm) and (b) magnified pictures of specific fields (scale bar = 100  $\mu$ m), showing living (green) and dead (red) cells.

LIVE/DEAD results showed that the HGFs cultured on Ti discs covered with the different peptides and ELRs were near 100% viable and proliferated appropriately during culture for up to 3 days in culture (**Figure 5.10**). This is in agreement with previous findings regarding the cyto- and biocompatibility of ELRs and the low toxicity of the GL13K peptide.<sup>[117,216,345]</sup> Overall, these results indicate that the antimicrobial coatings can likely to be safe for dental applications.

### **5.3. Conclusions**

We have designed an engineered molecular platform for AMPs based on a low-fouling ELR for the development of antibiofilm and cytocompatible coatings on titanium that can prevent IAIs. We have also demonstrated that hybrid coatings based on VCD paralleled the strong antimicrobial activity of D-GL13K coatings against both *S. gordonii* and oral microcosm biofilms when tested using challenging dynamic biofilm culturing conditions and, hence, their potential use as multivalent coatings. Molecular systems that combine AMPs with recombinant polypeptides may enable the development of safe multifunctional coatings for implants and other materials used in regenerative medical applications.

### **5.4. Experimental section**

#### *5.4.1. AMP/ELR/AMP-ELRs synthesis*

All the ELRs in this work (**Table 5.1**) were based on the polycationic polypeptide VC. VC, used as a negative control, and the hybrid ELR, which contained the L-enantiomer of GL13K (GVC), were recombinantly produced in *E. coli* BLR(DE3) as described elsewhere.<sup>[340]</sup> For production of the hybrid ELR containing D-enantiomers of the GK13K (VCD), the lysine side chains of VC were chemically modified using click chemistry

(SPAAC) with the designer D-peptide, as previously reported by Gonzalez de Torre et al. <sup>[5]</sup> and represented schematically in **Figure 5.1**.

First, approximately four amine groups on VC were modified with cyclooctyne (**Figure A5.1** and **A5.2**), then an average of three D-GL13K peptides were linked to each VC-cyclooctyne molecule via a click reaction (**Figure A5.3**). D-GL13K functionalized with an azide group at its N-terminus (N<sub>3</sub>-Gkiiklkaskll-NH<sub>2</sub>) was purchased from Pepscan (the Netherlands) with a purity >90%. D-GL13K peptide (Gkiiklkaskll-NH<sub>2</sub>), used as a positive control, was synthesized by AAPPTec, LLC (USA) with a purity >98%.

#### 5.4.2. *Covalent functionalization of titanium surfaces*

Immobilization of the AMP/ELR/AMP-ELRs onto titanium surfaces was performed using organosilanes as covalent linkers. As shown in Figure 2, Ti discs (six mm diameter) were fabricated from commercially pure (C.P.) titanium grade II sheets (McMaster-Carr<sup>®</sup>, US). These discs were polished and alkaline etched (16 h, 5 M NaOH, 60 °C), then the etched Ti (eTi) discs were washed with distilled water for 30 min (3 times) and modified with two different organosilanes, depending on the molecule to be immobilized. (3-Chloropropyl)triethoxysilane (CPTES) was used to tether D-GL13K peptides via their amine functional groups, as described elsewhere.<sup>[287]</sup> ELRs were tethered in an oriented manner via their C-terminal Cys-Cys motif using 3-aminopropyltriethoxysilane (APTES) and the bifunctional linker sulfosuccinimidyl 4-(N-maleimidomethyl) cyclohexane-1-carboxylate (sulfo-SMCC). Thus, eTi discs were immersed in an anhydrous ethanol solution of APTES (5%) at 60°C for 2 h. After that, samples were rinsed and ultrasonicated in ethanol, distilled water, isopropanol and acetone (to remove physisorbed molecules), then dried

under N<sub>2</sub>. Sulfo-SMCC was utilized to introduce the maleimide groups. Thus, APTES modified discs were immersed in a 1 mg mL<sup>-1</sup> sulfo-SMCC solution (dissolved in sodium phosphate buffer (PB, pH 7.2)) at room temperature (RT) for 1 h, then rinsed and ultrasonicated in PB. Finally, the maleimide-modified Ti discs (SMCC) were immersed in ELR solutions (0.2 mM in PB, pH 7.2) at 4 °C for 16 h. Samples were subsequently washed with ultrapure water in triplicate, dried under N<sub>2</sub> gas, sterilized with UV light (30 min per side) and stored at -80°C until further use.

#### *5.4.3. Physicochemical characterization of the coatings*

Ti discs functionalized with peptide/polypeptides, and discs obtained from intermediate modification steps, were characterized to assess the effectiveness of the modification by evaluating of the wettability of the surfaces measuring the water contact angle (WCA), and through the quantification of the elemental composition using X-ray Photoelectron Spectroscopy (XPS), as described below.

##### *Water Contact Angle*

Dynamic water contact angle measurements were determined using the sessile drop technique and a DM-CE1 instrument (Kyowa Interface Science, Japan). At least six 2- $\mu$ L drops of ultrapure water were analyzed. All images were collected at 100 ms after deposition of the drop and every second for 100 seconds. The left and right angles for each drop were averaged.

##### *X-ray photoelectron spectroscopy*

A PHI 5000 VersaProbe III (ULVAC, Inc., Japan) X-ray photoelectron spectrometer equipped with a monochromatic Al K $\alpha$  X-ray source (45°, 1486.6 eV, 50 W, sampling area; 200- $\mu$ m diameter) was used

to measure elemental composition. Survey spectra were collected using a pass energy of 280 eV and a step size of 1.0 eV. At least five different samples were analyzed per group.

#### 5.4.4. Mechanical and thermal stability of the coatings

Covalently coated Ti discs were ultrasonicated for 2 h in ultrapure water to test their mechanical stability in aqueous solvent. These discs were then incubated in phosphate buffered saline solution (PBS, pH 7.4) at 37 °C for 2 weeks. The stability of the coatings was checked by XPS and WCA after ultrasonication for 2 h and after incubation for one week and two weeks in PBS at 37 °C.

#### 5.4.5. Oral biofilms culture

Monospecies biofilms (*S. gordonii* DL-1) were grown on Ti discs coated with the polypeptides and the GL13K peptide; eTi discs were used as negative control. Biofilms were formed following a two stage method: **1) Inoculation/static stage:** coated Ti discs and controls were inoculated by adding 2 mL of a  $10^7$  CFU  $\text{mL}^{-1}$  bacterial inoculum from an overnight culture in Bacto Todd-Hewitt broth (THB; BD Biosciences, USA) at 37 °C. Incubation during this stage was performed under static conditions in a 24-well plate for 4 h at 37 °C; **2) Growth/dynamic stage:** discs were then transferred to a DFBR (Biosurface Technologies Corp., USA) and incubated for 48 h at 37 °C with a constant drip flow of  $0.3 \text{ mL min}^{-1}$  of THB medium. In order to mimic the oral cavity conditions that the implant coatings are likely to experience, the drip flow rate was selected from the low end of the unstimulated salivary flow rate,  $0.1\text{--}2 \text{ mL min}^{-1}$ .<sup>[346]</sup> The salivary flow rate at the gingival sulcus, where the implant would be located, is expected to be much lower than in the open areas in the oral cavity. At

the end of the experiment, Ti discs were carefully rinsed with 0.9% NaCl solution to remove unattached and loosely attached bacteria.

Oral microcosm biofilms were produced using the 769-NS model collected and characterized by Rudney *et al.*<sup>[347]</sup> At least 103 different taxons were identified within this biofilm model, which was produced from samples of whole saliva and plaque from a child at high risk of caries. Saliva samples were collected directly from the researcher who performed the experiments (healthy male, aged between 26 and 30 years, no periodontal disease) following established protocols, clarified by centrifugation and filtered through a 0.2- $\mu\text{m}$  filter.<sup>[348]</sup> A two-stage method was again used for biofilm formation: **1) Inoculation/static stage:** coated Ti discs and controls were first pre-incubated in filtered saliva for 10 min at RT in a 48-well plate. Then, 10  $\mu\text{L}$  of 769-NS glycerol stock was added to 20 mL of basal mucin medium (BMM), which is a complex medium used for the study of oral microcosm models,<sup>[342,347,349]</sup> and the discs were inoculated under static conditions at 37 °C for 24 h. **2) Growth/dynamic stage:** discs were transferred to the DFBR and incubated at 37 °C for 6 days with a drip flow of 0.3 mL min<sup>-1</sup> of BMM. Finally, the discs were gently rinsed with 0.9% NaCl solution, in a similar manner to the one-strain biofilm model.

#### *5.4.6. Antibiofilm potency: CFU, ATP and DNA quantification*

For quantification of the antibiofilm potency of the coatings, the biofilms formed on the Ti discs were collected by ultrasonication in 330 or 660  $\mu\text{L}$  of 0.9% NaCl solution, at 4 °C for monospecies *S. gordonii* or microcosm biofilms, respectively. Subsequently, 100  $\mu\text{L}$  of the bacterial extract was incubated for 2 hours at 37 °C in order to reactivate the metabolic activity of the bacteria, then the ATP was measured using the BacTiter-Glo™ Microbial Cell Viability Assay kit (Promega, USA), which

gives a luminescent signal in the presence of ATP. To that end, the bacteria solution was mixed with 100  $\mu\text{L}$  of the kit solution in a white 96-well plate and incubated for 5 min in the dark. Luminescence was subsequently measured in a micro-plate luminometer (BioTek, USA).

*S. gordonii* biofilms were evaluated by CFU counting. Thus, serial dilutions of the sonicated extract were performed in 0.9% NaCl solution at 4 °C, and 10  $\mu\text{L}$  of each dilution were plated on THB agar plates. Agar plates were incubated at 37 °C for 16 h, then the CFUs were counted. Oral microcosm biofilm model 769-NS contains at least 103 taxa and, in consequence, control of the incubation conditions in the agar plates for a thorough and reliable CFU count was not possible due to the different nutritional requirements and incubation time of the different strains. Alternatively, after microcosm biofilm sample collection, 500  $\mu\text{L}$  of bacterial extract was used for DNA extraction and purification using the MasterPure™ DNA Purification kit (Epicentre, Illumina, Inc., USA). The DNA concentration was then quantified using a Nanodrop 2000c spectrophotometer (ThermoFisher Scientific, USA).

#### 5.4.7. Bacterial viability assay

After incubation, the biofilms were stained with the FilmTracer™ LIVE/DEAD™ Biofilm Viability kit (ThermoFisher Scientific, USA) and analyzed by CLSM with a multiphoton confocal microscope (A1R-HD, Nikon Instruments Inc., Japan). A 25X water immersion objective (Apo LWD, 1.1 NA) was used to directly visualize the biofilms in 0.9% NaCl solution without a cover glass. Fluorescence emissions were collected at 488 nm for Syto9 (living cells) and at 561 nm for propidium iodide (dead cells). A 1024 x 1024 pixels ( $0.12 \mu\text{m px}^{-1}$ ) area was scanned, and the Z-stacks were recorded every 0.375  $\mu\text{m}$ . Images were analyzed using the NIS-Elements



Advanced Research analysis software (version 4.5, Nikon Corporation, Japan).

#### *5.4.8. Scanning electron microscopy*

After gentle removal of unattached bacteria, biofilms formed under static or dynamic conditions were fixed as described elsewhere.<sup>[350]</sup> First, the biofilms on Ti discs were incubated in a primary fixation solution (2% glutaraldehyde and 0.15% Alcian blue in 0.1 M sodium cacodylate buffer, pH 7.4), for 60 min at RT. Then, after washing the discs in 0.1 M sodium cacodylate buffer for 5 min at RT, the biofilms were treated with a secondary fixation solution (1% OsO<sub>4</sub> in 0.1 M sodium cacodylate buffer) for 60 min at RT, washed and dehydrated using ethanol solutions with increasing concentration (50%, 70%, 80%, 95% and 100%), critical point dried (Tousimis Samdi -780, USA) and coated with a 50 Å platinum layer. Finally, SEM images were recorded using a JEOL 6500 (JEOL USA, Inc., USA) field-emission gun scanning electron microscope (FEG-SEM).

#### *5.4.9. Cytocompatibility assay*

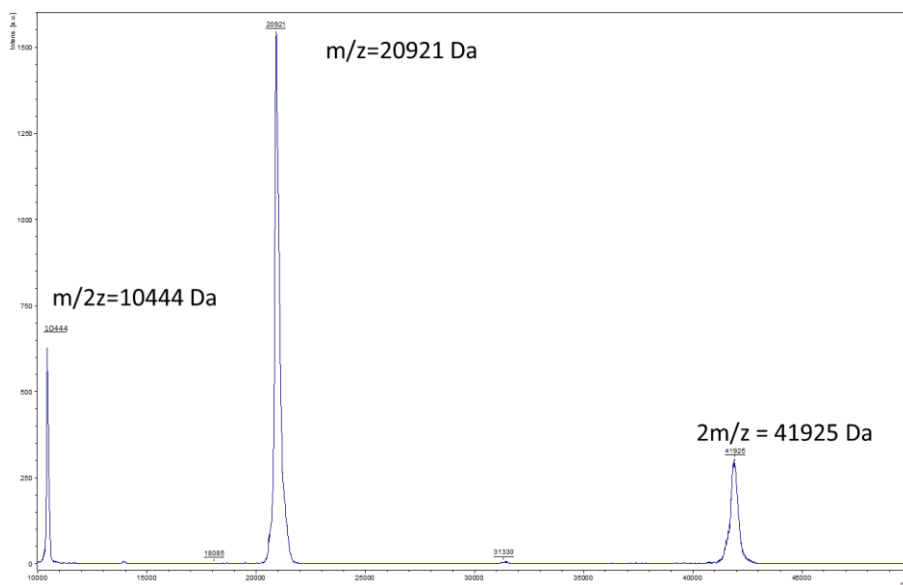
Human primary gingival fibroblasts (HGFs; PCS-201-018, ATCC, USA) were used to assess the cytocompatibility of the coated Ti discs. Cells were cultured for expansion in Fibroblast Basal Medium (PCS-201-030, ATCC, USA) supplemented accordingly (PCS-201-041, ATCC, USA), with no phenol red or antibiotics, at 37 °C, 5% CO<sub>2</sub>. Subsequently, cells were harvested and seeded on top of the Ti discs (6 mm diameter), previously placed in 24-well plates, at 20,000 cells cm<sup>-2</sup> (5655 cells per disc) in a 15-μL drop. Samples were then incubated at 37 °C for 3 h to allow cell attachment, and an excess of medium was added for further culture. After 1 and 3 days, samples were stained with the LIVE/DEAD<sup>®</sup> kit (ThermoFisher Scientific,

USA) following the manufacturer's instructions, and visualized upside-down with an inverted fluorescence microscope (Nikon Eclipse Ti-E coupled to a Nikon DS-2MBWc digital camera, Nikon Corporation, Japan) to confirm cell viability on the different coated Ti discs. Images were acquired and processed using the NIS-Elements Advanced Research software (version 4.5, Nikon Corporation, Japan).

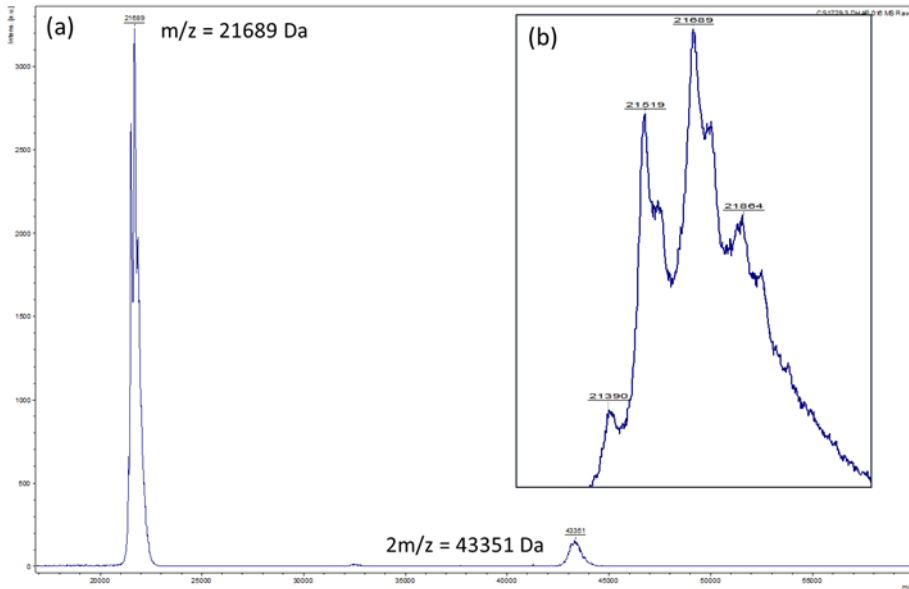
#### 5.4.10. *Statistical analysis*

A one-way analysis of variance (ANOVA) table with post-hoc Dunn's multiple comparison test was used to assess statistically significant differences between groups. A  $p$ -value of less than 0.05 was considered to be statistically significant (\*\*  $p < 0.001$ , \*  $p < 0.05$ ). Results are shown as mean  $\pm$  standard deviation (SD) ( $n \geq 3$ ).

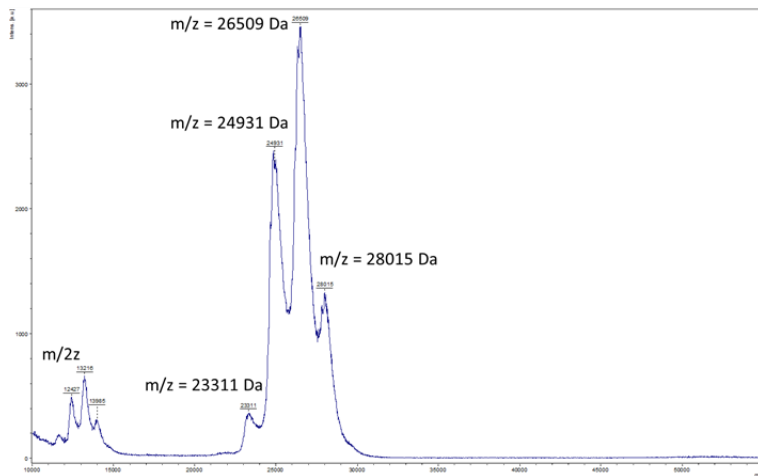
## 5.5. Appendix



**Figure A5.1.** MALDI-TOF spectrum of the VC polypeptide.

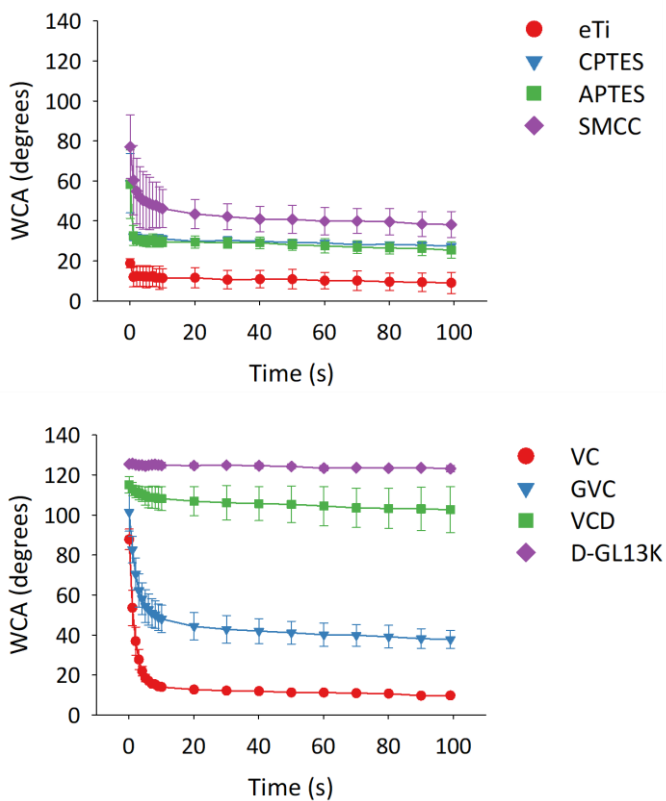


**Figure A5.2.** MALDI-TOF spectrum of the VC polypeptide after the modification of the Lys side-chains with the cyclooctyne groups. It revealed that 4 amine groups were modified per molecule with a Gaussian distribution. (b) shows the magnification of the  $m/z$  peak.

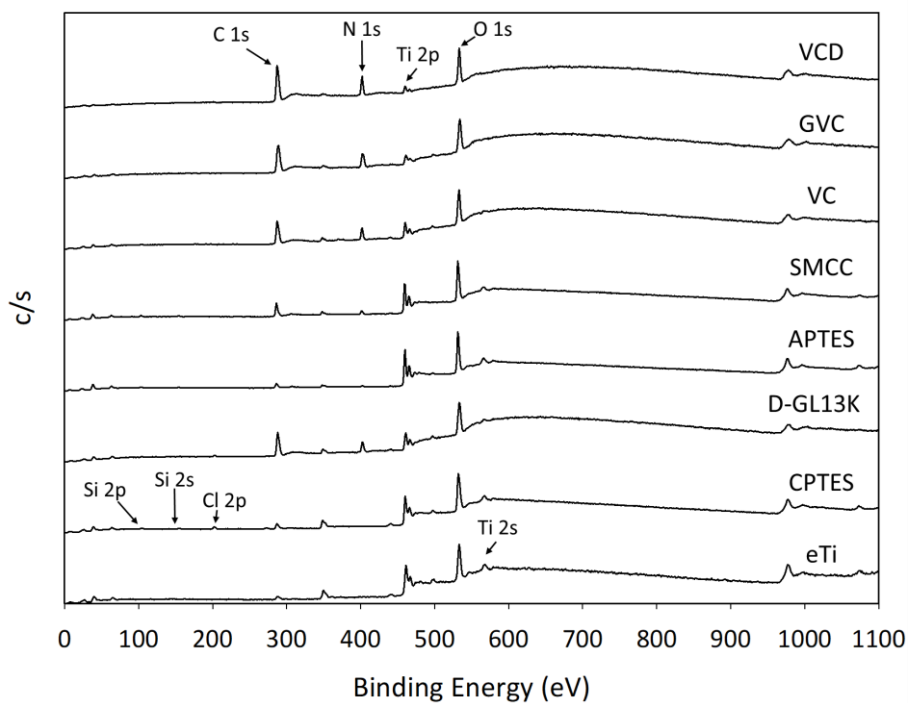


**Figure S5.3.** MALDI-TOF spectrum of the VCD polypeptide after the modification with D-GL13K-N<sub>3</sub> (H-Gkiiklkaslkll-N<sub>3</sub>, MW=1507.1 Da). An average of three D-GL13K peptides were incorporated per molecule with a Gaussian distribution.

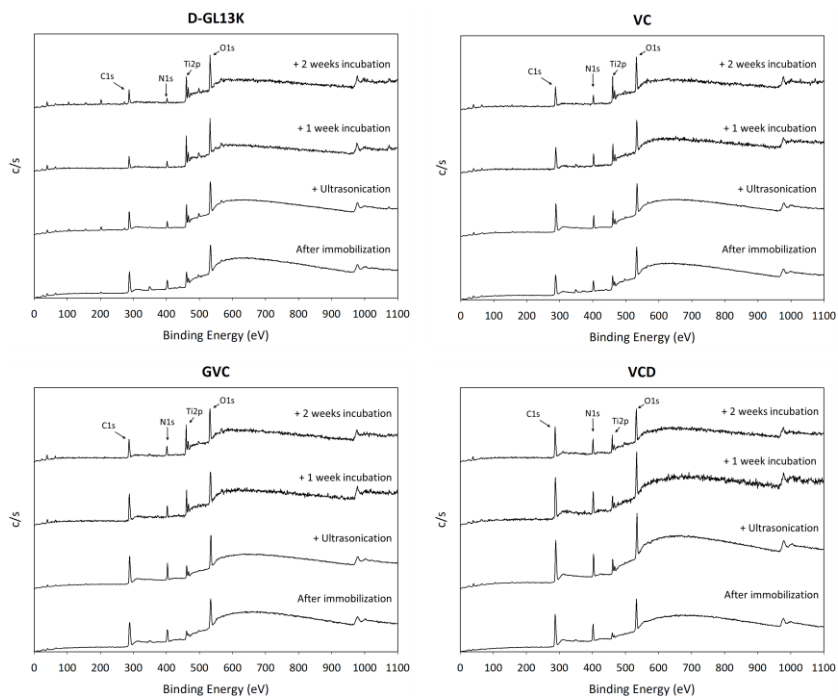




**Figure A5.4.** Dynamic WCA profile of the Ti surfaces after the different modification steps during the AMP/ELR/AMP-ELR coating fabrication.



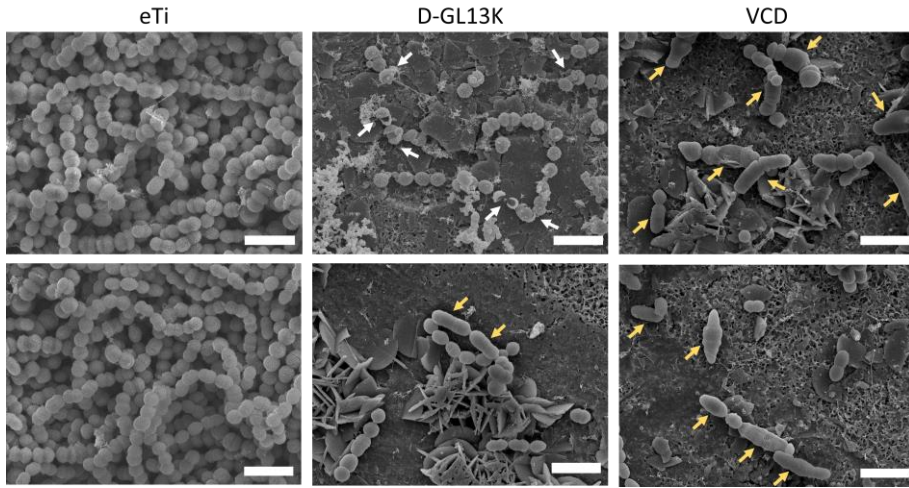
**Figure A5.5.** Representative XPS spectra of the surfaces after the diverse modification steps during the AMP/ELR/AMP-ELR coatings fabrication.



**Figure A5.6.** Representative XPS spectra of the Ti surfaces after the AMP/ELR immobilization and after the stability tests: ultrasonication in ultrapure water for 2 h and incubation in PBS at 37 °C for 1 and 2 weeks.

**Table A5.1.** Evolution of the C/Ti atomic ratio of the AMP/ELR/AMP-ELR coatings after the stability tests: ultrasonication in ultrapure water for 2 h and incubation in PBS at 37 °C for 1 and 2 weeks.

	C / Ti			
	After immobilization	After ultrasonication	After 1 week incubation	After 2 weeks incubation
D-GL13K	9.51	6.42	5.77	5.38
VC	20.66	8.41	4.34	5.34
GVC	21.37	14.14	6.95	5.13
VCD	22.50	18.06	8.27	10.22



**Figure A5.810.** SEM micrographs of the morphology of the streptococci that remained on the D-GL13K and VCD coatings after the incubation in the DFBR, compared with the eTi. Scale bar = 2  $\mu\text{m}$ . White arrows indicate cracked bacteria while elongated bacteria are indicated by yellow arrows.





# Chapter VI

---

Conclusions

---



## 6.1. Genetic engineering, biosynthesis and characterization of ELRs

In this thesis, it has been shown the successful development of several ELRs with modular design. Taking advantage of their recombinant nature, protein polymers with different building blocks have been produced. In Chapter 2, a library of amphiphilic ELRs with diblock design was biosynthesized to study the influence of charge distribution in the self-assembly of IDPPs. In Chapter 3 and 4, we engineered a novel design for the effective recombinant production of hybrid polypeptides based on AMP and ELRs. The incorporation of a sacrificial block enabled the production of hybrid AMP-ELRs avoiding toxicity to the heterologous host. In addition, it allowed the subsequent release without introducing any amino acid residue to the AMP-domain, that may affect its biological properties.

Gene construction was achieved and evaluated by agarose gel electrophoresis and DNA sequencing. ELRs or AMP-ELRs were further hyperexpressed in *Escherichia coli* as heterologous proteins and purification processes by inverse transition cycling leded yields from 220 to 600 mg per L of culture medium. Recombinant expression and ITC allowed to obtain highly pure and monodisperse products. Physico-chemical characterization (SDS-PAGE, MALDI-TOF and HPLC) confirmed the purity and the precise control over the composition of the distinct polypeptides.

Finally, in Chapter 5, we have also demonstrated that the versatility of the ELRs can be exploited for the chemical conjugation of bioactive peptides to explore new designs that cannot be achieved by recombinant

synthesis. In this way, D enantiomer of an AMP was bioconjugated to an ELR through SPCC.

## **6.2. Charge distribution as molecular modulator of nanostructuration in ELRs**

In Chapter 2, we have demonstrated that charge distribution plays a key role in the supramolecular assembly of IDPPs, by the study of ELdcRs as molecular model.

TEM and DLS characterization determined that high charge density in diblock designs contributed to stabilize micellar assemblies at low concentrations, in spite of highly unbalanced designs (hydrophilic hydrophobic block length ratio  $< 0.3$ ).

In contrast, electrostatic repulsion was the driving force that triggered the formation of higher-order assemblies in concentrations above  $125 \mu\text{M}$ , and the length of the charged hydrophilic blocks modulated the aggregation. Electrostatic repulsion between charged residues in the corona destabilized the micellar assemblies to favor the formation of micellar aggregates and collar-like structures. Additionally, it contributed to drive liquid-gel phase transition at higher concentrations ( $2.5 \text{ mM}$ ).

In summary, charge distribution seems to be a strong modulator of the nanostructuration at different length scales. It affected the hierarchical assembly of ELdcRs and phase separation. Thus, we have demonstrated that the presence of charges enables to reach alternative assemblies that may be used for the design of self-assembled devices for tissue engineering or drug delivery applications. This work set the basis not only for the rational design of hierarchically self-assembled devices based on ELdcRs, but also contributes to shed light in the complex structure-function

relationship of IDPs and the parameters that control the phase transition and hence, the formation of biomolecular condensates.

### **6.3. Dual self-assembly of genetically engineered protein polymers: the interplay between AMPs and ELRs**

In Chapter 3, the use of AMPs as self-assembled domains for the hierarchical assembly of protein polymers have been demonstrated. Two hybrid polypeptides with modular design were recombinantly produced based on amphiphilic diblock ELR and the AMPs GL13K and 1018.

The thermal behavior evaluation suggested that AMP aggregation temperature contributed to the phase transition, decreasing  $T_i$  and enhancing thermal hysteresis.

The AMPs induced self-assembly into nanofibers of the hybrid polypeptides below the  $T_i$ , whereas they led the formation of fibrillar aggregates above the  $T_i$ . Depending on the AMP, diverse molecular architectures could be achieved. Moreover, the hybrid nanosystems also retained thermo-sensitiveness of the ELRs, thus demonstrating that a dual self-assembly can be thermally triggered.

The dynamic interplay between AMPs and ELRs in the formation of stimuli-responsive nanostructures opens up opportunities that range from the scalable production of AMPs to the design of advanced self-assembling nanomaterials which recapitulate the properties of AMPs with ELRs.

## **6.4. Development of self-assembled monolayers with antibiofilm activity based on AMPs and ELRs**

Chapter 4 showed the covalent tethering of AMP/ELR/AMP-ELRs onto surfaces. The incorporation of a Cys-based motif into the C-terminus allowed the formation of self-assembled monolayers onto model gold surfaces.

The immobilization of ELRs onto gold surfaces provided a low-fouling effect that permitted to reduce the biofilm formation of two staphylococcal strains of medical relevance: *S. aureus* and *S. gordonii*. Additionally, when the hybrid AMP-ELR was tethered, low-fouling activity of the ELR and the antimicrobial effect of the AMP converged synergistically, thus enhancing the antibiofilm potential of the coating.

Cell viability assays showed excellent cytocompatibility of the coatings, which highlights their potential as safe coatings to prevent the biofilm formation onto biomedical devices.

## **6.5. Biofabrication of antibiofilm coatings based on AMP-ELRs to prevent implant-associated infections**

Finally, in Chapter 5, we have successfully biofabricated coatings based on hybrid AMP-ELRs on titanium surfaces through chemoselective bonding with organosilanes.

Hybrid coatings containing the D-GL13K peptide retained the antibiofilm potential of the AMP against two oral biofilm models under dynamic conditions. Additionally, cytocompatibility assays confirmed that the toxicity of the coatings did not compromise host cells behavior.

Therefore, we demonstrated that tethering AMPs onto biomaterial surfaces using ELRs as multivalent linkers is a reliable method that may be used to incorporate additional biofunctionalities by recombinant synthesis and enhance the biological response of the antibiofilm coatings.





# Chapter VII

---

References

---



- 
- [1] J. C. Rodríguez-Cabello, L. Martín, M. Alonso, F. J. Arias, A. M. Testera, *Polymer (Guildf)*. **2009**, *50*, 5159.
- [2] J. C. Rodríguez-Cabello, A. Girotti, A. Ribeiro, F. J. Arias, *Methods Mol. Biol.* **2012**, *811*, 17.
- [3] A. Girotti, Desarrollo de Una Plataforma Biotecnológica Para La Obtención de Polímeros Recombinantes Tipo Elastina, **2007**.
- [4] P. Goffin, P. Dehottay, *Genome Announc.* **2017**, *5*, DOI 10.1128/genomeA.00441-17.
- [5] I. González De Torre, M. Santos, L. Quintanilla, A. Testera, M. Alonso, J. C. Rodríguez Cabello, *Acta Biomater.* **2014**, *10*, 2495.
- [6] U. K. Laemmli, *Nature* **1970**, *227*, 680.
- [7] A. Micsonai, F. Wien, L. Kernya, Y.-H. Lee, Y. Goto, M. Réfrégiers, J. Kardos, *Proc. Natl. Acad. Sci. U. S. A.* **2015**, *112*, E3095.
- [8] A. Micsonai, F. Wien, É. Bulyáki, J. Kun, É. Moussong, Y.-H. Lee, Y. Goto, M. Réfrégiers, J. Kardos, *Nucleic Acids Res.* **2018**, *46*, W315.
- [9] M. Rodahl, F. Höök, C. Fredriksson, C. A. Keller, A. Krozer, P. Brzezinski, M. Voinova, B. Kasemo, *Faraday Discuss.* **1997**, *107*, 229.
- [10] M. Rodahl, B. Kasemo, *Sensors Actuators A Phys.* **1996**, *54*, 448.
- [11] G. Dantzig, *Computing* **1990**, 88.
- [12] I. Wiegand, K. Hilpert, R. E. W. Hancock, *Nat. Protoc.* **2008**, *3*, 163.
- [13] E. R. Fischer, B. T. Hansen, V. Nair, F. H. Hoyt, D. W. Dorward, in *Curr. Protoc. Microbiol.*, John Wiley & Sons, Inc., Hoboken, NJ, USA, **2012**, p. Unit 2B.2.
- [14] J. H. Merritt, D. E. Kadouri, G. A. O'Toole, *Curr. Protoc. Microbiol.* **2005**, *Chapter 1*, Unit 1B.1.
- [15] A. Ibáñez-Fonseca, T. Flora, S. Acosta, J. C. Rodríguez-Cabello, *Matrix Biol.* **2019**, DOI 10.1016/j.matbio.2019.07.003.
- [16] J. Despanie, J. P. Dhandhukia, S. F. Hamm-Alvarez, J. A. MacKay, *J. Control. Release* **2016**, *240*, 93.
- [17] H. Vindin, S. M. Mithieux, A. S. Weiss, *Matrix Biol.* **2019**, DOI 10.1016/j.matbio.2019.07.005.
- [18] C. Spezzacatena, T. Perri, V. Guantieri, L. B. Sandberg, T. F. Mitts, A. M. Tamburro, *European J. Org. Chem.* **2002**, *2002*, 95.
- [19] J. C. Rodríguez-Cabello, M. Alonso, T. Pérez, M. M. Herguedas, *Biopolymers* **2000**, *54*, 282.

- [20] Z. Peng, J. Yan, X. Fan, M. J. Mizianty, B. Xue, K. Wang, G. Hu, V. N. Uversky, L. Kurgan, *Cell. Mol. Life Sci.* **2015**, 72, 137.
- [21] V. N. Uversky, *Chem. Rev.* **2014**, 114, 6557.
- [22] E. Fischer, *Berichte der Dtsch. Chem. Gesellschaft* **1894**, 27, 2985.
- [23] P. Ehrlich, *Klin. Jahrb.* **1897**, 6, 299.
- [24] P. E. Wright, H. J. Dyson, *J. Mol. Biol.* **1999**, 293, 321.
- [25] A. K. Dunker, J. D. Lawson, C. J. Brown, R. M. Williams, P. Romero, J. S. Oh, C. J. Oldfield, A. M. Campen, C. M. Ratliff, K. W. Hipps, J. Ausio, M. S. Nissen, R. Reeves, C. Kang, C. R. Kissinger, R. W. Bailey, M. D. Griswold, W. Chiu, E. C. Garner, Z. Obradovic, *J. Mol. Graph. Model.* **2001**, 19, 26.
- [26] K. K. Turoverov, I. M. Kuznetsova, V. N. Uversky, *Prog. Biophys. Mol. Biol.* **2010**, 102, 73.
- [27] S. Roberts, M. Dzuricky, A. Chilkoti, *FEBS Lett.* **2015**, 589, 2477.
- [28] S. F. Banani, H. O. Lee, A. A. Hyman, M. K. Rosen, *Nat. Rev. Mol. Cell Biol.* **2017**, 18, 285.
- [29] L. D. Muiznieks, S. Sharpe, R. Pomès, F. W. Keeley, *J. Mol. Biol.* **2018**, 430, 4741.
- [30] K. M. Ruff, S. Roberts, A. Chilkoti, R. V. Pappu, *J. Mol. Biol.* **2018**, 430, 4619.
- [31] M. Fuxreiter, P. Tompa, *Fuzziness: Structural Disorder in Protein Complexes*, **2012**.
- [32] D. W. Urry, *Faraday Discuss. Chem. Soc.* **1976**, 61, 205.
- [33] J. R. McDaniel, D. C. Radford, A. Chilkoti, *Biomacromolecules* **2013**, 14, 2866.
- [34] A. M. Tamburro, V. Guantieri, A. Scopa, J. M. Drabble, *Chirality* **1991**, 3, 318.
- [35] L. D. Muiznieks, A. S. Weiss\*, **2007**, DOI 10.1021/BI700139K.
- [36] L. D. Muiznieks, A. S. Weiss, F. W. Keeley, *Biochem. Cell Biol.* **2010**, 88, 239.
- [37] S. Rauscher, R. Pomès, *Elife* **2017**, 6, DOI 10.7554/eLife.26526.
- [38] L. D. Muiznieks, A. S. Weiss, F. W. Keeley, in *Biochem. Cell Biol.*, **2010**, pp. 239–250.
- [39] D. E. Meyer, A. Chilkoti, *Biomacromolecules* **2004**, 5, 846.
- [40] A. Ribeiro, F. J. Arias, J. Reguera, M. Alonso, J. C. Rodríguez-Cabello, *Biophys. J.* **2009**, 97, 312.

- [41] T. Yamaoka, T. Tamura, Y. Seto, T. Tada, S. Kunugi, D. A. Tirrell, **2003**, DOI 10.1021/bm034120l.
- [42] C. Nicolini, R. Ravindra, B. Ludolph, R. Winter, *Biophys. J.* **2004**, *86*, 1385.
- [43] J. A. MacKay, D. J. Callahan, K. N. FitzGerald, A. Chilkoti, *Biomacromolecules* **2010**, *11*, 2873.
- [44] Y. Cho, Y. Zhang, T. Christensen, L. B. Sagle, A. Chilkoti, P. S. Cremer, *J. Phys. Chem. B* **2008**, *112*, 13765.
- [45] G. Pinedo-Martín, E. Castro, L. Martín, M. Alonso, J. C. Rodríguez-Cabello, *Langmuir* **2014**, *30*, 3432.
- [46] L. Ferreira, J. Cole, C. Reichardt, N. Holland, V. Uversky, B. Zaslavsky, *Int. J. Mol. Sci.* **2015**, *16*, 13528.
- [47] J. C. Rodríguez-Cabello, A. Girotti, A. Ribeiro, F. J. Arias, in *Methods Mol. Biol.*, **2012**, pp. 17–38.
- [48] R. E. Sallach, V. P. Conticello, E. L. Chaikof, *Biotechnol. Prog.* **2009**, NA.
- [49] R. W. Herzog, N. K. Singh, D. W. Urry, H. Daniell, *Appl. Microbiol. Biotechnol.* **1997**, *47*, 368.
- [50] A. J. Conley, J. J. Joensuu, A. M. Jevnikar, R. Menassa, J. E. Brandle, *Biotechnol. Bioeng.* **2009**, *103*, 562.
- [51] D. E. Meyer, K. Trabbic-Carlson, A. Chilkoti, *Biotechnol. Prog.* **2001**, *17*, 720.
- [52] R. E. Sallach, W. Cui, F. Balderrama, A. W. Martinez, J. Wen, C. A. Haller, J. V. Taylor, E. R. Wright, R. C. Long, E. L. Chaikof, *Biomaterials* **2010**, *31*, 779.
- [53] J. L. Schaal, X. Li, E. Mastria, J. Bhattacharyya, M. R. Zalutsky, A. Chilkoti, W. Liu, *J. Control. Release* **2016**, DOI 10.1016/j.jconrel.2016.02.040.
- [54] T. A. T. Lee, A. Cooper, R. P. Apkarian, V. P. Conticello, *Adv. Mater.* **2000**, *12*, 1105.
- [55] W. Hassounch, E. B. Zhulina, A. Chilkoti, M. Rubinstein, *Macromolecules* **2015**, *48*, 4183.
- [56] M. R. Dreher, A. J. Simnick, K. Fischer, R. J. Smith, A. Patel, M. Schmidt, A. Chilkoti, *J. Am. Chem. Soc.* **2008**, *130*, 687.
- [57] K. Widder, S. R. MacEwan, E. Garanger, V. Núñez, S. Lecommandoux, A. Chilkoti, D. Hinderberger, *Soft Matter* **2017**, *13*, 1816.
- [58] S. M. Janib, M. Pastuszka, S. Aluri, Z. Folchman-Wagner, P.-Y. Hsueh, P. Shi, Yi-An, H. Cui, J. A. Mackay, *Polym. Chem.* **2014**, *5*, 1614.
- [59] X. Duan, Y. Li, *Small* **2013**, *9*, 1521.

- [60] M. Zhu, S. Perrett, G. Nie, *Small* **2013**, *9*, 1619.
- [61] S. R. MacEwan, I. Weitzhandler, I. Hoffmann, J. Genzer, M. Gradzielski, A. Chilkoti, *Biomacromolecules* **2017**, *18*, 599.
- [62] L. Martín, E. Castro, A. Ribeiro, M. Alonso, J. C. Rodríguez-Cabello, *Biomacromolecules* **2012**, *13*, 293.
- [63] T. Luo, M. A. David, L. C. Dunshee, R. A. Scott, M. A. Urello, C. Price, K. L. Kiick, *Biomacromolecules* **2017**, *18*, 2539.
- [64] E. G. Roberts, N. Rim, W. Huang, A. Tarakanova, J. Yeo, M. J. Buehler, D. L. Kaplan, J. Y. Wong, *Macromol. Biosci.* **2018**, *18*, 1800265.
- [65] A. Fernández-Colino, F. J. Arias, M. Alonso, J. C. Rodríguez-Cabello, *Biomacromolecules* **2014**, *15*, 3781.
- [66] I. Weitzhandler, M. Dzuricky, I. Hoffmann, F. Garcia Quiroz, M. Gradzielski, A. Chilkoti, *Biomacromolecules* **2017**, *18*, 2419.
- [67] J. R. McDaniel, I. Weitzhandler, S. Prevost, K. B. Vargo, M. S. Appavou, D. A. Hammer, M. Gradzielski, A. Chilkoti, *Nano Lett.* **2014**, *14*, 6590.
- [68] S. R. Aluri, P. Shi, J. A. Gustafson, W. Wang, Y.-A. Lin, H. Cui, S. Liu, P. S. Conti, Z. Li, P. Hu, A. L. Epstein, J. A. MacKay, *ACS Nano* **2014**, *8*, 2064.
- [69] A. C. Rincón, I. T. Molina-Martinez, B. de las Heras, M. Alonso, C. Bañez, J. C. Rodríguez-Cabello, R. Herrero-Vanrell, *J. Biomed. Mater. Res. Part A* **2006**, *78A*, 343.
- [70] M. Shah, P. Y. Hsueh, G. Sun, H. Chang, S. M. Janib, J. A. MacKay, *Protein Sci.* **2012**, *21*, 743.
- [71] J. A. MacKay, M. Chen, J. R. McDaniel, W. Liu, A. J. Simnick, A. Chilkoti, *Nat. Mater.* **2009**, *8*, 993.
- [72] P. Zhao, S. Dong, J. Bhattacharyya, M. Chen, *Mol. Pharm.* **2014**, *11*, 2703.
- [73] P. Zhao, G. Xia, S. Dong, Z.-X. Jiang, M. Chen, *Biomaterials* **2016**, *93*, 1.
- [74] A. J. Simnick, M. Amiram, W. Liu, G. Hanna, M. W. Dewhirst, C. D. Kontos, A. Chilkoti, *J. Control. Release* **2011**, *155*, 144.
- [75] S. A. Costa, D. Mozhdghi, M. J. Dzuricky, F. J. Isaacs, E. M. Brustad, A. Chilkoti, *Nano Lett.* **2019**, *19*, 247.
- [76] V. Sarangthem, Y. Kim, T. D. Singh, B.-Y. Seo, S.-H. Cheon, Y.-J. Lee, B.-H. Lee, R.-W. Park, *Theranostics* **2016**, *6*, 2235.
- [77] M. T. Manzari, G. R. Anderson, K. H. Lin, R. S. Soderquist, M. Çakir, M. Zhang, C. E. Moore, R. N. Skelton, M. Fèvre, X. Li, J. J. Bellucci, S. E. Wardell, S. A. Costa, K. C. Wood, A. Chilkoti, *Sci. Adv.* **2019**, *5*, eaaw9162.

- [78] J. S. Ryu, D. Raucher, *Cancer Lett.* **2014**, *348*, 177.
- [79] J. S. Ryu, L. Robinson, D. Raucher, *J. Chemother.* **2019**, *31*, 23.
- [80] A. Weinberger, V. Walter, S. R. MacEwan, T. Schmatko, P. Muller, A. P. Schroder, A. Chilkoti, C. M. Marques, *Sci. Rep.* **2017**, *7*, 43963.
- [81] P. Zhao, D. Atanackovic, S. Dong, H. Yagita, X. He, M. Chen, *Mol. Pharm.* **2017**, *14*, 1494.
- [82] M. Amiram, K. M. Luginbuhl, X. Li, M. N. Feinglos, A. Chilkoti, *J. Control. Release* **2013**, *172*, 144.
- [83] P. Koria, H. Yagi, Y. Kitagawa, Z. Megeed, Y. Nahmias, R. Sheridan, M. L. Yarmush, *Proc. Natl. Acad. Sci.* **2011**, *108*, 1034.
- [84] Y. Assal, Y. Mizuguchi, M. Mie, E. Kobatake, *Bioconjug. Chem.* **2015**, *26*, 1672.
- [85] C. García-Arévalo, J. F. Bermejo-Martín, L. Rico, V. Iglesias, L. Martín, J. C. Rodríguez-Cabello, F. J. Arias, *Mol. Pharm.* **2013**, *10*, 586.
- [86] F. J. O'Brien, B. A. Harley, I. V. Yannas, L. J. Gibson, *Biomaterials* **2005**, *26*, 433.
- [87] S. R. Peyton, A. J. Putnam, *J. Cell. Physiol.* **2005**, *204*, 198.
- [88] S. Khetan, M. Guvendiren, W. R. Legant, D. M. Cohen, C. S. Chen, J. A. Burdick, *Nat. Mater.* **2013**, *12*, 458.
- [89] R. L. DiMarco, D. R. Hunt, R. E. Dewi, S. C. Heilshorn, *Biomaterials* **2017**, DOI 10.1016/j.biomaterials.2017.03.023.
- [90] M. G. Haugh, T. J. Vaughan, C. M. Madl, R. M. Raftery, L. M. Mcnamara, F. J. O'Brien, S. C. Heilshorn, **2018**, DOI 10.1016/j.biomaterials.2018.04.026.
- [91] Y. Shin, Y.-C. Chang, D. S. W. Lee, J. Berry, D. W. Sanders, P. Ronceray, N. S. Wingreen, M. Haataja, C. P. Brangwynne, *Cell* **2018**, *175*, 1481.
- [92] J. Park, J. Y. Kim, S.-K. Choi, J. Y. Kim, J. H. Kim, W. B. Jeon, J. E. Lee, *Nanomedicine Nanotechnology, Biol. Med.* **2017**, *13*, 1853.
- [93] S. M. Staubli, G. Cerino, I. Gonzalez De Torre, M. Alonso, D. Oertli, F. Eckstein, K. Glatz, J. C. Rodríguez Cabello, A. Marsano, *Biomaterials* **2017**, DOI 10.1016/j.biomaterials.2017.04.047.
- [94] D. J. Coletta, A. Ibáñez-Fonseca, L. R. Missana, M. V Jammal, E. J. Vitelli, M. Aimone, F. Zabalza, J. P. M. Issa, M. Alonso, J. C. Rodríguez-Cabello, S. Feldman, *Tissue Eng. Part A* **2017**, *23*, 1361.
- [95] L. Cai, C. B. Dinh, S. C. Heilshorn, *Biomater. Sci.* **2014**, *2*, 757.

- [96] T. Flora, I. G. de Torre, M. Alonso, J. C. Rodríguez-Cabello, *J. Mater. Sci. Mater. Med.* **2019**, *30*, 30.
- [97] K. S. Straley, S. C. Heilshorn, *Adv. Mater.* **2009**, *21*, 4148.
- [98] T. Flora, I. González de Torre, M. Alonso, J. C. Rodríguez-Cabello, *Biofabrication* **2019**, *11*, 035008.
- [99] C. M. Madl, B. L. LeSavage, R. E. Dewi, C. B. Dinh, R. S. Stowers, M. Khariton, K. J. Lampe, D. Nguyen, O. Chaudhuri, A. Enejder, S. C. Heilshorn, *Nat. Mater.* **2017**, *16*, 1233.
- [100] C. M. Madl, B. L. LeSavage, R. E. Dewi, K. J. Lampe, S. C. Heilshorn, *Adv. Sci.* **2019**, *6*, 1801716.
- [101] B. Gurumurthy, J. A. Griggs, A. V. Janorkar, *J. Mech. Behav. Biomed. Mater.* **2018**, DOI 10.1016/j.jmbbm.2018.04.019.
- [102] S. S. Amruthwar, A. V. Janorkar, *Dent. Mater.* **2013**, *29*, 211.
- [103] J. M. Caves, W. Cui, J. Wen, V. A. Kumar, C. A. Haller, E. L. Chaikof, *Biomaterials* **2011**, *32*, 5371.
- [104] J. M. Caves, V. A. Kumar, A. W. Martinez, J. Kim, C. M. Ripberger, C. A. Haller, E. L. Chaikof, *Biomaterials* **2010**, *31*, 7175.
- [105] I. Gonzalez de Torre, M. Weber, L. Quintanilla, M. Alonso, S. Jockenhoewel, J. C. Rodríguez Cabello, P. Mela, *Biomater. Sci.* **2016**, *4*, 1361.
- [106] K. E. Inostroza-Brito, E. Collin, O. Siton-Mendelson, K. H. Smith, A. Monge-Marcet, D. S. Ferreira, R. P. Rodríguez, M. Alonso, J. C. Rodríguez-Cabello, R. L. Reis, F. Sagués, L. Botto, R. Bitton, H. S. Azevedo, A. Mata, *Nat. Chem.* **2015**, *7*, 897.
- [107] D. Zhu, H. Wang, P. Trinh, S. C. Heilshorn, F. Yang, *Biomaterials* **2017**, *127*, 132.
- [108] H. Wang, D. Zhu, A. Paul, L. Cai, A. Enejder, F. Yang, S. C. Heilshorn, *Adv. Funct. Mater.* **2017**, *27*, 1605609.
- [109] E. Shirzaei Sani, R. Portillo-Lara, A. Spencer, W. Yu, B. M. Geilich, I. Noshadi, T. J. Webster, N. Annabi, *ACS Biomater. Sci. Eng.* **2018**, *4*, 2528.
- [110] J. S. Barbosa, A. Ribeiro, A. M. Testera, M. Alonso, F. J. Arias, J. C. Rodríguez-Cabello, J. F. Mano, *Adv. Eng. Mater.* **2010**, *12*, B37.
- [111] H. Wang, L. Cai, A. Paul, A. Enejder, S. C. Heilshorn, *Biomacromolecules* **2014**, *15*, 3421.
- [112] E. Meco, K. J. Lampe, *Biomacromolecules* **2019**, *20*, 1914.
- [113] E. R. Wright, R. A. McMillan, A. Cooper, R. P. Apkarian, V. P. Conticello, *Adv. Funct. Mater.* **2002**, *12*, 149.



- [114] A. Fernández-Colino, F. J. Arias, M. Alonso, J. C. Rodríguez-Cabello, *Biomacromolecules* **2015**, *16*, 3389.
- [115] A. Fernández-Colino, F. J. Arias, M. Alonso, J. Carlos Rodríguez-Cabello, *Biomacromolecules* **2014**, *15*, 3781.
- [116] S. Roberts, T. S. Harmon, J. L. Schaal, V. Miao, K. Li, A. Hunt, Y. Wen, T. G. Oas, J. H. Collier, R. V. Pappu, A. Chilkoti, *Nat. Mater.* **2018**, *17*, 1154.
- [117] A. Ibáñez-Fonseca, T. L. Ramos, I. González de Torre, L. I. Sánchez-Abarca, S. Muntión, F. J. Arias, M. C. del Cañizo, M. Alonso, F. Sánchez-Guijo, J. C. Rodríguez-Cabello, *J. Tissue Eng. Regen. Med.* **2018**, *12*, e1450.
- [118] D. Asai, D. Xu, W. Liu, F. Garcia Quiroz, D. J. Callahan, M. R. Zalutsky, S. L. Craig, A. Chilkoti, *Biomaterials* **2012**, *33*, 5451.
- [119] D. Asai, T. Kanamoto, M. Takenaga, H. Nakashima, *Acta Biomater.* **2017**, DOI 10.1016/j.actbio.2017.10.024.
- [120] Y.-N. Zhang, R. K. Avery, Q. Vallmajo-Martin, A. Assmann, A. Vegh, A. Memic, B. D. Olsen, N. Annabi, A. Khademhosseini, *Adv. Funct. Mater.* **2015**, *25*, 4814.
- [121] M. Putzu, F. Causa, V. Nele, I. G. de Torre, J. C. Rodríguez-Cabello, P. A. Netti, *Biofabrication* **2016**, *8*, 045009.
- [122] I. González de Torre, A. Ibáñez-Fonseca, L. Quintanilla, M. Alonso, J.-C. Rodríguez-Cabello, *Acta Biomater.* **2018**, *72*, 137.
- [123] A. Fernández-Colino, F. Wolf, S. Rütten, J. C. Rodríguez-Cabello, S. Jockenhoevel, P. Mela, *Macromol. Biosci.* **2018**, *18*, 1800147.
- [124] L. Martín, M. Alonso, A. Girotti, F. J. Arias, J. C. Rodríguez-Cabello, *Biomacromolecules* **2009**, *10*, 3015.
- [125] A. Fernández-Colino, F. Wolf, H. Keijdener, S. Rütten, T. Schmitz-Rode, S. Jockenhoevel, J. C. Rodríguez-Cabello, P. Mela, *Mater. Sci. Eng. C* **2018**, DOI 10.1016/j.msec.2018.03.013.
- [126] R. R. Costa, C. A. Custódio, A. M. Testera, F. J. Arias, J. C. Rodríguez-Cabello, N. M. Alves, J. F. Mano, *Adv. Funct. Mater.* **2009**, *19*, 3210.
- [127] M. Swierczewska, C. S. Hajicharalambous, A. V. Janorkar, Z. Megeed, M. L. Yarmush, P. Rajagopalan, *Acta Biomater.* **2008**, *4*, 827.
- [128] K. A. Woodhouse, P. Klement, V. Chen, M. B. Gorbet, F. W. Keeley, R. Stahl, J. D. Fromstein, C. M. Bellingham, *Biomaterials* **2004**, *25*, 4543.
- [129] S. W. Jordan, C. A. Haller, R. E. Sallach, R. P. Apkarian, S. R. Hanson, E. L. Chaikof, *Biomaterials* **2007**, *28*, 1191.
- [130] D. W. Urry, T. M. Parker, M. C. Reid, D. C. Gowda, *J. Bioact. Compat. Polym.*

- 1991, 6, 263.
- [131] E. Salvagni, G. Berguig, E. Engel, J. C. Rodríguez-Cabello, G. Coullerez, M. Textor, J. A. Planell, F. J. Gil, C. Aparicio, *Colloids Surfaces B Biointerfaces* **2014**, 114, 225.
- [132] G. K. Srivastava, L. Martín, A. K. Singh, I. Fernandez-Bueno, M. J. Gayoso, M. T. Garcia-Gutierrez, A. Girotti, M. Alonso, J. C. Rodríguez-Cabello, J. C. Pastor, *J. Biomed. Mater. Res. - Part A* **2011**, 97 A, 243.
- [133] A. K. Singh, G. K. Srivastava, L. Martín, M. Alonso, J. C. Pastor, *J. Biomed. Mater. Res. - Part A* **2014**, 102, 639.
- [134] M. Pierna, M. Santos, F. J. Arias, M. Alonso, J. C. Rodríguez-Cabello, *Biomacromolecules* **2013**, 14, 1893.
- [135] L. Li, C.-K. Mo, A. Chilkoti, G. P. Lopez, N. J. Carroll, *Biointerphases* **2016**, 11, 021009.
- [136] T. Flora, I. G. de Torre, L. Quintanilla, M. Alonso, J. C. Rodríguez-Cabello, *Eur. Polym. J.* **2018**, 106, 19.
- [137] Y. Li, X. Chen, A. J. Ribeiro, E. D. Jensen, K. V. Holmberg, J. C. Rodríguez-Cabello, C. Aparicio, *Adv. Healthc. Mater.* **2014**, 3, 1638.
- [138] G. Ciofani, G. G. Genchi, I. Liakos, A. Athanassiou, V. Mattoli, A. Bandiera, *Acta Biomater.* **2013**, 9, 5111.
- [139] *WHO* **2019**.
- [140] A. C. Singer, H. Shaw, V. Rhodes, A. Hart, *Front. Microbiol.* **2016**, 7, DOI 10.3389/fmicb.2016.01728.
- [141] R. E. W. Hancock, H. G. Sahl, *Nat. Biotechnol.* **2006**, 24, 1551.
- [142] J. P. Bradshaw, *BioDrugs* **2003**, 17, 233.
- [143] G. Wang, Ed. , *Antimicrobial Peptides - Discovery, Design and Novel Therapeutic Strategies*, CABI, **2017**.
- [144] K. A. Brogden, *Nat. Rev. Microbiol.* **2005**, 3, 238.
- [145] C.-F. Le, C.-M. Fang, S. D. Sekaran, *Antimicrob. Agents Chemother.* **2017**, 61, e02340.
- [146] M. Scocchi, M. Mardirossian, G. Runti, M. Benincasa, *Curr. Top. Med. Chem.* **2016**, 16, 76.
- [147] C. de la Fuente-Núñez, M. H. Cardoso, E. de Souza Cândido, O. L. Franco, R. E. W. Hancock, *Biochim. Biophys. Acta - Biomembr.* **2016**, 1858, 1061.
- [148] K. A. Brogden, *Nat. Rev. Microbiol.* **2005**, 3, 238.

- [149] M. Marxer, V. Vollenweider, P. Schmid-Hempel, *Philos. Trans. R. Soc. B Biol. Sci.* **2016**, *371*, 20150302.
- [150] A. Ahmed, G. Siman-Tov, G. Hall, N. Bhalla, A. Narayanan, *Viruses* **2019**, *11*, DOI 10.3390/v11080704.
- [151] N. Delattin, K. De Brucker, K. De Cremer, B. P.A. Cammue, K. Thevissen, *Curr. Top. Med. Chem.* **2017**, *17*, 604.
- [152] D. Gaspar, A. S. Veiga, M. A. R. B. Castanho, *Front. Microbiol.* **2013**, *4*, 294.
- [153] R. E. W. Hancock, E. F. Haney, E. E. Gill, *Nat. Rev. Immunol.* **2016**, *16*, 321.
- [154] X. Kang, F. Dong, C. Shi, S. Liu, J. Sun, J. Chen, H. Li, H. Xu, X. Lao, H. Zheng, *Sci. Data* **2019**, *6*, 148.
- [155] D. M. Rothstein, P. Spacciopoli, L. T. Tran, T. Xu, F. D. Roberts, M. D. Serra, D. K. Buxton, F. G. Oppenheim, P. Friden, *Antimicrob. Agents Chemother.* **2001**, *45*, 1367.
- [156] ‡ Manhong Wu, § Elke Maier, § and Roland Benz, ‡ Robert E. W. Hancock\*, **1999**, DOI 10.1021/BI9826299.
- [157] M. Xiong, Y. Bao, X. Xu, H. Wang, Z. Han, Z. Wang, Y. Liu, S. Huang, Z. Song, J. Chen, R. M. Peek, L. Yin, L.-F. Chen, J. Cheng, *Proc. Natl. Acad. Sci. U. S. A.* **2017**, *114*, 12675.
- [158] J. Mondal, *Drug Dev. Res.* **2019**, *80*, 28.
- [159] H. Hirt, J. W. Hall, E. Larson, S.-U. Gorr, *PLoS One* **2018**, *13*, e0194900.
- [160] T. L. Raguse, E. A. Porter, B. Weisblum, S. H. Gellman, *J. Am. Chem. Soc.* **2002**, *124*, 12774.
- [161] D. Knappe, P. Henklein, R. Hoffmann, K. Hilpert, *Antimicrob. Agents Chemother.* **2010**, *54*, 4003.
- [162] J. H. Nickling, T. Baumann, F.-J. Schmitt, M. Bartholomae, O. P. Kuipers, T. Friedrich, N. Budisa, *J. Vis. Exp.* **2018**, DOI 10.3791/57551.
- [163] A. Wang, Y. Su, S. Wang, M. Shen, F. Chen, M. Chen, X. Ran, T. Cheng, J. Wang, *Appl. Microbiol. Biotechnol.* **2010**, *87*, 1935.
- [164] S. Tomisawa, Y. Sato, M. Kamiya, Y. Kumaki, T. Kikukawa, K. Kawano, M. Demura, K. Nakamura, T. Ayabe, T. Aizawa, *Protein Expr. Purif.* **2015**, *112*, 21.
- [165] M. E. Pachón-Ibáñez, Y. Smani, J. Pachón, J. Sánchez-Céspedes, *FEMS Microbiol. Rev.* **2017**, *41*, 323.
- [166] E. Holaskova, P. Galuszka, I. Frebort, M. T. Oz, *Biotechnol. Adv.* **2015**, *33*, 1005.

- [167] R. Sinha, P. Shukla, *Protein Pept. Lett.* **2019**, *26*, 79.
- [168] H. Mohammad, S. Thangamani, M. Seleem, *Curr. Pharm. Des.* **2015**, *21*, 2073.
- [169] T. Takahashi, R. L. Gallo, *Dermatol. Clin.* **2017**, *35*, 39.
- [170] A. Pfalzgraff, K. Brandenburg, G. Weindl, *Front. Pharmacol.* **2018**, *9*, 281.
- [171] M. L. Mangoni, A. M. McDermott, M. Zasloff, *Exp. Dermatol.* **2016**, *25*, 167.
- [172] S. C. Mansour, C. de la Fuente-Núñez, R. E. W. Hancock, *J. Pept. Sci.* **2015**, *21*, 323.
- [173] R. Ramos, J. P. Silva, A. C. Rodrigues, R. Costa, L. Guardão, F. Schmitt, R. Soares, M. Vilanova, L. Domingues, M. Gama, *Peptides* **2011**, *32*, 1469.
- [174] A. J. Duplantier, M. L. van Hoek, *Front. Immunol.* **2013**, *4*, 143.
- [175] M. F. Mohamed, A. Abdelkhalek, M. N. Seleem, *Sci. Rep.* **2016**, *6*, 29707.
- [176] M. E. Stryjewski, H. F. Chambers, *Clin. Infect. Dis.* **2008**, *46*, S368.
- [177] H. Yan, R. E. Hancock, *Antimicrob. Agents Chemother.* **2001**, *45*, 1558.
- [178] G. Yu, D. Y. Baeder, R. R. Regoes, J. Rolff, *Antimicrob. Agents Chemother.* **2016**, *60*, 1717.
- [179] M. S. Zharkova, D. S. Orlov, O. Y. Golubeva, O. B. Chakchir, I. E. Eliseev, T. M. Grinchuk, O. V. Shamova, *Front. Cell. Infect. Microbiol.* **2019**, *9*, 128.
- [180] S. Nuding, T. Frasch, M. Schaller, E. F. Stange, L. T. Zabel, *Antimicrob. Agents Chemother.* **2014**, *58*, 5719.
- [181] Y. Zhang, Y. Liu, Y. Sun, Q. Liu, X. Wang, Z. Li, J. Hao, *Curr. Microbiol.* **2014**, *68*, 685.
- [182] S. Ruden, K. Hilpert, M. Berditsch, P. Wadhvani, A. S. Ulrich, *Antimicrob. Agents Chemother.* **2009**, *53*, 3538.
- [183] I. Pal, D. Bhattacharyya, R. K. Kar, D. Zarena, A. Bhunia, H. S. Atreya, *Sci. Rep.* **2019**, *9*, 4485.
- [184] H. Sun, Y. Hong, Y. Xi, Y. Zou, J. Gao, J. Du, *Biomacromolecules* **2018**, *19*, 1701.
- [185] U. Rajchakit, V. Sarojini, *Bioconj. Chem.* **2017**, *28*, 2673.
- [186] A. Reinhardt, I. Neundorff, *Int. J. Mol. Sci.* **2016**, *17*, DOI 10.3390/ijms17050701.
- [187] C. J. Arnusch, R. J. Pieters, E. Breukink, *PLoS One* **2012**, *7*, e39768.

- [188] S. Bera, G. G. Zhanel, F. Schweizer, *Carbohydr. Res.* **2011**, *346*, 560.
- [189] M. M. Konai, C. Ghosh, V. Yarlagadda, S. Samaddar, J. Haldar, *J. Med. Chem.* **2014**, *57*, 9409.
- [190] H. Lee, S. I. Lim, S.-H. Shin, Y. Lim, J. W. Koh, S. Yang, *ACS omega* **2019**, *4*, 15694.
- [191] C. J. Arnusch, H. Ulm, M. Josten, Y. Shadkchan, N. Osherov, H.-G. Sahl, Y. Shai, *Antimicrob. Agents Chemother.* **2012**, *56*, 1.
- [192] C. J. Morris, K. Beck, M. A. Fox, D. Ulaeto, G. C. Clark, M. Gumbleton, *Antimicrob. Agents Chemother.* **2012**, *56*, 3298.
- [193] A. Rai, S. Pinto, M. B. Evangelista, H. Gil, S. Kallip, M. G. S. Ferreira, L. Ferreira, *Acta Biomater.* **2016**, *33*, 64.
- [194] W.-Y. Chen, H.-Y. Chang, J.-K. Lu, Y.-C. Huang, S. G. Harroun, Y.-T. Tseng, Y.-J. Li, C.-C. Huang, H.-T. Chang, *Adv. Funct. Mater.* **2015**, *25*, 7189.
- [195] B. Lee, J. Park, M. Ryu, S. Kim, M. Joo, J.-H. Yeom, S. Kim, Y. Park, K. Lee, J. Bae, *Sci. Rep.* **2017**, *7*, 13572.
- [196] J.-H. Yeom, B. Lee, D. Kim, J. Lee, S. Kim, J. Bae, Y. Park, K. Lee, *Biomaterials* **2016**, *104*, 43.
- [197] M. Comune, A. Rai, K. K. Chereddy, S. Pinto, S. Aday, A. F. Ferreira, A. Zonari, J. Blersch, R. Cunha, R. Rodrigues, J. Lerma, P. N. Simões, V. Préat, L. Ferreira, *J. Control. Release* **2017**, *262*, 58.
- [198] A. Rai, S. Pinto, T. R. Velho, A. F. Ferreira, C. Moita, U. Trivedi, M. Evangelista, M. Comune, K. P. Rumbaugh, P. N. Simões, L. Moita, L. Ferreira, *Biomaterials* **2016**, *85*, 99.
- [199] Z. Xie, N. V Aphale, T. D. Kadapure, A. S. Wadajkar, S. Orr, D. Gyawali, G. Qian, K. T. Nguyen, J. Yang, *J. Biomed. Mater. Res. A* **2015**, *103*, 3907.
- [200] S. C. Gomes, I. B. Leonor, J. F. Mano, R. L. Reis, D. L. Kaplan, *Biomaterials* **2011**, *32*, 4255.
- [201] H. E. Trueman, A. Sriskantha, Y. Qu, T. D. Rapson, T. D. Sutherland, *ACS Omega* **2017**, *2*, 4456.
- [202] A. Da Costa, R. Machado, A. Ribeiro, T. Collins, V. Thiagarajan, M. T. Neves-Petersen, J. C. Rodriguez-Cabello, A. C. Gomes, M. Casal, *Biomacromolecules* **2015**, *16*, DOI 10.1021/bm5016706.
- [203] A. da Costa, A. M. Pereira, A. C. Gomes, J. C. Rodriguez-Cabello, M. Casal, R. Machado, *N. Biotechnol.* **2018**, *46*, 45.
- [204] F. Hu, T. Ke, X. Li, P. H. Mao, X. Jin, F. L. Hui, X. D. Ma, L. X. Ma, *Appl. Biochem. Biotechnol.* **2010**, *160*, 2377.

- [205] K. Yang, Y. Su, J. Li, J. Sun, Y. Yang, *Protein Expr. Purif.* **2012**, *85*, 200.
- [206] D. A. Sousa, K. C. L. Mulder, K. S. Nobre, N. S. Parachin, O. L. Franco, *J. Biotechnol.* **2016**, *234*, 83.
- [207] R. Herrero-Vanrell, A. C. Rincón, M. Alonso, V. Reboto, I. T. Molina-Martinez, J. C. Rodríguez-Cabello, *J. Control. Release* **2005**, *102*, 113.
- [208] Y. Liu, Y. Yang, C. Wang, X. Zhao, *Nanoscale* **2013**, *5*, 6413.
- [209] R. Goel, C. Garg, H. K. Gautam, A. K. Sharma, P. Kumar, A. Gupta, *Int. J. Biol. Macromol.* **2018**, *111*, 880.
- [210] C. Ye, Zhou; Zhu, Xiao; Acosta, Sergio; Aparicio, *Nanoscale* **2019**, *11*, 266.
- [211] A. Baral, S. Roy, S. Ghosh, D. Hermida-Merino, I. W. Hamley, A. Banerjee, *Langmuir* **2016**, *32*, 1836.
- [212] L. Jiang, D. Xu, T. J. Sellati, H. Dong, *Nanoscale* **2015**, *7*, 19160.
- [213] A. S. Veiga, C. Sinthuvanich, D. Gaspar, H. G. Franquelim, M. A. R. B. Castanho, J. P. Schneider, *Biomaterials* **2012**, *33*, 8907.
- [214] N. Nandi, K. Gayen, S. Ghosh, D. Bhunia, S. Kirkham, S. K. Sen, S. Ghosh, I. W. Hamley, A. Banerjee, *Biomacromolecules* **2017**, *18*, 3621.
- [215] G. Manzo, M. A. Scorciapino, P. Wadhvani, J. Bürck, N. Pietro Montaldo, M. Pintus, R. Sanna, M. Casu, A. Giuliani, G. Pirri, V. Luca, A. S. Ulrich, A. C. Rinaldi, *PLoS One* **2015**, *10*, e0116379.
- [216] D. G. Moussa, J. A. Kirihara, Z. Ye, N. G. Fischer, J. Khot, B. A. Witthuhn, C. Aparicio, *J. Dent. Res.* **2019**, 002203451986377.
- [217] L. Lombardi, Y. Shi, A. Falanga, E. Galdiero, E. de Alteriis, G. Franci, I. Chourpa, H. S. Azevedo, S. Galdiero, *Biomacromolecules* **2019**, *20*, 1362.
- [218] E. F. Haney, B. (Catherine) Wu, K. Lee, A. L. Hilchie, R. E. W. Hancock, *Cell Chem. Biol.* **2017**, *24*, 969.
- [219] F. Costa, P. Gomes, M. C. L. Martins, *Pept. Proteins as Biomater. Tissue Regen. Repair* **2018**, 329.
- [220] H. J. Busscher, H. C. Van Der Mei, G. Subbiahdoss, P. C. Jutte, J. J. A. M. Van Den Dungen, S. A. J. Zaat, M. J. Schultz, D. W. Grainger, *Sci. Transl. Med.* **2012**, *4*, 153rv10.
- [221] H. Van Acker, P. Van Dijck, T. Coenye, *Trends Microbiol.* **2014**, *22*, 326.
- [222] M. Godoy-Gallardo, C. Mas-Moruno, M. C. Fernández-Calderón, C. Pérez-Giraldo, J. M. Manero, F. Albericio, F. J. Gil, D. Rodríguez, *Acta Biomater.* **2014**, *10*, 3522.
- [223] X. Chen, H. Hirt, Y. Li, S. U. Gorr, C. Aparicio, *PLoS One* **2014**, *9*, e111579.

- [224] F. M. T. A. Costa, S. R. Maia, P. A. C. Gomes, M. C. L. Martins, *Biomaterials* **2015**, *52*, 531.
- [225] X. Li, P. Li, R. Saravanan, A. Basu, B. Mishra, S. H. Lim, X. Su, P. A. Tambyah, S. S. J. Leong, *Acta Biomater.* **2014**, *10*, 258.
- [226] B. Mishra, A. Basu, R. R. Y. Chua, R. Saravanan, P. A. Tambyah, B. Ho, M. W. Chang, S. S. J. Leong, *J. Mater. Chem. B* **2014**, *2*, 1706.
- [227] G. Gao, D. Lange, K. Hilpert, J. Kindrachuk, Y. Zou, J. T. J. Cheng, M. Kazemzadeh-Narbat, K. Yu, R. Wang, S. K. Straus, D. E. Brooks, B. H. Chew, R. E. W. Hancock, J. N. Kizhakkedathu, *Biomaterials* **2011**, *32*, 3899.
- [228] R. T. C. Cleophas, J. Sjollema, H. J. Busscher, J. A. W. Kruijtzter, R. M. J. Liskamp, *Biomacromolecules* **2014**, *15*, 3390.
- [229] N. Shtreimer Kandiyote, T. Avisdris, C. J. Arnusch, R. Kasher, *Langmuir* **2019**, *35*, 1935.
- [230] M. Bagheri, M. Beyermann, M. Dathe, *Antimicrob. Agents Chemother.* **2009**, *53*, 1132.
- [231] Y. J. Yang, A. L. Holmberg, B. D. Olsen, *Annu. Rev. Chem. Biomol. Eng.* **2017**, *8*, 549.
- [232] D. W. Urry, T. L. Trapane, K. U. Prasad, *Biopolymers* **1985**, *24*, 2345.
- [233] N. K. Li, F. G. Quiroz, C. K. Hall, A. Chilkoti, Y. G. Yingling, *Biomacromolecules* **2014**, *15*, 3522.
- [234] M. Dzuricky, S. Roberts, A. Chilkoti, *Biochemistry* **2018**, *57*, 2405.
- [235] K. M. Ruff, S. Roberts, A. Chilkoti, R. V. Pappu, *J. Mol. Biol.* **2018**, *430*, 4619.
- [236] U. Midic, Z. Obradovic, *Proteome Sci.* **2012**, *10*, S19.
- [237] M. M. Babu, *Biochem. Soc. Trans.* **2016**, *44*, 1185.
- [238] S. Boeynaems, S. Alberti, N. L. Fawzi, T. Mittag, M. Polymenidou, F. Rousseau, J. Schymkowitz, J. Shorter, B. Wolozin, L. Van Den Bosch, P. Tompa, M. Fuxreiter, *Trends Cell Biol.* **2018**, *28*, 420.
- [239] A. A. Hyman, C. A. Weber, F. Jülicher, *Annu. Rev. Cell Dev. Biol.* **2014**, *30*, 39.
- [240] M. Kato, T. W. Han, S. Xie, K. Shi, X. Du, L. C. Wu, H. Mirzaei, E. J. Goldsmith, J. Longgood, J. Pei, N. V. Grishin, D. E. Frantz, J. W. Schneider, S. Chen, L. Li, M. R. Sawaya, D. Eisenberg, R. Tycko, S. L. McKnight, *Cell* **2012**, *149*, 753.
- [241] E. Boke, M. Ruer, M. Wühr, M. Coughlin, R. Lemaître, S. P. Gygi, S. Alberti, D. Drechsel, A. A. Hyman, T. J. Mitchison, *Cell* **2016**, *166*, 637.

- [242] V. N. Uversky, V. Davé, L. M. Iakoucheva, P. Malaney, S. J. Metallo, R. R. Pathak, A. C. Joerger, *Chem. Rev.* **2014**, *114*, 6844.
- [243] J. R. Simon, N. J. Carroll, M. Rubinstein, A. Chilkoti, G. P. López, *Nat. Chem.* **2017**, *9*, 509.
- [244] J. R. Simon, S. A. Eghtesadi, M. Dzuricky, L. You, A. Chilkoti, *Mol. Cell* **2019**, DOI 10.1016/j.molcel.2019.05.010.
- [245] V. N. Uversky, *Protein Sci.* **2013**, *22*, 693.
- [246] S. Müller-Späth, A. Soranno, V. Hirschfeld, H. Hofmann, S. Rügger, L. Reymond, D. Nettels, B. Schuler, *Proc. Natl. Acad. Sci. U. S. A.* **2010**, *107*, 14609.
- [247] R. K. Das, R. V. Pappu, *Proc. Natl. Acad. Sci.* **2013**, *110*, 13392.
- [248] J. R. McDaniel, S. R. Macewan, X. Li, D. C. Radford, C. D. Landon, M. Dewhirst, A. Chilkoti, *Nano Lett.* **2014**, *14*, 2890.
- [249] J. C. Rodríguez-Cabello, F. J. Arias, M. A. Rodrigo, A. Girotti, *Adv. Drug Deliv. Rev.* **2016**, *97*, 85.
- [250] M. H. Misbah, L. Quintanilla, M. Alonso, J. C. Rodríguez-Cabello, *Polymer (Guildf)*. **2015**, *81*, 37.
- [251] C. E. Mills, Z. Michaud, B. D. Olsen, *Biomacromolecules* **2018**, *19*, 2517.
- [252] M. C. Huber, A. Schreiber, P. von Olshausen, B. R. Varga, O. Kretz, B. Joch, S. Barnert, R. Schubert, S. Eimer, P. Kele, S. M. Schiller, *Nat. Mater.* **2015**, *14*, 125.
- [253] A. Schreiber, M. C. Huber, S. M. Schiller, *bioRxiv* **2018**, 463356.
- [254] A. Schreiber, L. G. Stühn, M. C. Huber, S. E. Geissinger, A. Rao, S. M. Schiller, *Small* **2019**, 1900163.
- [255] T. Yamaoka, T. Tamura, Y. Seto, T. Tada, S. Kunugi, D. A. Tirrell, **2003**, DOI 10.1021/bm034120l.
- [256] F. G. Quiroz, A. Chilkoti, *Nat. Mater.* **2015**, *14*, 1164.
- [257] C. T. Chung, S. L. Niemela, R. H. Miller, *Proc. Natl. Acad. Sci. U. S. A.* **1989**, *86*, 2172.
- [258] E. Gasteiger, C. Hoogland, A. Gattiker, S. Duvaud, M. R. Wilkins, R. D. Appel, A. Bairoch, in *Proteomics Protoc. Handb.*, Humana Press, Totowa, NJ, **2005**, pp. 571–607.
- [259] J. Kyte, R. F. Doolittle, *J. Mol. Biol.* **1982**, *157*, 105.
- [260] C. D. Fjell, J. A. Hiss, R. E. W. Hancock, G. Schneider, *Nat. Rev. Drug Discov.* **2012**, *11*, 37.



- [261] B. Bechinger, S.-U. Gorr, *J. Dent. Res.* **2017**, *96*, 254.
- [262] J. D. Hale, R. E. Hancock, <http://dx.doi.org/10.1586/14787210.5.6.951> **2014**, DOI 10.1586/14787210.5.6.951.
- [263] S. Morizane, K. Yamasaki, B. Mühleisen, P. F. Kotol, M. Murakami, Y. Aoyama, K. Iwatsuki, T. Hata, R. L. Gallo, *J. Invest. Dermatol.* **2012**, *132*, 135.
- [264] L. S. Biswaro, M. G. da Costa Sousa, T. M. B. Rezende, S. C. Dias, O. L. Franco, *Front. Microbiol.* **2018**, *9*, 855.
- [265] J. C. Rodríguez-Cabello, I. G. de Torre, S. Acosta, S. Salinas, M. Herrero, *Self-assembling Biomater.* **2018**, 49.
- [266] M. S. Bahniuk, A. K. Alshememry, S. V. Elgersma, L. D. Unsworth, *J. Nanobiotechnology* **2018**, *16*, 15.
- [267] Z. Luo, X. Zhao, S. Zhang, *PLoS One* **2008**, *3*, e2364.
- [268] M. Kuna, F. Mahdi, A. R. Chade, G. L. Bidwell, *Sci. Rep.* **2018**, *8*, 7923.
- [269] Z. Ye, C. Aparicio, *Nanoscale Adv.* **2019**, DOI 10.1039/C9NA00498J.
- [270] P. Shi, S. Aluri, Y. A. Lin, M. Shah, M. Edman, J. Dhandhukia, H. Cui, J. A. MacKay, *J. Control. Release* **2013**, *171*, 330.
- [271] G. M. Dickinson, A. L. Bisno, *Antimicrob. Agents Chemother.* **1989**, *33*, 602.
- [272] R. M. Donlan, *Curr. Top. Microbiol. Immunol.* **2008**, *322*, 133.
- [273] H. W. Boucher, G. H. Talbot, J. S. Bradley, J. E. Edwards, D. Gilbert, L. B. Rice, M. Scheld, B. Spellberg, J. Bartlett, *Clin. Infect. Dis.* **2009**, *48*, 1.
- [274] M. Otto, *Curr. Top. Microbiol. Immunol.* **2008**, *322*, 207.
- [275] L. M. Weiner, A. K. Webb, B. Limbago, M. A. Dudeck, J. Patel, A. J. Kallen, J. R. Edwards, D. M. Sievert, *Infect. Control Hosp. Epidemiol.* **2016**, *37*, 1288.
- [276] V. T. H. Pham, C. M. Bhadra, V. K. Truong, R. J. Crawford, E. P. Ivanova, in *Antibact. Surfaces*, Springer International Publishing, Cham, **2015**, pp. 89–111.
- [277] M. Cloutier, D. Mantovani, F. Rosei, *Trends Biotechnol.* **2015**, *33*, 637.
- [278] R. O. Darouiche, I. I. Raad, S. O. Heard, J. I. Thornby, O. C. Wenker, A. Gabrielli, J. Berg, N. Khardori, H. Hanna, R. Hachem, R. L. Harris, G. Mayhall, *N. Engl. J. Med.* **1999**, *340*, 1.
- [279] R. Kuehl, P. S. Brunetto, A.-K. Woischnig, M. Varisco, Z. Rajacic, J. Vosbeck, L. Terracciano, K. M. Fromm, N. Khanna, *Antimicrob. Agents Chemother.* **2016**, *60*, 2467.

- [280] M. J. McGuffie, J. Hong, J. H. Bahng, E. Glynos, P. F. Green, N. A. Kotov, J. G. Younger, J. S. VanEpps, *Nanomedicine Nanotechnology, Biol. Med.* **2016**, *12*, 33.
- [281] A. Jain, L. S. Duvvuri, S. Farah, N. Beyth, A. J. Domb, W. Khan, *Adv. Healthc. Mater.* **2014**, *3*, 1969.
- [282] P. S. Stewart, J. William Costerton, *Lancet* **2001**, *358*, 135.
- [283] A. D. Politano, K. T. Campbell, L. H. Rosenberger, R. G. Sawyer, *Surg. Infect. (Larchmt)*. **2013**, *14*, 8.
- [284] C. Hanley, J. Layne, A. Punnoose, K. M. Reddy, I. Coombs, A. Coombs, K. Feris, D. Wingett, *Nanotechnology* **2008**, *19*, 295103.
- [285] L. Timofeeva, N. Kleshcheva, *Appl. Microbiol. Biotechnol.* **2011**, *89*, 475.
- [286] L. Townsend, R. L. Williams, O. Anuforum, M. R. Berwick, F. Halstead, E. Hughes, A. Stamboulis, B. Oppenheim, J. Gough, L. Grover, R. A. H. Scott, M. Webber, A. F. A. Peacock, A. Belli, A. Logan, F. de Cogan, *J. R. Soc. Interface* **2017**, *14*, DOI 10.1098/rsif.2016.0657.
- [287] K. V. Holmberg, M. Abdolhosseini, Y. Li, X. Chen, S.-U. Gorr, C. Aparicio, *Acta Biomater.* **2013**, *9*, 8224.
- [288] K. Yu, J. C. Y. Lo, M. Yan, X. Yang, D. E. Brooks, R. E. W. Hancock, D. Lange, J. N. Kizhakkedathu, *Biomaterials* **2017**, *116*, 69.
- [289] R. Chen, N. Cole, M. D. P. Willcox, J. Park, R. Rasul, E. Carter, N. Kumar, *Biofouling* **2009**, *25*, 517.
- [290] P. Kumar, A. Takayesu, U. Abbasi, M. T. Kalathottukaren, S. Abbina, J. N. Kizhakkedathu, S. K. Straus, *ACS Appl. Mater. Interfaces* **2017**, *9*, 37575.
- [291] Q. Gao, M. Yu, Y. Su, M. Xie, X. Zhao, P. Li, P. X. Ma, *Acta Biomater.* **2017**, *51*, 112.
- [292] M. Gabriel, K. Nazmi, E. C. Veerman, A. V. N. Amerongen, A. Zentner, *Bioconjug. Chem.* **2006**, *17*, 548.
- [293] K. Glinel, A. M. Jonas, T. Jouenne, J. Leprince, L. Galas, W. T. S. Huck, *Bioconjug. Chem.* **2009**, *20*, 71.
- [294] N. Shtreimer Kandiyote, G. Mohanraj, C. Mao, R. Kasher, C. J. Arnusch, *Langmuir* **2018**, *34*, 11147.
- [295] A. K. Muszanska, E. T. J. Rochford, A. Gruszka, A. A. Bastian, H. J. Busscher, W. Norde, H. C. van der Mei, A. Herrmann, *Biomacromolecules* **2014**, *15*, 2019.
- [296] S. Atefyekta, M. Pihl, C. Lindsay, S. C. Heilshorn, M. Andersson, *Acta Biomater.* **2019**, *83*, 245.

- [297] P. Wadhvani, N. Heidenreich, B. Podeyn, J. Bürck, A. S. Ulrich, *Biomater. Sci.* **2017**, *5*, 817.
- [298] L. Andersson, L. Blomberg, M. Flegel, L. Lepsa, B. Nilsson, M. Verlander, *Biopolymers* **2000**, *55*, 227.
- [299] J. Krahulec, M. Hyršová, S. Pepeliaev, J. Jílková, Z. Černý, J. Machálková, *Appl. Microbiol. Biotechnol.* **2010**, *88*, 167.
- [300] B. Bommarius, H. Jenssen, M. Elliott, J. Kindrachuk, M. Pasupuleti, H. Gieren, K.-E. Jaeger, R. E. W. Hancock, D. Kalman, *Peptides* **2010**, *31*, 1957.
- [301] B. Srinivasulu, R. Syvitski, J. K. Seo, N. R. Mattatall, L. C. Knickle, S. E. Douglas, *Protein Expr. Purif.* **2008**, *61*, 36.
- [302] B. Bommarius, H. Jenssen, M. Elliott, J. Kindrachuk, M. Pasupuleti, H. Gieren, K.-E. Jaeger, R. E. W. Hancock, D. Kalman, *Peptides* **2010**, *31*, 1957.
- [303] W.-Y. Wu, C. Mee, F. Califano, R. Banki, D. W. Wood, *Nat. Protoc.* **2006**, *1*, 2257.
- [304] W. Hassounh, T. Christensen, A. Chilkoti, *Curr. Protoc. Protein Sci.* **2010**, *1*.
- [305] M. Pierna, M. Santos, F. J. Arias, M. Alonso, J. C. Rodríguez-Cabello, *Biomacromolecules* **2013**, *14*, 1893.
- [306] R. Chen, M. D. P. Willcox, N. Cole, K. K. K. Ho, R. Rasul, J. A. Denman, N. Kumar, *Acta Biomater.* **2012**, *8*, 4371.
- [307] S. J. Xiao, M. Textor, N. D. Spencer, M. Wieland, B. Keller, H. Sigrist, in *J. Mater. Sci. Mater. Med.*, Kluwer Academic Publishers, **1997**, pp. 867–872.
- [308] S. S. Lateef, S. Boateng, T. J. Hartman, C. A. Crot, B. Russell, L. Hanley, *Biomaterials* **2002**, *23*, 3159.
- [309] L. Zhang, N. Vilà, T. Klein, G.-W. Kohring, I. Mazurenko, A. Walcarius, M. Etienne, **2016**, DOI 10.1021/acsami.6b02364.
- [310] M. Sabourin, C. T. Tuzon, T. S. Fisher, V. A. Zakian, *Yeast* **2007**, *24*, 39.
- [311] H. Etayash, L. Norman, T. Thundat, M. Stiles, K. Kaur, *ACS Appl. Mater. Interfaces* **2014**, *6*, 1131.
- [312] W. L. Maloy, U. P. Kari, *Biopolymers* **1995**, *37*, 105.
- [313] M.-C. Bourg, A. Badia, R. B. Lennox, *J. Phys. Chem. B* **2000**, *104*, 6562.
- [314] K. K. Kanazawa, J. G. Gordon, *Anal. Chem.* **1985**, *57*, 1770.
- [315] M. V Voinova, M. Rodahl, M. Jonson, B. Kasemo, *Phys. Scr.* **1999**, *59*, 391.
- [316] F. Höök, B. Kasemo, T. Nylander, C. Fant, K. Sott, H. Elwing, *Anal. Chem.*

- 2001, 73, 5796.
- [317] J. Malmström, H. Agheli, P. Kingshott, D. S. Sutherland, *Langmuir* **2007**, 23, 9760.
- [318] P. S. Stewart, M. J. Franklin, *Nat. Rev. Microbiol.* **2008**, 6, 199.
- [319] D. de Beer, P. Stoodley, F. Roe, Z. Lewandowski, *Biotechnol. Bioeng.* **1994**, 43, 1131.
- [320] E. A. Izano, M. A. Amarante, W. B. Kher, J. B. Kaplan, *Appl. Environ. Microbiol.* **2008**, 74, 470.
- [321] P. Speziale, G. Pietrocola, T. J. Foster, J. A. Geoghegan, *Front. Cell. Infect. Microbiol.* **2014**, 4, 171.
- [322] M. Xiao, J. Jasensky, L. Foster, K. Kuroda, Z. Chen, *Langmuir* **2018**, 34, 2057.
- [323] Y. Xue, X. Li, H. Li, W. Zhang, *Nat. Commun.* **2014**, 5, 4348.
- [324] D. Mack, N. Siemssen, R. Laufs, *Infect. Immun.* **1992**, 60, 2048.
- [325] S. S. Magill, J. R. Edwards, W. Bamberg, Z. G. Beldavs, G. Dumyati, M. A. Kainer, R. Lynfield, M. Maloney, L. McAllister-Hollod, J. Nadle, S. M. Ray, D. L. Thompson, L. E. Wilson, S. K. Fridkin, *N. Engl. J. Med.* **2014**, 370, 1198.
- [326] R. O. Darouiche, *N. Engl. J. Med.* **2004**, 350, 1422.
- [327] R. O. Darouiche, R. O. Darouiche, *Clin. Infect. Dis.* **2001**, 33, 1567.
- [328] World Health Organization, *Antimicrobial Resistance: Global Report on Surveillance*, **2014**.
- [329] J. D. Steckbeck, B. Deslouches, R. C. Montelaro, *Expert Opin. Biol. Ther.* **2014**, 14, 11.
- [330] D. G. Moussa, A. Fok, C. Aparicio, *Acta Biomater.* **2019**, 88, 251.
- [331] H. Yazici, M. B. O'Neill, T. Kacar, B. R. Wilson, E. E. Oren, M. Sarikaya, C. Tamerler, *ACS Appl. Mater. Interfaces* **2016**, 8, 5070.
- [332] D. T. Yucesoy, M. Hnilova, K. Boone, P. M. Arnold, M. L. Snead, C. Tamerler, *JOM* **2015**, 67, 754.
- [333] M. Salwiczek, Y. Qu, J. Gardiner, R. A. Strugnell, T. Lithgow, K. M. McLean, H. Thissen, *Trends Biotechnol.* **2014**, 32, 82.
- [334] C. Wisdom, S. K. VanOosten, K. W. Boone, D. Khvostenko, P. M. Arnold, M. L. Snead, C. Tamerler, *J. Mol. Eng. Mater.* **2016**, 04, 1640005.
- [335] C. Wisdom, Y. Zhou, C. C. Chen, C. Tamerler, M. L. Snead, *ACS Biomater. Sci. Eng.* **2019**, acsbiomaterials.9b01213.

- [336] K. Yu, J. C. Y. Lo, M. Yan, X. Yang, D. E. Brooks, R. E. W. Hancock, D. Lange, J. N. Kizhakkedathu, *Biomaterials* **2017**, *116*, 69.
- [337] L. Li, C.-K. Mo, A. Chilkoti, G. P. Lopez, N. J. Carroll, *Biointerphases* **2016**, *11*, 021009.
- [338] N. Harmouche, C. Aisenbrey, F. Porcelli, Y. Xia, S. E. D. Nelson, X. Chen, J. Raya, L. Vermeer, C. Aparicio, G. Veglia, S.-U. Gorr, B. Bechinger, *Biochemistry* **2017**, *56*, 4269.
- [339] M. Abdolhosseini, S. R. Nandula, J. Song, H. Hirt, S.-U. Gorr, *Peptides* **2012**, *35*, 231.
- [340] S. Acosta, L. Quintanilla-Sierra, M. Alonso, C. Aparicio, J. C. Rodríguez-Cabello, *ACS Biomater. Sci. Eng.* **2019**, acsbiomaterials.9b00247.
- [341] B. Rosan, R. J. Lamont, *Microbes Infect.* **2000**, *2*, 1599.
- [342] J. D. Rudney, R. Chen, P. Lenton, J. Li, Y. Li, R. S. Jones, C. Reilly, A. S. Fok, C. Aparicio, *J. Appl. Microbiol.* **2012**, *113*, 1540.
- [343] H.-M. Kim, F. Miyaji, T. Kokubo, T. Nakamura, *J. Biomed. Mater. Res.* **1996**, *32*, 409.
- [344] P. Sevilla, J. Gil, C. Aparicio, *IRBM* **2017**, *38*, 256.
- [345] M. Abdolhosseini, S. R. Nandula, J. Song, H. Hirt, S.-U. Gorr, *Peptides* **2012**, *35*, 231.
- [346] C. Fenoll-Palomares, J. V Muñoz Montagud, V. Sanchiz, B. Herreros, V. Hernández, M. Mínguez, A. Benages, *Rev. Esp. Enferm. Dig.* **2004**, *96*, 773.
- [347] J. D. Rudney, P. D. Jagtap, C. S. Reilly, R. Chen, T. W. Markowski, L. Higgins, J. E. Johnson, T. J. Griffin, *Microbiome* **2015**, *3*, 69.
- [348] C. Dawes, *J. Physiol.* **1972**, *220*, 529.
- [349] A. J. McBain, C. Sissons, R. G. Ledger, P. K. Sreenivasan, W. De Vizio, P. Gilbert, *J. Appl. Microbiol.* **2005**, *98*, 624.
- [350] R. Alink, D. Gerteisen, in *PEM Fuel Cell Diagnostic Tools*, John Wiley & Sons, Inc., Hoboken, NJ, USA, **2011**, pp. 315–332.



# Chapter VIII

---

Appendix

---





## List of abbreviations



---




aa	Amino acid
Ala	Alanine
AMP	Antimicrobial peptide
AMR	Antimicrobial resistance
ANOVA	Analysis of variance
APTES	3-aminopropyltriethoxysilane
ATCC	American type culture collection
ATP	Adenosine triphosphate
BAI	Biomaterial-associated infection
BHI	Brain heart infusion
bp	Base pair
CD	Circular dichroism
CFU	Colony forming unit
CLSM	confocal laser scanning microscopy
CP	Commercially pure
CPTES	(3-chloropropyl)triethoxysilane
cuELdcRs	Charged unbalanced elastin-like diblock co-recombinamers
CV	Crystal violet
CW EPR	Continuous wave electron paramagnetic resonance
Cys	Cysteine
$D_b$	Hydrodynamic radius
DFBR	drip flow biofilm reactor
DLS	Dynamic light scattering
DNA	deoxyribonucleic acid
DRAMP	Data repository of antimicrobial peptides
DSC	Differential scanning calorimetry
ECM	Extracellular matrix
EDTA	Ethylenediaminetetraacetic acid
ELbcR	Elastin-like block co-recombinamer
ELdcR	Elastin-like diblock co-recombinamer
ELP	Elastin-like polypeptide
ELR	Elastin-like recombinamer
Glu	Glutamic acid
Gly	Glycine
HDP	Host defense peptide
HGFs	Human gingival fibroblasts
His	Histidine
HPLC	High performance liquid chromatography

IDP	Intrinsically disordered protein
IDPP	Intrinsically disordered protein polymer
IDPR	Intrinsically disordered protein region
Ile	Isoleucine
ITC	Inverse transition cycling
LCST	Lower critical solution temperature
Leu	Leucine
LVR	Linear viscoelastic region
MALDI-TOF	Matrix-assisted laser desorption/ionization – time-of-flight
MIC	Minimal inhibitory concentration
MHB	Mueller Hinton Broth
MW	Molecular weight
NA	Numerical aperture
OD	Optical density
PB	Phosphate buffer
PBS	phosphate buffered saline solution
PdI	Polydispersity index
Pro	Proline
QCM-D	Quartz crystal microbalance with dissipation
rH	Relative humidity
SAD	Self-assembly domain
SAM	Self-assembled monolayer
SD	Standard deviation
SDS-PAGE	sodium dodecyl sulfate – polyacrylamide gel electrophoresis
SEM	Scanning electron microscopy
SPAAC	strain-promoted alkyne-azide cycloaddition
Sulfo-SMCC	sulfosuccinimidyl 4-(N-maleimidomethyl) cyclohexane-1-carboxylate
TEM	Transmission electron microscopy
THB	Todd-Hewitt broth
$T_t$	Transition temperature
Val	Valine
XPS	X-ray photoelectron spectroscopy
WCA	Water contact angle
ZP	Zeta potential
S	Entropy
$\Delta T_t$	Thermal hysteresis


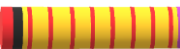

---

## List of recombinant biomaterials developed

ELR	Schematic representation	Sequence
E-I (Chapter 2)		MESLLPVPGVGVPGVGVPGE <sup>G</sup> VP <sup>G</sup> VGVP <sup>G</sup> VP <sup>G</sup> VP <sup>G</sup> VP <sup>G</sup> VP <sup>G</sup> VP <sup>G</sup> VP <sup>G</sup> VP <sup>G</sup> GV <sup>G</sup> VP <sup>G</sup> VP <sup>G</sup> VP <sup>G</sup> VP <sup>G</sup> VP <sup>G</sup> VP <sup>G</sup> VP <sup>G</sup> VP <sup>G</sup> VP <sup>G</sup> VP <sup>G</sup> VP <sup>G</sup> VP <sup>G</sup> VP <sup>G</sup> VP <sup>G</sup> VP <sup>G</sup> GV <sup>G</sup> VP <sup>G</sup> VP <sup>G</sup> VP <sup>G</sup> VP <sup>G</sup> VP <sup>G</sup> VP <sup>G</sup> VP <sup>G</sup> GEG <sup>V</sup> VP <sup>G</sup> VP <sup>G</sup> VP <sup>G</sup> VP <sup>G</sup> VP <sup>G</sup> VP <sup>G</sup> VP <sup>G</sup> VP <sup>G</sup> VP <sup>G</sup> VP <sup>G</sup> VP <sup>G</sup> VP <sup>G</sup> VP <sup>G</sup> GV <sup>G</sup> VP <sup>G</sup> VP <sup>G</sup> VP <sup>G</sup> VP <sup>G</sup> VP <sup>G</sup> VP <sup>G</sup> GV <sup>G</sup> VP <sup>G</sup> VP <sup>G</sup> VP <sup>G</sup> VP <sup>G</sup> VP <sup>G</sup> VP <sup>G</sup> VP <sup>G</sup> VP <sup>G</sup> VP <sup>G</sup> VP <sup>G</sup> VP <sup>G</sup> VP <sup>G</sup> VP <sup>G</sup> GV <sup>G</sup> VP <sup>G</sup> VP <sup>G</sup> VP <sup>G</sup> VP <sup>G</sup> VP <sup>G</sup> VP <sup>G</sup> GV <sup>G</sup> VP <sup>G</sup> VP <sup>G</sup> VP <sup>G</sup> VP <sup>G</sup> VP <sup>G</sup> VP <sup>G</sup> VP <sup>G</sup> VP <sup>G</sup> VP <sup>G</sup> VP <sup>G</sup> VP <sup>G</sup> VP <sup>G</sup> VP <sup>G</sup> GV <sup>G</sup> VP <sup>G</sup> VP <sup>G</sup> VP <sup>G</sup> VP <sup>G</sup> VP <sup>G</sup> VP <sup>G</sup> PGVGIPGVGIPGVGIPGVGIPGVGIP GVGIPGVGIPGVGIPGVGIPGVGIPGV VGIPGVGIPGVGIPGVGIPGVGIPGV GIPGVGIPGVGIPGVGIPGVGIPGVGIP PGVGIPGVGIPGVGIPGVGIPGVGIP GVGIPGVGIPGVGIPGVGIPGVGIPGV VGIPGVGIPGVGIPGVGIPGVGIPGV GIPGVGIPGVGIPGVGIPGVGIPGV PGVGIPGVGIPGVGIPGVGIPGVGIP GVGIPGVGIPGVGIPGVGIPGVGIPGV VGIPGVGIPGVGIPGVGIPGVGIPGV GIPGVGIPGV
S-I (Chapter 2 and 3)		MESLLPVP <sup>G</sup> SGVP <sup>G</sup> SGVP <sup>G</sup> SGVP <sup>G</sup> SGVP <sup>G</sup> SGVP <sup>G</sup> SGVP <sup>G</sup> SGVP <sup>G</sup> SGVP <sup>G</sup> GSGVP <sup>G</sup> SGVP <sup>G</sup> SGVP <sup>G</sup> SGVP <sup>G</sup> SGVP <sup>G</sup> VP <sup>G</sup> SGVP <sup>G</sup> SGVP <sup>G</sup> SGVP <sup>G</sup> SGVP <sup>G</sup> GV <sup>G</sup> PGSGVP <sup>G</sup> SGVP <sup>G</sup> SGVP <sup>G</sup> SGVP <sup>G</sup> GSGVP <sup>G</sup> SGVP <sup>G</sup> SGVP <sup>G</sup> SGVP <sup>G</sup> SGVP <sup>G</sup> VP <sup>G</sup> SGVP <sup>G</sup> SGVP <sup>G</sup> SGVP <sup>G</sup> SGVP <sup>G</sup> GV <sup>G</sup> PGSGVP <sup>G</sup> SGVP <sup>G</sup> SGVP <sup>G</sup> SGVP <sup>G</sup> GSGVP <sup>G</sup> SGVP <sup>G</sup> SGVP <sup>G</sup> SGVP <sup>G</sup> SGVP <sup>G</sup> VP <sup>G</sup> SGVP <sup>G</sup> SGVP <sup>G</sup> SGVP <sup>G</sup> SGVP <sup>G</sup> GV <sup>G</sup> PGSGVP <sup>G</sup> SGVP <sup>G</sup> SGVP <sup>G</sup> SGVP <sup>G</sup> GSGVP <sup>G</sup> SGVP <sup>G</sup> SGVP <sup>G</sup> SGVP <sup>G</sup> SGVP <sup>G</sup> VP <sup>G</sup> SGVP <sup>G</sup> SGVP <sup>G</sup> SGVP <sup>G</sup> SGVP <sup>G</sup> GV <sup>G</sup> PGSGVP <sup>G</sup> SGVP <sup>G</sup> SGVP <sup>G</sup> SGVP <sup>G</sup> PGVGIPGVGIPGVGIPGVGIPGVGIP GVGIPGVGIPGVGIPGVGIPGVGIPGV VGIPGVGIPGVGIPGVGIPGVGIPGV GIPGVGIPGVGIPGVGIPGVGIPGVGIP PGVGIPGVGIPGVGIPGVGIPGVGIP GVGIPGVGIPGVGIPGVGIPGVGIPGV VGIPGVGIPGVGIPGVGIPGVGIPGV GIPGVGIPGVGIPGVGIPGVGIPGV PGVGIPGVGIPGVGIPGVGIPGVGIP GVGIPGVGIPGVGIPGVGIPGVGIPGV VGIPGVGIPGVGIPGVGIPGVGIPGV GIPGVGIPGV

ELR	Schematic representation	Sequence
E <sub>1/2</sub> -I (Chapter 2)		MESLLPVPGVGVPGVPGEGVPG VGVPGVGVPGVGVPGVGVPGE GVGVPGVGVPGVGVPGVGVPGE VPGVGVPGVGVPGVGVPGVGVPE GVPGVGVPGVGVPGVGVPGVGVP GEGVPGVGVPGVGVGIPGVGIPGV GIPGVGIPGVGIPGVGIPGVGIPGV PGVGVGIPGVGIPGVGIPGVGIPGV GVGIPGVGIPGVGIPGVGIPGVGIPGV VGIPGVGIPGVGIPGVGIPGVGIPGV GIPGVGIPGVGIPGVGIPGVGIPGV PGVGVGIPGVGIPGVGIPGVGIPGV GVGIPGVGIPGVGIPGVGIPGVGIPGV VGIPGVGIPGVGIPGVGIPGVGIPGV GIPGVGIPGVGIPGVGIPGVGIPGV PGVGVGIPGVGIPGVGIPGVGIPGV GVGIPGVGIPGVGIPGVGIPGVGIPGV V
oE-I (Chapter 2)		MESLLPVPGEVPGEGVPGEGVPG EGVPGEGVPGEGVPGEGVPGEGV GEGVPGEGVGVGIPGVGIPGVGIPGV PGVGVGIPGVGIPGVGIPGVGIPGV GVGIPGVGIPGVGIPGVGIPGVGIPGV VGIPGVGIPGVGIPGVGIPGVGIPGV GIPGVGIPGVGIPGVGIPGVGIPGV PGVGVGIPGVGIPGVGIPGVGIPGV GVGIPGVGIPGVGIPGVGIPGVGIPGV VGIPGVGIPGVGIPGVGIPGVGIPGV GIPGVGIPGVGIPGVGIPGVGIPGV PGVGVGIPGVGIPGVGIPGVGIPGV GVGIPGVGIPGVGIPGVGIPGVGIPGV VGIPGVGIPGVGIPGVGIPGVGIPGV V
oE <sub>1/2</sub> -I (Chapter 2)		MESLLPVPGEVPGEGVPGEGVPG EGVPGEGVGVGIPGVGIPGVGIPGV GVGIPGVGIPGVGIPGVGIPGVGIPGV VGIPGVGIPGVGIPGVGIPGVGIPGV GIPGVGIPGVGIPGVGIPGVGIPGV PGVGVGIPGVGIPGVGIPGVGIPGV GVGIPGVGIPGVGIPGVGIPGVGIPGV VGIPGVGIPGVGIPGVGIPGVGIPGV GIPGVGIPGVGIPGVGIPGVGIPGV PGVGVGIPGVGIPGVGIPGVGIPGV GVGIPGVGIPGVGIPGVGIPGVGIPGV VGIPGVGIPGVGIPGVGIPGVGIPGV GIPGVGIPGVGIPGVGIPGVGIPGV



ELR	Schematic representation	Sequence
VC (Chapter 4 and 5)		MESLLPVGVPGVGVPKGVPGVGV PGVGVPGVGVPGVGVPGVGVPGK GVPGVGVPGVGVPGVGVPGVGV GVGVPKGVPGVGVPGVGVPGV VPGVGVPGVGVPGKGVPGVGVPGV GVPGVGVPGVGVPGVGVPGKGV GVGVPGVGVPGVGVPGVGVPGV VPGKGVPGVGVPGVGVPGVGV GVPGVGVPGKGVPGVGVPGVGV GVGVPGVGVPGVGVPGKGVPGV VPGVGVPGVGVPGVGVCC
GVC (Chapter 4 and 5)		GKIIKLKASLKLVLGGGGGGGGG LVGVPGVGVPGKGVPGVGVPGVGV PGVGVPGVGVPGVGVPGKGVPGV GVPGVGVPGVGVPGVGVPGVGV GKGVPGVGVPGVGVPGVGVPGV VPGVGVPGKGVPGVGVPGVGVPGV GVPGVGVPGVGVPGKGVPGVGV GVGVPGVGVPGVGVPGVGVPGK VPGVGVPGVGVPGVGVPGVGV GVPKGVPGVGVPGVGVPGVGV GVGVPGVGVPGKGVPGVGVPGV VPGVGVPGVGVCC
VCD* (Chapter 5)		MESLLPVGVPGVGVPKGVPGVGV PGVGVPGVGVPGVGVPGVGVPGK GVPGVGVPGVGVPGVGVPGVGV GVGVPKGVPGVGVPGVGVPGV VPGVGVPGVGVPGKGVPGVGVPGV GVPGVGVPGVGVPGVGVPGKGV GVGVPGVGVPGVGVPGVGVPGV VPGKGVPGVGVPGVGVPGVGV GVPGVGVPGKGVPGVGVPGVGV GVGVPGVGVPGVGVPGKGVPGV VPGVGVPGVGVPGVGVCC

\*D-GL13K were bioconjugated to 2-4 Lys side chains

## Author's contributions

### • Publications

**Sergio Acosta**, Zhou Ye, Conrado Aparicio and José Carlos Rodríguez-Cabello. *Dual self-assembly of genetically engineered polypeptides based on antimicrobial peptides and smart polymers*. ACS Nano. 2019. *Submitted*.

**Sergio Acosta**, Leander Poocha, Luis Quintanilla-Sierra and José Carlos Rodríguez-Cabello. *Charge distribution as molecular modulator of nanostructuring of intrinsically disordered protein polymers*. Biomacromolecules. 2019. *Submitted*.

**Sergio Acosta**, Arturo Ibañez-Fonseca, Conrado Aparicio and José Carlos Rodríguez-Cabello. *Antibiofilm hybrid coatings based on antimicrobial peptides and genetically engineered polypeptides for preventing implant-associated infections*. ACS Applied Materials and Interfaces. 2019. *Submitted*.

Leander Poocha, **Sergio Acosta**, M. Alonso and José Carlos Rodríguez-Cabello. *Introduction of thermoreversible UCST gelation by hydrophobically hijacking LCST related secondary structure motifs in a model elastin-like recombinamer*. Biomacromolecules. 2019. *Submitted*.

Arturo Ibáñez-Fonseca, Tatjana Flora, **Sergio Acosta** and José Carlos Rodríguez-Cabello. *Trends in the design and use of elastin-like recombinamers as biomaterials*. Matrix Biology. **2019**. *In press*. DOI: 10.1016/j.matbio.2019.07.003.

**Sergio Acosta**, Luis Quintanilla, Conrado Aparicio, Matilde Alonso and José Carlos Rodríguez-Cabello. *Recombinant AMP/polypeptide self-assembled monolayers with synergistic antimicrobial properties for bacterial strains of medical relevance*. ACS Biomaterials Science and Engineering. **2019**, 5, 9, 4708-4716. DOI: 10.1021/acsbiomaterials.9b00247.

Zhou Ye, Xiao Zhu, **Sergio Acosta**, Dhiraj Kumar, Ting Sang and Conrado Aparicio. *Self-assembly dynamics and antimicrobial activity of all L- and D-amino acid enantiomers of a designer peptide*. Nanoscale. **2019**, 11, 266-257. DOI: 10.1039/C8NR07334A.

José Carlos Rodríguez-Cabello, Israel Gonzalez de Torre, **Sergio Acosta**, Soraya Salinas and Marcos Herrero. *Elastin-like proteins: molecular design for self-assembling*. Chapter of the book: “*Self-assembling Biomaterials: Molecular Design, Characterization and Application in Biology and Medicine*”. Woodhead Publishing Series. **2018**, 49-78. DOI: 10.1016/B978-0-08-102015-9.00004-6.

Francisco Javier Arias-Vallejo, **Sergio Acosta-Rodríguez**, Tatjana Flora and Sofía Serrano. *Biomedical applications of recombinant proteins and derived polypeptides*. Chapter 8 of the book: “*Biopolymers for Medical Applications*”. CRC-Press, Taylor & Francis Group. **2017**. DOI: 10.1201/9781315368863-9.



## • Conferences

2019 – XLII Congress of the Iberian Society of Biomechanics and Biomaterials (Sociedad Ibérica de Biomecánica y Biomateriales, SIBB). Madrid (Spain). **Oral Communication.** *Molecular reservoirs based on self-assembled AMP/polypeptides.* Sergio Acosta et al.

**Best oral communication award**

2019 – Gordon Research Conference on Elastin, Elastic Fibers and Microfibrils. Manchester, NH (USA). **Oral and Poster Communication.** *Elastin-like recombinamers and antimicrobial Peptides: Self-Assembly dynamics and antimicrobial properties of hybrid polypeptides.* Sergio Acosta et al.

2019 – Gordon Research Seminar on Elastin, Elastic Fibers and Microfibrils. Manchester, NH (USA). **Oral and Poster Communication.** *Self-assembly dynamics of elastin-like recombinamers and antimicrobial peptides.* Sergio Acosta et al.

2019 – 13<sup>th</sup> International Symposium on Frontiers in Biomedical Polymers. Puerto de la Cruz (Spain). **Oral Communication.** *Advanced antimicrobial recombinant polymers: insights into the self-assembly - bactericidal properties relationship.* Sergio Acosta et al.

2018 – XLI Congress of the Iberian Society of Biomechanics and Biomaterials (Sociedad Ibérica de Biomecánica y Biomateriales, SIBB). Madrid (Spain). **Oral Communication.** *Drug-free biomimetic coatings with antibiofilm activity.* Sergio Acosta et al.

- 2018 – XV reunión del grupo especializado de polímeros (GEP) de la RSEQ y RSEF. Punta Umbría (Spain). **Oral Communication.** *Self-assembled amphiphilic elastin-like diblock co-recombinamers: insights into hierarchical nanostructuring.* Sergio Acosta et al.
- 2018– 29<sup>th</sup> Annual Conference of the European Society for Biomaterials (ESB 2018). Maastricht (The Netherlands) **Oral Communication.** *Antibiofilm coatings based on ELRs and AMPs for preventing orthopaedic implant-associated infections.* Sergio Acosta et al.
- 2018 – 5<sup>th</sup> World Congress of the Tissue Engineering and Regenerative Medicine International Society (TERMIS). Kyoto (Japan). **Oral Communication.** *Biomimetic recombinant coatings with antimicrobial properties for preventing implant infections.* Sergio Acosta et al.
- 2018 – 96<sup>th</sup> General Session of the international Association for Dental Research (IADR). London (UK). **Oral Communication.** *Antimicrobial recombinant coatings for peri-implant disease prevention.* Sergio Acosta et al.
- 2017 – XL Congress of the Iberian Society of Biomechanics and Biomaterials (Sociedad Ibérica de Biomecánica y Biomateriales, SIBB). Barcelona (Spain). **Oral Communication.** *Antimicrobial properties of recombinant polymeric coatings.* Sergio Acosta et al.
- 2017 – Future Investigators of Regenerative Medicine (FIRM) Congress. Girona (Spain). **Oral and Poster Communication.**

*Antistaphylococcal coatings based on chimeric ELRs.* Sergio Acosta et al.

2017 – 28<sup>th</sup> Annual Conference of the European Society for Biomaterials (ESB 2017). Athens, (Greece). **Oral Communication.** *Antimicrobial coatings based on elastin-like recombinamers and antimicrobial peptides.* Sergio Acosta et al.

2016 – XXXII LIAC Meeting on Vascular Research. Ustica, Sicily (Italy) **Oral Communication.** *New insight into the structure-property relationship of physically crosslinked elastin-like hydrogels.* Sergio Acosta et al.

2015 – 1st Young Researchers Workshop on Biomaterials and Bioapplications - BIOMAPP 15. San Sebastian (Spain) **Poster.** *Physically crosslinked elastin-like hydrogels: insight into the structure-properties relationship.* Sergio Acosta et al.

## • Teaching

2019 - Co-supervision of Master's degree thesis entitled "Caracterización de micelas autoensambladas basadas en polipéptidos anfifílicos multibloque" by Julio Fernández Fernández at the University of Valladolid (Spain).

- Co-supervision of BSc thesis entitled "Caracterización de nanopartículas mediante técnicas de dispersión dinámica de luz de recombinámeros tipo elastina (ELRs)" at Gonzalo López Caubilla in the University of Valladolid (Spain).

- 2018 - Teaching activities in the Master degree in Physics at the University of Valladolid.
- Teaching activities in the BS Degree in Industrial Engineering at the University of Valladolid (Spain).
- 2017 - Teaching activities in the BS Degree in Industrial Engineering at the University of Valladolid (Spain).



